Gene therapy in combination with an approach targeting the tumour microenvironment in Glioblastoma

Asya Petkova

Supervisors: Professor Ijeoma Uchegbu

Professor Andreas Schätzlein

A dissertation submitted in part fulfilment of the requirements for Doctor of Philosophy degree at

THE SCHOOL OF PHARMACY

UNIVERSITY COLLEGE LONDON

2019

DECLARATION

I, Asya Petkova confirm that the work presented in this thesis is my own. Where information has been derived from other sources, I confirm that has been indicated with the respective reference. The thesis outlines research that has been conducted in the UCL School of Pharmacy between May 2016 and September 2019 under the supervision of Professor Ijeoma Uchegbu and Professor Andreas Schatzlein.

……………………… ………………………

Asya Petkova Date

ABSTRACT

The objective of this work is to develop glycol chitosan (GC) based gene delivery vehicles with an extracellular matrix (ECM) targeting capacity incorporating hyaluronidase as part of a three-component electrostatic complex of a polymer, a plasmid and an enzyme to improve the diffusion of the nanosystems in the tumor microenvironment. This is also to the best of our knowledge the first study, describing a quantitative strategy using an HPLC method to estimate the amount of bound enzyme to the ternary electrostatic complex.

Our data showed that molecular weight, polymer to DNA mass ratio, treatment and complexation time as well as complexation medium all influence the potential of the nanosystems to deliver genes in the U87 glioma cell line *in vitro*. When compared to the positive control, Lipofectamine a GC polymer of 37 kDa (GC37) showed about 70 % of Lipofectamine's transfection efficiency to deliver a β-Gal reporter gene to U87 cells after 17 h treatment time and 24 h complexation time at 4° C. The ternary electrostatic complexes were ineffective at delivering β-Gal DNA *in vitro,* although they showed some transfection potential in mice on nasal administration. However further studies are needed to confirm these findings and to identify the brain regions where the β-Gal protein is expressed. A subcutaneous and an intranasal route of administration were used to test the *in vivo* transfection efficiency of the GC37 polyplexes in mice and to compare it to the positive control Lipofectamine and naked β-Gal. Lipofectamine/β-Gal lipoplexes (LF2) appeared with the highest signal measured by IVIS, 48 h post subcutaneous administration when compared to the naked plasmid (D2) and the GC37/β-Gal polyplex (GCP3) all at the same dose (0.207 $\mu g\ kg^{-1}$ β-Gal DNA), although statistical analysis identified no significant differences between any of the treatments. On the other hand, the main intranasal study showed baseline levels of active β-Gal enzyme for mice treated with Lipofectamine/ β-Gal lipoplexes (LF1), naked β-Gal DNA (D1) and GC37/β-Gal polyplexes (GCP2) all at the same dose (0.067 $mg\ kg^{-1}$ β-Gal DNA). This raised important questions, which need addressing such as the suitability of the enzyme activity assay for nasal administration along with reproducibility concerns surrounding nasal administration in mice. Although further studies are needed to reveal the full *in vivo* potential of GC37 for effects occurring away from the administration site, GC37 could offer a considerable advantage as an attractive candidate for polymer-mediated gene therapy due to its significantly lower cytotoxicity than Lipofectamine and comparable transfection potential.

IMPACT STATEMENT

Gene therapy or the intracellular delivery of genetic material with a therapeutic potential has sparked a great deal of research interest due to the possibility of providing a radical treatment solution rather than just alleviating disease symptoms. Viral vectors and non-viral vectors (liposomes, polymers and proteins) have been widely used in pre-clinical studies for the delivery of genetic material, offering protection from enzymatic degradation, promoting intracellular trafficking of the packaged nucleic acid, hence efficiency [1].

The real hope for the clinical relevance of gene therapy came in 1989 with the first approved clinical trial using a retroviral vector introducing a marking neomycin gene in tumor-infiltrating lymphocytes (TILs) [2]. TILs were then transferred intravenously in five patients with advanced malignant melanoma with no reported safety concerns and considerable regression of the cancer in almost half of the patients. This marker study served as the first direct evidence for the successful genetic modification of cells, which were returned to patients without any harm. It paved the way for the approval of many more gene therapy clinical trials with reports of 2597 entries until 2017 of ongoing and completed clinical trials targeting cancer, monogenic diseases (cystic fibrosis), infectious diseases and cardiovascular diseases [1]. However, only 0.1 % of all gene therapy products have been reported to arrive to Phase IV with no polymer-mediated gene products being currently marketed.

Polymer-mediated gene transfer is still facing some challenges related to its complex nature. The three main events in polymer-mediated gene therapy, which have an impact on the transfection efficiency are cellular uptake, endosomal escape and nuclear import (the latter being important only for the delivery of plasmid DNA). The lack of understanding, which physicochemical characteristics of the polymer and/or the resulting polyplex play a role in each of those stages and their effect on transfection efficiency make their clinical application a cumbersome task. This work outlines an approach for the modification of the structure of the polymer vector aiming to increase its efficiency by facilitating endosomal escape. Next, it gives a systematic approach for the optimisation of the *in vitro* transfection efficiency of the nanocomplexes in the glioma cell line U87. Moreover, it sheds light on the importance of polymer molecular weight for transfection. Additionally, it simultaneously focuses on a strategy targeting the tumor microenvironment in glioblastoma, which is a physical barrier for the delivery of therapeutic molecules further into the tumor. Finally, it explores the *in vivo* potential of the nanocomplexes to reach the brain via an intranasal route of administration bypassing the blood brain barrier.

The new knowledge generated will be used to gain a better understanding of the factors influencing the transfection efficiency of polymers *in vitro* and *in vivo*. This in turn may change the *status quo* of polymer-mediated gene delivery and set up the scene for their improved clinical performance. Additionally, on a narrower scope the work undertaken will have a direct impact on our research group. The findings will open new research opportunities seeking to answer the remaining questions and will further contribute to achieving the overarching goal of expanding the clinical relevance of polymers in gene therapy.

ACKNOWLEDGEMNTS

I would like to express my deepest gratitude to the Centre for Doctoral Training (CDT) in Nanomedicines and Targeted Therapeutics for giving me this incredible opportunity to complete the four-year PhD program in the UCL School of Pharmacy. I would like to thank Professor Steve Brocchini for his unconditional support, for his kindness and help throughout the duration of the course. My PhD experience would not have been the same without the CDT and I am extremely grateful to all the people I met. The CDT was also the reason for the beginning of a very special friendship. A parallel that springs in mind is a relationship one has with family. Thank you, Karolina for all the funny moments together, for all the little rituals we created and all the memories we shared. This friendship has always been marked by strong emotions on either end of the spectrum and it has passed multiple tests. Thanks to our great memories, I would be able to tell my future grandchildren about the day their grandmother spent researching dinosaurs instead of doing her PhD work, the day she spent hours on a double decker, making a roundtrip of London with IKEA shopping or everything about London's burger culture. I must say I always remember those with a big smile on my face. I would also want to thank, Rachael, Raphael and Alexander for their major contribution to the unforgettable PhD journey, thank you for all the moments we shared together.

I have no words to describe how much appreciation and admiration I have for both my supervisors – Prof Ijeoma Uchegbu and Professor Schätzlein. Thank you, Ijeoma for the invaluable scientific guidance and advice, for all the help and support you have given me not only with my work, but also when I was going through a lot in my personal life. Thanks to you, I can call myself an independent researcher and thanks to you I gained confidence and developed as a scientist. I will always look up to you with an enormous amount of respect and value your opinion and advice. Thank you, Andreas for always being so easy to reach and ready to discuss scientific or non-scientific matters with me. Thank you, for the words of encouragement when I needed them the most, for your advice, support and input on my work and of course for your sense of humor, which on many occasions improved my mood.

I would like to say how privileged I feel, because of the people I met in my group and in the School of Pharmacy in general. Thanks to all the people in my group for the long lunches, coffee breaks and dinners full of random topics and funny moments. I will miss all the traditions we created together and the bonding sessions in the bar and in the office or in the park. I would like to say a huge thank you to Dr Rui Lopes, Dr Ilona Kubajewska, Dr Alex Vaideanu, Dr David Workman, Dr Xian Weng, Ryan Mellor, Liisa Niitsoo, Savvas Dimiou, Moutaz Badr, Gang Li, Corinna Schosser, Akunnaya Ezekwem and Abdurahman Halwanii. Thank you, Rui and Ryan, for all the help, advice, trainings, explanations, guidance and for sacrificing your precious time to prioritize tasks, which aren't yours. Thank you, Ilona, for all the conversations we had, for your help and support on any matter (scientific or personal) at any time of the day or night. Thanks for being there for me, when I needed you and for sharing all those incredible moments, we had together during these few years. Thank you, Alex for all your help with my in vivo work, with TEM, my cells and for always being ready to answer some of the random questions I had. Liisa, I am so glad we managed to spend a year together in the office, thanks a lot for being so patient when answering my technology questions or any other random questions with obvious to you answers.

I would also like to thank my friends outside the School of Pharmacy for their perseverance. Sincere appreciation and love go to Sandra, Amy, Holly, Anna, Maria Galia for tolerating my mood swings and complaints and still sticking by my side besides my long periods of absence. Special thanks to you, Sandra for being my friend for ten years already and most importantly for taking care of my cultural and holiday life during these years. I am extremely lucky to have you as a friend, thanks for being part of my life.

Finally, I would like to express my deepest love and appreciation for my family. Mum, thank you for your unequivocal care, for always finding the right words to console me or distract me, for being my absolute pillar of support during these four years. Sis, I am so grateful to have you by my side, thank you for always being there for me, for your unconditional love and your invaluable advice. I would have not made it here, if it wasn't for your permeant encouragement to be braver and take more risks. Finally, I would like to dedicate this thesis to my dad, who I am sure would have been extremely proud of me and my achievements.

Table of Contents:

LIST OF FIGURES:

LIST OF TABLES:

LIST OF ABBREVIATIONS:

ACN - acetonitrile

ATP - adenosine triphosphate

Ajs - adherens junctions

AdV - adenovirus

2-AEB - 2-(Boc amino-ethyl) bromide

Ago - argonaute protein

BSA - bovine serum albumin

β**-Gal** - β-Galactosidase

BBB - blood brain barrier

BCSF - blood-cerebrospinal fluid barrier

CMV - cytomegalovirus

CNS - central nervous system

CAF - cancer-associated fibroblasts

CPPs - cell penetrating peptides

CED - convection enhanced delivery

COSY - correlation spectroscopy

DLS - dynamic light scattering

DC - dendritic cells

CD - cytosine deaminase

DOPE - 1,2-dioleoyl-sn-glycero-3-phosphoethanolamine

DOTMA - N-[1-(2,3-dioleyloxy) propyl]-N,N,N-trimethylammonium chloride

DOTAP - N-[1-(2,3-dioleoyloxy)]- N,N,N-trimethylammonium propane methyl-sulfate

DMRIE - C 1,2-dimyristy-loxypropyl-3-dimethyl-hydroxy ethyl ammonium bromide

DCM - dichloromethane

dGTP - deoxy guanosine triphosphate

DGL - dendrigraft poly-L-Lysine -

DEPT - distortionless enhancement of polarisation transfer

EAGC - ethyl-amino glycol chitosan

EPR - enhanced permeation and retention effect

EDTA - ethylenediaminetetraacetic acid

EPH - ethyl-amino polyplex coated with hyaluronidase

EGFR - epidermal growth factor receptor

EC - endothelial cells

EP - ethyl-amino polyplex

EPI - epirubicin

FBS - foetal bovine serum

5-FU - 5-flurocytosine

GC - glycol chitosan

GFP - green fluorescent protein

GCP - glycol chitosan polyplex

GCPH - glycol chitosan polyplex with hyaluronidase

GAG - glycosaminoglycans

GBM - glioblastoma multiforme

GCV - ganciclovir

GCV-3P - ganciclovir 3-phosphate

GPC - gel permeation chromatography

HAS - hyaluronan synthase

HSV-1 - herpes simplex virus type I

hATTR - hereditary transthyretin amyloidosis

HMQC - heteronuclear multiple quantum coherence

IGFIR - Insulin-like growth factor 1 receptor

IDH-1 - isocitrate dehydrogenase

ITC – Isothermal Titration Colorimetry

LF - lipofectamine

LOX - lysil oxidase

LPL - lipoprotein lipase

LuGal - 6-O-β-galactopyranosylluciferin

MTS - [3-(4,5-dimethylthiazol-2-yl)-5-(3-carboxymethoxyphenyl)-2-(4-sulfophenyl)-2H-tetrazolium

MEME - minimal essential medium eagle

MMP - matrix metalloproteinases

mRNA - messenger RNA

Mw - molecular weight

MALLS - multi-angle laser light scattering

NLS - nuclear localisation signal

NPC - nuclear pore complex

NPs - nanoparticles

NADPH - nicotinamide adenine dinucleotide phosphate

NMR - nuclear magnetic resonance

NMP - N-methyl pyrolidone

pDNA - plasmid DNA

ONPG - o–nitrophenyl–β-D- galactopyraniside

PDI - polydispersity

PBS - phosphate buffered saline

PTEN - phosphatase and tensin homologue

PDGFRA - platelet-derived growth factor receptor alpha

PLL - poly(L-lysine)

PLA - polyarginine

PEI - polyethylene imine

PAMAM - poly amidoamine,

PBAE - poly beta amino esters

PEG - polyethylene glycol

PES - phenazine ethosulfate

RGD - arginine, glycine, aspartate

RHAMM - hyaluronan-mediated motility receptor

RNAi - RNA interference

RISC - RNA inducing silencing complex

RP-HPLC - reversed-phase high performance liquid chromatography

RSV - respiratory syncytial virus

RFP - red fluorescent protein

RCF – relative centrifugal force

SLRP - small leucine-rich proteoglycans

SMS - starch modified spermine

SGT - somatic gene therapy

SEC - size exclusion chromatography

siRNA - short interfering RNA

TIP - tumour interstitial pressure

TAE - tri acetate ethylenediaminetetraacetic acid

TIL - tumour infiltrating lymphocytes

Tjs - tight junctions

TGF β **-** tumour necrosis factor

TMZ - temozolomide

TTR - transthyretin gene

Tk - thymidine kinase

T-PER - tissue protein extraction reagent

TS - thymidine synthase

TFA - trifluoracetic acid

TMS - tetramethysilane

VEGF - vascular endothelial growth factor

VDAs - vasculature disrupting agents

VTAs - vasculature targeting drugs

WHO - world health organization

1 Introduction

1.1 Delivery of drugs to the Central Nervous System (CNS)

Treating neurological disease such as brain tumours, neurodegenerative diseases, inborn metabolic errors or infectious diseases is a challenging task due to the presence of two protective barriers *en route* to the brain, the blood brain barrier (BBB) and the blood-cerebrospinal fluid barrier (BCSF) [3,4]. These two barriers regulate the transport of molecules across in order to maintain homeostasis. They represent the intrinsic defence mechanism of the brain against toxic and infectious agents, but at the same time they are a major obstacle for the efficient delivery of drugs targeting neurological diseases and conditions.

1.1.1 The Blood Brain Barrier (BBB) and the blood-cerebrospinal fluid barrier (BCSF)

The BBB is a capillary barrier of endothelial cells (ECs), packed closely together by tight junctions (Tjs) and adherens junction (Ajs), which prevent paracellular transport[5] with low pinocytotic activity [6,7] but limited transcellular transport occur [8]. Unlike the BBB, which consists of endothelial cells connected via Tjs, the BCSF barrier consists of choroid plexus cells (vascular tissue found in all brain ventricles) connected with Tjs surrounding a macrovascular endothelium with an intracellular gap and fenestrations [9,10]. On the other side of the BCSF barrier is the arachnoid membrane, which covers the brain and is also made from cells connected with Tjs. The transport of molecules to the brain and the CSF under physiological conditions is mediated by transcellular pathways including passive transport (diffusion), active transport or both Various active transport mechanisms of molecules (carrier-mediated influx or efflux) have been reported along with paracellular passive diffusion [11,12] (**Figure 1-1**). The movement of molecules depends largely on their charge, hydrophobicity and molecular weight [12,13]. Low molecular weight lipophilic molecules transverse the BBB by passive diffusion, while hydrophilic ones use receptor-mediated or adsorptive active transport [14]. These mechanisms are in place to ensure the supply of the brain with amino acids, nucleotides, carboxylic acids and glucose. Receptor-mediated transport ensures the movement of macromolecules with a conjugated receptor ligand such as insulin, transferrin and lactoferrin. Adsorptive-mediated endocytosis aids in the transport of cationic substances (**Figure 1-1**).

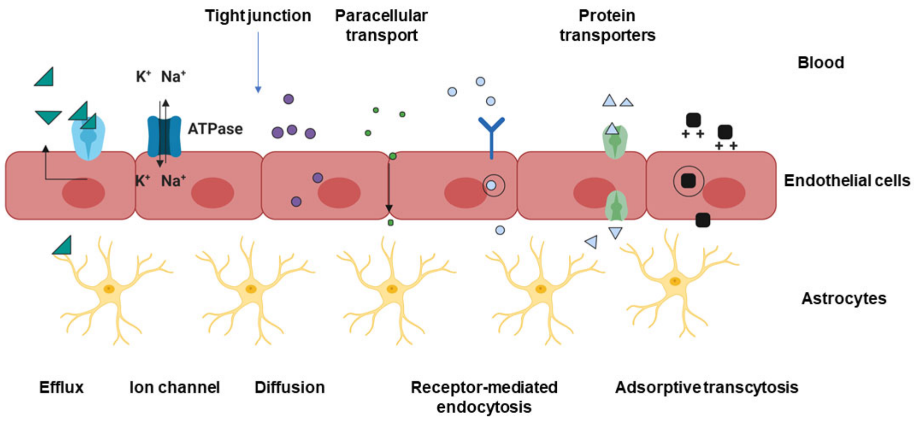

Figure 1-1: *The Blood Brain Barrier regulates the transport of molecules and ions through a variety of mechanisms.*

1.1.1.1 Intranasal administration to bypass the BBB

Typically, intranasal administration has been largely explored as an administration route to treat minor local conditions such as nasal congestion, rhinorrhea, nasal infections or rhinosinusitis [15]. Nasal delivery undoubtedly has numerous advantages such as ease of administration, non-invasiveness, rapid onset of action, relatively large and permeable surface area and avoidance of the first pass hepatic metabolism. However, the novelty of using intranasal delivery comes from its suitability to mediate the transport of therapeutic molecules through the olfactory “neuroepithilim” to the brain since this is the only part of the CNS unprotected by the BBB [16].

Intranasal administration is mediated through the olfactory neuronal pathway, the trigeminal neuronal pathway or systemically (**Figure 1-2**). Olfactory neurons connect the olfactory region of the nasal cavity to the brain – olfactory bulb and frontal cortex. By contrast, the trigeminal neurons connect the respiratory region to more rostral parts of the brain – pons, medulla and spinal cord. The trigeminal nerve has three branches, mandibular, maxillary and ophthalmic, but only the last two are proven to be involved in the transport of molecules from the nose to the brain due to the presence of maxillary and ophthalmic neurons passing through the nasal mucosa [17]. It is hard to differentiate if molecules are using the olfactory or the trigeminal pathway, since the olfactory regions is also innervated by branches of the trigeminal nerve, it is generally believed that both are involved. Moreover, trigeminal nerve branches passing through the cribriform plate (a horizontal segment forming the roof of the nasal cavity) Is involved in the delivery of substances from the nose to the forebrain[18].

An intranasally administered drug will diffuse through the nasal mucosa reaching the branches of the trigeminal nerve present in the olfactory and respiratory region. A variety of transport mechanism have been proposed for the movement of drugs through the nasal mucosa such as paracellular, transcellular, carrier-mediated transport, receptor-mediated transport, and transcytosis [19,20]. It is thought that the transport of the drug to the brain via the trigeminal pathway is mediated through either intracellular trafficking or endocytosis. The olfactory pathway includes the transport of the drug through paracellular and transcellular mechanisms from the nasal cavity through the olfactory mucosa. Then transport through the axon and nerve bundles across the cribriform plate deliver the molecule to the olfactory bulb. Finally, intraneuronal slow (axonal transport) and extra-neuronal rapid transport (through perineural channels) is involved in the delivery of the drug from the olfactory bulb to the brain [17].

On nasal administration after mucocilliary clearance the molecule will be transported to the interior of the nasal cavity to the respiratory, olfactory neuronal networks and blood vessels [21,22]. It will then be transported through the blood vessels into the systemic application and then across the BBB to the brain. The neuronal pathway through the olfactory or trigeminal nerves via intra or extracellular routes to reach the olfactory bulb and the brain is the preferred pathway of drugs after intranasal delivery[21,23].

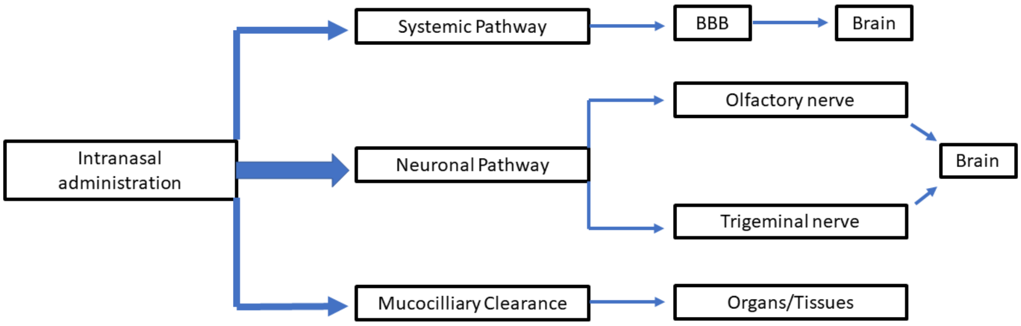

Figure 1-2*: Diagram illustrating the nose to brain transport of drug molecules and the central role of the olfactory and trigeminal neuronal pathways.*

1.2 The extracellular matrix of healthy tissues

The extracellular matrix (ECM) is the non-cellular component of all connective tissues. It consists of a variety of macromolecules such as fibrous proteins; collagen, fibronectin, elastins and laminins; glycosaminoglycans (GAGs) such as hyaluronic acid, chondroitin sulfate, heparan sulfate; proteoglycans (PGs) e.g. decorin, syndecans, perlecan, and agrin. [24]. These macromolecules form complex self - assemblies and three-dimensional structures, which are heavily hydrated and provide a mechanical support for the surrounding cells and organs. In addition to the physical scaffolding function of the ECM it is known to play a very important role in cell signalling pathways and be involved in cell growth, cell survival, differentiation and homeostasis [25,26].

1.2.1 Collagens

Collagens represent around 30 % of the total protein mass of multicellular organisms, which makes them also the most predominant structural component of the ECM [26] . Collagens of different types can form fibres, which provide high tensile strength and regulate cell adhesion and migration [26]. The fibrillar structures are formed due to the presence of repeating $(\text{Gly-X-Y})_n$ amino acid sequences, where X is usually a proline and Y is a hydroxyproline. The unique repeating sequences form triple helical structures, which are thought to be the reason for the formation of the rod-like structures of the collagen fibres [27,28]. Interstitial collagen is secreted by either stromal fibroblasts or fibroblast recruited from neighbouring tissues [29].

1.2.2 Elastins

Elastins are fibrous proteins, which are also abundant in connective tissues. Elastins can also form fibres, which facilitate passive recoil of connective tissues exposed to continuous stretch and account for their resilience and extensibility [30]. Enzymes of the lysyl oxidase (LOX) family are responsible for crosslinking the secreted tropoelastin (the precursor of elastin) into elastin fibres [31].

1.2.3 Fibronectins

Fibronectins are another type of fibrous ECM proteins, which are closely associated with cell attachment[32]. Fibronectins have many important functional domains including a heparin, fibrin, collagen and most importantly an integrin binding domain (Arg-Gly-Asp or RGD motif)[33]. Integrins function as a linker mediating the interactions between the extracellular matrix and the cytoskeleton hence they are referred to as transmembrane adhesion proteins [32]. *Takashashi et al.* showed that the integrin binding domain is a binding site for a5β1 and aVβ3 integrin adhesion molecules[34]. They also showed that interaction with the RGD motif is essential for the formation of fibronectin fibrils. The integrin binding domain is exposed after an extensive mechanical stretch by cellular traction forces, which is shown to be several times over its resting length [35].

1.2.4 Glycosaminoglycans and Proteoglycans

GAGs can be either sulfated (heparan sulfate, chondroitin sulfate and keratin sulfate) or non-sulfated (hyaluronic acid) [34] polysaccharides consisting of repeating disaccharide sugar units (N-acetylglucosamine, N-acetylglucosamine sulfate, D-glucuronic acid or L-iduronic acid and galactose). The molecules of GAGs are very hydrophilic and interact with water molecules in the ECM to form extensive hydrogel networks, which allows them to withstand high compressive forces[36]. GAGs are usually modified with specific proteins in the rough endoplasmic reticulum and Golgi apparatus and secreted as proteoglycans[37].

Proteoglycans may be classified into three groups based on the GAG chain and the core protein localization. The three groups are small leucine rich proteoglycans (SLRPs), modular PGs and cell surface PGs. [34]. Proteoglycans are part of very important signalling pathways, hence mutations in the genes coding for PGs result in many genetic diseases [24]. SLRPs can bind and activate epidermal growth factor receptor (EGFR), insulin-like growth factor 1 receptor (IGFIR) as well as tumour growth factor TGF β [34,38]. Modular PGs are known to perform a variety of functions facilitating cell adhesion, migration and proliferation. Additionally basement modular PGs, such as agrin and perlecan) have dual functions of pro and anti-angiogenic factors [39]. Syndecans and glypicans as cell surface PGs can act as co-receptors of other cell surface receptors [34].

Hyaluronic acid (also known as hyaluronate or hyaluronan) is a negatively charged, unbranched polysaccharide consisting of N-acetylglucosamine and glucuronic acid covalently attached with β-(1,4) glyosidic bonds. It is synthesized by the hyaluronan synthase enzymes HAS 1, HAS 2 and HAS 3 [40] . By contrast to the above-mentioned proteoglycans hyaluronan is an unmodified GAG, which is not attached to a specific protein to form a proteoglycan. In humans hyaluronan is found to be degraded by a family of six enzymes called hyaluronidases [41], which have different locations in the body. Similarly, to all the other GAGs, hyaluronan networks retain water molecules and hyaluronic acid together with the other ECM components play a crucial role in maintaining water balance, porosity and malleability of the ECM as part of homeostasis mechanisms.

1.3 The extracellular matrix of solid tumours as a barrier for the delivery of drugs

Malignant solid tumours are characterised by the presence of a stroma and an extracellular matrix (ECM). The stroma comprises of stromal cells, which include cancer-associated fibroblasts (CAFs) [42] , pericytes [43], endothelial cells [44], tumour infiltrating hematopoietic cells and innate and adaptive immune cells [45]. The ECM is composed of glycoproteins, GAGs and a variety of ECM proteins such as, collagens, laminins, elastins *etc.* An event related to tumorigenesis is the uncontrolled extensive fibrosis called desmoplasia, which is characterised by an increase in the synthesis of matrix proteins by myofibroblasts **(Figure 1-3).** Myofibroblasts are transdifferentiated fibroblasts depositing copious amounts of collagen, which may be crosslinked by the LOX (lysyl oxidasees) resulting in a stiffened ECM [46]. Myofibroblasts and tumour cells are also responsible for the deposition of matrix metalloproteinases (MMPs), which degrade all kinds of ECM proteins facilitating the remodelling of the ECM[47]. In addition to the rigid, rich in collagen ECM, a number of solid tumours and neoplastic tissues in the body have also been shown to overexpress hyaluronan [48]. In a healthy state hyaluronan is a polysaccharide universally distributed in different parts of the body. Its function is to ensure not only the rigidity of connective tissues, where it is abundant, but also to bind to the CD44 receptor and RHAMM (hyaluronan-mediated motility receptor) triggering signal transduction pathways associated with cell proliferation, migration and recruitment of neutrophils [48]. In the diseased cancer state these roles of hyaluronan, exacerbate further the condition by decreasing the accessibility of the tumour stromal cells from one side and by increasing the tumour aggressiveness on the other, promoting cell proliferation, migration and metastasis [49]. In the same way while in normal tissues the ECM as a whole plays a role in protecting the cells from bacterial invasion, maintaining homeostasis, ensuring functional relations between cells and regulating macromolecule transport through the interstitium: in solid tumours the stiffened, rigid ECM blocks the transport of macromolecules contributing to their physical resistance to drugs [25], antibodies [50], immunotoxins [51] and oncolytic adenoviruses [52] **(Figure 1-3)**.

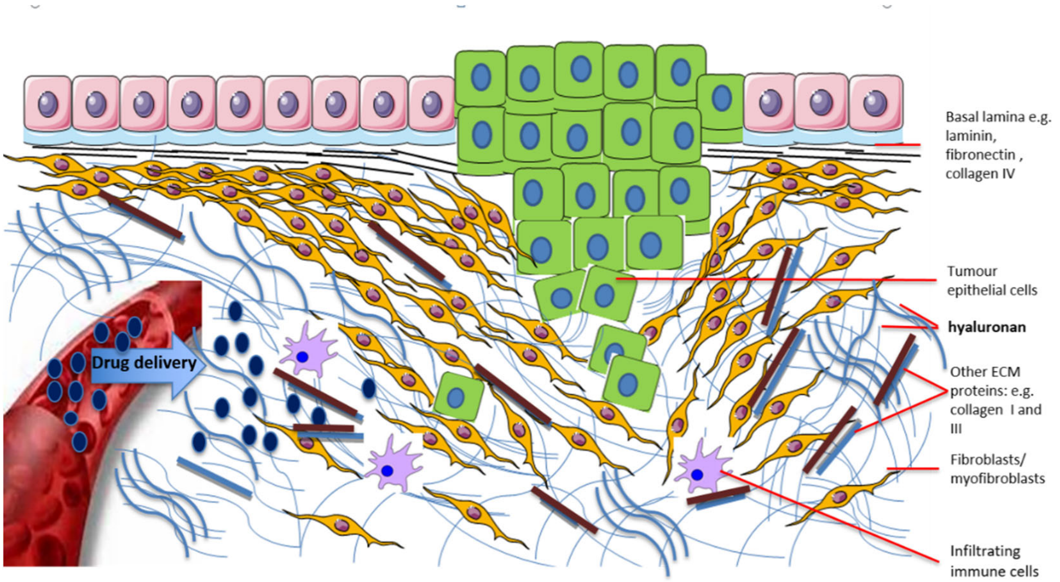

Figure 1-3: *The desmoplasmic reaction and the overexpression of matrix components hampers the delivery of therapeutics in solid tumours.*

1.3.1 Gliomas

Malignant gliomas are extremely aggressive brain tumours and they progress by invading the normal brain parenchyma, which makes them very difficult to treat by local surgery and radiotherapy [53]. High-grade gliomas (III and IV) are classified as diffuse gliomas due to their aggressive nature of infiltrating the surrounding healthy brain tissue, which results in low chances of remission due to continues expansion of the tumour. Fast spreading of the tumour even for low-grade gliomas (I and II) results in a rapid progression to high grade III and IV gliomas [6,54]. The World Health Organization (WHO) classifies Glioblastoma multiforme (GBM) as a grade IV glioma, which arises from astrocytes [54,55]. GBM affects about three per 100,000 people every year with recurrence in nearly all patients [56].

The standard of care currently includes brain surgery, followed by radiotherapy in combination with temozolomide (TMZ) [8]. Additionally, a monoclonal antibody (bevacizumab) targeting the vascular endothelial growth factor (VEGF) is used for the treatment of recurrent gliomas [57]. However, the median survival post diagnosis and treatment is between 12 and 15 months with a patient’s death rate of greater than 95 % within 5 years of diagnosis [58]. GBM remains an incurable disease and new alternatives are urgently needed to improve treatment outcomes.

1.3.1.1 Gene expression in GBM

The sequential acquisition of genetic mutations in benign gliomas leads to the development of malignant gliomas [59]. Four clinical subtypes have been identified for

GBM including: classical, neural, proneural and mesenchymal [60]. The difference in the clinical subtypes comes from the set of characteristic mutations for each one of them.

Classical GBM is described in 95% of the cases, arising *de novo*, within 3 - 6 months in older patients [55]. The genetic alterations in a classical GBM include an amplification of chromosome 7 along with a deletion of chromosome 10, overexpression of epidermal growth factor (EGFR) and mutations in phosphatase and tensin homologue (PTEN) [55,60]. The overexpression of EGFR results in increased proliferation through the Ras-Sch-Grb-2 pathway, which in turn leads to uncontrolled cell growth together with a reduction in apoptosis [61]. Furthermore a point mutation in the EGFR amplicons has been reported for almost half of the classical GBM cases analysed [60]. The mutant variant III of the receptor vIII EGFR is associated with permanent activation, which causes mitogenic effects and induces cell division[62]. PTEN is a tumour suppressor and the loss of function caused by a mutation results in failure to attenuate the signalling cascade in the P13K/Akt/mTOR causing proliferation, uncontrolled growth and migration [63].

Proneural or secondary GBM usually takes 10 - 15 years to develop and arises from a lower grade astrocytoma [61]. Typical mutations often present in proneural GBM are overexpression of the platelet derived growth factor receptor alpha (PDGFRA), mutated p53 tumour suppressor, retinoblastoma genes and isocitrate dehydrogenase (IDH-1) [58,60,61]. PDGFRA is a mitogen, the increased expression of which leads to tumour cell proliferation [61]. p53 acts as a switch to G1 in cell cycle promoting cellular death and apoptosis, hence a mutated p53 leads to cell immortalization and uncontrolled division. IDH-1 mutations have been associated with changes in histone acetylation which can in turn alter gene expression (upregulate PDGFRA) and chromatin structure [64,65].

Mesenchymal GBM is characterised with deletions or mutations in neurofibromin-1, which is another tumour-suppressor gene described for 32 % of the mesenchymal cases [60]. High levels of necrosis are reported for patients with mesenchymal GBM, which could be attributed to the overexpression of proteins from the tumour necrosis factor superfamily [60] .

The neural GBM type has the closest gene expression patterns as to normal neurons and nerve cells and is characterised with changes associated with the other subgroups of GBM and no specific genetic modifications, which would make it easy to distinguish it from the other GBM subgroups [60].

1.3.1.2 The ECM of gliomas

Similar to the ECM of other solid tumours, the ECM of gliomas is rich in fibrillar collagens, fibronectin and laminins [66]. Moreover, hyaluronan content is also found to be higher in malignant glioma tissue [67] with an increase in the levels of CD44 and RHAMM receptors as well, which is in contrast to normal brain tissue. *Radotra et al.* found that glioma invasion *in vitro* is mediated through hyaluronan binding to the CD44 receptor [49], a fact that further emphasizes the importance of hyaluronan not only as a key component of the glioma ECM, but also as a key player in the signal transduction pathways governing glioma invasion and metastasis.

1.4 **Gene therapy**

Gene therapy is an emerging field in the pharmaceutical sciences, because of the great potential that the variety of techniques offer for treating acute as well as chronic diseases such as cancers, viral infections and genetic disorders. The basic concept behind this general term is intracellular delivery of genetic material to generate a therapeutic effect. The treatment can target cells where an abnormal gene, causing a disease is repaired by introducing a healthy copy of the gene. This is referred to as gene editing and it is mediated by the CRISPR/Cas 9 system, where Cas 9 is a nuclease complexed to a synthetic guide (gRNA). The action of the guide RNA and the nuclease ensure that the genome is cut at a desired place, where a gene can be excised and/or new genes added [68,69]. The new gene can be introduced to help fight a disease or a “faulty gene” (mutated gene) can be inactivated. It can be applied to either germ-line cells or somatic cells. Germ-line gene therapy is not used in humans as it poses many ethical questions, while somatic gene therapy is widely used as the changes in the genes have an impact on the cells of the individual only and will not be passed on to the next generation.

1.4.1 Delivery vehicles of nucleic acids.

Naked nucleic acid cannot reach the cells if administered systemically, as there is a high risk they will be quickly degraded by nucleases [70]. In addition to that the passive uptake of nucleic acids by the cells is a highly inefficient process, because of their large size and their negative charge so smart carriers and ways for targeted delivery are needed. However, the rule has its exceptions as naked DNA delivery was attempted and has been successful to some extent in routes of local administration such as intramuscular injection for DNA vaccination, intratumoral injection for some cancers etc, but generally the efficiency of naked nucleic acids is limited [71]. The delivery of plasmid DNA requires nuclear transport, which is a limitation of the approach as it adds another barrier to the delivery process i.e. crossing the nuclear membrane [72]. By contrast siRNA and mRNA perform their functions in the cytoplasm where mRNA initiates the synthesis of the coded therapeutic protein, while siRNA attenuates the translation of the target protein by the process of RNA interference.

Small interfering RNA molecules (siRNA) are relatively short length nucleic acids (21-25 nucleotides, or with a molecular weight of approximately 13 kDa), which can "switch on" the RNA interference (RNAi) pathway [73]. siRNAs are short double stranded molecules consisting of a "sense" passenger strand and an "antisense" guide strand [73]. Once in the cytoplasm siRNA associates with the RNA-inducing silencing complex (RISC)[74]. The RISC complex is activated when the passenger strand is cleaved from the siRNA duplex by Ago (Argonaute) protein, a main component of the RISC complex. The "antisense" guide strand then guides the complex to the complementary mRNA [75]. The mRNA molecule is cleaved at position 10 and 11 from the paired siRNA counting from the 5^{I} end resulting in the formation of mRNA fragments [76]. The mRNA fragments are then consequently degraded by exonucleases, which prevents the translation of the coded protein.

The development of suitable gene delivery methods plays a pivotal role in the success and the future of gene therapy. Currently the strategies for gene delivery can be classified into two main groups: viral gene delivery systems or non-viral gene delivery systems.

1.4.1.1 Viral-mediated gene delivery

In viral-mediated gene delivery, the viral genomes are modified so the genes responsible for viral replication are removed, while a therapeutic gene is inserted[77]. Viral vectors may be divided into two groups: lytic and non-lytic vectors [77]. Non-lytic vectors produce virions and leave the host cells intact (adenoviruses and lentiviruses), while lytic viruses produce virions and destroy the host cells (human herpes simplex virus) [71,78]. Viral vector mediated gene delivery is considered the most successful and has a higher efficiency than non-viral mediated gene delivery. However, safety concerns due to insertional mutagenesis and immunogenicity are challenges for their systemic application [79]. Additionally, novel nucleic acid-based therapies using synthetic siRNAs, DNA oligonucleotides or mRNAs cannot be delivered by viral vectors. This is the reason why efforts in research have shifted towards the discovery of new systems that can facilitate gene delivery without the need for a viral vector.

Despite the problems associated with viral mediated gene delivery, around 70 % of the clinical trials include carries modified with adenoviruses, lentiviruses or retroviruses [80]. There are currently thirteen approved gene therapeutics in different countries twelve of which are with viral vectors [81]. In 2003 Gendicine® was the first gene therapy approved in China for the treatment of non-squamous head and neck cell carcinoma. It is an adenoviral vector carrying the therapeutic p53 gene. Only two years later Oncorine™ was another gene therapy available in China for the treatment of nasopharyngeal carcinoma. In 2012 the European market had finally its first approved adenoviral gene therapy under the name Glybera,.The drug targets a rare disease, which is the characterised by absence of the enzyme lipoprotein lipase LPL[82]. LPL facilitates the clearance of fat containing chylomycrons after the consumption of a rich in fat meal. Glybera has been withdrawn shortly after due to low patient demand and high cost. Between 2015 and 2018 there were another three gene therapeutics using viral vectors approved in Europe: Imlygic™, Stramvelis™ and Zalmoxis™ for the treatment of melanoma, lymphopenia and leukemia.[83]

1.4.1.2 Non-viral mediated gene delivery

Non-viral gene delivery strategies combine both chemical and physical methods [84,85]. Physical methods rely on techniques such as the gene gun, electroporation, particle bombardment and ultrasound while chemical methods include the use of liposomes and cationic polymers. A major advantage of non-viral gene transfer methods is their lower antigenicity in comparison to viral mediated gene delivery methods [86]. There are three major events in lipoplex and polyplex delivery (**Figure 1-4**): internalisation via endocytosis (**1**), endosomal escape and release (**2**), nuclear import for DNA delivery (**3a**) release of siRNA in the cytoplasm and association with the RISC complex (**3b**), release of mRNA and association with the ribosome (**3c**).

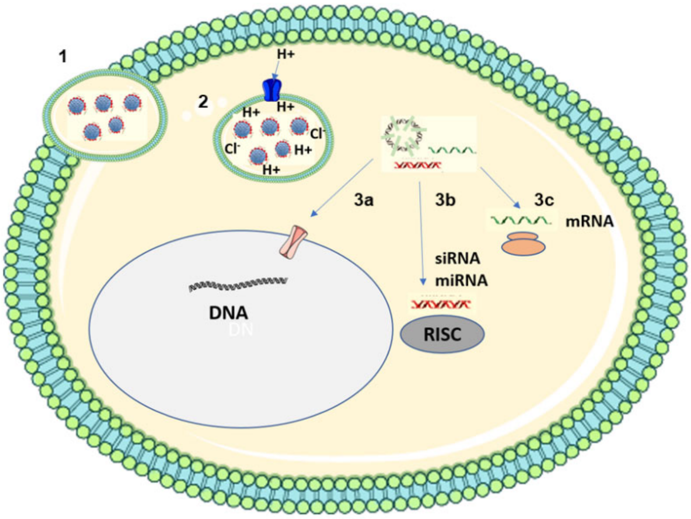

Figure 1-4: *The three major events in non-viral mediated gene delivery, endocytosis (1), endosomal escape (2) nuclear import for nanocomplexes with a DNA cargo (3a), nanocomplexes release siRNA (3b) or mRNA (3c).*

1.4.1.2.1 Lipoplex formation, internalisation and endosomal escape

Lipids are amphiphilic molecules, which consist of a polar head group, which can be positive, neutral or negative and a hydrophobic tail. The hydrophobic tail consists of hydrocarbon chains of different length (between eight and eighteen carbon atoms). The positive charge of the head group may originate from a peptide, amino acid or from guanidinium or pyridinium groups [87–89] . The positive head group of the lipids interacts with the negatively charged phosphate groups from the nucleic acid, which leads to the formation of an electrostatic complex called a lipoplex. Lipoplexes can include a neutral lipid such as 1,2-dioleoyl-sn-glycero-3-phosphoethanolamine (DOPE) and cholesterol (Chol), cationic lipids such as [e.g., N-[1-(2,3-dioleyloxy) propyl]-N,N,N-trimethylammonium chloride (DOTMA) or N-[1-(2,3-dioleoyloxy)]-N,N,N-trimethylammonium propane methyl-sulfate (DOTAP), 1,2-dimyristy-loxypropyl-3-dimethyl-hydroxy ethyl ammonium bromide (DMRIE-C), *etc.*

The transfection efficiency of lipid-nucleic acid formulations depends on the overall charge of the lipoplex, the size, the mechanism of entering the cell and the release mechanism, which leads to dissociation of the cargo nucleic acid from the lipoplex. A study by *Esposito et al.*, showed that nanoparticles between 400 – 450 nm are more effective than nanoparticles between 950 – 1050 nm [90]. *Kenny et al.* show that their liposome entrapped siRNA LEsiRNA with a size lower than 100 nm attenuates the translation of the anti-apoptotic protein survivin, which is overexpressed in a number of tumours [91]. It is important to note that size as a parameter affecting transfection efficiency cannot be considered independently but rather in combination with other characteristics of the lipid-nucleic acid formulations.

Lipoplexes are thought to enter the cell using two pathways; either by endocytosis or by membrane fusion [92]. The endocytic pathway appears to be the preferred mechanism of cell entry. Prior to internalisation the overall positive charge of the lipoplex is responsible for the interaction with the negatively charged phospholipids on the cell membrane. There are several endocytic pathways that operate in the cell and the contribution of each one for the internalisation of lipoplexes is not fully understood. Endocytosis can be clathrin dependent or clathrin independent (phagocytosis, micropinocytosis or caveolae-mediated internalisation) [93–95]. The endocytic pathway used for lipoplex internalisation appears to be dependent on the type of the lipid. A clathrin-mediated endocytic pathway has been reported for DOTAP/DNA lipoplexes [96] , while a caveolin-mediated endocytosis is described for 1,2-dimyristy-loxypropyl-3-dimethyl-hydroxy ethyl ammonium bromide (DMRIE-C)[97]. Additionally, cell entry of the lipoplex depends on the type of “cargo” nucleic acid. *Lu et al.*, showed that a small amount of siRNA/lipoplexes are internalised into the cell via simple fusion of the lipoplexes with the cell membrane [98].

The release mechanism of the cargo nucleic acid from the lipoplex is thought to occur through fusion of the lipids with the endosomal membrane. The process leads to the formation of temporary perturbations in the endosome membrane, which facilitate the escape of the nucleic acid into the cytoplasm [99]. A crucial step in the process is the inward “flip flop” of negatively charged lipids on the cytoplasmic side of the endosome towards the inner side of the endosome [100], which leads to the formation of neutral charge ion pairs with the cationic lipids [101]. The result of the “flip flop” and the consecutive neutralisation of charges causes destabilisation in the lamellar organization of the endosomal membrane and the release of the nucleic acid.

The first gene therapy using lipid carrier was approved in 2011. ONPATTRO or Patisiran has been developed to target nerve damage caused by hereditary transthyretin amyloidosis (hATTR). hATTR is an autosomal dominant disease resulting from a mutation in the transthyretin gene (TTR) that leads to the accumulation of misfolded TTR proteins in the nerves, heart and GI tract [102]. Patisiran is a lipid nanoparticle delivering siRNA to hepatocytes, which are the primary source of the misfolded protein in the circulation as a result of the mutation.

1.4.1.2.2 Polyplex formation, internalisation and endosomal escape

In a similar to lipoplexes manner, polyplexes are formed by an electrostatic interaction between the nucleic acid and the cationic polymer [103]. Polyplexes are made of cationic and in some cases amphiphilic polymers. Cationic polymers can be either linear: poly(L-lysine) (PLL) and polyarginine (PLA), polyethyleneimine (PEI), chitosan or branched (cationic dendrimers) such as poly (amidoamine, PAMAM), poly (dimethylaminoethyl methacrylate) [89,104]. Polyplex complexation is crucial for the interaction with the negatively charged groups of the phospholipid bilayer. Since complexation and binding affinity is pivotal also for unpacking of the cargo nucleic acid in the right cellular compartment, the importance of the balance between binding and dissociation will be discussed together in section **1.4.1.3.**

Polyplex cellular uptake is a consequence of electrostatic and/or hydrophobic interactions between the polyplex and the membrane. It has been shown that the adsorption of polyplexes with hydrophobic moieties on membranes induces membrane deformations which in turns leads to endocytosis [105]. Therefore, hydrophobic interactions with the membrane are promoting cellular uptake. In a similar fashion electrostatic interactions are said to enhance cellular uptake, but at the same time an increase in the number of positive charges can result in cytotoxicity [106]. Similarly, an increase in polyplex hydrophobicity has also been reported to cause membrane deformation and cytotoxicity. *Kozielski et al.* showed that poly beta amino esters (PBAE) co-polymerised with different ratios of hydrophobic monomers carrying siRNA possessed optimal gene silencing activity and were less toxic when having moderate hydrophobicity[107]. Toxicity is also associated with the molecular weight and the type of the polymer structure: linear or branched [108,109]. Higher molecular weight polymer and branched structures are described to be more toxic than lower molecular weight polymers and linear structures Similarly, enhanced positive charge and high transfection efficiency is usually associated with high cytotoxicity for lipoplexes too[110]. A strategy to preserve the transfection efficiency but to reduce the cytotoxicity is the use of anionic lipids to overcome the cationic lipid associated toxicity. *Kapoor et al.* incorporated siRNA into liposomes composed of anionic lipids using calcium ion bridges, the positive charge of which was needed for complexation [111]. The obtained lipoplexes showed significant silencing and lower toxicity when compared to cationic lipoplexes. Chemical modifications in the structure of both lipoplexes and polyplexes by addition of polyethylene glycol (PEG) to reduce the surface positive charge have also been explored as strategies to reduce toxicity [112].

Cellular uptake may be promoted by grafting a ligand to the structure of the nanoparticle. This would not only facilitate internalisation through receptor - mediated endocytosis, but also add targeting potential to the system. Conjugation of folic acid to PEG shielded pDNA and siRNA nanoparticles increased their cellular uptake and gene transfer/silencing activity when compared to control nanoparticles with no ligand functionalisation [113]. Both lipoplexes and polyplexes are shown to enter the cell through different endocytic pathways, however a major difference between the two types of gene delivery platforms is the endosomal escape mechanism which for polyplexes is a consequence of the "proton sponge" effect, while for lipoplexes is a result of direct interaction of the lipids with the endosomal membrane [92].

The ability of cationic polymers to buffer the acidic pH in the endosome is known as their buffer capacity. Buffer capacity is closely related to the positive charges of the polymer and their proton affinities (basicity). A polymer with higher basicity will readily accept a proton and this in the context of the endosome will result in a continuous influx of protons from the cytoplasm resulting in an increased influx of Cl^- ions and water creating osmotic pressure, swelling and consequent disruption of the endosome, a process described as the "proton sponge" effect [114,115]. *Sonawane et al.* advocated strongly in favour of the proton sponge effect as the mechanism through which polyplexes exert their release from the endosome [116]. Even though the "proton sponge" is widely accepted as the release mechanism of the cargo nucleic acid in the cytoplasm, research in the area is ongoing as the theory has recently been challenged [117]. This notwithstanding buffer capacity is still an important parameter for the efficient performance of polyplexes as transfection agents, which needs to be considered when designing new polymer vectors. *Lachelt et al.* synthesized a small library of oligo (ethanamino) amides containing ethanamino and histidine amino acids carrying pDNA. The authors demonstrated that increased buffer capacity of the polymers due to increased continuous cationization coincides with improved gene transfer [118].

Another strategy to improve endosomal escape is the engineering of sequences with direct disruptive properties on the endosomal membrane, including the incorporation of cell penetrating peptides (CPPs) in the composition of the nanoparticle. In such cases the intrinsic activity of CPPs to introduce detergent like pores in the plasma membrane is used to create pores in the endosomal membrane. KALA and GALA sequences have been successfully grafted to nanoparticles to induce endosome leakage [119]. KALA is a peptide that adopts an α - helical conformation at acidic pH

(4.5) and it has been shown to promote 100 % endosomal leakage at a variety of pH (4.5 – 8) [120].

1.4.1.3 Spatial release depending on the cargo nucleic acid

The rate of dissociation of the nanocomplexes and the influence of the size of the cargo nucleic acids along with the carrier physical characteristics and their effects on gene delivery are not yet clear. Previous studies demonstrated that gene expression from plasmids injected in the cell cytoplasm is a lot less pronounced in comparison to plasmids injected directly into the nucleus [121,122]. It has also been reported that naked DNA is unstable in the cytoplasm and is susceptible to degradation by numerous endogenous nucleases and has a half-life of 50 - 90 mins [123]. Unlike DNA, nanocomplex disassembly must happen in the cytoplasm for other types of nucleic acids such as siRNA, shRNA, mRNA, as these nucleic acids exert their function in the cytoplasm. Live cell imaging of lipoplexes carrying siRNA, showed an immediate release in the cytoplasm straight from the endosome [124,125]. Single particle live tracking analysis of lipoplexes and PEI polyplexes revealed that direct movement using microtubules governs intracellular trafficking of both lipo – and polyplexes residing in the endosome *en route* to the nucleus. On the other hand, random diffusion through the cytoplasm to reach the perinuclear space is described for nanocomplexes that have already escaped the endosome. This was proven by the fact that 90 % of the lipoplexes and PEI-polyplexes had direct movement using microtubules when they co - localised with the lysosome [126,127]. Nuclear import and access to the transcription cell machinery has been nominated as the potential transfection rate limiting step for DNA delivery. Additionally, rapidly dividing cells have been reported to be easier to transfect because of their frequently dissociating nuclear envelope by contrast to quiescent cells which have an intact nuclear membrane [128]. In the case of quiescent cells, lipo - and polyplexes have been reported to enter the nucleus with fusion or penetration of the nuclear membrane respectively [129]. Smart carriers incorporating a nuclear localisation signal (NLS) have been also developed to improve the nuclear import of nanocomplexes. NLS is a short peptide sequence PKKKRKV derived from the viral T antigen. It recognises and binds directly to importin–β or to the adapter protein importin-α. The binding to importin-β guides the NLS - importin complex to the docking site in the nuclear pore complex (NPC) and facilitates nuclear internalisation by an unknown mechanism [130]. An NLS modified ternary polyplex incorporating PEI/cyclodextran and DNA showed the same transfection efficiency in both dividing and non-dividing cells [131].

Since nuclear import is an intracellular barrier for efficient DNA delivery a balance between a stable nanocomplex, which can deliver the target gene protected from enzymatic degradation, allowing its dissociation from the complex in the nucleus is crucial. By contrast to DNA delivery, siRNA and mRNA delivery requires the nucleic acid release to happen in the cytoplasm. Different strategies to modify the structure of the carriers in order to ensure control on the cellular compartments where unpacking occurs have been also employed. *Feng et al.* report on the fine balance between hydrophobicity of the carrier, charge density and carrier length as a pre-requisite for efficient packaging during internalisation, intracellular trafficking and release in the nucleus [132]. On demand spatial siRNA release from light-sensitive, pH or redox responsive carriers have been all reported to enhance gene silencing by controlled release in the cytoplasm [133–136]

1.4.1.3.1.1 Gene therapy approaches targeting *GBM*

The evaluation of epigenetic and genetic data about changes in gliomas on a genome-wide level have shed light on common pathways disrupted in these tumours and contributed to an improved understanding of important key mutations. The progress made in expanding the genetic knowledge of gliomas and particularly glioblastoma (GBM) have resulted in multiple strategies focusing on gene therapy approaches targeting GBM. Common strategies include the use of suicide genes, immunomodulatory and tumour-suppressor gene therapy [137].

Suicide gene therapy uses genes that code for an enzyme, which targets an inactive precursor (prodrug) to convert it to its active cytotoxic form. Suicide gene therapy for the treatment of GBM has been widely used with viral vectors. The two common systems include the delivery of thymidine kinase (tk) or cytosine deaminase (CD) by two retroviruses: a herpes simplex virus type I (HSV) and Toca 511. The enzymes convert the systemically administered prodrugs ganciclovir (GCV) or 5-flurocytosine (5-FC) to the active chemotherapeutic agents, ganciclovir 3-phosphate (GCV-3P) or 5-flurouracil (5-FU) respectively [138,139]. As a structural analogue of deoxy guanosine triphosphate (dGTP) GCV 3-P competes for DNA polymerases and inhibits DNA replication, while 5-FU blocks the action of thymidine synthase (TS) interrupting the synthesis of DNA[140]. By contrast to the HSV-tk/GCV system, which showed no improvement in 1-year survival rates in a Phase 3 trial including 248 patients newly diagnosed with GBM [138], the Toca 511/CD and FC administered orally showed tumour regression at the infusion site of patients with recurrent high-grade glioma [141]. The system is currently in Phase 2/3 clinical trial for the treatment of GBM (**Table 1-1**).

The overarching goal of immunotherapy is to overcome the tumour induced immune suppression by stimulating the immune system through the introduction of genes encoding cytokines or antibodies. Although for a long time it has been widely accepted that immune cells are unable to cross the BBB, there is a substantial amount of evidence supporting the tumour-induced suppression in gliomas [142,143]. HSV-tk system, but with an adenovirus (AdV-tk) instead of a retrovirus was used in conjunction with the prodrug valacyclovir. Valacyclovir is converted to the cytotoxic anti-herpetic drug acyclovir, which stimulates the synthesis of toxic nucleotide mimics resulting in tumour cell death and activation of the tumour-associated immune cells [144] . A Phase 1B study of newly diagnosed patients used the valacyclovir AdV-tk system directly administered in the tumour bed after re-section, radiotherapy and chemotherapy with temozolomide (TMZ) showed a small increase (25 % and 33 % in 2- and 3-year survival rates respectively) when compared to the standard of care (**Table 1-1**). The immunotherapy approach applied in the study was verified by the detection of CD3+ cells after post-treatment analysis of tumours [144]. Moreover, a phase II clinical trial showed improved median survival rates when compared to the standard of care (13.5 % vs 17.9 %) [145]. The AdV-tk valacyclovir system was also recently used in combination with radiotherapy in a Phase 1 clinical trial in paediatric patients diagnosed with malignant glioma and recurrent ependymoma [146] (**Table 1-1**). At least 16 months survival rate post-treatment was reported for half of the participants with no dose-limited toxicities, but grade 3 lymphopenia was common [146].

Tumour-suppressors are crucial for prevention of oncogenesis. It has been reported that at least 1 tumour suppressor gene in all GBM patients is deleted or mutated, while in fact 91 % of the patients have 2 or more dysfunctional tumour-suppressor genes [147]. Pre-clinical studies in animal models have demonstrated promising results and increased survival by delivering genes coding for functional tumour-suppressors such as p53 [148] and cyclin inhibitors [149]. Unfortunately, the pre-clinical data did not match the clinical outcome, which was demonstrated by *Lang et al.* in a Phase I clinical trial with 12 recurrent glioma patients treated with adenovirus transferring a p53 coding gene. Only minimal toxicity has been reported, but a limited distribution of the therapy was achieved [150] (**Table 1-1**).

Despite the 25-year long history in the use of viral vectors in clinical trials for the treatment of malignant gliomas their efficiency to penetrate the tumour is limited and they have showed only marginal increase in survival rates so far. Non-viral vectors as gene transfer agents for GBM treatment on the other hand have not been investigated to the same extent in the clinic as viral vectors. Although 15.6 % of all gene therapy clinical trials up to 2014 are reported to be non-viral vectors mediated [83]. The combination of gene therapy approaches with nanotechnology offers the possibility of new therapeutic options for the treatment of gliomas. In parallel with the progress of biological delivery vectors, nanotechnology approaches for gene therapy and chemotherapy using synthetic carriers such as polymers [151] and liposomes [152] have also been widely studied. Nanoparticles are usually several hundred nm in size, they are able to cross the capillary to accumulate in tumours due to the leaky tumour vasculature and impaired lymphatic system and improve the pharmacokinetics of encapsulated drugs [153,154]. The characteristics of the polymer nanoparticles can be customised in order to provide improved biocompatibility, biodistribution, low toxicity and optimal cell penetration [155].

In the early 2000's a lipid-based formulation (LIPO-HSV-1-tk) of a plasmid coding for the suicide gene HSV-1-tk was used in a phase I/II clinical trial in patients with recurrent GMB via intratumoral infusion [156]. A pilot clinical trial with a liposome formulation carrying a TNF-related apoptosis inducing ligand (TRAIL) and a cytotoxic drug (paclitaxel) together with a peptide (angiopep-2), mediating passage through the blood brain barrier (BBB) was used in patients with GBM or anaplastic astrocytoma[157]. Unfortunately, both clinical trials did not result in satisfactory results and were terminated. Currently, there are only two non-viral mediated gene therapies in clinical trials for the treatment of GBM. A liposome carrying a p53 gene (SGT-53) in combination with TMZ is in Phase II clinical trial for the treatment of recurrent glioblastoma (**Table 1-1**). The SGT-53 is a transferrin-targeted liposome carrying p53 DNA, which can cross the BBB and showed enhanced anti-tumour activity when compared to TMZ alone [158]. Additionally, gold nanoparticles (NU-0129) carrying a siRNA targeting Bcl-2-like protein 12 (Bcl2L12) involved in resistance to apoptosis and tumour progression [159] entered an early Phase I clinical trial (**Table 1-1**).

A very promising study describes the preclinical evaluation of air-core liposomes carrying siRNA attenuating the synthesis of the anti-apoptotic protein sirtuin. The authors combined a physical and a chemical method for the delivery of the siRNA lipoplexes. A low frequency ultrasound was used with a subcutaneous injection of the lipid formulation in mice. The ultrasound induced bursting of the nanobubbles and resulted in increased siRNA release and spread of the nanoparticles which resulted in elevated cancer apoptosis [160].

There are no clinical trials of polymer-based complexes bearing nucleic acids described in literature targeting GBM. The research in this area for now is focused at the experimental pre-clinical stage aiming to increase the understanding of polymer-based gene delivery. Several research papers describe the use of polymer-based transfection systems targeting gliomas. PEI polymers modified by the addition of myristic acid carrying plasmid DNA coding for TRAIL were shown to increase the survival rate of mice with an intercranial glioma tumour model after an intravenous injection [161]. In addition to the chemical modifications introduced in the polymer structure, the synthesis of branched polymers (dendrimers) has been attempted in a different study to improve the surface/volume ratio of DNA binding. PAMAM dendrimers were conjugated to a viral peptide Tat to mediate membrane crossing [162]. The polymer was used to deliver anti-EGFR shRNA in mice bearing flank subcutaneous gliomas. The polyplex was shown to supress the EGFR/Akt signalling and decrease tumour growth [162]. Like dendrimers, dendrigrafts are also branched structures, which have shown potential as gene delivery vehicles. Dendrigraft poly-L-Lysine (DGL) in combination with a laminin targeted peptide was able to cross the BBB [163] and deliver DNA coding for the anti-apoptotic protein survivin. The study showed prolonged survival of mice bearing a U87 xenograft in comparison to the non-targeted dendrigraft [164]. Similarly, to dendrimers, dendrigraft cytotoxicity increases in a dose-dependent manner with a resulting hemotoxicity [165,166]. Successful reduction of toxicity has been achieved by the incorporation of anionic polymers [165] or PEGylation [167] in the structure of DGLs. A very recent study by *Mastokaros et al.* showed that PEGylation was used to improve the penetration of PBAEs in brain tissue in combination with convection-enhanced delivery (CED). CED is a local delivery strategy used in glioma, with catheters which can be placed within the tissue ensuring the infusion of therapeutic agents over the course of a few hours. PEGylated polyplexes showed a 20-fold increase in volume distribution when compared to non-PEGylated ones [168]. Studies in glioma brain models are necessary in order to confirm the potential clinical relevance of the PEGylated PBAEs systems for local delivery.

A common reoccurring trend for all of the listed examples in a clinical and in a pre-clinical set up is the limited diffusion of therapeutic molecules in solid tumours impeded by the presence of a dense ECM, the increased interstitial pressure and the heterogeneous vasculature of the tumour [169]. Targeting the ECM and the neoplastic cells have also shown promise to enhance the efficacy of a therapy. *Dmitrieva et al.* showed that an oncolytic virus expressing chondroitinase had greater efficacy when compared to a virus without the ECM targeting. It has been recently demonstrated that chitosan nanoparticles carrying anti Gal-1 siRNA delivered intranasally were able to reach the olfactory bulbs and inhibit the synthesis of Gal-1, which is a key regulator of the tumour ECM and promotes resistance to conventional chemotherapy and experimental immunotherapy [170].

1.4.1.4 Glycol chitosan as a gene delivery vector

Chitosan is a polysaccharide consisting of repeating N-acetylglucosamine and D-glucosamine units linked by β-(1→4) - glyosidic bonds **(Figure 1-4, A).** It is derived from chitin by deacetylation in strong alkali solutions and elevated temperatures [171] . Chitin is a polysaccharide abundant in nature and it is the major constituent of the exoskeleton of crustaceans, insects and some fungi, however due to its poor solubility chitin has limited medical and pharmaceutical application. By contrast chitosan with a degree of deacetylation of about 50 % or higher is soluble in aqueous acidic media, because of the protonation of the primary amine groups ($-NH_2$) attached to the C2 of the sugar units. It is used clinically as a wound healing dressing material [172] and experimentally for controlled drug release [173,174] and a. non-viral gene delivery vector[175–177].

The protonation of the $-NH_2$ groups in acidic conditions gives the polymer an overall positive charge at pH lower than 6.5 (pKa of $-NH_2$-6.5) [178]. This property of chitosan has been widely explored through its ability to form electrostatic complexes with oppositely charged polyanions such as nucleic acids and oligonucleotides for the preparation of gene delivery carriers. Chitosan can condense the cargo nucleic acid at an efficient amine to phosphate (N-P) ratio into nanoparticles, where the nucleic acid is protected from the action of nucleases. The factors that are affecting transfection efficiency in general such as the molecular weight of the polymer vectors, the positive charge density (which in the case of chitosan is determined by the degree of deacetylation, DD), the N-P ratio and the route of administration are also factors affecting the gene delivery efficiency of chitosan. The variation of all these factors result in changes of the size of the particles and their charge, which in turns has an effect on the cell uptake and release of the nucleic acid, hence they all need to be considered for the design of efficient transfection agents.

The molecular weight of chitosans is an important parameter influencing their transfection efficiency. Higher molecular weight chitosans form stable complexes with both pDNA and siRNA, however the larger Mw chitosans used the larger the obtained siRNA/chitosan or pDNA/chitosan complexes are formed. Large and stable complexes provide good protection of the cargo nucleic acids from nucleases, but lead to an overall increase in size, which can result in poor cellular uptake. *Ishii et al.*, demonstrated that with the increase in the Mw of the chitosans used in SOJ cells, expression of the pGL3-Luc plasmid was also decreased [179] and the lower Mw chitosans of 40 and 84 kDa were better as transfection agents than the 100 kDa. Chitosan-siRNA complexes prepared with chitosan of 20 kDa molecular weight showed enhanced gene silencing in HeLa cells *in vitro* in comparison to complexes obtained from a 200 kDa and 460 kDa polymers [180]. On the other hand, molecular weight influences the level of transfection not only by affecting cellular uptake, but also the ability of the complex to dissociate so the nucleic acid can be released. However, the preparation of a very unstable complex as showed by *Liu et al.* with a 10 kDa chitosan and siRNA resulted in the formation of large aggregates and insufficient gene silencing [181]. These findings confirm the complicated interplay of the parameters affecting transfection and the need for their fine tuning when designing polymer-based nucleic acid carriers.

Besides the Mw, the degree of deacetylation (DD) of chitosan is of major importance for the charge of the polymer and its solubility. Higher degrees of deacetylation for both siRNA and pDNA formulations of different molecular weight chitosans result in improved complexation ability with the target nucleic acid, due to an increase in the number of primary amines [182,183].

The route of administration of gene delivery vectors plays a very important role and it is a major obstacle for some gene delivery systems. A crucial advantage over other polymeric gene delivery vectors are chitosan's mucoadhesive properties [184], which makes it a suitable candidate for intranasal, oral and intratracheal routes of administration. An intranasal route of administration of siRNA (chitosan-based siNS1 nanoparticles) before or after infection with (respiratory syncytial virus) RSV showed significantly decreased virus titres in the lungs and decreased inflammation compared to controls [185].

Chitosan has some of the important characteristics needed for an efficient transfection agent. It is biodegradable [184] and possesses mucoadhesive properties, which makes it an attractive candidate for a promising gene delivery vector for mucosal application. However, the transfection efficiencies reported are poor in comparison to other polymeric vectors because of solubility issues and the lack of buffering capacity. To overcome these problems a variety of modifications have been introduced to its structure. The investigation of chitosan's properties focuses primarily on the Introduction of groups to improve its solubility at physiological pH and buffer capacity. Unfortunately, most of the modifications, which aim to increase chitosan's solubility decrease the fraction of free primary amines [186,187] which has a negative effect on its complexation potential with the nucleic acids. A variety of different chitosan derivatives have been synthesized by grafting hydrophilic molecules to improve its water solubility. The modifications include the grafting of polyethylene glycols [186], carboxymethyl [188], dicarboxymethyl, succinyl [187] functional groups to the primary amines. Another derivative of chitosan developed to increase water solubility is glycol chitosan [189–191]. By contrast glycol chitosan is an O-glycosylated derivative of chitosan with an incorporated glycol, which makes it even more attractive as a water-soluble chitosan derivative, because of the retained potential for complexation due to the unmodified primary amines. However, *Knight et al.,* showed that besides the currently accepted structure of O-glycosylated GC **(Figure 1-4 , B)** they prove that GC is a mixture N-glycosylated and O-glycosylated polymer molecules **(Figure 1-4, C)** Modifications aiming to increase the charge density of chitosan and glycol chitosan are also of particular interest due to the increased buffer capacity of the resultant polymers, which facilitates intracytoplasmic release of the carried nucleic acid.

Trimethylated chitosan or introducing quaternization of the *N*-terminal primary amine groups [192], which carries a permanent positive charge is a chitosan derivative with an increased solubility and 16 to 50 fold increase in transfection efficiency when compared to other polyamines. The resultant N-trimethyl chitosan derivatives of 100 kDa with the highest quaternization showed the highest transfection efficiency, however this coincided with an increase in toxicity. To overcome the toxicity problems some further modifications of the polymers were made with grafted PEG molecules [112]. The PEGylated trimethyl chitosan showed decreased toxicity. A similar strategy to increase the charge density of chitosan was also investigated by *Kim et al.* who conjugated urocanic acid (an imidazole containing compound) to chitosan and reported a 1 to 3 fold improvement in the transfection efficiency when compared to unmodified chitosan, but still lower levels of gene expression when compared to Lipofectamine [193].

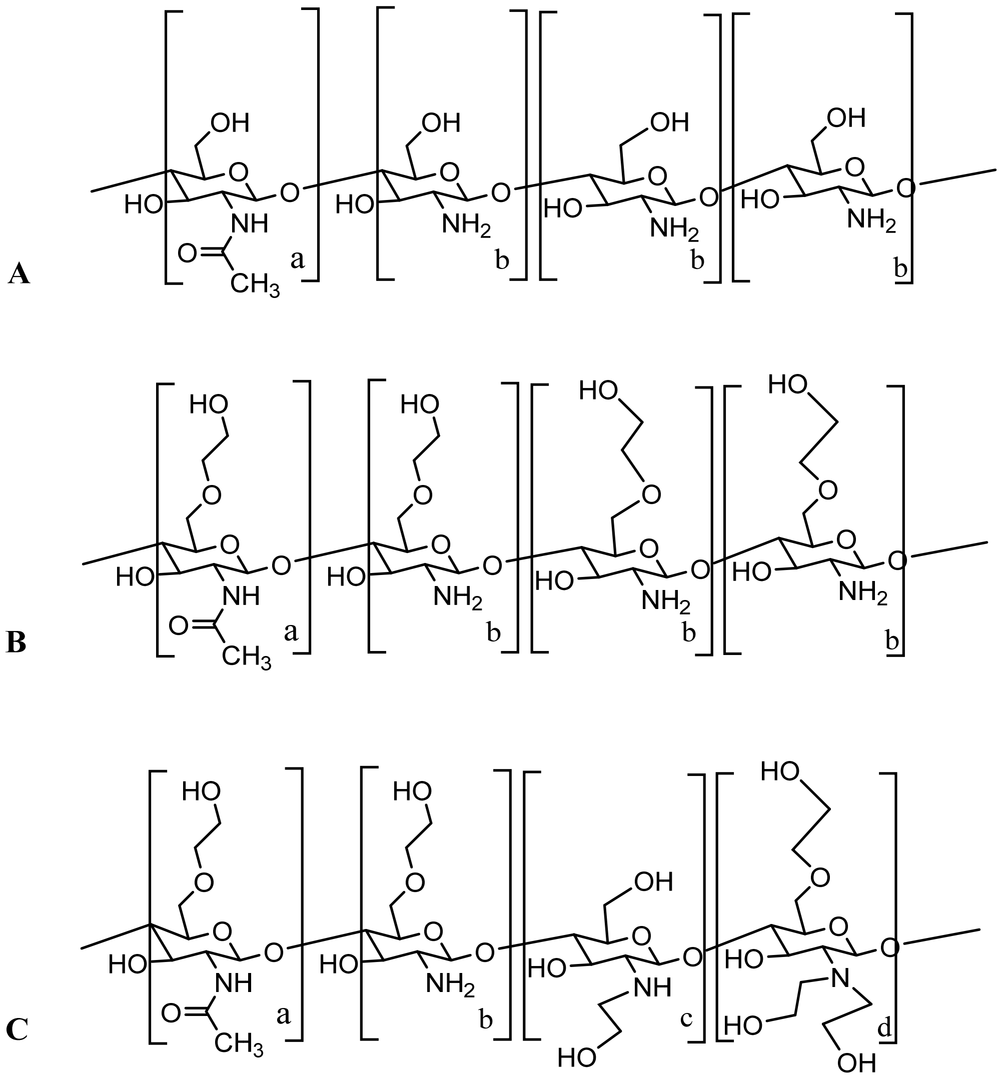

***Figure 1.4:** Chemical structure of chitosan (**A**), O-glycolated glycol chitosan (**B**) (widely accepted chemical structure), N,O - glycolated glycol chitosan (**C**) (chemical structure proposed by Knight et al.)* [194]**.**

Table 1-1: *Clinical trials of gene therapy approaches in glioblastoma*

Gene therapy	Advantage	Limitations	Vector	Mechanism	Clinical trial phase	Combination Therapy	Clinical trial number
Suicide genes	Safety in clinical trials Requires short-term gene expression Enhances sensitivity to conventional therapy	Limited spatial distribution Poor gene transfer efficiency Inability to target dispersed tumour cells	Retrovirus	HSV-tk	I	Ganciclovir	NCT00001328
			Toca 511	Toca 511/CD	II/III	Oral 5 - FC	NCT02414165
			Retro or Adenovirus	HSV-tk	I	Ganciclovir	*Sandmair et al.*.
Tumour-suppressor	Eradication of individual tumour cells Long – term immunity Does not require tumour - associated antigens	Must overcome tumour induced immunosuppression Autoimmune adverse side effects. Tumour immunoediting as a means of tumour escape	SCH – 58500	p53 transfer	I	N/A	NCT00004080
			Adenovirus AdV-p53	p53 transfer	I	N/A	NCT00004041
			Liposome SGT – 53	P53 transfer	II	TMZ	NCT02340156
			Gold nanoparticles NU-0129	Oncogene Bcl2L12	Early Phase I	N/A	NCT03020017
Immunotherapy	Safety in clinical trials Potential to sensitize tumour cells	Poor in vivo gene transfer Limited spatial distribution	AdV – tk	HSV - tk	I	Valacyclovir	NCT00751270
			AdV – tk	HSV -tk	IIa	Valacyclovir and radiation therapy	NCT02340156

1.5 **Aim and Ojectives**

1.5.1 Aim

The aim of the project is to develop a GC-based and a PEG (polyethylene glycol) -based gene delivery vehicle with low toxicity and good efficiency that may be used for gene therapy in glioblastoma. A strategy focusing on the modification of the GC and PEG backbone to incorporate ionizable groups, which are thought to play role in the endosomal escape of polyplexes due to the "proton sponge" effect and the resulting endosomal rapture is going to be employed first. Next, the aim of this work is to explore for the first time the possibility of combining the promise that gene therapy holds for cancer therapy together with an ECM targeting approach using GC-based nanoparticles carrying pDNA coated with hyaluronidase. To test the *in vivo* transfection potential of the polyplexes and the ECM targeting approach of the three-component system (plasmid, polymer and hyaluronidase) we will explore two administration routes. The first one will involve the intranasal delivery of the nanoparticles (NPs) to the brain. An intranasal route of delivery of polymer-based NPs carrying siRNA has been already attempted in our lab and downregulation of the target gene was observed in the olfactory bulbs and cortex [195]. Intranasal delivery represents an attractive way to bypass the BBB, however the lack of understanding of the NPs diffusion *en route* to the brain and the problem of delivering them to a specific area can make it difficult to predict and interpret the effect of hyaluronidase. Therefore, we propose to have a second route of administration, which would involve the delivery of the NPs via a subcutaneous injection in mice.

1.5.2 Objectives

2.2.1 To synthesize and characterise different polymers with a range of molecular weights based on either glycol chitosan or PEG backbones and different number of grafted terminal amines.

2.2.2 To determine and compare the pDNA condensation potential of all the polymers to complex pDNA. To characterise the obtained nanocomplexes for their size and zeta potential.

2.2.3 To optimise their *in vitro* transfection potential in the glioma cell line U87 by varying different parameters: complexation time, temperature during complexation time, complexation medium and treatment time.

2.2.4 To coat the obtained complexes with hyaluronidase. To develop a quantitative strategy to estimate the amount of free and bound enzyme and to test their *in vitro* potential to digest hyaluronic acid.

2.2.5 To test the *in vivo* transfection efficiency of the polyplexes coated with hyaluronidase and the non-coated polyplexes using an intranasal and a subcutaneous route of administration and to compare their transfection potential to Lipofectamine and naked DNA.

2 Synthesis and characterisation of cationic ethyl-amino derivatives of Glycol Chitosan and cationic polyamine derivatives of Polyethylene Glycol

The following two chapters will describe the synthesis and characterisation of new polymer vectors. This chapter will focus on the synthesis and characterisation of the semi-synthetic glycol chitosan variants functionalised with an ethyl-amino group to obtain different substitution levels of N-ethyl-amino substituted variants of GC (EAGC). The second synthetic chapter will show the synthesis and characterisation of a polyethylene glycol functionalised with the polyamine spermidine. The synthesized compounds will give us the opportunity to explore the nucleic acid condensation potential and transfection efficiency of multi-amine functionalised molecules. The variety of structures generated in our small library of potential gene delivery vectors will give us the opportunity to evaluate the parameters that contribute to an efficient gene delivery platform.

2.1 **Introduction**

EAGC variants are synthesized by grafting an ethyl-amino group to the primary amines of glycol chitosan (GC). EAGC polymers carrying siRNA have already been synthesized and characterised by *Carlos et al.*, who were able to show an increase buffer capacity and improved *in vivo* gene silencing [196].

In an attempt to increase the charge density of glycol chitosan and improve its buffer capacity we will graft an ethyl-amino group to the primary amines attached to C2 of the sugar to obtain N-ethylamine derivatives of GC.

2.1.1 Characterisation methods

2.1.1.1 Nuclear Magnetic Resonance (NMR)

Nuclear magnetic resonance spectroscopy (NMR) is widely used as an analytical technique for structure prediction in organic chemistry. Subatomic particles (neutrons, protons and electrons) spin around their axes. The nuclei of some atoms have no overall spin (e.g. ^{12}C) in such cases the number of protons and the number of neutrons is even. By contrast some nucleus have a non-zero overall spin (I). In such cases the sum of neutrons and protons is an odd number or if the number of protons and neutrons is an odd number, then the nucleus has either half-integer spin (e.g. 1/2) or integer spin (e.g. 1) respectively. ^{13}C and ^{1}H are the most common elements in organic molecules, which have a ½ spin and their spinning behaviour is widely used in NMR spectroscopy to determine the structure of organic molecules [197].

For a nucleus with an overall spin (I) quantum mechanics predicts 2I+1 orientations, so in the case of a nucleus with a ½ spin there are 2 possible orientations. If there is no external magnetic field applied the two orientations of a nucleus with ½ spin will be of equal energy, however if there is an applied magnetic field they split and each level has a magnetic quantum number m**. Figure 2-1** shows the changes in the energy level of the nucleus when an external magnetic field is applied on the nuclei. At the lower energy level, some of the nuclei will be aligned with the magnetic field. When they are irradiated with a radio frequency at some of the lower energy level nuclei will absorb radiation and their nuclear spin will flip and will no longer be aligned with the field but will be opposing it instead. The absorption of electromagnetic energy by the nucleus and the consecutive flip of its nuclear spin from the lower energy level to the higher energy level is called nuclear resonance and it is recorded as a signal.

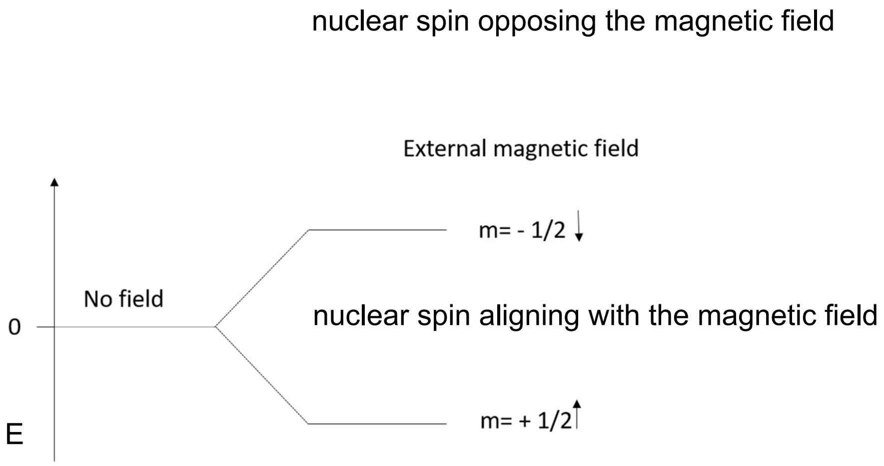

Figure 2-1:*The change in electron spin moment when an external magnetic field is applied*

In a molecule, the nuclei are surrounded by an electron density. The electrons surrounding the nuclei have a shielding effect protecting it from the influence of the external magnetic field. Additionally, the resonance frequency of a nucleus will also depend on the neighbouring atoms in a molecule. The influence of one atom over another is the important information, which provides details on the structure of the molecule [197,198]. The presence of electron-withdrawing atoms, π-bonds or higher electron density will influence the resonance frequency of the nuclei in a molecule and will all have an effect on their chemical shifts (δ). All chemical shifts are recorded as peaks compared to tetramethysilane (TMS), which is widely used for ^{13}C and ^{1}H

NMR spectroscopy calibration. $(CH_3)_4Si$ (TMS) has 12 identical hydrogen atoms, which have the same magnetic environment resulting in the same spin flip energy. These protons will give rise to a single peak in the ^1H-NMR spectrum of TMS or a singlet. During analysis of a molecule the resonance frequency of the analyte nuclei are recorded as peaks, which are compared to the chemical shift of TMS, which is assigned to be 0.

2.1.1.2 2-Dimensional NMR experiments, correlation NMR spectroscopy

Complex molecules and polymers have a structure which is difficult to be characterised fully by the information provided by one dimensional ^{13}C or ^1H-NMR experiments. The development of more advanced spectroscopic methods and their combination with computational power made it possible to perform also two-dimensional NMR experiments. ^1H-^1H COSY (**Co**rrelation **S**pectroscop**y**) indicates which hydrogen atoms are coupled to each other. The ^1H spectra are plotted in the x and y axis in a grid, the correlations of coupling hydrogen atoms are in the grid and information for the structure is obtained by matching these correlations with the x and y axis. The same principle applies to HMQC (Heteronuclear Multiple Quantum Coherence) experiments where instead of detecting hydrogen atoms, which are coupled to other hydrogen atoms, the correlation in the grid or the map appear when there is a hydrogen coupled to a heteroatom (either ^{13}C or ^{15}N). The x from the grid shows the chemical shifts of the ^1H atoms, while the y-axis shows the chemical shifts of the ^{13}C atoms. Additionally, ^{13}C DEPT (Distortionless Enhancement of Polarisation Transfer) experiments can also be plotted against a ^1H spectrum to provide information for the number of hydrogens coupled to a carbon atom. In a CDEPT 135 experiment a series of pulses with a various delay times are used to create a DEPT spectra where secondary carbons appear in the opposite site of the spectrum when compared to primary and tertiary carbons, which helps in the structure elucidation.

2.1.1.3 Multi detector gel permeation chromatography (GPC)

GPC or size exclusion chromatography (SEC) is a technique which separates molecules based on their size. The operating principle in conventional SEC includes the interaction of molecules with a column packed with porous beads. Molecules, which are bigger in size (larger hydrodynamic radii and molecular mass) do not enter the pores of the beads and elute first, while smaller in size molecules elute later as they are retained in the column when passing through the pores [199]. Conventional size exclusion chromatography needs calibration of the column with standards of known molecular weight before the analysis of an unknown sample. A major problem with the technique is that it is assumed that the unknown sample and the reference standards used for calibration have the same conformation hence elution from the column. In the case of polymers, which are generally polydisperse and can adopt different conformations in solution, this could result in erroneous molecular weight measurements. To overcome this problem a MALLS detector working on the principle of Rayleigh scattering can be coupled with SEC. Light scattering detectors are very useful as they provide an absolute measurement of molecular weight without the need of column calibration and the use of standards.

In a classical light scattering experiment when a collimated laser beam hits a macromolecule much smaller than the wavelength of radiation the molecule behaves as point scatter. In this case the light is scattered isotropically meaning that it will be the same at every angle on the perpendicular plane of the scattered light. However large molecules can scatter light through different parts of the molecule and the scattered light varies significantly with angle. The different detectors of MALLS can measure the intensity of the scattered light. The reduction in scattering in higher angles compared to lower angles can be used to estimate the size of the molecule through measuring the radius of gyration Rg. Rg is the root mean square averaged distance of the components of the molecule from its centre of gravity. The intensity of the scattered light is measured as the Rayleigh ratio Rθ, which is the ratio between the excess scattered light by the sample and solvent combination over that of the solvent alone. The Rayleigh ratio is directly proportional to the molecular weight of the sample (1)

$$Kc/R_\theta = 1/Mw + 1/Mw\ (16\pi^2/3\lambda^2)\sin^2(\theta/2)\ (< r >_z)^2 + A_2c \tag{1}$$

C is the solute concentration; R_θ is the Rayleigh ratio; Mw is the weight-averaged molecular weight, λ the wavelength of incident light, θ the angle of collection, $<r>_z$ the z-averaged mean radius of gyration and A_2 is the second virial coefficient, which quantifies the interaction between the macromolecule and the solvent, N_0 is Avogadro's number, Kc is given by (2)

$$Kc = \frac{2\pi^2\eta^2(dn/dC)}{N_0\lambda^4} \tag{2}$$

A very important parameter in light scattering calculations is the refractive index increment. The refractive index increment dη/dC shows the degree by which the refractive index of a solution varies with the change in the concentration of the solute. Therefore, to measure the absolute molecular weight of a polymer in solution the GPC-MALLS is also coupled to a refractive index detector.

2.2 **Materials and methods**

2.2.1 Materials

Materials	Purity	Supplier
Glycol chitosan	≥ 60% no information on whether it is endotoxin free)	Wako Chemicals (Gillingham, UK)
Hydrochloric acid	≥ 98 %	VWR (VWR BDH Prolabo (Fontenay-sous-Bois, France)
2-(Boc-amino) ethyl bromide	99.5 %	Sigma Aldrich (Gillingham, UK)
Triethylamine	≥ 99.5 %	Sigma Aldrich (Gillingham, UK)
Diethyl ether	≥ 99.5 %	Sigma Aldrich (Gillingham, UK)
N-methyl-2-pyrrolidone (NMP)	99 %	Sigma Aldrich (Gillingham, UK)
Methanol D4	99.8 %	(Cambridge Isotope Laboratories (Nantwich, UK)
Deuterium Oxide (D_2O)		Sigma Aldrich (Gillingham, UK)

Sodium acetate anhydrous	≥ 99 %	Sigma Aldrich (Gillingham, UK)
Acetic Acid Glacial		Merck, Sigma Aldrich (Gillingham,UK)
Sodium citrate monobasic	≥ 99.5 %	Sigma Aldrich (Gillingham, UK)
Citric Acid	≥ 99.5 %	Sigma Aldrich (Gillingham, UK)
Visking Dialysis Tubing		Medicell Membranes Ltd. (London, UK)

2.2.2 Methods

2.2.2.1 Degradation of Glycol Chitosan

10 g of glycol chitosan were weighed out and transferred to an Erlenmeyer flask and dissolved in 375 ml of 4 M HCl (13 mg ml $^{-1}$) as described previously [191] . The content of the Erlenmeyer flask was then equally split in three and transferred to three new flasks. The flasks were then incubated for 1 h, 2 h and 6 h in a preheated water bath at 50° C. After the acid degradation was completed the content of the flasks was transferred to three dialysis bags (3.5 kDa MWCO) and they were then placed in a 5 L beaker filled with distilled water. Dialysis was carried out for 24 hours with a minimum of 5 - 6 changes of the water. Electroconductivity measurements were taken before every change of the water and the dialysis was considered completed when the reading on the portable electroconductivity meter was below 40 siemens per meter, S m $^{-1}$. The dialysed solution was then freeze dried on a ScanVac Freeze Dryer.

2.2.2.2 Reaction of degraded Glycol chitosan (dGC) with 2-(Boc-amino) ethyl bromide

Small scale reactions were prepared to obtain a range of substitution levels with a variation in the temperature used and the equivalents of the 2-(Boc-amino) ethyl bromide (2-Boc AEB) per sugar chitosan monomer (**Table 2-1**). The reactions were as follows: 2 eq ,5 eq ,10 eq of 2-Boc AEB at 40° and a double reaction of 10 eq 2-Boc AEB at 40° C (topping up by a fresh solution of 2-Boc AEB in NMP) and 5eq of

2-Boc AEB at room temperature (RT). All the reactions were carried out with 20 mg of dGC in 4 ml of NMP with 5 eq of triethylamine. Glass vials (7 ml) were used for all the reaction mixtures and they were left stirring for 24 hours at either 40° C or at room temperature. The double reaction with approximately 20 eq of 2-Boc AEB was left at 40° C in an oil bath for 48 hours. After the incubation of the samples an ether extraction was performed with 3x (v:v) diethyl ether (12 ml), which was added to the samples and afterwards the vials were left to settle for a few minutes in order for phase separation to occur. The aqueous phase of all the samples was collected and the ether extraction was repeated three times per sample. The collected aqueous fractions were then transferred to dialysis bags (MWCO 3.5 kDa), the bags were placed in 5 L beakers filled with distilled water. Dialysis was performed over 24 hours with 5 - 6 changes of the water every 1 - 2 hours as described previously. The conditions for the small-scale reactions set up were replicated for both GC batches used. A range of substitution levels were chosen based on the estimated ethyl-amino (EA) substitution levels from the ^{1}H-NMR data. Then the polymers with the chosen modification levels were synthesized on a larger scale using the same protocol as for the small-scale reactions but with 100 mg of dGC in 20 ml of NMP.

2.2.2.3 Deprotection of N-ethyl-amino glycol chitosan variants

The samples were deprotected in 4 M HCl (5 mg ml $^{-1}$) for 4 hours stirring at room temperature. At the end of the reaction samples were transferred to dialysis bags (MWCO 3.5 kDa) and were dialysed against water for 24 hours with as many changes of the water as needed to bring the electroconductivity of the water close to a negligible value (>40 S/m).

2.2.2.4 Nuclear magnetic resonance (NMR)

The samples for NMR analysis were prepared at 20 mg ml $^{-1}$ in the appropriate deuterated solvent. 1 ml of the clear solution was added to an NMR tube and the samples were analysed on either AMX 400 MHz or AMX 500 MHz Bruker spectrometer. Boc protected EAGC variants were dissolved in deuterated methanol and analysed, while dGC and the deprotected EAGC variants were analysed using deuterium oxide.

Percent ethyl-amino substitution of the Boc protected polymers and the deprotected polymers is calculated form their ^{1}H-NMR spectra using the integration (I) of the Boc protons for the protected polymers or the protons representative of a single or double ethyl-amino substitution attached to the C2 of the sugar for the deprotected polymers.

All the spectra were analysed via Topspin 2.3 software. Details of the corresponding substitution calculations are given in the legend of the ^{1}H-NMR spectra of the corresponding polymer together with all peak assignments in the structure.

2.2.2.5 Multi-detector Gel Permeation Chromatography (GPC)

The MALLS and dRI detector used were a 120 mW solid-state laser (wave length, λ658 nm) DAWN® HELEOSTM and Optilab rEX Interferometric Refractometer respectively, which were supplied by Wyatt Technology Corporation, USA. The MALLS detector was also coupled to a Quasi Elastic Light Scattering (QELS) detector supplied by Wyatt Technology Corporation. SEC was performed using Phenomenex PolySep™ - GFC-P 4000 column (300 x 7.8 mm) protected by a Phenomenex PolySep™ - GFG-P guard column (35 x 7.8 mm). An Agilent 1200 series liquid chromatography (LC) system with an isocratic pump, a degasser and an auto sampler unit was used to provide the flow rate of the mobile phase to the column.

Sodium acetate/acetic acid and sodium citrate/citric acid buffer systems were prepared at different pH values using the Henderson Hasselbach equation [200] (3). **Table 2-1** gives information on the details for the recipes of the buffers used to 1L volume.

$$\text{pH} = \text{pKa} + \log_{10} ([A-])/([HA]) \qquad (3)$$

Table 2-1: *Buffer systems used for the GPC - MALLS*

Buffer system	Buffer Molarity (mM)	Mass of sodium acetate (g)	Volume of glacial acetic acid (ml)	pH
Sodium acetate/acetic acid	500	24.6	11.4	5
	1000	24.6	40.4	4
	500	6.1	22	4
	250	3.05	11	4
	125	1.5	10.5	4
Sodium citrate/citric acid	**Buffer Molarity (mM)**	**Mass of sodium citrate (g)**	**Mass of citric acid (g)**	**pH**
	250	2.6	10.3	3
	125	5.3	20.5	3

The refractive index increments (dη/dC) were measured by manually injecting a series of dilutions of the polymer in the mobile phase at different concentrations (0.1 to 0.6 mg ml $^{-1}$) into the dRI detector. The dRI detector was pre-set at 25° C and a wavelength of 658 nm and a stable baseline was observed before the start of the manual injections.

GPC-MALLS experiments were performed by preparing a 5 mg ml $^{-1}$ solution of the polymer to be analysed in the mobile phase used for the run at a flow rate of 0.7 ml min $^{-1}$ for 20 minutes. The data obtained from both dη/dC and GPC-MALLS experiments was analysed using ASTRA software for Windows, version 5.3.2 supplied by Wyatt Technologies.

2.3 **Results**

2.3.1 Degradation and characterisation of Glycol Chitosan (GC)

The different molecular weight glycol chitosan batches obtained after 1 h, 2 h and 6 h of degradation were of 57kDa (GC57), 37 kDa (GC37) and 21 kDa (GC21). All the degraded GC (dGC) were characterised by GPC - MALLS and NMR. **Table 2-2** shows that longer degradation times resulted in the preparation of smaller in size GC polymers. Peak assignments for the degraded GC were made from the ^{1}H-NMR spectrum shown on **Figure 2-2.**

***Table 2-2:** Molecular weight and polydispersity values for degraded GCs*

GC batch	Mn (Da)	Mw (Da)	Mw/Mn (polydispersity)
GC100	98000	113021	1.153
GC57	55231	57212	1.036
GC37	37200	37440	1.006
GC21	20940	21180	1.025

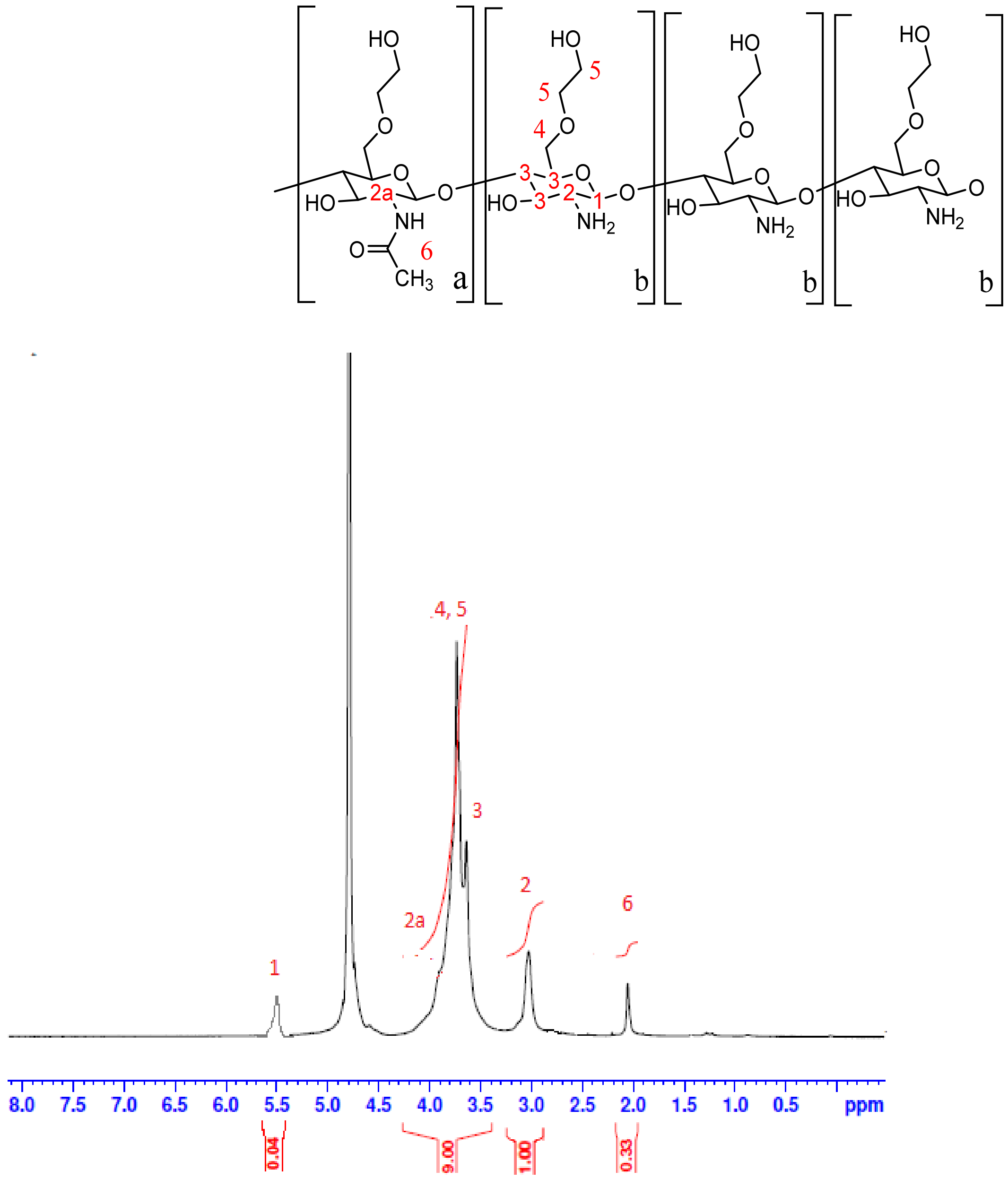

Figure 2-2: *degraded GC37* ^{1}*H-NMR* (*D_2O*)*:* $\delta_{2.1}$=[CH_3-CO-NH-), $\delta_{2.9\text{-}3.2}$=[-CH-(OH)-CH-(NH_2)], $\delta_{3.4\text{-}4.2}$=[-CH(OH), -CH_2(OH) and -CH-(OH)-CH-NH-CO-)], $\delta_{4.79}$=[D_2O], $\delta_{5.5}$=[-O-CH-O-]. *Yield of GC 1=0.8g (27%), yield GC 2 (24%).*

In attempts to check if we have N-glycolated residues of GC as reported by *Kinght et al.* we performed ^{1}H-NMR and ^{1}H-^{1}H COSY experiments of GC37 at pH < 2 and pH > 10 following the method descried in their paper. The study describes NMR analysis of glycol chitosan at 90° C. Due to the problems of elevating the temperature to 90° C with the Bruker AD 400 Mhz Spectrometer we used 50° C instead. The ^{1}H-NMR spectrum for the two different pH values is shown on **Figure 2-3.** Our results showed the presence of a few small peaks at pH >10 between $\delta_{2.8\text{-}3.4}$. We observed the same pattern of the spectra reported by *Knight et al.* for both pH values, who proposed that the small peak ($\delta_{2.8}$, pH > 10) upfield from the signal in the proton spectrum of GC assigned as **2 (Figure 2-3)** is a N-glycosylated C2 of the sugar**.** The chemical shifts of the same peaks reported by *Knight et al.* are different ($\delta_{3.1\text{-}3.6}$), but this is due to the higher temperature used for their NMR experiments. In addition to the proton spectra we performed ^1H-^1H COSY NMR experiments for GC37 at pH > 10 and pH < 2. The ^1H-^1H COSY spectra of the samples showed a correlation of the peak at $\delta_{2.8}$ with the protons attached to C1 and C3 from the sugar. The correlation with C1 is visible only for the high pH since the protons attached to C1 are buried behind the water protons. Based on these findings and on the data reported by *Knight et al.* we marked the small peak ($\delta_{2.8}$) immediately upfield of **2** as **N-gly 2** (red line in **Figure 2-4**). The figure shows the presence of another correlation with the protons of one of the small peaks ($\delta_{3.2\text{-}3.4}$) with protons from the sugar (green line, **Figure 2-4**). The same correlations are present for GC37 at pH < 2, however they appear immediately downfield from the protons attached to C2 **(2)** by contrast to the high pH sample **(Figure 2-5**). *Knight et al.*, explained this as an effect related to amine groups directly affected by protonation/deprotonation effects. The correlation of **2** with the multiplet representing the sugar protons and with the protons attached to C1 assigned as **1** are also visible (blue line, **Figure 2-4**). The colour coding of the lines is kept the same for the grids representing the COSY experiments for the GC37 samples at the two extreme pH environments (**Figure 2-4** and **Figure 2-5**).

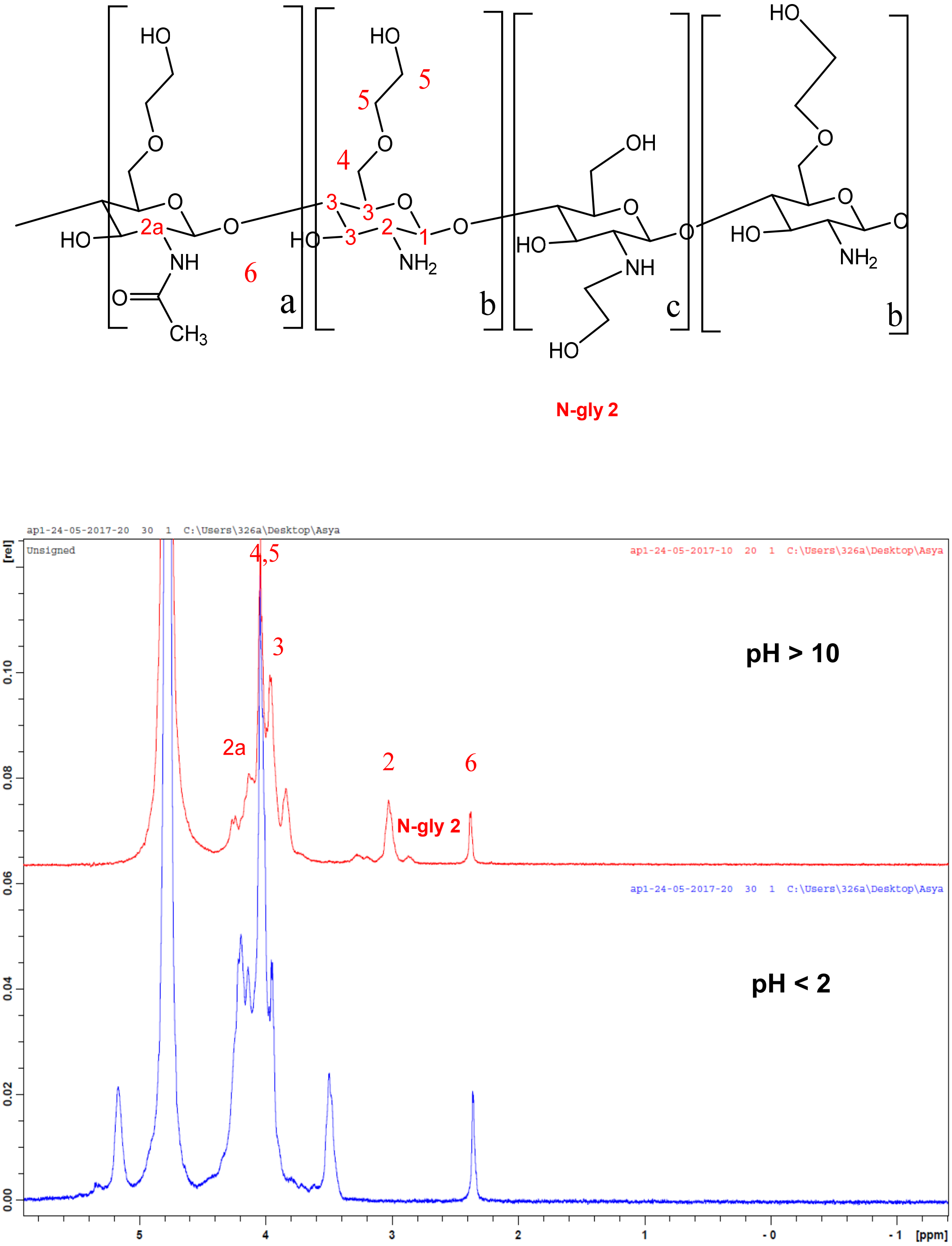

Figure 2-3: *Elevated temperature ^{1}H -NMR spectra of degraded N,O-Glycolated glycol chitosan GC37 at pH > 10 and pH < 2 in D$_2$0 and a proposed structure for glycol chitosan-based on a study by Knight et al.*

pH.>.10: *$\delta_{2.38}$=[C**H**$_3$-CO-NH-), acetyl protons; $\delta_{2.8}$=[-CH-(OH)-C**H**-(NH)-CH$_2$CH$_2$OH] N-glycolated C2 sugar protons (N-gly 2) ; $\delta_{3.00}$=[-CH-(OH)-C**H**-(NH$_2$)], C2 sugar protons; $\delta_{3.7\text{-}4.5}$=[-C**H**(OH), -C**H**$_2$(OH) and -CH-(OH)-C**H**-NH-CO-),sugar protons $\delta_{4.79}$=[D$_2$O]*

pH < 2: *$\delta_{2.36}$=[C**H**$_3$-CO-NH-),acetyl protons; $\delta_{3.5}$=[-CH-(OH)-C**H**-(NH$_2$)],C2 sugar protons; $\delta_{3.8\text{-}4.5}$=[-C**H**(OH), -C**H**$_2$(OH) and -CH-(OH)-C**H**-NH-CO-), sugar protons]; $\delta_{4.79}$=[D$_2$O], $\delta_{5.18}$=[-O-C**H**-O-], C1 sugar protons*

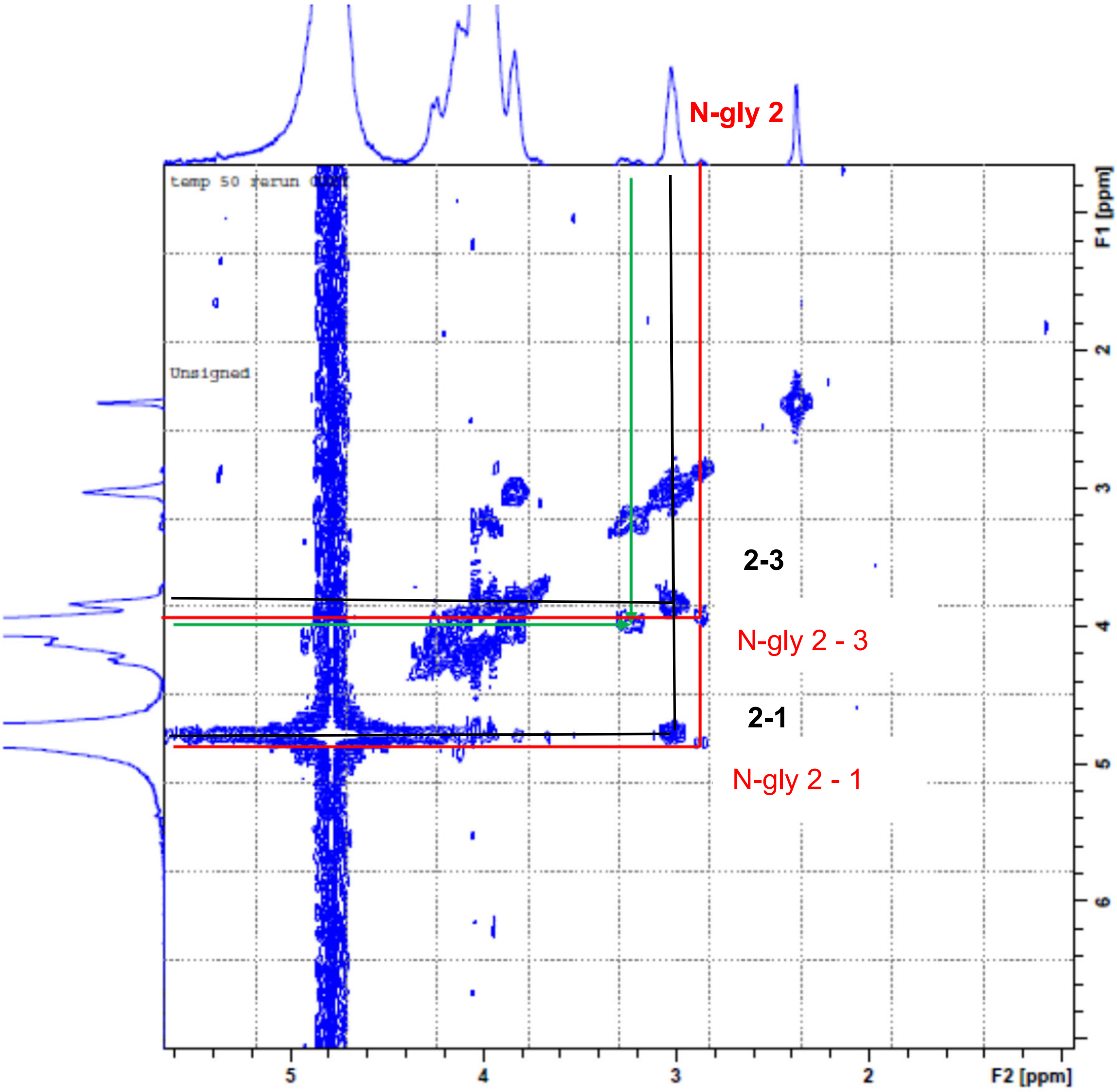

Figure 2-4: *^{1}H-^{1}H COSY NMR of GC37, pH > 10.*

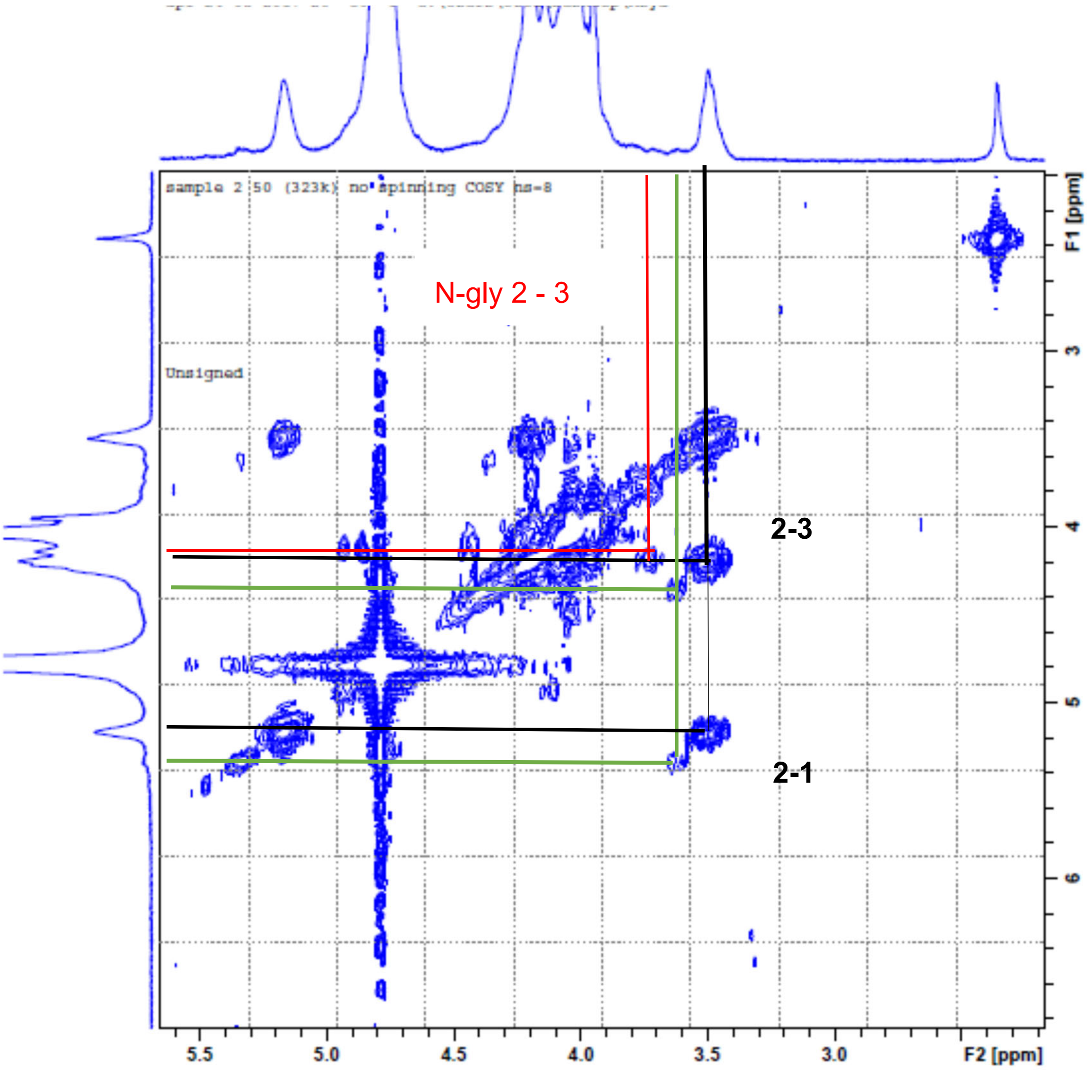

Figure 2-5:^{1}H-^{1}H COSY NMR of GC37, pH < 2.

2.3.2 Testing for optimal conditions for the reaction of 2-(Boc-amino ethyl) bromide and degraded GC

Small scale reactions were prepared to test a range of conditions, which were then used to synthesize EAGC variants with different EA substitution levels. **Table 2-3** represents the range of conditions and the substitution levels calculated from the ^{1}H-NMR spectra of the samples using the protons representing the Boc group (**Figure 2-6**).

Table 2-3: *Conditions for small scale reactions of 2-Boc-AEB with degraded GC*

Small scale reactions (20mg dGC)

2 Boc--AEB*(eq), t (°)	Mass of 2-BocAEB (mg)	NMP (ml)	2-AEB substitution (%)
2eq, 40°C	37	2	3
5eq, 40°C	92	2	7
10eq, 40°C	185	2	11
10eq, 40°C (double reaction)	372	2	17
5eq, RT	92	2	2

***2-Boc-AEB-2-(Boc-amino-ethyl) bromide**

Two reactions and 60° C and 80° C were also performed, but after the completion of the reaction we were unable to solubilise the obtained polymers potentially due the high level of modification. 5 eq and 10 eq of 2-Boc-AEB at 40° C as well as a double reaction of the 10 eq (by adding a fresh solution of 2-Boc-AEB for another 24 h) were used to synthesize EAGC variants with low, medium and high EA substitution levels.

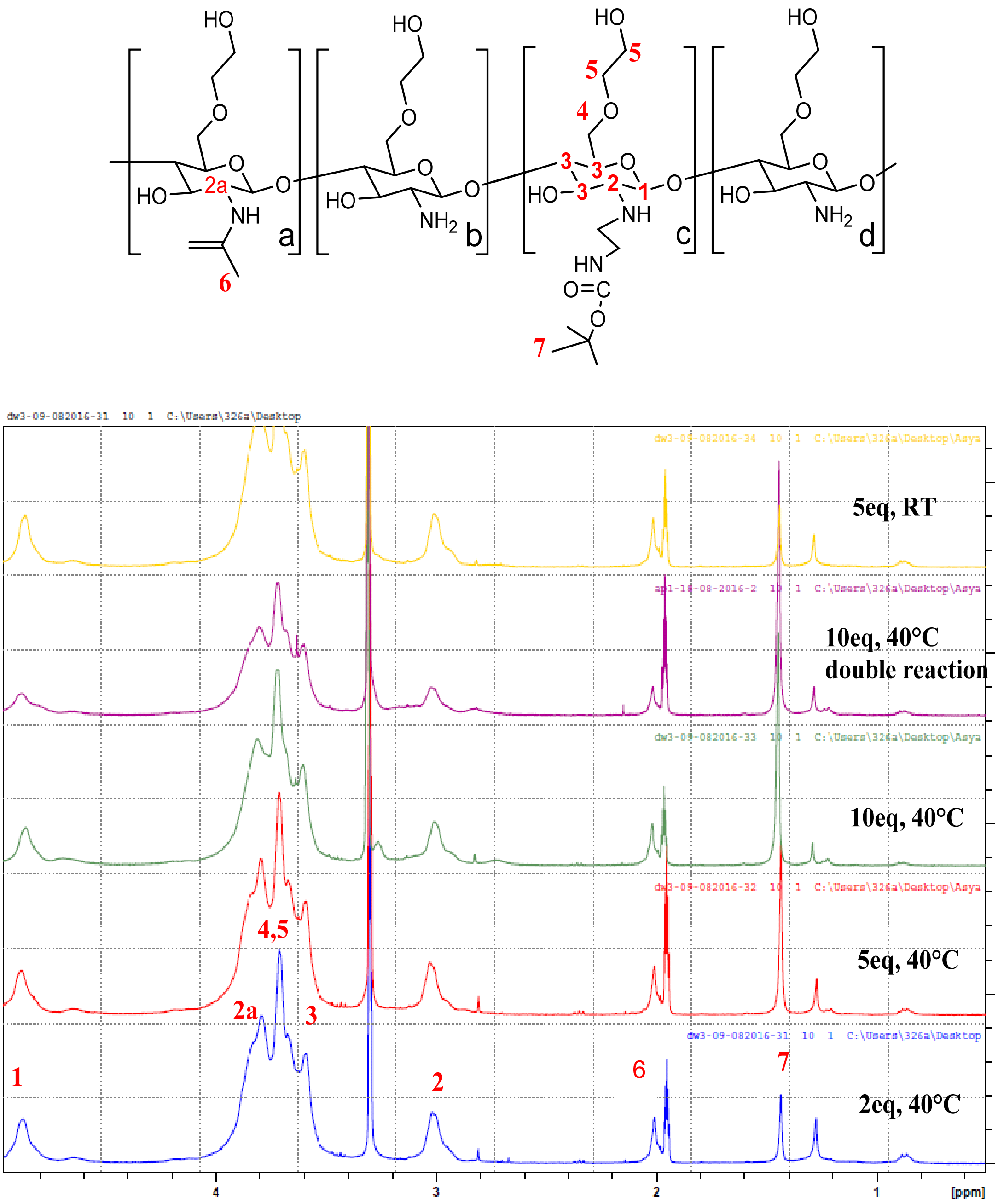

Figure 2-6: *Small scale reactions of dGC and 2-Boc-AEB (CD_3OD):* ***7****,* $\delta_{1.48}$ *[C**H₃**-C0-NH-, Boc protons],* ***6****:* $\delta_{2.1}$*=[C**H₃**-CO-NH-) – acetyl protons;* ***2.*** $\delta_{2.9-3.3}$*=[-CH-(OH)-C**H**-(NH₂)] – protons attached to the non-substituted C2 of the sugar;* ***2a****,* ***3****,****4*** *and* ***5*** *-* $\delta_{3.4-4.2}$*=[-C**H**(OH), -C**H₂**(OH) and -CH]-(OH)-C**H**-NH-CO-)], sugar protons;* $\delta_{4.79}$*=[D_2O],****1*** *-* $\delta_{4.8-5.0}$*=[-O-C**H**-O-], protons attached to C1 from the sugar. Percent substitution is calculated using the integration of the Boc protons (divided by 9) over the integration of the sugar protons (divided by 9) times 10*

2.3.2.1 Characterisation of EAGC variants by NMR

The two molecular weight GCs were used to synthesize six different EAGC variants with low (EA6GC37, EA9GC21), medium (EA13GC37, EA16GC21) and high level of ethyl-amino (EA) substitution (EA23GC37, EA24GC21). The level of substitution in the codes for the different variants is given as a number, which corresponds to the percentage substitution calculated from the ^{1}H-NMR spectrum of the deprotected samples. The yield for all the variants is listed in **Table 2-4** and as clear from the table the yield for all the polymers was equal or higher than 30 % potentially due to extensive dialysis**.** The reaction was repeated three times, ones for the small scale set up and another two times for the two different Mw GC (GC37 and GC21). **Figure 2-7** represents the general reaction scheme for the synthesis of the variants.

***Table 2-4:** Conditions for large scale reactions of 2- Boc-AEB with dGC and reaction yield*

Large scale reactions (100mg dGC)				
EAGC code	**Mass of 2-Boc-AEB (mg)**	**NMP (ml)**	**2-Boc-AEB substitution (%)**	**Yield (%)**
EA6GC37	920	10	6	22
EA13GC37	1850	10	13	28
EA23GC37	3720	10	23	31
EA9GC21	920	10	9	9
EA16GC21	1850	10	16	17
EA24GC21	3720	10	24	22

As a quality control measurement, the reagents GC **(1)** and the 2-(Boc-amino) ethyl bromide **(2)** were analysed via NMR before the start of the reaction. Peak assignments of the corresponding protons for GC **(1)** are shown on **Figure 2-2.** NMR analysis was used also to control the reaction with the 2-(Boc-amino)-ethyl bromide and to calculate the level of substitution before deprotection as well as after Boc removal. A set of NMR experiments were performed for all the EAGC variants in order to assign all the peaks in the NMR spectrum. The analysis of the correlations after the 2D NMR experiments (^{1}H-^{1}H COSY NMR and ^{1}H-^{13}C DEPT NMR) showed that the low and medium level of substitution EAGC variants (EA6GC37, EA9GC21 and, EA13GC37, EA16GC21) share the same characteristics. Similarly, the NMR spectra of the high level of EA substitution (EA23GC37 and EA24GC21) showed the same patterns. The reaction yielded consistency in the substitution levels regardless of the different molecular weights GC used before and after deprotection (**Table 2-5**).

Table 2-5: *Level of EA substitution between the two different batches of GC (GC37 and GC21) before and after deprotection*

Level of EA substitution for the two GC batches	EAGC	% EA substitution level before deprotection	% EA substitution level after deprotection
High	EA24GC21	24	24
	EA23GC37	23	24
Medium	EA13GC37	11	13
	EA16GC21	14	16
Low	EA6GC37	4	6
	EA9GC21	8	9

EA24GC21 or the highest level of substitution for the tested conditions revealed the presence of secondary and tertiary amines, **4**. ^{1}H-NMR spectrum of EA24GC21 on **Figure 2-8** shows the presence of a single EA substitution **(2b)** and the double EA substitution **(2c)**. ^{1}H-^{1}H COSY confirmed that the two new peaks in the ^{1}H-NMR of EA24GC21 represent proton **2** of the sugar (**Figure 2-9**). ^{13}C-CDEPT NMR and ^{1}H-NMR correlation spectroscopy confirmed that **2c**^{C} is a tertiary carbon, same as **2**$^{\mathbf{C}}$ (where C as a superscript indicates a carbon atom (**Figure 2-10**). However, no peak is detected in the ^{13}C DEPT NMR corresponding to **2b**$^{\mathbf{C}}$. The ^{13}C DEPT135 spectrum could confirm that protons assigned as **7** and **8 (Figure 2-8)** are the two sets of protons of the amino-ethyl group, as they are attached to secondary carbons. The ethyl-amino origin of protons **7** and **8** was further confirmed by 2D ^{13}C-^{1}H HMQC correlation NMR spectroscopy (data not shown).

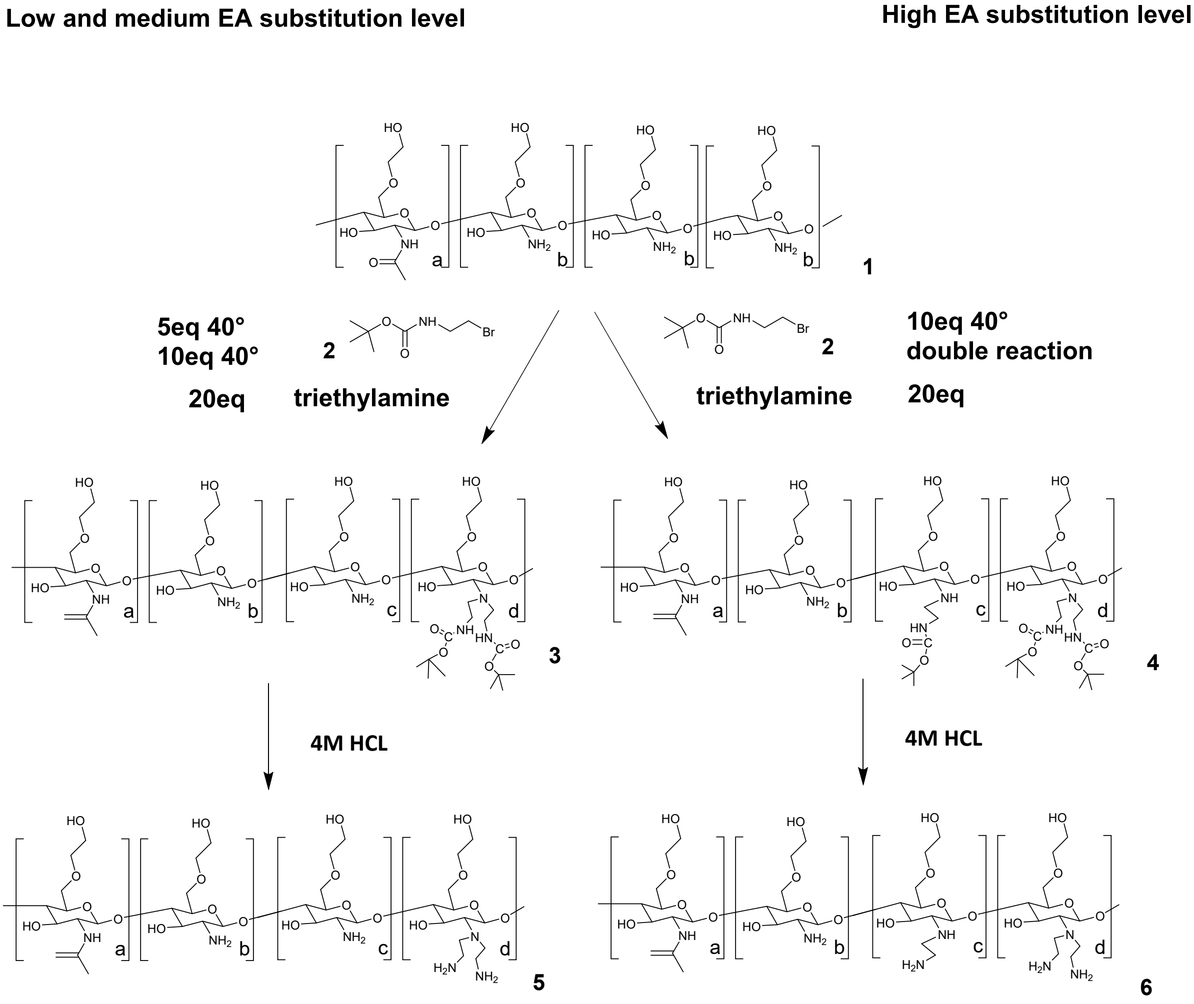
Low and medium EA substitution level

High EA substitution level

Figure 2-7: *General reaction scheme for the synthesis of the EAGC variants with different substitution levels.* ***4*** *represents EAGC variants with the highest substitution level for the tested conditions while the low and medium substitution level EAGC polymers are indicated as* ***3****.* ***4*** *shows the presence of a mixture of secondary and tertiary amines, while* ***3*** *shows the presence of only tertiary amines* ***1*** *represents GC (both molecular weights) before the reaction with* ***2*** *2-(Boc-amino) ethyl bromide takes place. 5 and 10 equivalents of* ***2*** *were used to synthesize EAGC variants with low and medium substitution levels respectively, while the high substitution level EAGC variants are synthesized by repeating the reaction with 10 eq 2-(Boc-amino) ethyl bromide. 20 eq of triethylamine and 40° C are kept constant for all the reactions*

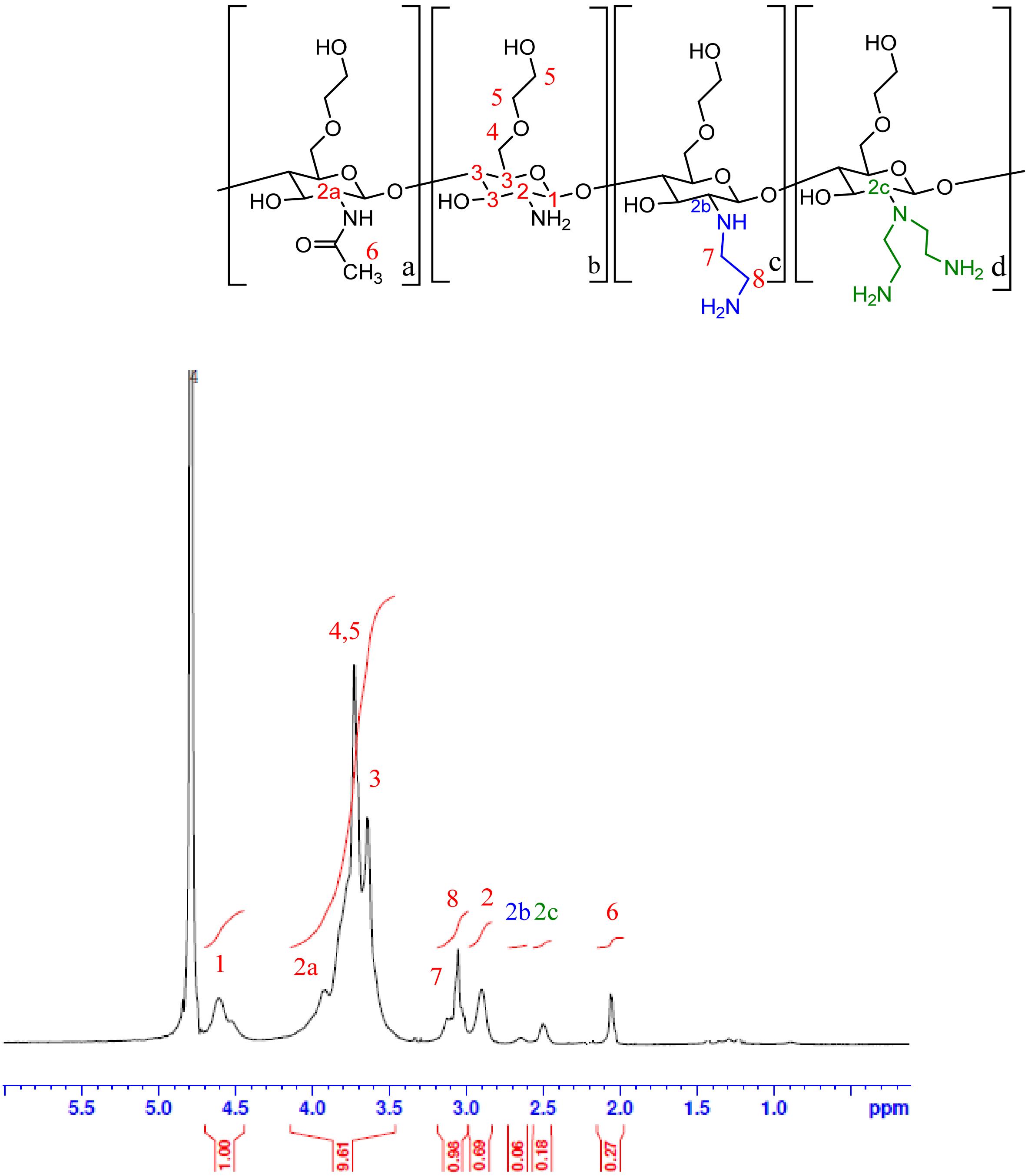

***Figure 2-8**: ^{1}H-NMR EA24GC21 in (D$_2$O) δ$_{2.1}$=[C**H**$_3$-CO-NH-), δ$_{2.5}$=[-C**H**-N-(CH$_2$-CH$_2$NH$_2$)$_2$], δ$_{2.65}$=[C**H**-NH-CH$_2$-CH$_2$-NH$_2$] , δ$_{2.8\text{-}2.95}$=[-CH-(OH)-C**H**-(NH$_2$)], δ$_{3.1}$=[-C**H$_2$**-CH$_2$-NH$_2$], δ$_{3.2}$=[-CH$_2$-C**H$_2$**-NH$_2$], δ$_{3.4\text{-}4.1}$=[-C**H**(OH), -C**H$_2$**(OH) and -CH]-(OH)-C**H**-NH-CO-)], δ$_{4.6}$=[-O-C**H**-O-]. δ$_{4.79}$=[D$_2$O], Yield of EA24GC21 =0.058g (22%). Percent substitution is calculated from the integration of **2b** **(**divided by 1**)** and **2c** protons (divided by 1) over the integration of the sugar protons (divided by 9) times 100.*

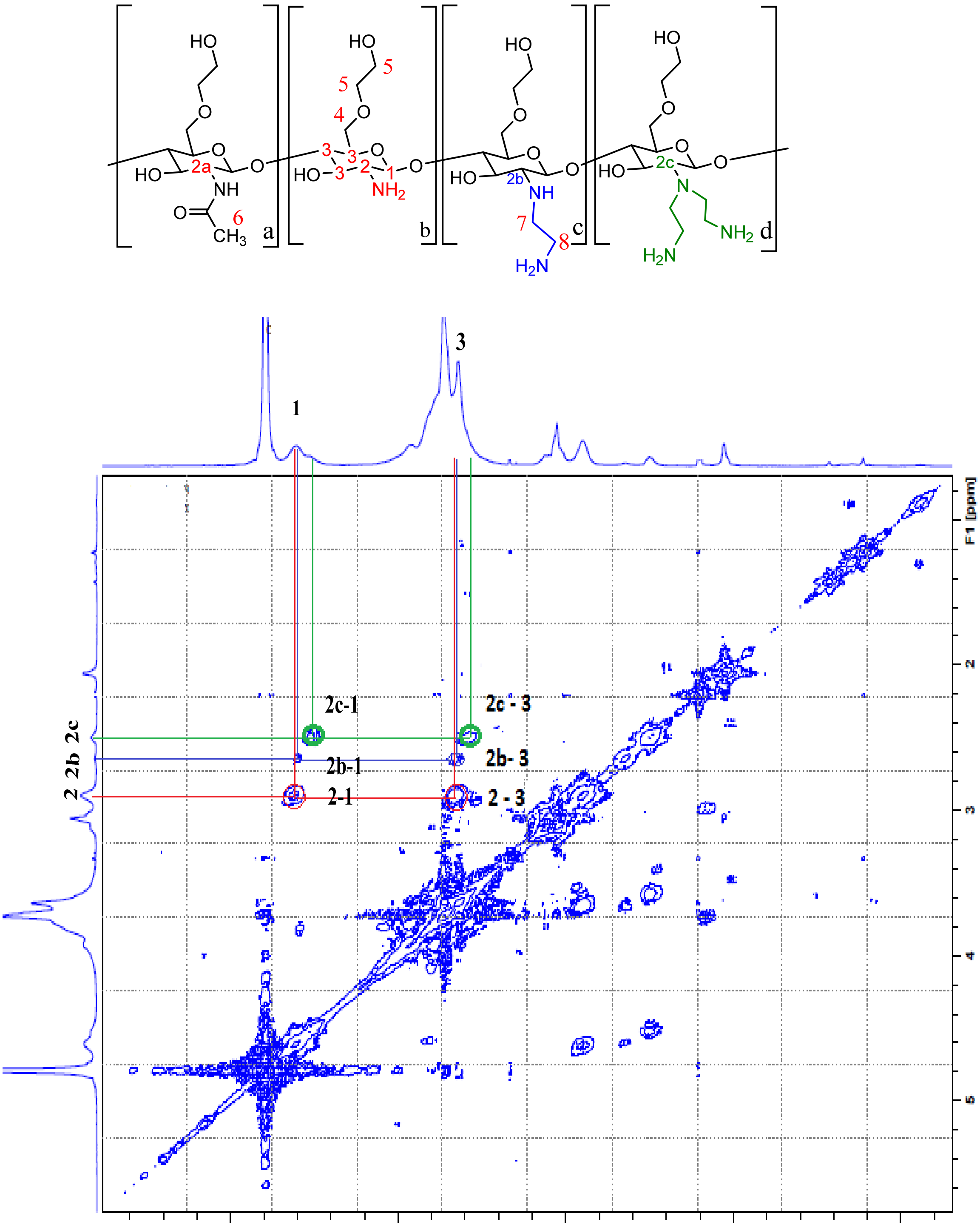

Figure 2-9: *^1H-^1H COSY NMR) of EA24GC21 in (D_2O) , the 2D spectrum shows the protons of* ***(2b)*** *and* ***(2c),*** *which have the same correlations as protons* ***(2)****.* ***2b*** *and* ***2c*** *correlate with C1 and C3, which confirms the presence of two types of EA substitutions - a single EA substitution and a double EA substitution, hence the presence of secondary and tertiary amines in the structure of EA24GC21.*

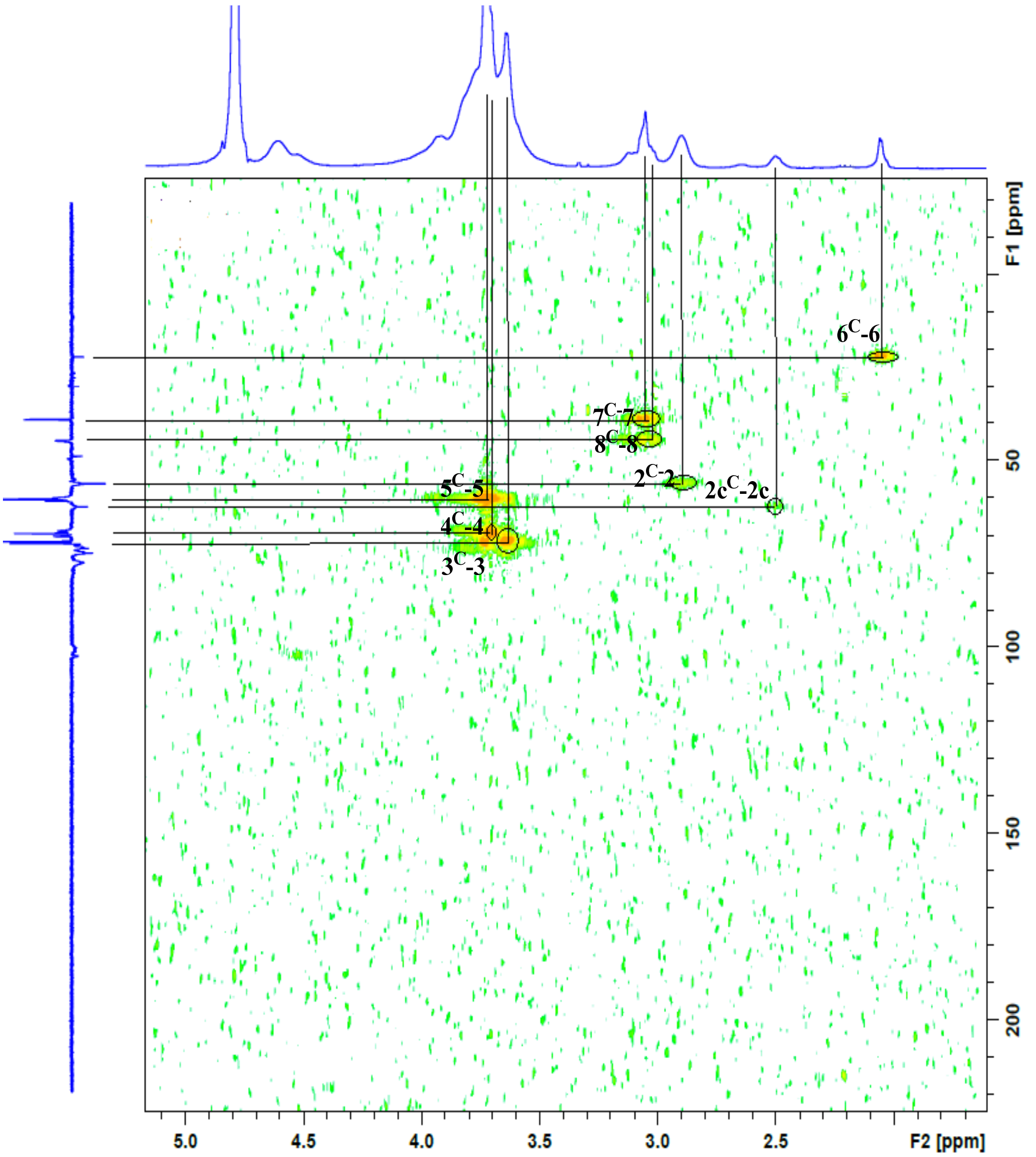

***Figure 2-10**: (^{1}H-NMR – ^{13}C DEPT NMR) of EA24GC21 – The ^{13}C spectrum is shown on the y axis, the carbons attached to the protons shown on the x axis are marked with the same number, but with a I as a superscript. On the y axis **6^I** $\delta_{21.5}$= [**C**H$_3$-CO-NH – acetyl group of the sugar), **7^I** δ_{38}=[-**C**H$_2$-CH$_2$-NH$_2$, ethyl amino group], **8^I** δ_{44}=[-CH$_2$-**C**H$_2$-NH$_2$,, ethyl amino group],**2^I** $\delta_{55.3}$=[-CH-(OH)-**C**H-(NH$_2$)], **5^I** δ_{59-60} =[-(**C**H$_2$)$_2$OH, glycol],**2c^I** δ_{61}= [-**C**H-N-(CH$_2$-CH$_2$NH$_2$)$_2$, double ethyl amino substitution of **2^I**],**4^I** $\delta_{69.3}$=[-CH-C**H**$_2$-O, sugar moiety), **3^I**, δ_{73}=[**C**H-OH-**C**H-O-**C**H-CH$_2$, sugar moiety].*

By contract to the high EA substitution level EAGC variants of both GC37 and GC21, the low and medium EA substitution level EAGC variants did not show the presence of a mixture of secondary and tertiary amines, but only tertiary amines (**3** and **5**, **Figure 2-7**). The ^{1}H-NMR results showed the presence of a peak at $\delta_{2.5}$ and $\delta_{2.58}$ for the larger and smaller polymers respectively, hence 2c or tertiary amines were detected only. No peak representing **2b** (secondary amines) was found at $\delta_{2.7}$ (**Figure 2-11**).

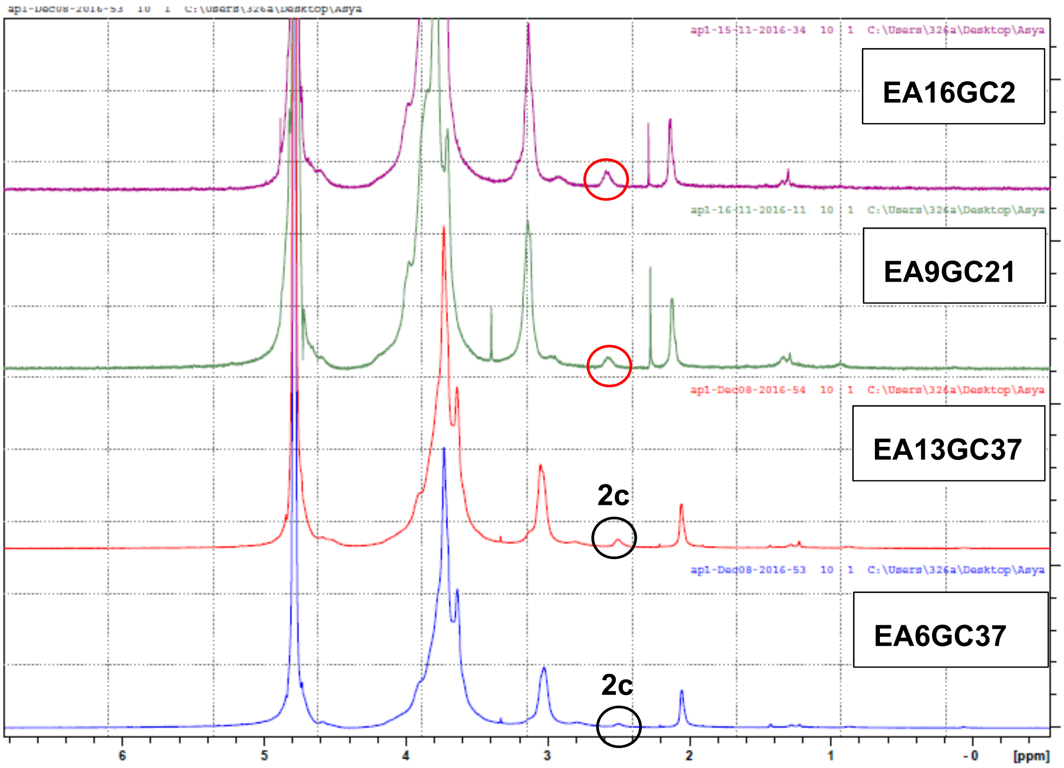

Figure 2-11:*Comparison between the ^{1}H-NMR of the EAGC variants with low and medium EA substitution levels . The spectra show the presence of **2c** protons at $\delta_{2.5}$ (black circle) for EA6GC37 and EA13GC37 and at $\delta_{2.58}$ (red circle) for EA9GC21 and EA16GC21.*

The ^{1}H-^{1}H COSY and ^{1}H-^{13}C DEPT NMR of the medium and low EA substitution levels confirmed the speculations that only tertiary amines are present. Similarly, to the high EA substitution level EAGC variant **2c** protons were found to correlate with proton **1** and **3**, however in the ^{1}H-^{1}H COSY spectrum of all the samples no other correlations with protons **1** and **3** were detected, hence we were unable to detect the presence of secondary amines **(Figure 9-1** and **Figure 9-2**, see Appendix). ^{13}C DEPT NMR confirmed that **2c** protons are attached to a tertiary carbon. From the ^{13}C DEPT NMR spectrum it was also visible that the two sets of EA protons **7** and **8** were attached to secondary carbons as in the case of the high EA level of substitution EAGC variants **(Figure 9-3** and **Figure 9-4**, see Appendix).

2.3.2.2 Characterisation of EAGC variants by GPC

In attempt to measure the molecular weight of the EAGC variants many factors were taken into consideration and the conditions of the method were altered as different problems were encountered. The information generated for the influence of the different factors is very useful and would help us to measure the molecular weight of the EAGC variants more accurately.

2.3.2.2.1 Optimisation of the GPC method for accurate molecular weight measurements of the low, medium and high substitution level EAGC variants.

The molecular weight of the EAGC variants was measured with a buffer system consisting of 1 M sodium acetate/acetic acid, pH=4. The results of the measurements are shown in **Table 2-6**

Table 2-6: *Molecular weight and polydispersity values for EAGC variants*

EAGC	Mn (Da)	Mw (Da)	Mw/Mn (polydispersity)	dn/dc
EA6GC37	51030	52750	1.034	0.1461
EA13GC37	52460	55450	1.057	0.1647
EA23GC37	39650	44280	1.041	0.1568
EA9GC21	25560	26600	1.042	0.1607
EA16GC21	33290	34700	1.117	0.1331

The table shows that with the increase of the modification levels, the molecular weight of the polymers increases as well, which is to be expected. However, two problems were encountered. First, the fact that the increase in molecular weight does not correspond to the molecular weight, which can be predicted roughly based on the NMR experiments. Based on the NMR results EA23GC37 with a substitution level of 23 % should have a molecular weight of approximately 39 kDa, while the measured molecular weight is 44 kDa (**Table 2-6**). Second with the increase of the EA substitution level, the light scattering profiles of the tested EAGC polymers showed the presence of a second peak, eluting before the one of the polymers. The increase in the EA modification resulted in an increase in intensity of the shoulder peak (**Figure 2-12).** An anomalous dn/dc value is shown in **Table 2-6** for EA16GC21, which could be attributed to an error in dilutions during standards preparation for dRI analysis as all other dn/dc values are similar. Interestingly, polydispersity is low for all the polymers, which could be explained with the extensive dialysis resulting in the removal of small molecular weight polymers, hence improved molecular weight distribution and polydispersity, although at the cost of lower yields.

2.3.2.2.1.1 Effect of the dissolution time

It was hypothesised that an increased time for dissolution before analysis would encourage the polymer-solvent interactions rather than the polymer-polymer interactions hence aggregation will be reduced. By contrast the results of the experiment showed that increasing time for dissolution, by leaving the polymer solution in the mobile phase overnight before analysis increased drastically the shoulder peak in the light scattering monitor (**Figure 9-5**, see Appendix).

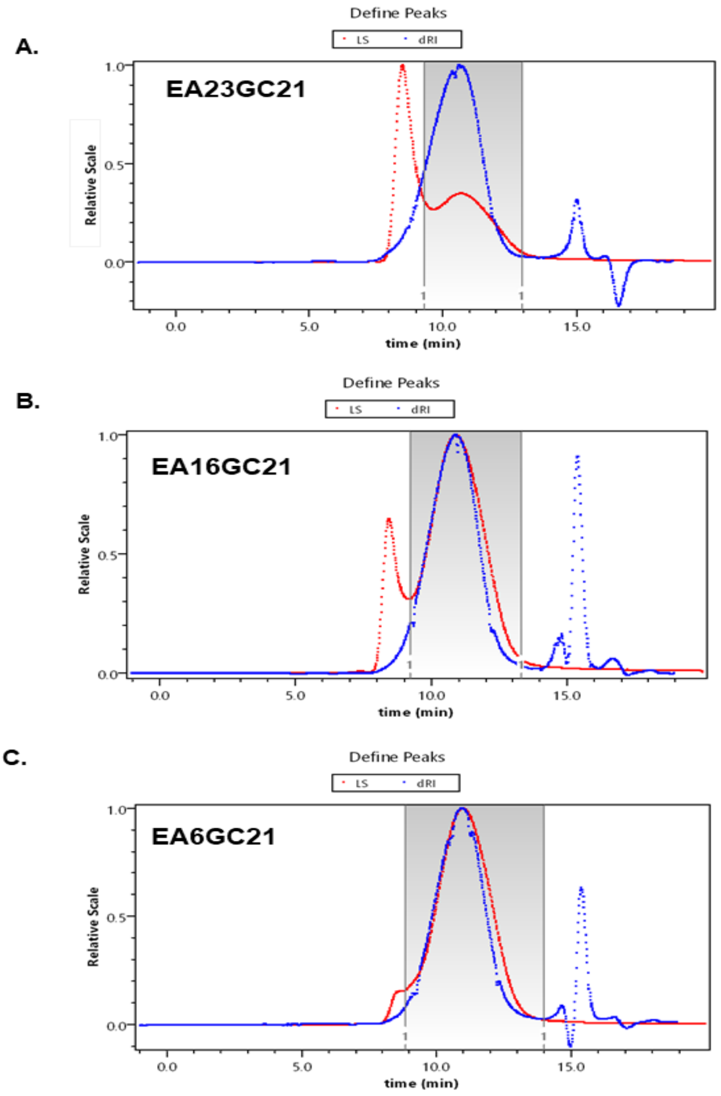

Figure 2-12: *GPC-MALLS profiles of EAGC variants in 1 M sodium acetate/acetic acid buffer system, pH=4, LS (light scattering in red), dRI (differential refractive index in blue): Shoulder peak increases in intensity with the increase of EA substitution level (LS-light scattering, red line). From bottom to top EA9GC21 – low level of EA substitution (**C**), EA16GC21 – medium level of EA substitution (**B**) and EA24GC21-high level of EA substitution (**A**).*

The peak at the end of the **run** is referred in literature as ghost peak or system peak., it's commonly caused by a loss of equilibrium in the system [201]. This could be due to different sample composition, buffer used or anything which could influence the equilibrium between the mobile phase and the stationary phase. The polymers shown on **Figure 2-12** were analysed on the same day with the same buffer, hence salt content and pH. A potential solution to this would be to use blanks in between runs in order to allow for longer equilibration time. It is worth mentioning that the so-called system peak does not have any influence on the quality of the analysis of the results.

2.3.2.2.1.2 Effect of the ionic strength of the buffer

The ionic strength of the sodium acetate/acetic acid buffer was varied (1M,0.5M, 0.25 M and 0.125 M) and the pH was kept constant at 4. The sample for analysis was chosen on purpose to be an EAGC variant with the highest EA level of substitution as the shoulder peak for the high-level substitution EAGC variants appeared with the highest intensity on the light scattering monitor. The results of the experiment showed that the decrease in ionic strength results in decrease of the observed shoulder. (**Figure 2-13**).

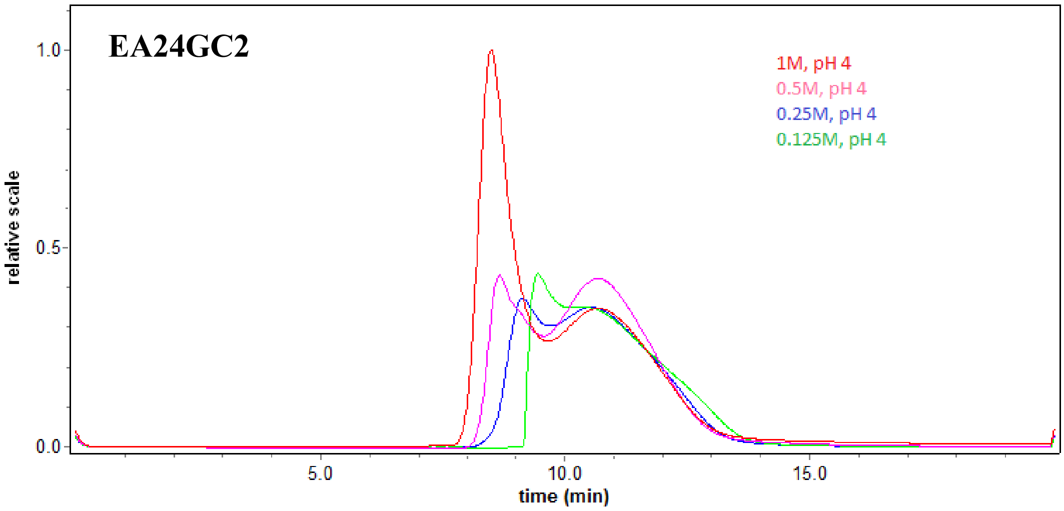

Figure 2-13: *Effect of ionic strength on aggregation of EA24GC21 . The graph shows four different runs of EA24GC21 with sodium acetate buffer, pH=4 and 1 M (in red), 0.5 M (in pink), 0.25 M (in blue) and 0.125 M in green. The shoulder peak of EA24GC21 is decreasing with the decrease in molarity of the buffer.*

The intensity of the shoulder peak is decreasing with the decrease in molarity of the buffer, but the graph also shows that the non-specific interactions of the polymer with the column increase, which is clear from the tailing of the peaks. So, reducing further the strength of the buffer is potentially going to solve the problem of aggregation, but at the same time the excessive tailing will cause a non-symmetrical profile, which will affect the accuracy of the molecular weight measurements. It was then hypothesised that charge is another very important factor, which can influence the behaviour of the polymer in the buffer and the polymer interactions with the column. In an attempt to strike a balance between the ionic strength of the buffer and the charge of the polymer to avoid the chances of aggregation/tailing in the light scattering we investigated the effect of polymer charge by altering the pH of the buffer.

2.3.2.2.1.3 Effect of charge

The reduced ionic strength of the buffer showed a trend towards a reduction of aggregation. To study the effect of charge experiments with a sodium citrate/citric acid buffer, pH=3 were performed. By decreasing the pH a more positively charged polymer chain is obtained as more amines will be protonated. This will then lead to a more open conformation of the polymer, because of an electrostatic repulsion between the positive charges, which is used to avoid aggregation. Two runs with sodium citrate/citric acid buffer, pH=3 were performed with a molarity of 0.25 M and 0.125 M were used. The results showed that a major improvement was achieved as the aggregation appears to be reduced to a minimum even with the 24 % EA modified polymer and a more symmetrical profile of EA24GC21 was obtained. (**Figure 2-14)**

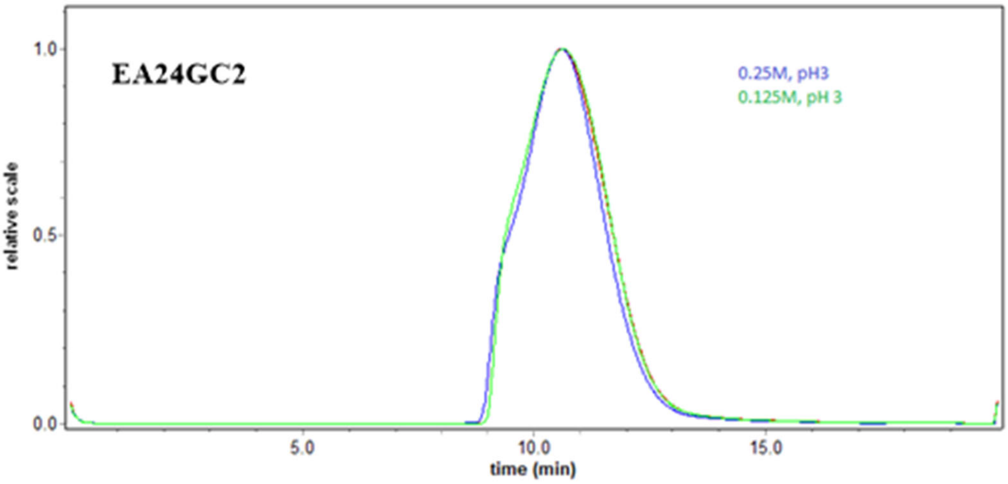

Figure 2-14: *Light scattering profile of EA24GC21 in 0.25 M sodium citrate buffer, pH=3 and 0.125 M sodium citrate buffer, pH=3. The graph shows that the combination of an optimal ionic strength and positive charge of the polymer decreased aggregation to a minimum as visible from the light scattering profile of both runs.*

The optimisation of the method led to identifying the right conditions to measure accurately the molecular weight of the synthesized EAGC variants. Unfortunately, due to technical problems with the GPC-MALLS we were unable to re-measure the molecular weight of the EAGC variants

2.4 **Discussion**

To improve the buffer capacity of glycol chitosan we synthesized a range of EAGC variants with low, medium and high substitution levels for the tested conditions. The introduction of secondary (-NH) and tertiary (-N-) amines with higher proton affinities than primary amines ($-NH_2$) is hypothesised to improve the buffer capacity of GC [202]. Improved buffer capacity will facilitate endosomal escape and transfection efficiency. However, as described previously an increase in positive charge can result in elevated toxicity, hence in search of the fine balance we designed EAGC variants with three different modification levels. Additionally, as molecular weight is also known to play a crucial role not only for complexation of the polymers with the cargo nucleic acids, but also for the ability of the obtained nanoparticles to cross the cellular membrane (size dependent)[180,203–205] we used GCs with two molecular weights. A study by *Carlos et al.* showed that EAGC variants with a range of substitutions showed increased buffer capacity when compared to the unmodified GC [206] [($-NH_2$) pKa 6.41± 0.05)][178] due to the presence of a mixture of secondary and tertiary amines in some of the polymers. Secondary and tertiary amines have higher pKa values (9-10) [207,208] as they are more basic than primary amines. However, the authors show that the presence of tertiary amines coincides with an increase in toxicity [196]. The synthesis of EAGC variants with low, medium and high level of ethyl-amine (EA) substitution is a three-stage process with two intermediate purification steps. 1d and 2D NMR experiments were used to characterise the obtained polymers and to calculate the percentage substitution.

The first stage of the reaction is the acid degradation of glycol chitosan. A relationship between degradation time and the range of Mw obtained has been established in our lab previously [209,210]. Based on this reference the time points for degradation were chosen to be 1 h 2 h and 6 h In order to obtain dGC with a Mw range between 20 000 – 60 000 kDa. The Mw of the three GC batches was 57220 (GC57), 37200 Da (GC37) and 20940 Da (GC21) (**Table 2-2**) for 1 h, 2 h and 6 h degradation respectively. Dialysis was used to remove the excess hydrochloric acid from the degradation mixture. NMR analysis provided information for the structure of GC before the start of the reaction with 2-Boc AEB and all the peak were assigned **(Figure 2-2)** As a quality control measurement, the 2-Boc AEB was also analysed via ^{1}H-NMR (data not shown). The peak with a chemical shift $\delta_{1.48}$ corresponds to the protons of the methyl groups (CH_3) of the *tert*-butyloxycarbonyl group (Boc) group (**Figure 2-6**). Boc groups are used for protection of amine groups to avoid side reactions. Boc groups are easily removed in strong acids such as trifluoroacetic acid/dichloromethane and hydrochloric acid/methanol mixtures with the addition of a scavenger, which traps the *tert*-carbonyl cation [211,212].

The next stage of the synthesis process is the reaction between GC and 2-Boc-AEB. To provide a range for the EA substitution level, small scale reactions testing, two different temperatures and different equivalents of 2-Boc AEB were prepared. Percent substitution for the Boc protected EAGC variants was calculated using the integration of the Boc protons over the integration of the sugar protons since the peak representing the modification (EA protons) is overlapping with the C2 protons of the sugar, hence we were unable to use it to calculate the % EA substitution. The different conditions of the small-scale reactions are listed in (**Table 2-3)**. From the table, it is clear that an elevated temperature leads to an increase in modification level as the lowest modification level is 2.5 % of EA substitution (RT) vs 6.9 % (40° C), comparing two reactions with 5 molar equivalents of 2-Boc AEB. The reaction between 2-Boc AEB and GC is also proven to be more effective at 40°C as shown by *Carlos et al.* [206]. Therefore, based on the results of the small-scale reactions we chose three conditions (5, 10 and a double reaction of 10 molar equivalents of 2-Boc AEB) with GC37 and GC21 at 40° C, which we synthesized on a five times larger scale.

The third stage of the synthesis is the deprotonation of the EAGC variants, which was performed in 4 M HCl in water for 3 h with triethylamine used as a proton scavenger. Successful removal of the Boc group was confirmed by ^{1}H-NMR. After deprotection the ^{1}H-NMR of the samples showed the presence of two new peaks for the highest level of substitution EAGC variants (EA23GC37 and EA24GC21). The first peak assigned as **2b** appeared at $\delta_{2.75}$ for EA23GC37 (data not shown) and ($\delta_{2.65}$) for EA24GC21 respectively (**Figure 2-8**). The second peak assigned as **2c** (**Figure 2-8**) appears with the same chemical shift for both high EA substitution level EAGC variants at $\delta_{2.5}$.

^{1}H-^{1}H COSY showed that the two peaks at $\delta_{2.75}$ and $\delta_{2.65}$ **(2b)** and $\delta_{2.5}$ **(2c)** have correlations with the protons attached to C1 and C3, the same as the peak at $\delta_{2.8\text{-}2.95}$ (**2)** representing the protons of C2 from the sugar, next to the N of the primary amine group (**Figure 2-9)**. Therefore, the two sets of protons **2b** and **2c** giving rise to the two peaks in the spectra of the high EA level of substitution EAGC after deprotection are both substituted C2 from the sugar, hence two modifications are detected. This is further confirmed by the results obtained from the CDEPT 135 experiments when correlated with the proton spectra as **2c** represents protons attached to a tertiary carbon ($2c^{C}$-2c, **Figure 2-10**). However, we were unable to confirm that the peak at

$\delta_{2.65}$ (**2b**) represents protons attached to a tertiary carbon as no correlation of **2b** is visible on **Figure 2-10.**

Interestingly **2c** is also present for the low and medium EAGC variants. However, for EA9GC21 and EA16GC21 it appears with a slight downfield shift at $\delta_{2.58}$ (**Figure 2-11**). EA9GC21 and EA16GC21 are both obtained from GC21, which is almost half of the molecular weight of GC37 (21180 vs 37440). The stack plot of the proton experiments shows that the whole spectra of EA9GC21 and EA16GC21 is shifted downfield when compared to EA6GC37 and EA13GC37. A potential explanation for this could be the presence of more hydrogen bonds between EAGC and water molecules for the larger polymer which will provide more shielding from the external magnetic field. Moreover, there is a peak at $\delta_{2.9}$ for EA9GC21 and EA16GC21 and $\delta_{2.8}$ EA6GC37 and EA13GC37 **(Figure 2-11).** These peaks do not show any correlations in 2D NMR experiments with the protons attached to C1 and C3 from the sugar (data not shown). Based on these findings we concluded that the two modifications in the structure EA23GC37 and EA24GC21 are a result of a single and a double EA substitution, hence in agreement with the findings of *Carlos et al.* these polymers have a mixture of secondary and tertiary amines (**Figure 2-7**, structures **4** and **6**). By contrast the low and medium level EAGC variants (EA9GC21, EA6GC37, EA13GC37 and EA16GC21 appeared to have only tertiary amines (**Figure 9-1-Figure 9-4**, see Appendix, **Figure 2-7**, structures **3** and **5**).

The reaction with 2-Boc (amino-ethyl bromide is a halide alkylation reaction of primary amines, the mechanism of which is shown below on (**Figure 2-15).** The N from the primary amine acts as a nucleophile as it has a lone electron pair and attacks the electrophile C of 2-(Boc-amino) ethyl bromide displacing the bromide and creating the new C-N bond. Triethylamine (: B) deprotonates the positive N centre yielding a secondary amine. Secondary amines as mentioned earlier have higher pKa values than primary amines, hence behave as stronger nucleophiles, which leads to a double substitution and the production of tertiary amines as shown by *Carlos et al.*

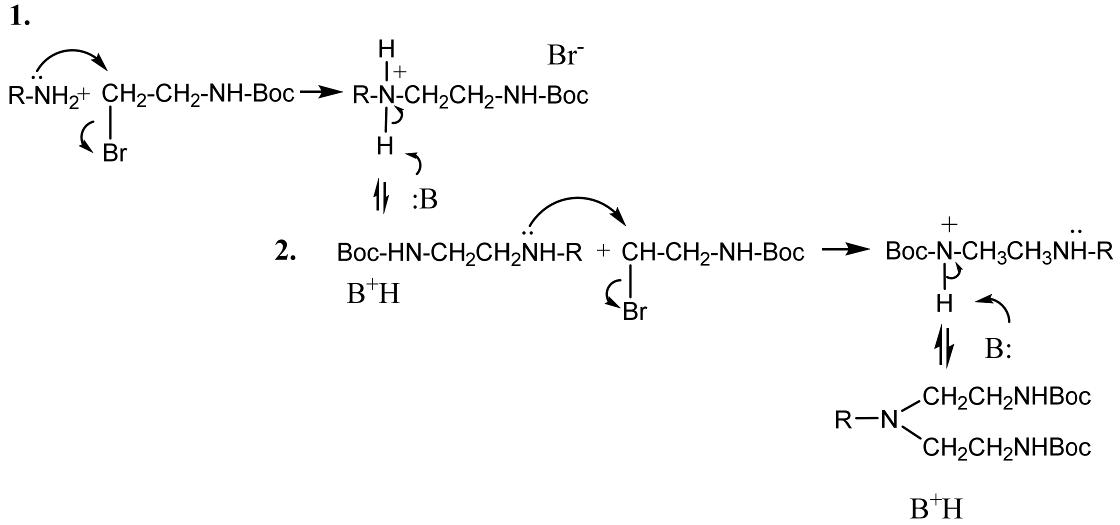

***Figure 2-15:** Mechanism of the reaction of halide alkylation of the primary amines of glycol chitosan . **1:** Formation of secondary amines **2:** Formation of tertiary amines. R-represents the polymer chain, while B represents triethylamine.*

As mentioned before the peaks at $\delta_{2.9}$ (EA9GC21, EA16GC21) and $\delta_{2.8}$ (EA6GC37, EA13GC37), did not show any correlations with the C1 and C3 from the sugar. However, a small peak at $\delta_{2.8}$ is also present for the degraded GC37 before the reaction with 2-Boc AEB was performed (**Figure 2-2**). *Knight et al.* reported the presence of N-glycolated secondary and tertiary amines and proposed a new structure of glycol chitosan contradictory to the widely accepted O-glycolated glycol chitosan[194] (**Figure 1-4**, **B** and **C**). The general scheme for the synthesis of glycol chitosan from chitin, includes a reaction with ethylene oxide, followed by deacetylation. It has been shown that if chitin is initially deacetylated the epoxide would react more favourably with the amine groups than the hydroxyl groups which would yield N-glycolated residues instead of O-glycolated ones. In attempt to check whether the glycol chitosan we used has a mixture of N-glycolated and O-glycolated residues we performed ^{1}H-NMR experiments at acidic (pH < 2) and basic (pH >10) as described by *Knight et al.* Similarly, to *Knight et al.* the high pH sample of GC showed the presence of several small peaks, however instead of the chemical shifts reported by them ($\delta_{3.1\text{-}3.6}$) the small peaks in our experiments appear at $\delta_{2.8\text{-}3.4}$. This is probably due to the higher temperature (90° C) used for their experiments versus (50° C) for ours. Exposure of the polymer at high temperature could cause de-shielding of the structure, because of the breaking of hydrogen bonds between the polymer and the water molecules. We have confirmed the temperature dependent downfield chemical shift of the whole spectrum with an increase in temperature (**Figure 9-6,** see Appendix).

The stack NMR spectra on **Figure 2-3** shows the downfield chemical shift of the peaks from 2.8-3.4 ppm to 3.4-3.8 ppm in the low pH case. The downfield shift is also visible for the protons attached to C1 assigned as **1** (**Figure 2-2)**, which for the GC (pH < 2) are no longer buried underneath the protons of the water peak and appear at $\delta_{5.2\text{-}5.4.}$ *Knight et al.* explain this with the occurring protonation and deprotonation of the amine groups in the acidic and basic environments, which the polymer experiences. As visible from the stack spectra of the samples at the two pH values there is no chemical shift for the methyl protons of the acetyl group, assigned as **6 (Figure 2-2).** This further confirms that the chemical shifts noted for the groups above for the two pH values are due to protonation/deprotonation effects. Therefore, *Knight et al.* suggested that the peak immediately upfield from H2 represents protons attached to a C next to a N exactly like H2 does (the protons attached to the carbon next to the nitrogen from the primary amines of GC), hence a N-glycolated secondary amine of GC is present. Our data from the 2D NMR experiments is in agreement with these findings as the new peak (**N-gly 2**, **Figure 2-3**) correlates with protons from the sugar (H3) and with (H1) (red line, **Figure 2-4 and Figure 2-5**). The figure shows the presence of another correlation with the protons of one of the small peaks ($\delta_{3.2\text{-}3.4}$) with protons from the sugar (green line, **Figure 2-4**). Due to the complexity of the structure it is hard to assign these protons, *Knight et al.* speculated that they are coming from the methylene groups of the glycol attached to the primary amine and they even proposed the presence of tertiary N-glycolated amines (**Figure 1-4**, **C)**. However, we are unable to make this conclusion based on the results we have. Although there is some proof for the presence of N-glycolated secondary amines in the structure of our glycol chitosan, more experiments with intermediate pH values need to be performed to rule out the possibility to have changes in the two spectra because of protonation/deprotonation events related solely to the primary amines in the structure.

In attempt to measure the molecular weight of the EAGC polymers we performed a series of optimisation steps of the protocol used for the GPC - MALLS. **Table 2-6** shows the molecular weight averages and the polydispersity values for the EAGC variants (except EA24GC21). The increasing level of modification resulted in an increase of the measured molecular weight for both GC37 and GC21, however the measured molecular weight averages are not accurate as the increase for all the polymers is not representative of the modification level calculated from the NMR. In addition to that we observed a shoulder peak in the light scattering profiles of the polymers (red **Figure 2-12**). The intensity of the shoulder peak increases with the increase in modification. As the light scattering is more sensitive the shoulder peak is visible only when the sample is passing through the LS detector, a possible indication of aggregation. Aggregates scatter light aggressively, however they are not detected by the dRI possibly due to their low concentration hence no shoulder is observed in the dRI.

In search of the reason for the observed effects in the light scattering we altered a few parameters, which we considered important to prevent aggregation: i) the dissolution time of the polymers before sample analysis ii) the type of the buffer system used iii) the ionic strength of the buffer and iv) the charge of the polymer. EA24GC21 was chosen to be the polymer for all the tests as its light scattering profile had the highest intensity shoulder peak. We considered first increasing the dissolution time of the polymer before the run was performed as a common practice in the lab is to run the samples immediately after adding the mobile phase and after filtration. We hypothesised that this could encourage the polymer-solvent interactions over the polymer-polymer interactions. Contrary to what we expected an overnight dissolution of EA24GC21 in the sodium acetate buffer resulted in a light scattering profile with a shoulder (data not shown). The next parameter to change was the type of the mobile phase used. Instead of the widely used sodium acetate/acetic acid system we tried a 5 % ammonium sulphate/3 % acetonitrile, pH=4, a buffer used for GPC-MALLS measurements of PLL [213]. The results showed no change in the LS profile of EA24GC21 and in this instance the type of the ions used did not prevent the aggregation.

Ionic strength of the buffer is a crucial parameter, which plays an important role in screening the charges along the chain of a polyelectrolyte by facilitating an electrostatic interaction between the salt ions and the ionic groups of the polymer in solutions, which is thought to minimise the inter-chain electrostatic interactions [214] . However, high ionic strength is proven to increase the chance of a hydrophobic microdomains formation in the polymer chain, which is shown to induce inter-chain association and aggregation due to enhanced hydrophobic interactions [215]. By decreasing the ionic strength of the sodium acetate buffer from 1 M to 0.125 M, pH=4 we managed to achieve a significant improvement in the reduction of the observed shoulder peak in the LS spectra of EA24GC21 at 0.125 M (**Figure 2-13**). The ions of the mobile phase in GPC are of major importance as they prevent secondary electrostatic interactions of the polymers with the stationary phase of the column, hence tailing of the eluted peaks. The recommended salt concentration to be used is in the range of 0.1 M - 0.5 M [215]. We have attempted to reduce even further the ionic strength of the buffer to 65 mM, but the obtained LS profile of EA24GC21 showed a completely non-symmetrical peak with excessive tailing (data not shown). This result prompted us to consider reducing the pH of the buffer to 3 in an attempt to strike a balance between charge of the polymer and ionic strength. The new mobile phase used was sodium citrate/citric buffer, pH=3. The new buffer prepared showed a considerable improvement in the LS spectra of EA24GC21 with an improved peak symmetry for both 0.25 M and 0.125 M sodium citrate. Unfortunately, due to almost permanent technical problems with the machine we have as yet been unable to use the optimised conditions to measure the molecular weight of the polymers.

2.5 **Conclusions**

To sum up EAGC polymers with a variation in the substitution level namely (low, medium and high ethyl-amino substitution level were successfully synthesised and purified. The characterisation of the EAGC polymers presented several challenges related to structure elucidation due to the complexity of the polymer molecules, the polymer-polymer interactions and the polymer-solvent interactions. The work of the chapter demonstrated that some of the problems were solved and an optimised method for molecular weight determination using GPC and light scattering was presented. The data helped us learn more about the behaviour of our polymers in solution and defined polymer charge and ionic strength as key parameters affecting the polymer’s conformation and aggregation behaviour in light scattering experiments

3 Synthesis and characterisation of BS PEG (5) bis spermidine

3.1 Introduction

The term polyamines is collectively used to describe organic compounds bearing one or more amino groups. Polyamines such as spermine, spermidine and putrescine are meant to play crucial roles in maintaining cellular growth and differentiation. [216–219]. These functions have been shown to be important for cancer cell proliferation where a decrease in the polyamine concentration results in triggering apoptosis and cellular growth inhibition [220,221]. The mechanisms through which polyamines regulate gene expression and facilitate cell proliferation are still not well understood. Interestingly, synthetic polyamine analogues show *in vitro* anti-proliferative activity in many cell lines [222,223]. Polyamine analogues use a polyamine transporter to enter the cell but have no cell growth accelerating functions. They can be either chemically designed mimetics, which block their binding sites or anti-metabolites [224]. Very successful analogues with anti-tumour activity are the bis (ethyl) polyamines. N^1,N^{11} di - (ethyl) norspermine is in clinical trials for the treatment of hepatoma [225].

It has been shown that cationic biogenic polyamines and their synthetic analogues interact and stabilize DNA and RNA molecules [226,227] Therefore, in addition to the synthesis of polyamine analogues research has focused also on the use of the intrinsic affinity of polyamines to complex DNA and RNA molecules as polycationic loads grafted to polymers or liposomes to enhance nucleic acid binding. The presence of secondary amines in the structure of polyamines results in an increased buffer capacity of the polyamine functionalised structures hence it may facilitate endosomal escape.

Jiang et al. have successfully synthesized a chitosan graft spermine (CHI-g-SPE), which showed improved transfection efficiency of pDNA and low cytotoxicity *in vitro* and *in vivo* in lung cancer mice models [228]. A study by *Huang et al.* demonstrated the functionalisation of another polysaccharide with spermine [229]. Starch molecules of around 50 kDa were modified with spermine to obtain starch modified spermine (SMS). The molecule containing the highest primary amine content showed approximately 40 % transfection efficiency of plasmid pAC-GFP-C1 in a liver cancer cell line (HepG2). High transfection efficiency and low toxicity was also reported for a spermine grafted polyethylene glycol diacrylate PEG-alt-SPE *in vitro* [230]. The formed nanocomplexes with pEGFP-N2 and PEG-alt-SPE were introduced by a non-invasive aerosol delivery in Kras^{LA1} lung cancer model mice and confirmed the non-toxic nature of the nanocomplexes as well as the efficient delivery of the plasmid. Spermine grafted lipids or lipo-spermines were investigated for their *in vivo* transfection efficiency in a study by *Viola et al.* [231]. The research of the group identified that lipo-spermines with the longest fatty acid chains are also the most toxic gene carriers. Butanoyl-spermine was found to be the most successful gene carrier, forming non-cytotoxic and homogeneous nanocomplexes, which could transfect BALB/c mice effectively with a firefly luciferase gene. A recent study by *Xie et al.* constructed a hyperbranched poly-spermine by conjugating it to citric acid [232]. The new biodegradable non-toxic vector showed significant decrease of lung tumours and fully supressed lung tumorigenesis in K-ras^{LA1} mice.

In this chapter, we report on the synthesis and characterisation of a small polyethylene glycol molecule bi functionalised with spermidine.

3.2 Materials and Methods

3.2.1 Materials

Materials	Purity	Supplier
BS (5) hydroxysuccinimde suberate		Thermo Fisher Scientific (Loughborough, UK)
N^1, N^5 bis Boc spermidine	≥ 95 %	Sigma Aldrich (Gillingham, UK)
Dichloromethane (DCM)	99 %	Merck, Sigma Aldrich (Loughborough, UK)
Sodium carbonate	≥ 99.5 %	Sigma Aldrich (Gillingham, UK)
Diethyl ether	≥ 99.5 %	Sigma Aldrich (Gillingham, UK)

Deuterated Chloroform	99.8 %	Cambridge Isotope Laboratories (Nantwich, UK)
Methanol D4	99.8 %	(Cambridge Isotope Laboratories (Nantwich, UK)
Deuterium Oxide (D_2O)		Sigma Aldrich (Gillingham, UK)
Triethylamine	≥ 99.5 %	Sigma Aldrich (Gillingham, UK)
Methanolic Hydrochloric acid		Merck, Sigma Aldrich (Gillingham,UK)

3.2.2 Methods

3.2.2.1 Synthesis of BS PEG (5) bis spermidine

80 mg of BS (5) PEG hydroxysuccinimde were dissolved in 2 ml of DCM (40 mg ml $^{-1}$) in a 7 ml glass vial. 2 eq of N ^{1}, N ^{5} bis Boc spermidine with 2 eq of triethylamine were added to the mixture. The reaction was left stirring at room temperature with the glass vial closed for 24 hours.

3.2.2.1.1 A two-step purification process of BS PEG (5) tetra Boc spermidine

DCM and water are immiscible liquids, hence phase separation allowed us to purify the mixture. Two washes with a 5 % Na_2CO_3 followed by two washes of 0.05 M HCl were performed. The solutions were added to the mixture and were shaken for 30 seconds then left to settle to allow the two immiscible liquids to separate. The density of DCM is higher than water (1.33 g/cm^3 vs 1 g/cm^3) hence the organic fraction containing the modified molecule was at the bottom of the vial, while the aqueous fractions containing the N-hydroxysuccinimde and triethylamine chloride were situated on top of the organic phase. The aqueous fractions from the four washes were carefully extracted from the vial with a Pasteur glass pipette.

3.2.2.1.2 Deprotection of BS PEG (5) tetra Boc spermidine

After purification, the glass vial containing the purified modified molecule was placed on a rotary evaporator to remove the DCM. 4 ml of 3 M HCl/methanol were added to the oily droplet observed after DCM evaporation. The glass vial with the deprotection cocktail was left stirring for 3 h at room temperature with the cap open. The residual methanol from the reaction mixture was evaporated on a rotary evaporator.

3.2.2.2 Characterisation of BS PEG (5) bis spermidine

3.2.2.2.1 ^{1}H-NMR and ^{1}H-^{1}H COSY NMR

20 mg of BS PEG (5) tetra Boc spermidine were dissolved in 0.7 ml of deuterated chloroform and transferred to an NMR tube. The analysis of the sample was performed on a 500 MHz Bruker Spectrometer at 16 scans for the proton spectrum, while for the COSY spectrum the number of scans was increased to 64.

3.2.2.2.2 ^{1}H-NMR and ^{1}H-^{1}H COSY NMR of BS PEG (5) bis spermidine

20 mg of BS PEG (5) bis spermidine was dissolved in 0.7 ml of deuterium oxide and transferred to an NMR tube. The proton spectrum was obtained using 16 scans, while the COSY spectrum was obtained using 64 scans. The spectra from all NMR experiments was analysed via Topspin v 3.2.

3.3 **Results**

3.3.1 Synthesis and characterisation of BS PEG (5) bis spermidine

N-hydroxysuccinimde BS (5) PEG suberate was reacted with N ^{1}, N ^{5} bis Boc spermidine in the presence of triethylamine to obtain BS PEG (5) bis spermidine, a PEG-based oligomer functionalised with the polyamine spermidine. A general scheme of the reaction is presented on **Figure 3-1**. Starting material **1** and **2** were analysed by ^{1}H-NMR prior the reaction. The obtained ^{1}H-NMR of compound **3** is shown on **Figure 3-2**. The peak with a chemical shift $\delta_{6.5\text{-}6.8}$ represents the protons attached to the N atom form the newly formed amide bond. The integration of the peak at $\delta_{6.5\text{-}6.8}$ is 2.01, which confirms the presence of two amide bonds formed, one on each side of **3.** An additional step, which is not shown on **Figure 3-1** is the purification step, which takes place before Boc deprotection. The reaction mixture needs to be purified from the N-hydroxysuccinimde released from **(1)** and triethylamine. **Figure 3-2** shows the presence of a triplet at $\delta_{1.35}$ representing the protons of the methyl groups of triethylamine. The protons of the methylene groups of triethylamine are overlapping with the multiplet at $\delta_{3\text{-}3.3}$, hence there are not visible on **Figure 3-2**. A two-step purification process was used to clean the reaction mixture and the reaction was monitored through ^{1}H-NMR. Additionally, ^{1}H-^{1}H COSY NMR was used to assign the protons of the multiplet at $\delta_{3-3.3}$.

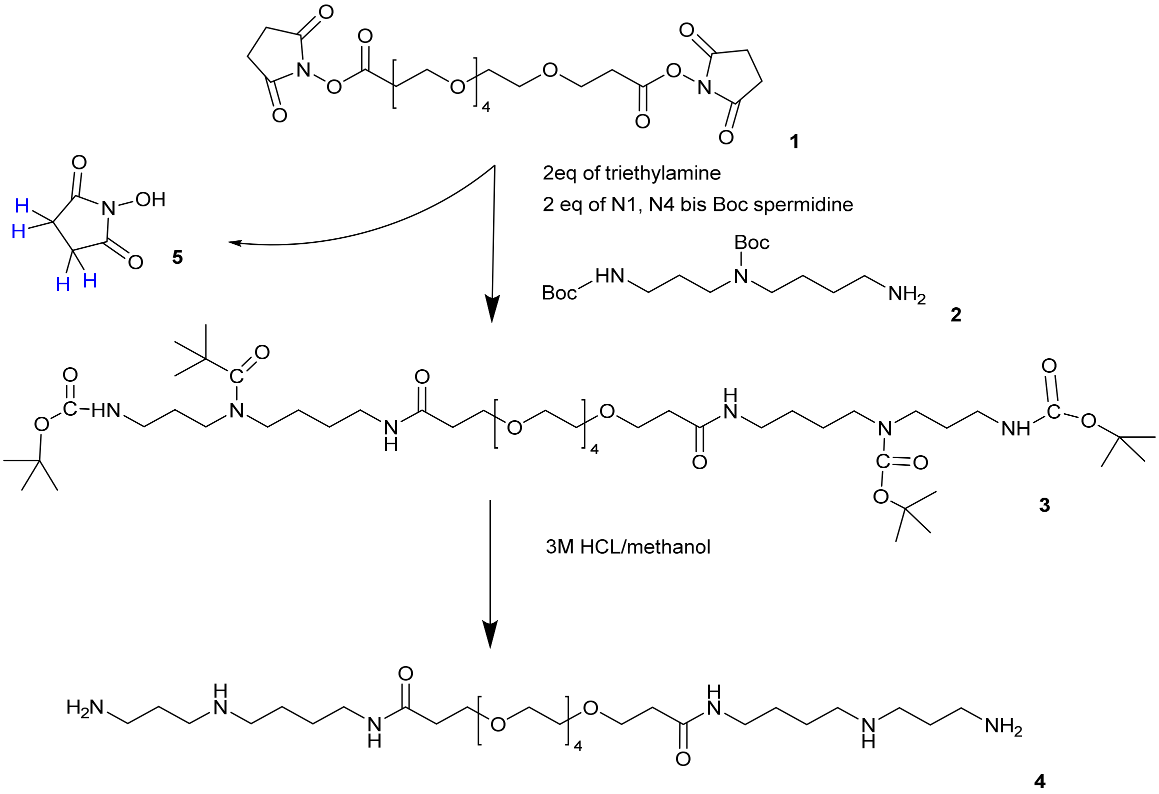

Figure 3-1: *General scheme for the synthesis of BS PEG (**5**) bis-spermidine. N-hydroxysuccinimde BS (**5**) PEG suberate (**1**) reacts with 1N, 5N bis Boc spermidine (**2**) in the presence of triethylamine to form BS PEG (**5**) tertra-Boc-spermidine (**3**). The removal of the Boc group is performed in the presence of 3M HCl in methanol. The deprotected BS PEG (**5**) bis-spermidine is then obtained (**4**). The hydrolysed N-hydroxysuccinimde (**5**) is released.*

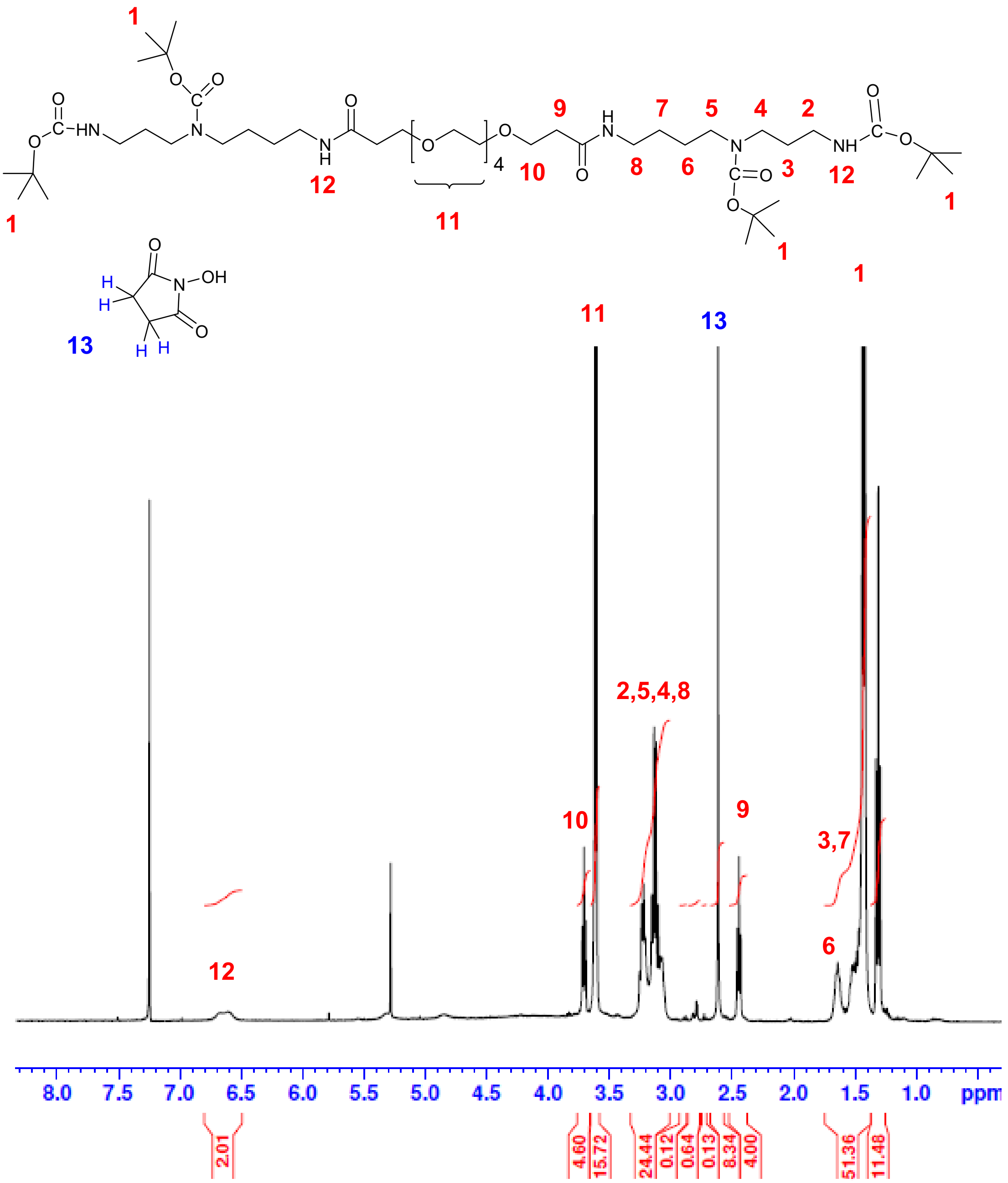

***Figure 3-2**: ^{1}H-NMR spectrum of BS PEG (5) tetra Boc spermidine in CDCl$_3$**:** $\delta_{1.35}$ [N-(CH$_2$CH$_3$), (q), triethylamine], **3,7:** δ1.6 [(-CH$_2$-) , methylene protons of spermidine)],**1:** $\delta_{1.5}$[-O-C-(CH$_3$)$_3$, protons od the tert-butyl carbonyl group (Boc)] **6:** $\delta_{1.7}$ [(-CH$_2$)- methylene protons of spermidine], **9:** $\delta_{2.5}$[NH-CO-CH$_2$-methylene protons of PEG], 13 $\delta_{2.65}$ [-CH$_2$-CH$_2$-, methylene protons of N-hydroxysuccinimde), **2,5,4 and 8:** $\delta_{3-3.3}$ [-CH$_2$NH-CO-O-C-(CH$_3$)$_3$, CH$_3$-C-O-CO-N-(CH$_2$)$_2$, (-CO-NH-CH$_2$-), methylene protons of spermine], **11:** $\delta_{3.65}$[(-CH$_2$-CH$_2$-O-)$_4$, protons of ethylene glycol], **10:** $\delta_{3.75}$ [-O-CH$_2$-CH$_2$, methylene protons of PEG], $\delta_{5.4}$ (solvent peak, residual DCM], **12:** $\delta_{6.5-6.8}$ [(-NH-CO-)$_2$, protons of amide group], $\delta_{7.21}$[CDCl$_3$], 87 % modification level. The modification level was calculated using the integration of the amide protons (divided by 2) (**12**) over the integration of the methylene protons next to an oxygen (divided by 4) (**10**) multiplied by 100 to show percent.*

3.3.2 A two-step purification process of BS PEG (5) tetra Boc spermidine

BS PEG (5) tetra Boc spermidine was purified with two washing steps with Na_2CO_3 and HCl. Na_2CO_3 was used to remove N-hydroxysuccinimde, while HCl was used to remove triethylamine. The cleaning of the sample was possible, because the reaction was done in dichloromethane (DCM) and the aqueous fractions from the washing step was removed after the organic phase with BS PEG (5) tetra Boc spermidine was separated at the bottom of the glass vial. ^{1}H-NMR of the purified compound showed that the peak at $\delta_{2.6}$ corresponding to the protons of N-hydroxysuccinimde is no longer visible (**Figure 3-3**). However, a very small amount of triethylamine is still present in the sample ($\delta_{1.35,}$ I=2.08)

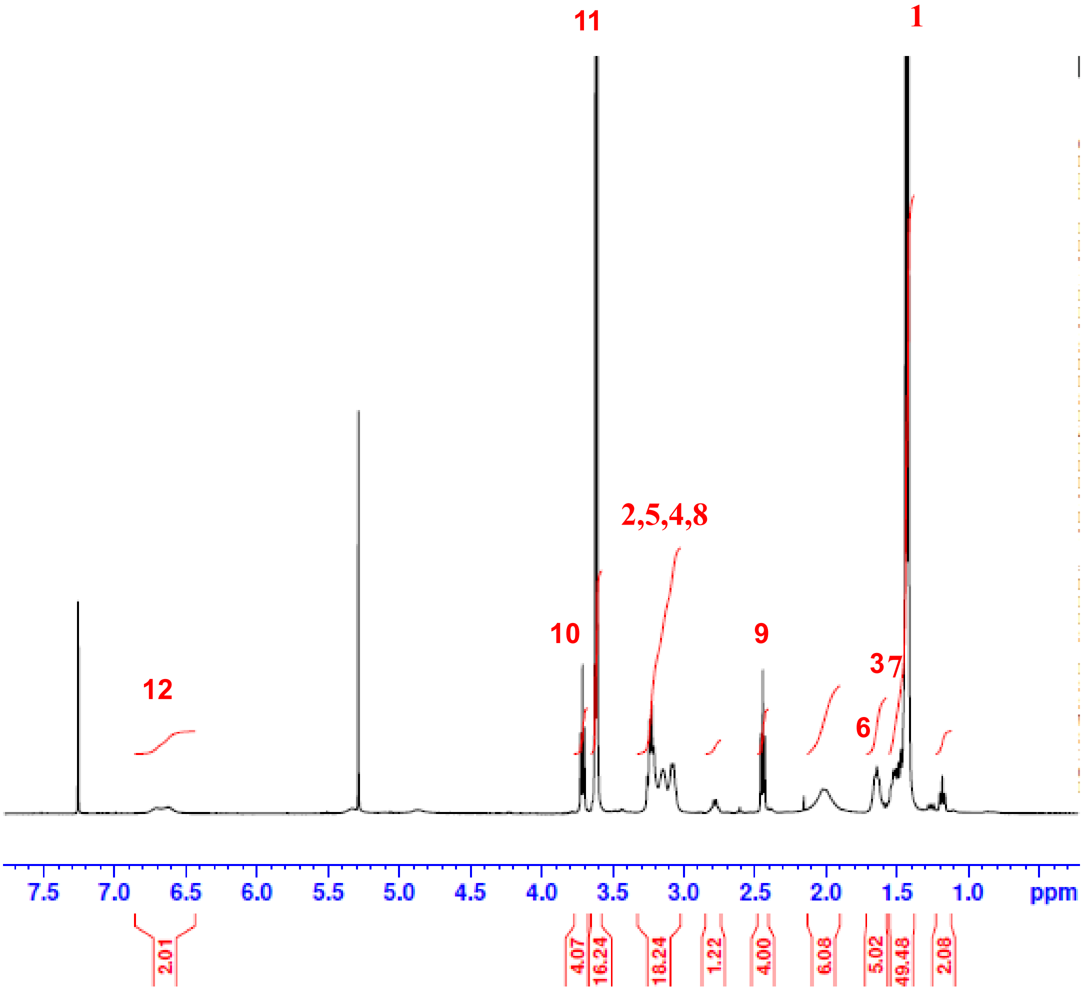

Figure 3-3: *^{1}H -NMR spectrum of the purified BS PEG (5) tetra Boc spermidine in CDCl3*

3.3.3 Characterisation of BS PEG (5) bis spermidine via NMR

After deprotection of the Boc groups in 4 M HCl in methanol BS PEG (5) bis spermidine was analysed via ^{1}H-NMR. The results showed complete Boc deprotection after 3 h of incubation. The sample was analysed in D_2O as after deprotection the molecule was soluble in water. Peak assignments are shown on **Figure 3-4**, the assignments were made only after performing ^{1}H-^{1}H COSY NMR and determining the correlations as shown on **Figure 3-5**.

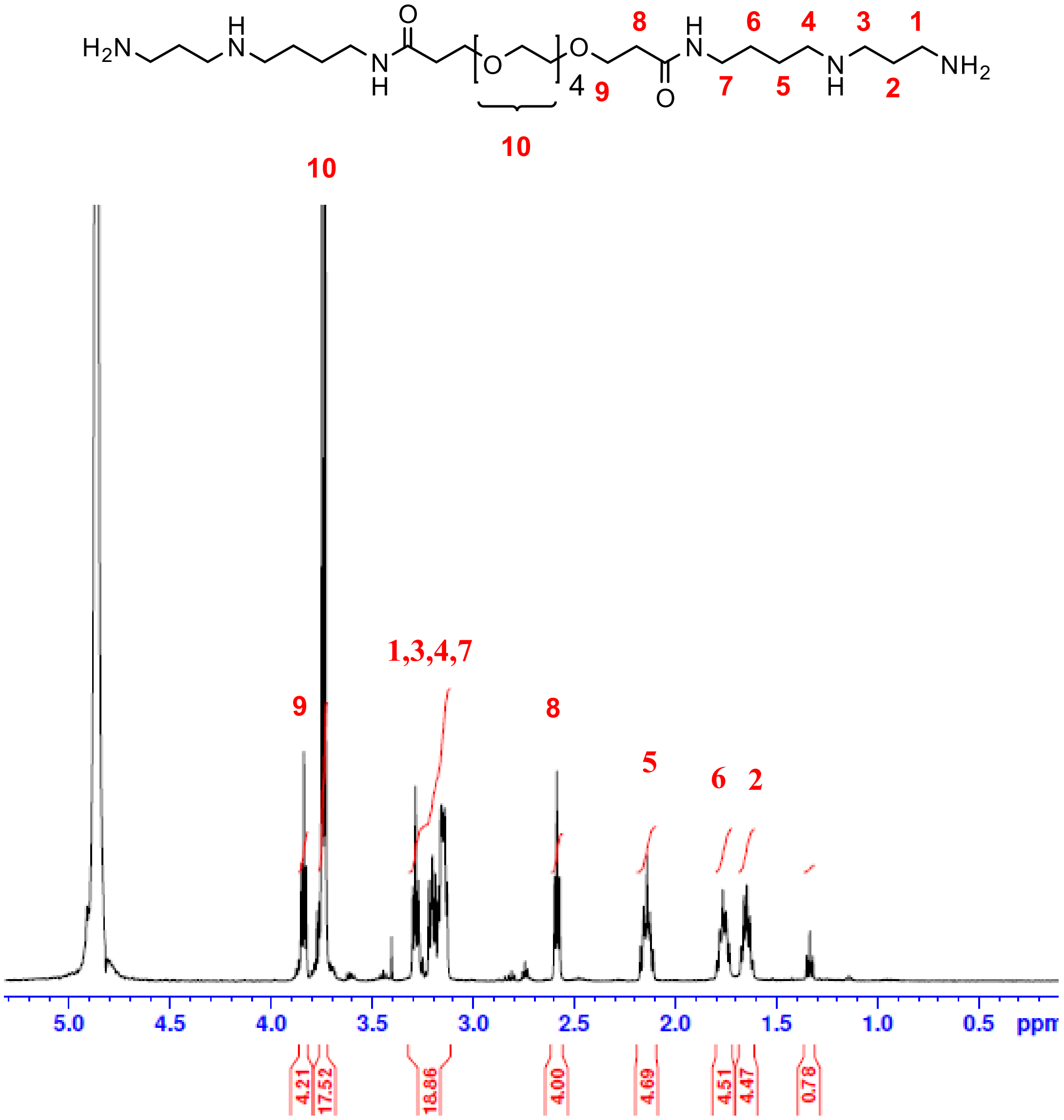

Figure 3-4: *^{1}H-NMR of BS PEG (5) bis spermidine in D_2O.* ***2***: *$\delta_{1.7}$ [NH_2-CH_2-C**H_2**-),* ***6***: *$\delta_{1.83}$[-CO-NH-CH_2-C**H_2**-],* ***5***: *$\delta_{2.2}$[CH_2-C**H_2**-CH_2],* ***8***: *$\delta_{2.63}$ [NH-CO-C**H_2**],**1**,**3**,**4** and **7**: $\delta_{3.1\text{-}3.32}$ [-C**H_2**NH-CO-CH_2-], CH_2-NH-(C**H_2**)$_2$, (-CH_2-C**H_2**-NH)],* ***10***: *$\delta_{3.8}$ [(-C**H_2**-C**H_2**-O-)$_4$],* ***9***: *$\delta_{3.9}$ [-O-C**H_2**-CH_2], $\delta_{4.79}$[D_2O]*

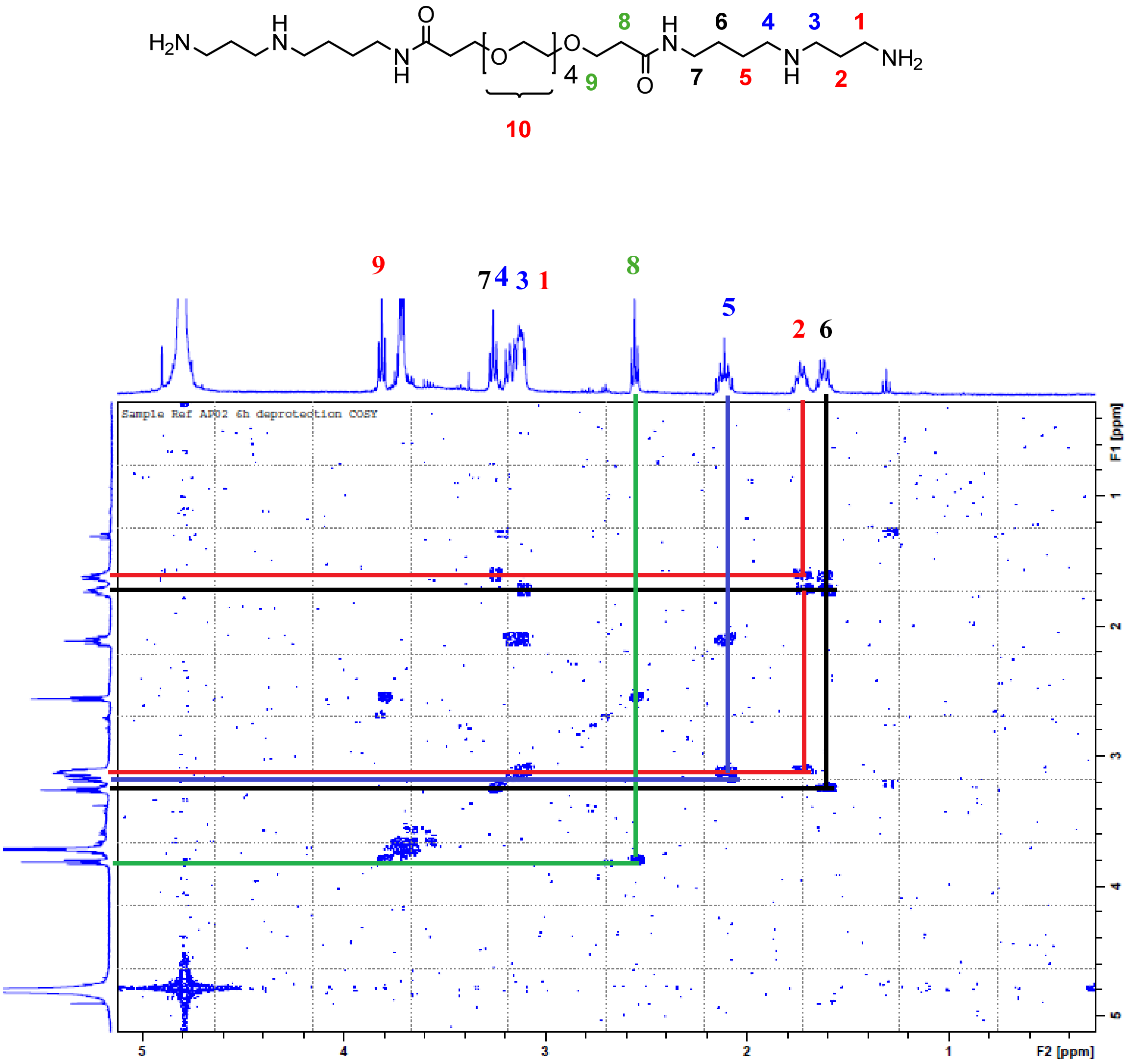

***Figure 3-5:** ^{1}H-^{1}H COSY NMR of BS PEG (5) bis spermidine in D_2O **:** The correlations are colour coded and the colour corresponds to the colour of the adjacent protons in the structure.*

3.4 **Discussion**

This chapter describes the synthesis and characterisation of a novel polyamine functionalised molecule as a potential gene delivery platform. We designed an efficient and simple synthesis scheme, which involved a fast purification two-step process. NMR was used for the full characterisation of the molecule at the different stages of the synthesis and the purification.

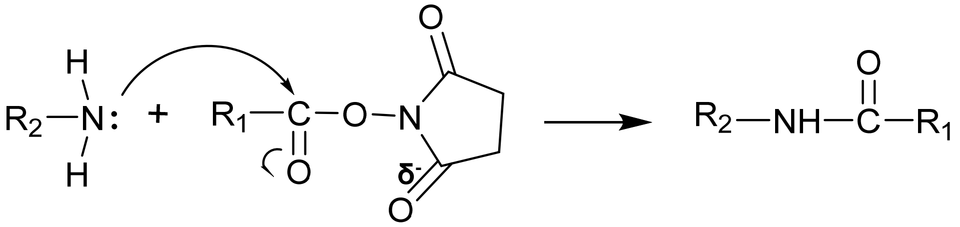

__Figure 3-6:__ Mechanism of amide bond formation between N-hydroxysuccinimde ester and a primary amine.

The lone pair of electrons of the nitrogen from the primary amine group acts as a nucleophile and attacks the C from the carbonyl of the ester, which is an electrophile (δ^+) as the oxygen is withdrawing the electron density and acquires a partial negative charge (δ^-). This makes the N-hydroxysuccinimde **(5) (Figure 3-1)** a good leaving group and facilitates the amide bond formation. The reaction is widely used in bioconjugate techniques of functionalising molecules [233]. The ^{1}N-^{5}N bis Boc spermidine has two primary amines and one secondary, one is used for the amide bond formation, while the other two are protected by a Boc group to avoid cross reactivity. At this stage NMR analysis confirmed the presence of **3 (Figure 3-1).** The singlet at 2.6 ppm represents the protons of the methylene groups of the N-hydroxysuccinimde, which integrates as 8.34 (expected integration of 8 protons if the molecule is functionalised from both ends). The spectrum is calibrated using the triplet at 2.4 ppm originating from the ^{1}H-NMR of the PEG. The reaction was considered completed due to the presence of the broad peak with a chemical shift of 6.5 - 6.8 ppm. This peak is not present in the ^{1}H-NMR spectra of the starting materials, it represents the protons of the amide bond and integrates as 2 confirming an amide bond formation on each end of the molecule. Amide protons in ^{1}H-NMR are with reported chemical shifts between 5-9 ppm [234]. The integration of this peak is used to calculate the level of modification of BS PEG (5) tetra Boc spermidine estimated to be 87 %. **Figure 3-2** shows the presence of triethylamine in the sample (triplet at $\delta_{1.34}$ and a quintet overlapping with the multiplet of spermine at $\delta_{3\text{-}3.3}$. The reported chemical shifts of triethylamine in chloroform are slightly different (t. 0.99, q.2.48) [235], however this is probably due to the fact that there is also some dichloromethane left in the reaction mixture ($\delta_{5.3}$).

The purification steps involved washing of the sample with a Na_2CO_3 solution and a dilute solution of HCl to extract the N-hydroxysuccinimde and the triethylammonium chloride. **Figure 3-3** shows the successful removal of the impurities as the peak with a 2.6 ppm is no longer detected and the majority of triethylamine is also removed.

However there appears to be trace amounts of triethylamine trapped in the mixture (t. $\delta_{1.34}$), **Figure 3-3.**

After the purification was completed the second stage of the synthesis include the removal of the Boc group. Boc deprotection was performed for 3 hours in 3 M HCl/methanol (structure **4**, **Figure 3-1**) and the completion of the deprotection was monitored via ^{1}H-NMR, no peak at $\delta_{1.5}$ is visible (**Figure 3-4**). Peak assignments were made after ^{1}H-^{1}H COSY experiments (**Figure 3-5**) and only after comparison with the literature data. The methylene protons of spermidine next to the N from the secondary and primary amines together with the amide give rise to the complex multiplet of at $\delta_{3\text{-}3.3.}$ **Figure 3-7** shows the structure of spermidine and its equivalent sets of protons. There are four sets of equivalent protons, which give rise to four signals in the NMR. However, in the case of BS PEG (5) bis spermidine the primary amine attached to 1^I is an amide. In a study by *Frassineti et al.*, the combined efforts of structure prediction tools and NMR experiments helped in elucidating the protonation constants of spermine [236]. They showed that the methylene protons attached to a N 1, 1^I, 2 and 2^I from the amine groups give rise to the multiplet in the proton spectra. In another study by *Geall et al.* polyamines were used in a homoligation reaction to produce lipo-spermine conjugates with different lipids (palmitic acid, stearic, oleic and elaidic acids. All the different lipids were conjugated to spermine by an amide bond. The authors assigned the peaks in the multiplet by performing ^{1}H and ^{13}C NMR experiments. The data corresponds to our results from the ^{1}H -^{1}H COSY NMR (**Figure 3-5**). It appears that the amide protons in the multiplet will be the furthest downfield, followed by the protons attached to the C next to N form the secondary amines and the C next to N from the primary amine. This findings are in consensus with other studies which prove that methylene groups α to a secondary amine are reported to have larger upfield chemical shifts than those α to a primary amine [237].

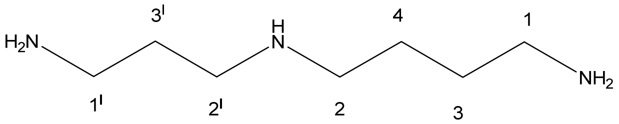

Figure 3-7: *Equivalent sets of protons in the structure of Spermidine. There are 4 sets of chemically equivalent protons.*

3.5 **Conclusions**

The chapter focuses on the synthesis and purification of a short PEG oligomer bi functionalised with spermidine. Our data demonstrates the successful synthesis of BS PEG (5) bis spermidine and its full characterisation via a set of NMR experiments. The chapter describes also the challenge related to the limited options for purification due to the small size of the molecule and the minor size differences between product and impurities. To overcome this a smart and efficient synthesis scheme was designed with an intermediate purification step, which yielded 87% modification calculated from the NMR and a pure product.

4 Preparation and characterisation of glycol chitosan and polyethylene glycol-based nucleic acid nanocomplexes and their *in vitro* activity in U87 cells

4.1 Introduction

Polymer-mediated gene therapy relies on the formation of electrostatic complexes, between the negatively charged phosphate groups of the nucleic acid and the positive charges of the polymer carrier. The resulting complex, called a polyplex offers the cargo nucleic acid protection from enzymatic degradation, possesses an overall positive charge and size in the nm range [238], Polymer-mediated gene delivery is facing several barriers, which so far have been hampering their application in the clinic. These challenges are related to the three main events associated with polymer -mediated gene transfer: cellular uptake, release in the cytoplasm and uptake by the nucleus (the latter being important only for pDNA). Additionally, these three major stages in polymer-mediated gene transfer incorporate a complex network of physicochemical parameters, the interplay of which makes assigning individual contributors for cell entry, endosomal escape and nuclear import difficult. Furthermore, serum stability, short half-life in the circulation with fast clearance and haemolysis are additional obstacles, which impede the clinical application of polymers as gene carriers [239]. Therefore, polymer vector design is a troublesome task and in fact results in strategies that work against each other.

Interactions of the negatively charged phospholipids in the cell membrane with the positive charges of the polyplexes is considered the first step prior to endocytosis, so it is important for internalisation [240,241]. On the other hand since a positive charge contributes to plasma protein binding and haemolytic effects, strategies to develop neutral or anionic polyplexes have been also employed [242,243].

Some other examples of design strategies focus on polyplex stability/flexibility optimisation as a crucial step for cell uptake [244], but others report that increased stability can result in poor polyplex dissociation in the cytoplasm [245]. *Wei et al.,* implemented a method for the reversable hydrophilization to improve polyplex stability without obstructing dissociation in the cytoplasm [246]. On the other hand, pre -mature dissociation in the cytoplasm can result in poor plasmid transfection efficiency since it is believed that the polyplex rather than the released naked DNA enters the nucleus [247].

This chapter will focus on describing a systematic approach for optimisation of transfection parameters based on EAGC polyplexes performance to deliver β-Gal DNA in U87 cell. First, we modified several parameters with an effect on transfection efficiency: complexation time, treatment time, complexation medium and temperature during complexation time for EAGC polyplexes. Then, we investigated the effect of Mw of the gene carriers, polyplex size and PDI of GC polyplexes to deliver β-Gal DNA to U87 cells. Finally, we considered polyplex size as an important parameter governing entry in U87 cells, which outweighed the importance of endosomal escape as a barrier under the test conditions we used.

4.2 **Materials and methods**

4.2.1 Materials

Materials	Supplier
LB broth (Lennox) powder growth medium	Sigma Aldrich (Dorset, UK)
LB agar (Lennox)	Sigma Aldrich (Dorset, UK)
EndoFree plasmid mega extraction kit	Qiagen (Manchester, UK)
Illustra™ NAP™ columns	GE Healthcare Life Sciences (London, UK)
UltraPure™ agarose Invitrogen	Thermo Fisher (Loughborough, UK)
50 x Tris – acetate (TEA) buffer with ethylenediaminetetraacetic acid (EDTA)	Thermo Fisher (Loughborough, UK)

Invitrogen SYBR safe DNA gel stain	Thermo Fisher, (Loughborough, UK)
luciferin	Perkin Elmer (MA, United States)
T-PER™ tissue protein extraction reagent	Thermo Fisher (Loughborough, UK)
EDTA free halt protease inhibitor cocktail	Thermo Fisher (Loughborough, UK)
BlueJuice™ gel loading buffer 10x	Thermo Fisher (Loughborough)
200 mesh copper grids	Agar Scientific (Stansted, UK)
uranyl acetate	Agar Scientific (Stansted, UK)
U87 cells (ATCC® HTB - 14™	ATCC (Teddington, UK)
minimal essential medium eagle	Sigma Aldrich (Dorset, UK)
Gibco™ sodium pyruvate	Thermo Fisher, Loughborough)
Gibco™ GlutaMAX™	Sigma Aldrich (Dorset, UK)
penicillin/streptomycin	Sigma Aldrich (Dorset, UK)

trypsin (0.25 w/v with 0.53 mM EDTA)	Sigma Aldrich (Dorset, UK)
trypan blue	Sigma Aldrich, Dorset, UK)
foetal bovine serum	Sigma Aldrich (Dorset, UK)
β-Galactosidase reporter assay system (E2000)	Promega (Southampton, UK)
label IT® tracker™ MIR 7015	Mirus (Coventry, UK)
Hoechst stain 3342	Thermo Fisher, Loughborough)
Invitrogen lipofectamine 2000	Thermo Fisher, Loughborough)

4.2.2 Methods

4.2.2.1 Plasmid preparation

E.coli DH5α strain, containing CMV β-Galactosidase or luciferase reporter gene expression plasmids with an ampicillin resistance gene were used . A streak plate of *E.coli* DH5α was prepared on an LB agar supplemented with ampicillin (50 μg ml^{-1}) and incubated upside down at 37° C for 12 - 24 hours until single colonies were formed. A single colony was then isolated from a freshly streaked selective plate and pre-cultured in 10 mL autoclaved LB broth medium containing ampicillin (50 μg ml^{-1}). The pre-culture was left shaking at 37° C for 16 hours. The LB broth medium was prepared by dissolving 25 g of LB broth powder in 1 L MilliQ water divided over 2 conical flasks with 2.5 L capacity (0.5 L of medium per flask) followed by autoclaving. Subsequently, 2 mL of the pre-culture *E. coli* DH5α strain was transferred to each conical flask containing the autoclaved medium. The flasks were then incubated at 37° C for 18 h with shaking at 120 rpm. The bacterial cells in medium were then transferred to four 0.5 L centrifuge containers. The bacterial cultures were centrifuged at 6000 rpm and 4° C for 15 min (Hermle Z323K, Baltimore, USA). The supernatant was discarded, and the pellet from the four containers was further processed using a plasmid extraction kit protocol. The DNA solution in MilliQ water was desalted through the illustra NAPTM Columns. The concentration of DNA was estimated by a NanoDrop (NanoDrop ™ 2000/2000c) by measuring absorbance at 260 nm and purity by considering the 260/280 ratio. A ratio of approximately 1.8 is indicative of a successful extraction procedure and a pure DNA sample.

4.2.2.2 Preparation of polymer-based nanocomplexes

Nanocomplexes for *in vitro* studies were prepared at 6 μg ml $^{-1}$ concentration of β-Gal DNA in either water or 20 mM phosphate buffered saline (PBS), pH=6.8. Equal volumes of plasmid DNA in PBS or water and different polymer to β-Gal mass ratios (1 to 1, 1 to 10, 1 to 40 and 1 to 60) were prepared for all EAGC and GC-based nanocomplexes, while BS PEG (5) bis spermidine-based nanocomplexes were prepared at (1 to 10, 1 to 20, 1 to 30, 1 to 40, 1 to 50 and 1 to 60). β-Gal DNA was always added to the polymer solution followed by mixing up and down with a pipette for 10 s. Complexation was performed at different time intervals (0.5 h, 1 h, 2 h, 3 h, 24 h) for EAGC polyplexes at room temperature (RT), 4° C and 37° C. GC polyplexes were prepared at the same concentration after 24 h of complexation time at 4° C in 20 mM PBS, pH=6.8. BS PEG (5) bis spermidine nanocomplexes were prepared in water after 2 h complexation at RT.

4.2.2.3 Characterisation of polymer-based nanocomplexes

4.2.2.3.1 Gel retardation assays

Agarose gel electrophoresis is a technique in molecular biology widely used to separate nucleic acids based on their size [248]. Separation is possible due to the net negative charge of the nucleic acid analytes, which will allow them to move towards the positive pole under the influence of an electric field. Shorter fragments will generally move faster through the agarose matrix when compared to longer fragments for a given time [248]. The separation quality of the fragments will vary depending on the percentage of agarose used for the analysis. A higher percentage of agarose would provide better separation for shorter nucleic acids, while a lower percentage is more suitable for longer nucleic acids.

1 g of agarose was dissolved in 100 ml of 1x TAE buffer, which was diluted fifty times from the stock solution (50x TAE 243 g Tris, 100 ml 0.5 M EDTA, 57.1 ml acetic acid) and 10 μl of SYBR Safe). Then the bottle was placed in the microwave until the solution turned clear. Next, the solution was kept open under the laminar flow to cool until it reached room temperature, to allow for holding the bottle with bare hands. An

electrophoretic chamber with a comb was assembled beforehand and the solution was poured into the chamber. After approximately 20 mins, when the solution had set, the comb was removed, and the gel was placed in an electrophoretic cell attached to a power supply station (PowerPac™, Bio Rad, Hemel, UK). An excess of the 1x TAE buffer was poured in the cell to cover the gel completely. Polyplex samples and control samples containing naked plasmid were prepared in a total volume of 22 µl (20 µl of sample and 2 µl of loading dye.

4.2.2.3.2 Dynamic light scattering (DLS)

Dynamic light scattering is a physical technique used to measure size distribution in the sub-micron range of particles in suspension or in solution [249]. Since particle size measurements are performed in a liquid, Brownian motion or the random movement of particles promoted by the collision with the fast-moving solvent molecules, is used by DLS to determine particle size. The velocity of the Brownian motion is given by a property known as the translational diffusion coefficient (D). D is used to calculate particle size using the Stokes-Einstein (4).

$$D\,(h) = \frac{kT}{3\pi\pi D} \tag{4}$$

D (h) is the hydrodynamic diameter, D is the translational diffusion coefficient, k is the Boltzmann's constant, T is absolute temperature and η is viscosity. As it becomes clear from the formula an absolute temperature is required for DLS measurements, because the viscosity of a liquid is related to its temperature [250].

Stationary particles in a cuvette illuminated by a laser will produce a stationary in position and size speckle pattern. The speckle pattern is characterised with the presence of bright and dark patches, which can be seen on a glass screen when a sample is illuminated by a laser. The bright patches form as a result of constructive interference of scattered by the particles light, which arrives in the same phase. Conversely, the dark patches in the speckle pattern arise from mutually destructive phase addition of scattered by the particles light, which cancel each other out. The speckle pattern for a system undergoing Brownian motion is constantly evolving due to the phase addition of the light scattered by the moving particles, which is creating new patterns. The size of the particles will determine the rate at which these intensity fluctuations occur.

The polyplexes were prepared as described previously and size and zeta potential measurements were carried out using a Malvern Zetasizer Nano S/N (Malvern Instruments Ltd, UK). Size measurements were performed in low volume dispersible cuvettes with 100 µl of the respective polyplex. Zeta potential measurements were performed in a reusable zeta cell and the electrical potential difference between the electrodes was measured using the 'Surface Zeta Potential' mode in the instrument. Standard solutions supplied by Malvern, were used prior sample measurements for machine calibration. Polyplex samples were prepared at a concentration 0.1 mg ml $^{-1}$ for both zeta and size measurements in 100 µl or 1 ml volume respectively.

4.2.2.3.3 Transmission Electron Microscopy (TEM)

Transmission electron microscopy operates in the same way as light microscopy but uses an electron beam instead of light. Since the wavelength of electrons is much smaller than the wavelength of light TEM is a more powerful technique with improved resolution of thousand times when compared to light microscopy images [251]. TEM imaging can be used to reveal the finest details of internal structures, in some cases even as small as atoms.

The electron beam from the electron source passes through a condenser lens in a vacuum, which makes the beam thinner and more coherent. The coherent beam then reaches the specimen and parts of it are transmitted depending on the thickness and electron transparency of the specimen. The specimen is an ultrathin section (less than 100 nm) or a suspension on a grid. The transmitted portion of electrons passes through the objective lens, strikes the phosphor screen and an image is generated by converting the electrons to light. The image is then passed down the column through the intermediate and the projector lens and it is enlarged all the way. The lighter regions form the high-resolution black and white image generated represent areas of the specimen where greater number of electrons were able to pass through, while the darker ones represent the denser areas of the specimen [251].

One drop of polyplex (prepared as previously described, was placed onto a carbon/Formvar coated 200 mesh copper grid (Agar Scientific, Stansted, UK) and negatively stained with 1 % aqueous uranyl acetate solution. Polymer and naked nucleic acid solutions were used as negative controls. Imaging was carried out under Philips CM120 Biotwin Transmission Electron Microscope (Philips, Eindhoven, The Netherlands). Digital images were captured using a 5MP AMT camera (Deben Uk Ltd, Suffolk, UK).

4.2.2.4 Cell culture

U87 cells (ATCC® HTB-14™) were maintained in 75 cm^2 blue vent cap culture flasks (Corning, Fisher Scientific Loughborough, UK) in 10 – 12 ml of Minimal Essential Medium Eagle (MEME) supplemented with 1% Sodium Pyruvate (v/v), 1% GlutaMAX^{TM} (v/v) , 1 % Penicillin/Streptomycin (v/v) and 10 % foetal bovine serum (v/v). When cell confluency reached 90 %, cells were detached from the 75cm^2 culture flasks using 4 - 5 ml trypsin (0.25 % w/v with 0.53 mM EDTA) after 4 - 5 mins of incubation at 37° C in the presence of 5 % CO_2. To inactivate the trypsin, the cell suspension was topped up with 8 – 10 ml fresh MEME medium and it was transferred to 15 ml tubes. The tubes were centrifuged at 400 rcf for 4 mins (Hettich, Microlitre Centrifuge, Mikro 200/200R) and the cell pellets resuspended in 10 – 12 ml of fresh medium. 1/3 dilutions of the cell suspension were prepared in new 75 cm^2 flasks.

For the U87 growth curve 5x10^5 U87 cells ml $^{-1}$ were seeded in 6 well plates coated with lysine. Cells were harvested from the plate by replacing the medium with 0.5 ml of trypsin (after 12 h, 24 h, 60 h, 72 h and 90 h). The plates were then incubated for 4 - 5 mins at 37° C in the presence of 5 % CO_2. After that the trypsin was inactivated by topping up the wells with 1 ml fresh MEME medium. The cell suspension was transferred to a 1 ml Eppendorf tube and then the tube was centrifuged at 12,000 rpm (Hettich, Microlitre Centrifuge, Mikro 200/200R) for 5 mins. The supernatant was discarded and the pellet of cells was re-suspended in 1 ml of MEME. Next, ½ dilution of the cell suspension was performed with 0.4 % solution of Trypan Blue in distilled water in a total volume of 20 µl. Cell counting was performed using a haemocytometer (Neubauer - improver depth 0.1 mrr 1/400 mm^2). A 10 µl sample was loaded in the haemocytometer chamber with a cover slip and placed under the microscope to count cells. Three squares were counted diagonally (always including the middle one) and the average number of cells from the three squares (n) was used to calculate the concentration of cells per millilitre (ml) with the following formula: cells/ml = n x 2 x 10^4.

4.2.2.4.1 Transfection experiments in U87 cells

U87 cells were seeded in lysine coated 6 well plates at a density of 5 x 10^5 cells per well in 1 ml of MEME. The cells were left for 72 h to reach exponential phase and were then treated with nanocomplexes, prepared as described in **section 4.2.2.2**. After 72 h the full MEME medium from each well of the plate was replaced by 1.5 ml of FBS free MEME medium. Then, 0.5 ml of the tested nanocomplexes were added to each well containing 1.5 ml of FBS free medium MEME to make up the total volume to 2 ml per well. The plates were then left for either 4 h, 6 h or 17 h in an incubator at 37° C in the presence of 5 % CO_2. After that the FBS free medium with the treatments was aspirated and replaced with 2 ml per well of full MEME medium containing 10 % FBS. The plates were then left in the incubator at 37° C for another 24 h before performing the β-Galactosidase assay.

4.2.2.4.2 β-Galactosidase assay

Transfection efficiency of the nanocomplexes was measured by a reporter assay using the substrate of β-Galactosidase enzyme O–nitrophenyl–β-D-galactopyraniside (ONPG). Transfection efficiency of the nanocomplexes was expressed in mU of active enzyme per well using a calibration curve with a commercial β-Galactosidase enzyme. The reporter assay system including the substrate and the commercial enzyme was purchased from Promega. U87 cells after the 24 h recovery period were treated with 0.25 ml lysis buffer per well. Complete lysis of cells was achieved after 15 mins incubation of the plates at room temperature, while shaking at a slow speed. To confirm lysis occurred the plates were placed under a light microscope, Next, the cells were scraped off the wells of the plate and transferred to Eppendorf tubes. After 5 mins of centrifugation at 10 000 rcf (relative centrifugal force) supernatants were collected in new tubes, while the pellets with the cell debris were discarded. 30 µl of cell extracts for each treatment were pipetted onto a 96 well transparent plate and 30 µl of the commercial 2x ONPG. The 96 well plate with the enzymatic reaction was left incubating at 37° C for 45 mins to a maximum of 1 hour. Simultaneously with the test samples, dilutions of the commercial enzyme in distilled water were prepared. 30 µl of the enzyme dilutions were pipetted onto the same plate. Absorbance at 495 nm was measured on a spectrophotometer (Spectra Max M series). Calibration curves were prepared every time with the test samples, to ensure the validity and reproducibility of the assay. Absorbance measurements for cells alone were subtracted from the absorbance readings of the test samples and the linear equation from the calibration curve was used to calculate mU active β-Galactosidase enzyme per well.

4.2.2.4.3 Live confocal imaging

Confocal microscopy is widely used optical imaging technique to obtain high-resolution and contrast micrographs. The technique offers a significant advantage over conventional wide -field [252] fluorescence microscopy, because it is using a spatial pinhole, which blocks out of focus flare that appears in image formation of specimens having a thickness greater than 2 μm [252]. In scanning confocal microscopy, the image is produced by scanning one or more focused beams of light from a laser across the specimen, these images are called optical sections. Additionally, 3d structures can be analysed by stacking several images from different optical planes creating a z -stack. Confocal imaging is suitable for the analysis of multicolour staining that include several lasers and excitation/emission filters [252].

β-Galactosidase DNA was labelled using fluorescein (Label IT® Tracker™ and following the manufacturer's instructions. The labelled plasmid was then used to prepare nanocomplexes as described in **section 4.2.2.2** and transfection experiments were performed as explained in **section 4.2.2.4.2** using a 4 h treatment time point for both Lipofectamine/β-Gal and EA13GC37/β-Gal nanocomplexes. U87 cells were seeded at 5 x 10^5 cells ml $^{-1}$ on 35 mm glass bottom dishes (Nunc™, Thermo Fisher Scientific, Altrincham, UK) instead of the 6 wells lysine coated plates. The nucleus of the cells was stained with Hoechst 3342. Briefly, prior imaging Hoechst stock solution (10 mg ml $^{-1}$ in distilled water) was diluted 1:2000 in PBS. The cell medium from the plates was discarded and 0.5 ml of Hoechst working solution was added to each plate. The plates were left incubating at 37° C in the presence of 5 % CO_2 for 5 – 10 mins. Finally, the staining solution was aspirated, and the cells were washed carefully three times with PBS, pH=7.4.

4.2.2.5 Statistical analysis

All data sets were analysed using either One-way or Two-way ANOVA, multiple comparisons with Bonferroni test on GrapPad Prism 7.

4.3 **Results**

4.3.1 Plasmid yield after extraction

The yield of both plasmids (β-Gal DNA and Luc-DNA) was calculated using absorbance measurements at 260 nm. Luc-DNA yield was calculated to be 535 mg ml $^{-1}$, while the yield for β-Gal was estimated to be 438 mg ml $^{-1}$. Information about the purity of the samples was obtained by the measured 260/280 ratio, which was 1.86 and 1.87 for β-Gal DNA and Luc -DNA respectively. The two ratios are close to 1.8, which is indicative of a pure DNA sample and successful extraction.

4.3.2 Growth curve of U87 cells

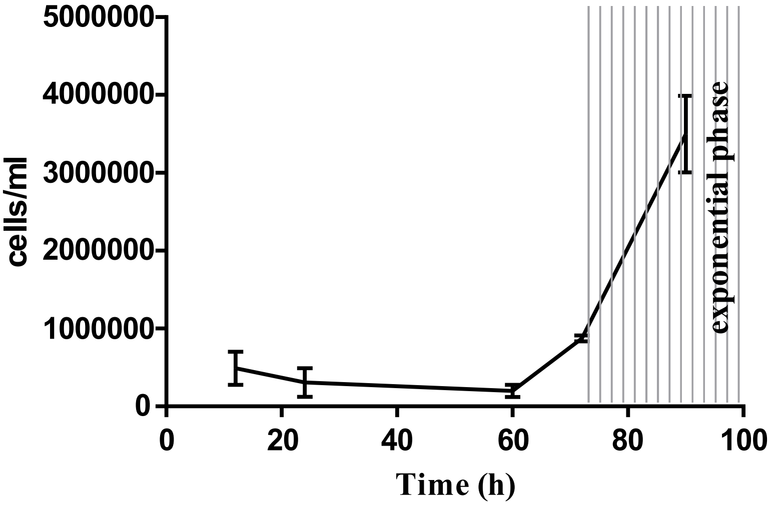

Figure 4-1: U87 cells enter exponential phase after 72 h

A growth curve of U87 cells was needed, because it is important to identify the start of exponential phase for each cell line prior to transfection experiments. When cells are in actively dividing state the nuclear membrane loses its integrity, which facilitates nuclear uptake of the nanocomplexes [128]. U87 cells enter exponential phase 72 h after sub-culturing (**Figure 4-1**), which is why for the consecutive transfection experiments 72 h was chosen as a starting point.

4.3.3 Characterisation of EAGC-based nanocomplexes with β-Gal

The low (EA6GC37), medium (EA13GC37) and high (EA24GC37) ethyl-amino substituted glycol chitosan variants were complexed with β-Gal at 1 to 1, 1 to 10, 1 to 40 and 1 to 60 β-Gal to polymer ratio and left for 2 h at room temperature. Nanocomplex formation and zeta potential at the different mass ratios were monitored with DLS.

4.3.3.1 Size distribution and zeta potential

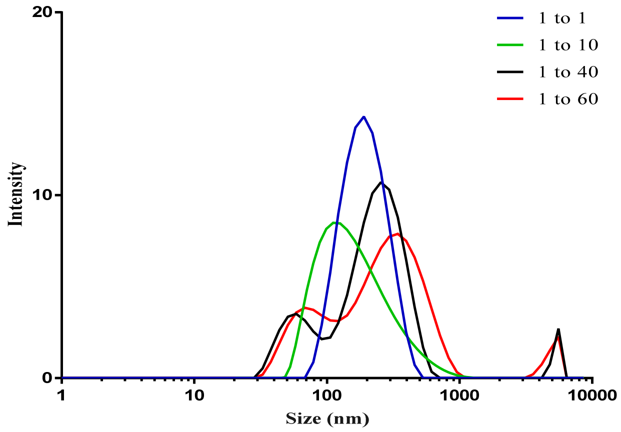

Figure 4-2: *Representative intensity size graphs of EA6GC37/β-Gal nanocomplexes with different polymer to β-Gal mass ratios after 2 h complexation time at RT in water*

Table 4-1: *Size and PDI of EA6GC37/β-Gal nanocomplexes from polyplexes prepared on two separate days represented in the two separate rows.*

β-Gal DNA to EA6GC37 (mass ratio)	Size (nm)	Polydispersity PDI
1 to 1	150 ± 13	0.111 ± 0.015
	192 ± 29	0.150 ± 0.027
1 to 10	87 ± 13	0.391 ± 0.060
	111 ± 16	0.279 ± 0.033
1 to 40	86 ± 15 (25%), 260 ± 31 (75%)	0.269 ± 0.025
	68 ± 13 (21%), 202 ± 36 (79%)	0.229 ± 0.028
1 to 60	64 ± 15 (24%), 320 ± 45 (76%)	0.415 ± 0.066
	86 ± 10 (27%), 280 ± 28 (73%)	0.380 ± 0.031

The increase of polymer to β-Gal mass ratio resulted in increased polydispersity: PDI - 0.111 and 0.150 for 1 to 1 EA6GC37 to β-Gal DNA in comparison to PDI - 0.391 and 0.271 for 1 to 10 $*p < 0.05$; PDI - 0.269 and 0.229 for 1 to 40, $*p < 0.05$ and PDI - 0.415 and 0.380 for 1 to 60, $**p < 0.01$. **Figure 4-1 and Table 4-1**. Moreover, the higher mass ratios 1 to 40 and 1 to 60 resulted in a bimodal size distribution.

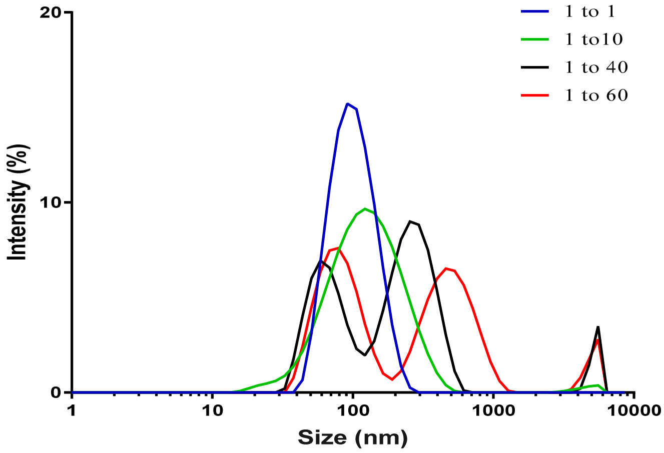

Figure 4-3: *Representative intensity size graphs of EA13GC37/β-Gal nanocomplexes with different polymer to β-Gal mass ratios after 2 h complexation time at RT in water . Each experiment was conducted independently two times.*

Similarly, to EA6GC37/β-Gal DNA nanocomplexes, EA13GC37/β-Gal DNA nanocomplexes showed a bimodal distribution for mass ratios 1 to 40 and 1 to 60, **Figure 4-3** (black and red intensity size plots). Although not as pronounced, two peaks were also present in the intensity size plot for mass ratio 1 to 10 (green size plot).

Table 4-2: *Size and PDI of EA13GC37/β-Gal nanocomplexes from polyplexes prepared on two separate days represented in the two separate rows.*

β-Gal ±EA13GC37 (mass ratio)	**Size (nm)**	**Polydispersity PDI**
1 to 1	74 ± 12	0.160 ± 0.012
	112 ± 13	0.186 ± 0.014
1 to 10	18 ± 2, 147 ± 12 (97%)	0.278 ± 0.028
	130 ± 9 (100 %)	0.267 ± 0.008
1 to 40	83 ± 14 (41%), 320 ± 61 (57%)	0.481 ± 0.014
	67 ± 11 (39 %), 360 (61%)	0.279 ± 0.013
1 to 60	138 ± 15 (45%), 787 ± 45 (45%)	0.515 ± 0.021
	98 ± 34 (51%), 800 (49%)	0.611 ± 0.011

In parallel with the findings for EA6GC37/β-Gal nanocomplexes, PDI also increased with the increase in polymer to β-Gal DNA ratios for EA13GC37/β-Gal nanocomplexes: PDI - 0.160 and 0.186 for 1 to 1 mass ratio when compared to PDI - 0.278 and 0.267 for 1 to 10 (**$p < 0.01$), PDI - 0.481 and 0.279 for 1 to 40 (**$p < 0.01$) and PDI - 0.515 and 0.611 for 1 to 60 (***$p < 0.001$), **Table 4-2**. Both the low and medium substitution nanocomplexes showed a tendency to increase also in size with the increase of polymer to β-Gal ratio (**Table 4-1** and **Table 4-2**). The addition of more polymer to both systems seemed to affect the stability of the nanocomplexes, which is indicated by the bimodal size distribution and increased polydispersity. Stability in this chapter with reference to the DLS data is used to describe the dynamic nature of the interaction between the plasmid and the polymer. Unimodal size distribution and low PDI values are considered innate characteristics of more stable polyplexes for the 2 h time point tested, while bimodal size distribution and increased

PDI values are considered as indications for a less stable polyplex with some fusion/aggregation effects or incomplete complexation.

By contrast the EA23GC37β-Gal nanocomplexes showed different intensity size plots with a single peak for the higher 1 to 40 and 1 to 60 mass ratios when compared to EA6GC37 and EA13GC37 (red and black size plots, **Figure 4-4**). Additionally, the PDI values increase only for the 1 to 10 mass ratio PDI - 0.381 and 0.270, when compared to the 1 to 1 mass ratio PDI - 0.180 and 0.192 (**$p < 0.01$), but for the higher ratios 1 to 40 and 1 to 60 there is no significant difference PDI – 0.186 vs PDI - 0.253 and 0.187 and PDI - 0.180 and 0.158 respectively (ns) (**Table 4-3**). A potential explanation could be that a more compact nanocomplex is formed with the high ethyl-amino substitution polymer.

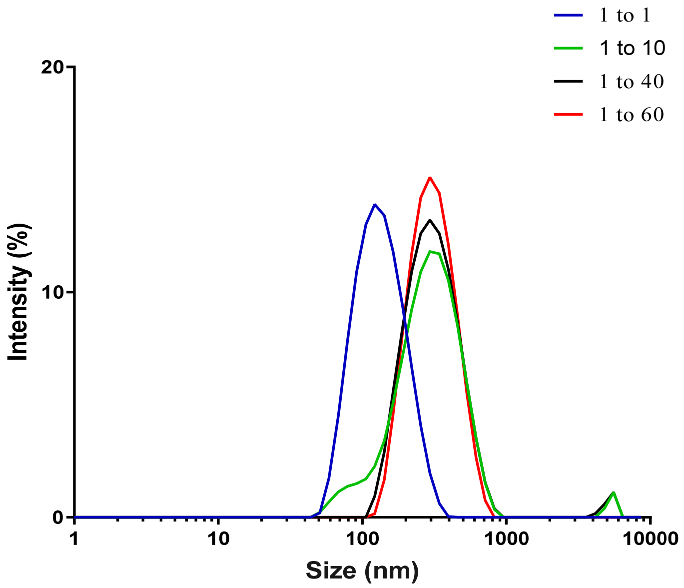

Figure 4-4: *Representative intensity size graphs of EA23GC37/β-Gal nanocomplexes with different polymer to β-Gal mass ratios after 2 h complexation time at RT in water . Each experiment was conducted independently two times.*

Table 4-3: *Size and PDI values for EA23GC37/β-Gal nanocomplexes from two independent experiments represented in the two separate rows.*

β-Gal DNA to EA23GC37 (mass ratio)	**Size (nm)**	**Polydispersity PDI**
1 to 1	133 ± 15	0.180 ± 0.018
	112 ± 19	0.192 ± 0.009
1 to 10	11 ± 6, 262 ± 31 (94%)	0.381 ± 0.060
	12 ± 4, 320 ± 41 (91%)	0.270 ± 0.031
1 to 40	325 ± 19	0.259 ± 0.024
	261 ± 41	0.187 ± 0.054
1 to 60	301 ± 37	0.158 ± 0.020
	245 ± 31	0.180 ± 0.023

Zeta potential measurements were performed for the nanocomplexes prepared with the low, medium and high EAGC polyplexes (**Figure 4-5 A**, **B** and **C**). The data showed that all nanocomplexes are positively charged (+35 mV – +40 mV) while naked β-Gal DNA is negatively charged (- 23 mV ± 2 mV). Interestingly, the increase of polymer to β-Gal DNA mass ratio did not show a trend in increasing the charge for any of the EAGC polymers used to prepare the nanocomplexes. There were no significant differences between the different mass ratios for any of the polyplexes.

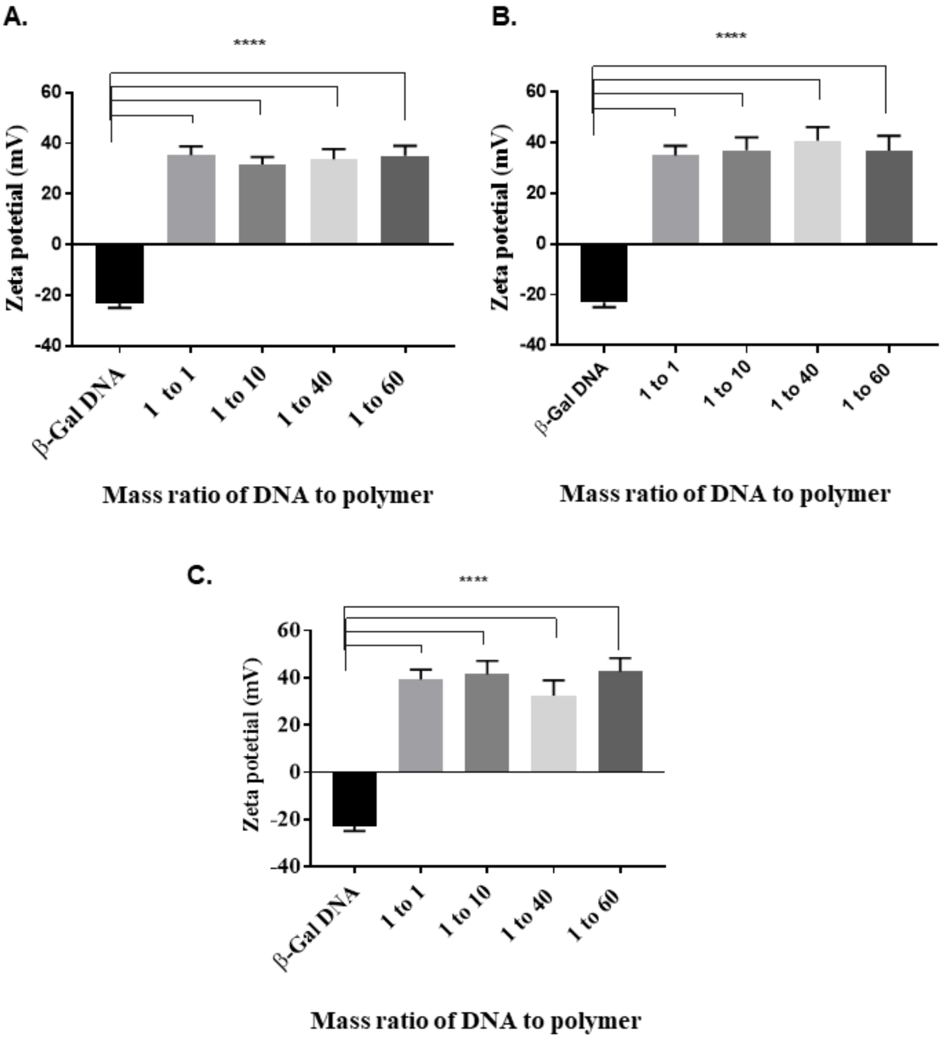

***Figure 4-5**: Zeta potential of EAGC-based nanocomplexes after 2h of complexation time at RT in water. EA6GC37/β-Gal DNA (**A**), EA13GC37/β-Gal DNA (**B**) and EA23GC37/β-Gal DNA (**C**). The graph shows average results of three measurements on three different days (n=3 ± S.D), ****p < 0.0001*

4.3.3.2 Gel retardation assays

A gel retardation assay was used to complement the DLS data for the low, medium and high levels of substitution nanocomplexes at the different mass ratios. Mass ratios of polymer to DNA of 1 to 1 and 1 to 5 for all EAGC variants showed release of the plasmid indicated by bands corresponding to the one of free plasmid in lane 1 (**Figure 9-13**, see Appendix). Naked β-Gal DNA plasmid was used as a control for the experiment (lane 1, **Figure 4-6**). The presence of a band (1 to 10 mass ratio, EA6GC37/β-Gal DNA, lane 2 **Figure 4-6**) showed that there is free β-Gal DNA, indicative of partial or incomplete complexation. The higher ratios for both EA6GC37/β-Gal DNA nanocomplexes and EA13GC1/β-Gal DNA (1 to 40 and 1 to 60, lanes 2, 3, 6 and 7 respectively, **Figure 4-6**) did not show the presence of free β-Gal DNA. These findings appear to conflict the DLS results, which suggest the presence of more unstable nanocomplexes with the increase of polymer to DNA ratios for EA6GC37/β-Gal and EA13GC37/β-Gal. On the other hand, the increase of PDI could indeed suggest a looser, more dynamic structure for the nanocomplexes, yet still capable of retaining the plasmid. No free DNA was detected for the EA23GC37/β-Gal nanocomplexes for any of the ratios tested (lane 8, 9 and 10, **Figure 4-6**).

***Figure 4-6:** Gel retardation assay of EAGC nanocomplexes with β-Gal plasmid . EA6GC37 at 1 to 10 mass ratio showed no retardation of the plasmid indicated by the presence of a band (lane 2) corresponding to the band present in lane 1 (naked β-Gal DNA). EA13GC37 showed some DNA release at mass ratio 1 to 10 indicated by a less intense band (lane 5). All the other mass ratios for the medium and high substituted EAGC variants showed complete retardation of the plasmid (lanes 2 - 4 and 6 - 10).*

4.3.3.3 TEM

The morphology of the EAGC-based nanocomplexes was studied by TEM. EA13GC37/β-Gal was chosen at a 1 to 10 mass ratio for the analysis (**Figure 4-7**, **Left**). A naked β-Gal DNA at the same concentration was used as a control (**Figure 4-7**, **Right**). EA13GC37/β-Gal nanocomplexes appeared as spherical particles with higher electron density (dark core). The picture showed the presence of smaller (˜ 70 nm) and larger in size spherical particles (˜ 200 nm). By contrast naked β-Gal appeared as highly disordered structure, which resembles a network [253]. It has already been reported that the different mass ratios of EAGC variants to β-Gal DNA (as well as different levels of ethyl-amino substitution) did not result in any morphological differences, hence one polymer and one ratio were chosen for TEM analysis [254].

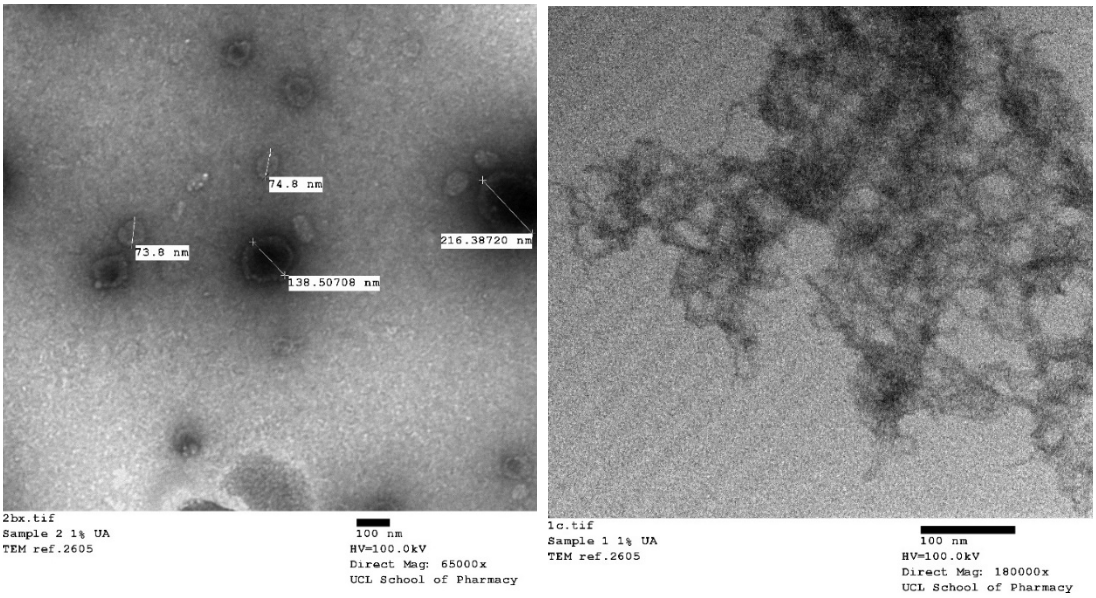

Figure 4-7: *Representative TEM images of β-Gal DNA and EA13GC37/β-Gal nanocomplexes β-Gal DNA (0.1 mg ml^{-1}) (**Right**) and EA13GC37/β-Gal at a 1 to 10 mass ratio (**Left**).*

4.3.3.4 *In vitro* transfection studies with EAGC nanocomplexes

An *in vitro* screening β-Gal assay was used to find, which of the mass ratios of EAGC polymer to β-Gal DNA is resulting in U87 cells transfection with the β-Gal plasmid and its product the hydrolytic β-Galactosidase enzyme. EAGC polymer (low, medium and high ethyl-amino levels of substitution) were used at 1 to 1, 1 to 10, 1 to 40 and 1 to 60 mass ratios to β-Gal DNA. Additionally, variation in the complexation time of the different nanocomplexes was used (0.5 h, 1 h, 2 h, 3 h and 24 h). The positive control Lipofectamine/β-Gal was also subjected to the same conditions

4.3.3.4.1 Mass ratio and complexation time

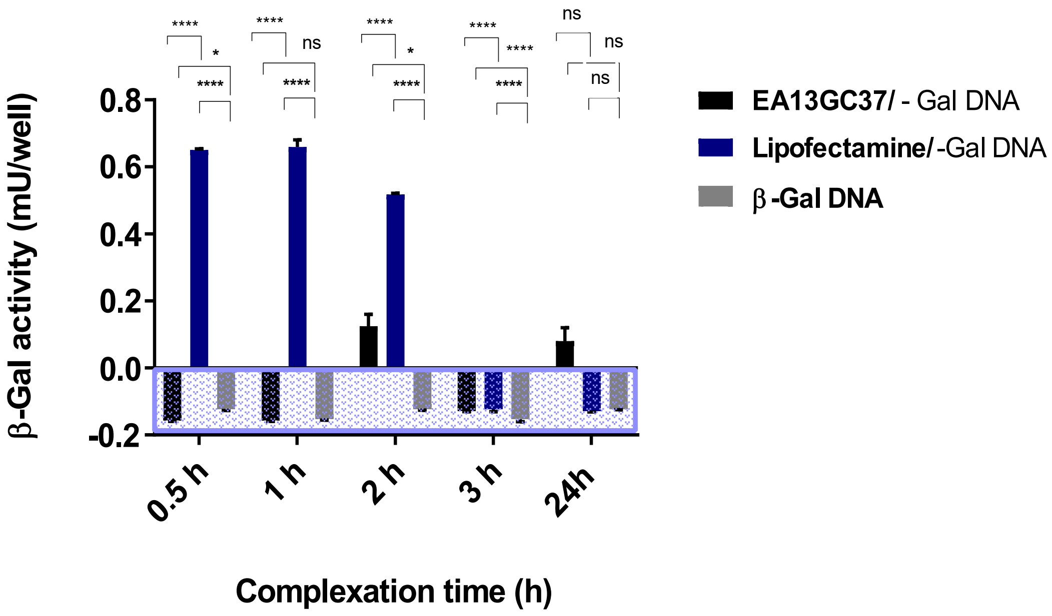

__Figure 4-8:__ Transfection efficiency of polyplexes and lipoplexes at different complexation times (0.5 h, 1 h, 2 h, 3 h and 24 h) of EA13GC37 (1 to 60 β-Gal to EA13GC37 mass ratio) and Lipofectamine (1 to 2 β-Gal to Lipofectamine mass ratio) at room temperature (RT) with water as complexation medium). EA13GC37/β-Gal after 2 h of complexation showed 23 % of Lipofectamine's transfection efficiency (0.12 ± 0.04 mU/well vs 0.52 ± 0.003 mU/well). EA13GC37/β-Gal after 24 h of complexation showed 15 % of the transfection potential of Lipofectamine (0.08 ± 0.04 mU/well). The results represent three independent experiments (n=3 ± S.D). The light blue rectangle represents an area of no transfection. Lipofectamine's transfection efficiency was considered 100 % for 2 h and 24 h and the polyplex transfection efficiency was then calculated as a percent of that for the two time points.

The high-throughput screen for the mass ratios and complexation time identified one EAGC-based nanocomplex EA13GC37/β-Gal (1 to 60 mass ratio) with a five times weaker potential to transfect U87 cells at the tested conditions when compared to the positive control Lipofectamine (**Figure 4-8**). Both 2 h and 24 h complexation time resulted in similar levels of active β-Galactosidase enzyme (23 % and 15 % of the transfection efficiency of Lipofectamine respectively). For convenience 2 h complexation time was chosen as an optimal incubation time point, since Lipofectamine/β-Gal DNA lipoplexes showed transfection potential for this incubation period too. This data suggests that complexation time matters both for lipo - and polyplexes, Lipofectamine/β-Gal DNA lost its potential to transfect U87 cells after 2 h of complexation time at RT. These effects could be related to changes in the rigidity of nanocomplexes, which can result in differences in transfection efficiency (entry of the nanocomplex in the cells and/or the release of the cargo nucleic acid in the cytoplasm or the nucleus) [255,256]. Interestingly, no trend in transfection efficiency was observed for the different mass ratios and the different EAGC variants.

4.3.3.5 Treatment time

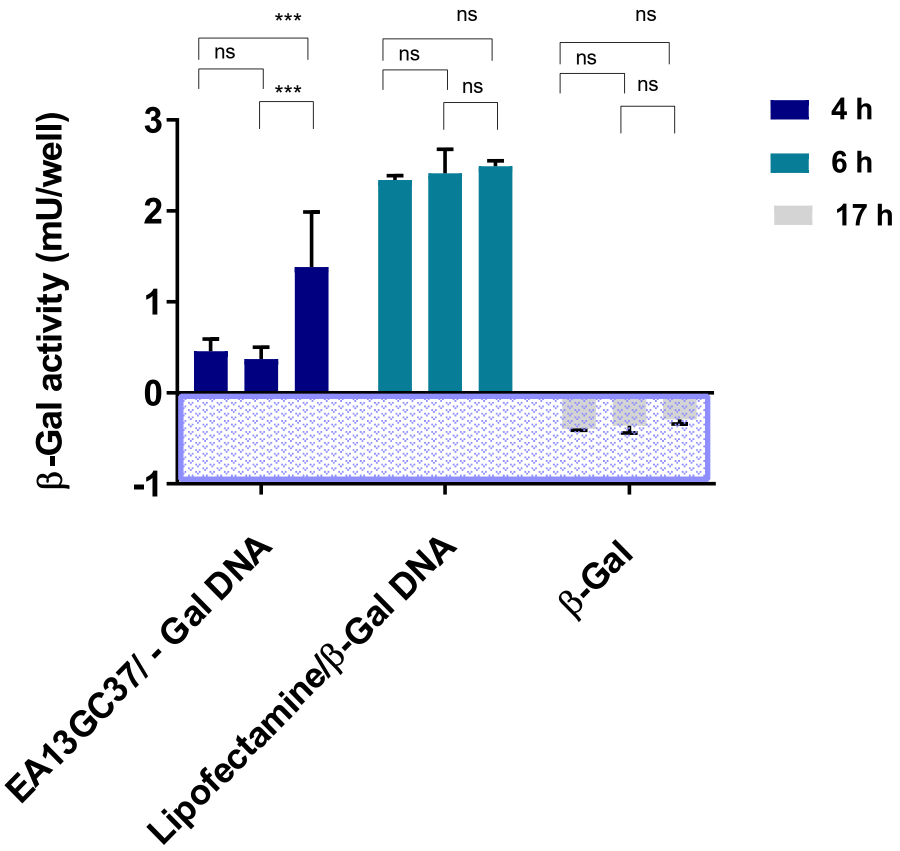

Figure 4-9: *Transfection efficiency of polyplexes and lipoplexes at different treatment times (4 h, 6 h and 17 h) EA13GC37/β-Gal DNA polyplexes showed an increase in transfection efficiency with the increase of treatment time (4 h: 0.46 ± 0.13, 6 h: 0.37 ± 0.13 and 17 h: 1.38 ± 0.63 β-Gal DNA mU/well), while Lipofectamine/β-Gal DNA remained almost unchanged for the three time points tested (4 h: 2.34 ± 0.04, 6 h: 2.41 ± 0.26 and 17 h: 2.49 ± 0.05 β-Gal DNA mU/well). The results represent three independent measurements (n=3 ± S.D). Lipofectamine's transfection efficiency was considered 100 % for the different treatment times and the polyplex transfection efficiency was then calculated as a percent of that for the 4 h. 6h and 17h.*

Standard transfection protocols report 4 h and 6 h as recommended time points to treat cells. Transfection efficiency is cell type specific, so optimisation and tailoring of the protocol towards the cell type used is needed. To test if treatment time affects the transfection potential of EA13GC37 polyplexes, U87 cell were left with the nanocomplexes and assayed after 4 h, 6 h and 17 h. The levels of active β-

Galactosidase enzyme after 17 h was estimated to be 1.38 mU/well in comparison to 0.37 and 0.46 mU/well for 6 h and 4 h respectively, which is 55 % of Lipofectamine's transfection efficiency (**Figure 4-9**, dark blue bars). Interestingly the time-dependent increase in transfection efficiency was not detected for the control lipoplexes, which retained their transfection potential constant throughout the experiment (**Figure 4-9**, blue-green bars). Naked β-Gal DNA did not result in any active β-Galactosidase enzyme (**Figure 4-9**, grey bars). These findings are further supported by confocal live imaging experiments, where fluorescein labelled β-Gal DNA carried by Lipofectamine was already in the nucleus of U87 cells after 4 h treatment time (**Figure 4-10**, **Right panel**, red circle indicating the nuclear localization of β-Gal DNA), while β-Gal DNA carried by EA13GC37 was still outside the cells, surrounding the cell membrane after 4 h of incubation (**Figure 4-10**,**Left panel**, red arrows indicating that β-Gal DNA is outside the cell). Z-stacks for both treatments confirmed these conclusions. (**Figure 9-10** and **Figure 9-11**, see Appendix)

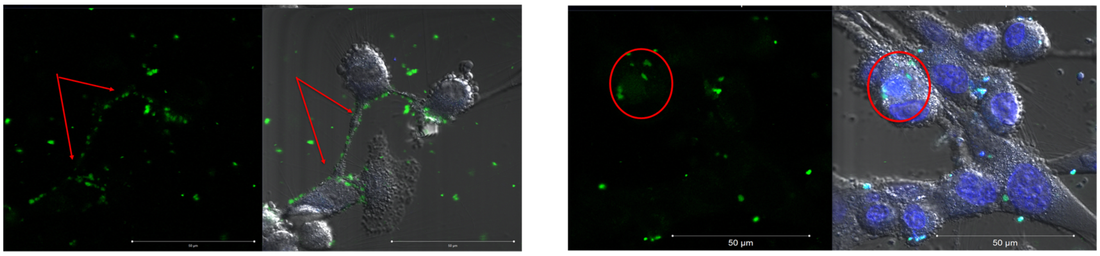

Figure 4-10: *Live confocal imaging of U87 cells after 4 h of treatment with EA13GC37/β-Gal DNA (**Left panel**) nanocomplexes and Lipofectamine/β-Gal DNA complexes lipoplexes (**Right panel**) . β-Gal DNA labelled with fluorescein (green) and Hoescht 33342 as a nuclear stain in blue.*

4.3.3.5.1 Transfection efficiency of nanocomplexes prepared in water at 4°C and RT

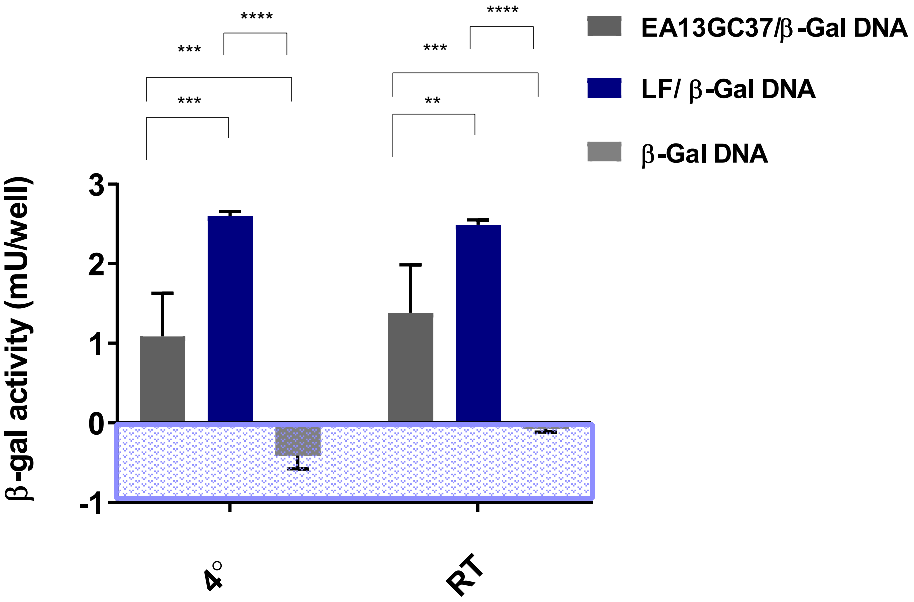

***Figure 4-11**: Transfection efficiency of EA13GC37 polyplexes and lipoplexes incubated for 2 h at RT (blue bars) and 2 h at 4° C (grey bars) in water . EA13GC37/β-Gal DNA incubated at 4° C resulted in 1.08 ± 0.54 mU active β-Gal enzyme, EA13GC37/β-Gal DNA incubated at RT resulted in 1.38 ± 0.60 mU/well active enzyme, while Lipofectamine's transfection efficiency remained constant for both temperatures (2.63 ± 0.06 and 2.5 ± 0.06 for 4° C and RT respectively).*

To investigate the variation in transfection efficiency indicated by the standard deviation for the longest treatment time of 17 h with EA13GC37 (**Figure 4-9**) two different temperatures were used 4° C and RT and a 2 h complexation time and water used as a complexation medium. Complexation in water and in the cold after 2 h did not improve transfection efficiency and the fluctuations in the levels of active β-Gal enzyme were still present for EA13GC37/β-Gal (1.08 ± 0.54 at 4° C vs 1.38 ± 0.63 at RT) or 42 % vs 52 % of Lipofectamine's transfection efficiency respectively. To further investigate the variation in transfection efficiency of EA13GC37 polyplexes when compared to lipoplexes complexation time was increased to 24 h and a comparison between water and 20 mM PBS, pH=6.8 was made. Size and polydispersity of the nanocomplexes are considered as parameters, which can provide a potential explanation for the effect of complexation medium and temperature on the stability/flexibility of the polyplex and the resulting effect on transfection efficiency.

4.3.3.5.2 Transfection efficiency of nanocomplexes prepared in PBS at 4° C, 37° C and RT

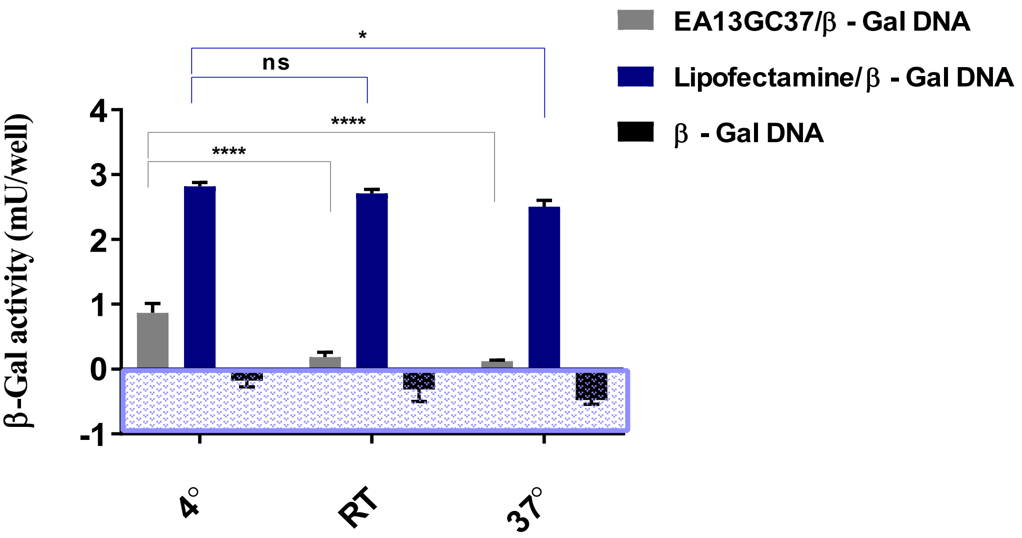

Figure 4-12: *Transfection efficiency of EA13GC37 polyplexes prepared in 20 mM PBS, pH=6.8 and incubated for 24 h at RT and 4° C. EA13GC37/β-Gal DNA prepared at 4° C result in 1.14 ± 0.15 mU/well active β-Galactosidase enzyme (43 % of Lipofectamine's transfection efficiency). EA13GC37/β-Gal prepared at RT result in 0.48 ± 0.09 mU/well active β-Galactosidase (18 % of Lipofectamine's transfection efficiency). Lipoplexes yield 2.8 ± 0.04 and 2.7 ± 0.06 mU/well active β-Galactosidase enzyme when incubated for 2 h at 4° C and RT respectively. Naked β-Gal DNA does not result in the translation of active β-Gal enzyme in U87 cells.*

Transfection efficiency of the polyplexes prepared in PBS showed a temperature dependent increase where polyplexes stored at 4° C appeared more effective to deliver the β-Gal plasmid to U87 cells in comparison to complexes stored at RT.

PDI for polyplexes stored at 4° C and water were significantly higher than PDI for those prepared in water and stored at RT (PDI: 0.41 ± 0.12 vs PDI: 0.155 ± 0.09). Interestingly regardless of the complexation temperature PBS as complexation medium resulted in polyplexes with no difference in PDI values (PDI: 0.277 ± 0.04, PDI: 0.258 ± 0.09 for RT and 4°C respectively, ns), **Figure 4-13**). These results suggest that PBS provided conformational consistency of the polyplexes, however there was no significant difference in the size of the polyplexes prepared in PBS and water for the two temperatures. Although, a trend for less variability seems to be present for the size of polyplexes prepared in PBS instead of water regardless of the temperature (**Figure 4-14**). Since the objective of the optimisation steps of the transfection protocol was to investigate the variation in transfection efficiency for the polyplexes, 24 h incubation time in 20 mM PBS at 4° C were chosen as optimal conditions for all consecutive transfection experiments.

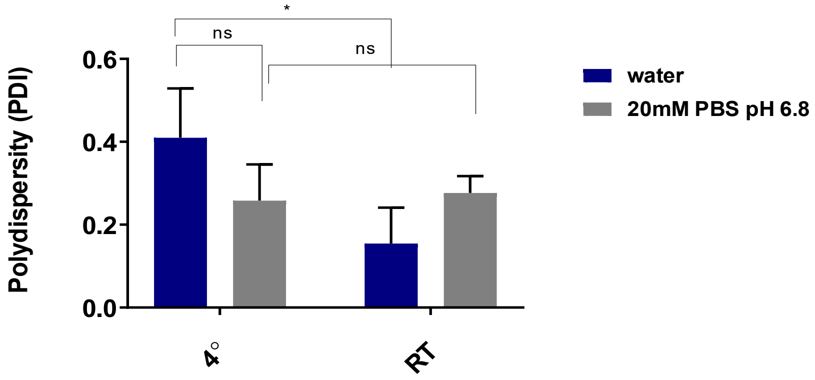

Figure 4-13: *Comparison of PDI values between polyplexes prepared in water and 20 mM PBS, pH=6.8 over 24 h incubation period at RT and 4° C . The results represent three independent measurements (n=3 ± S.D).*

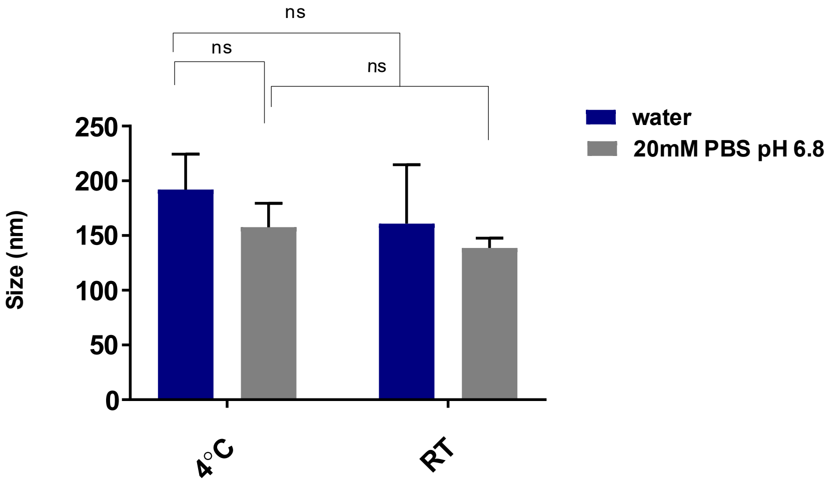

Figure 4-14: *Comparison of size values between polyplexes prepared in water and 20 mM PBS, pH=6.8 over a 24 h incubation period at RT and 4° C.*

4.3.4 Characterisation of GC-based nanocomplexes

The optimised protocol for mass ratio of polymer to β-Gal DNA, complexation time and complexation medium was applied to GC-based polyplexes obtained after 0 h, 1 h, 2 h and 6 h of degradation (GC100 - Mw ~ 100 kDa, GC57 – Mw = 57 kDa, GC37 – Mw = 37 kDa and GC21 – Mw = 21 kDa respectively).

4.3.4.1 Effect of GC molecular weight on transfection efficiency

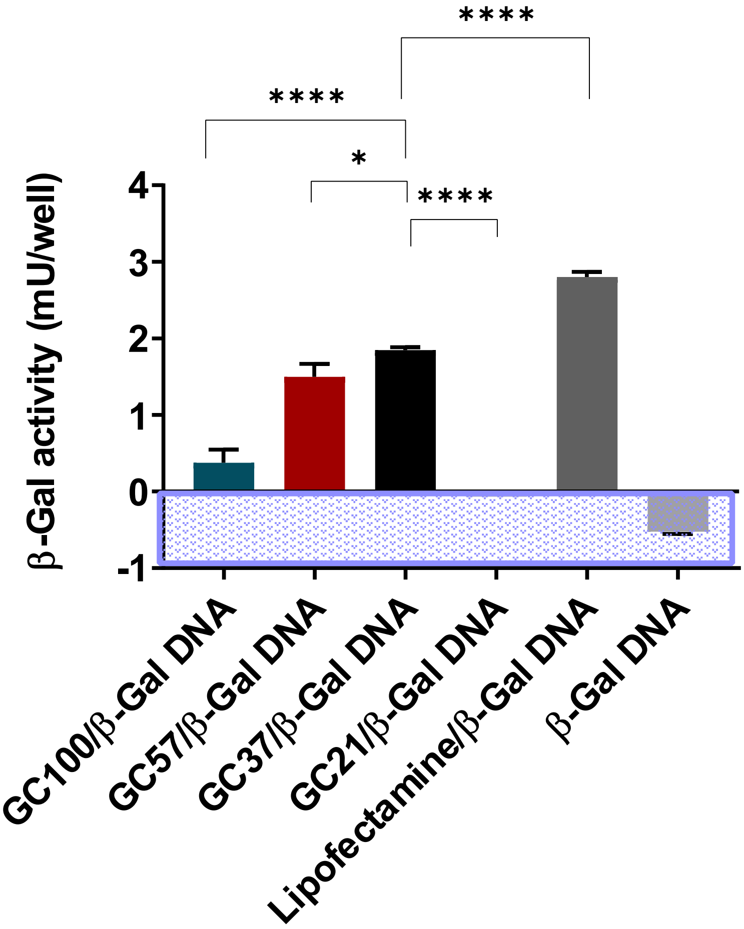

Figure 4-15: *Transfection efficiency of polyplexes prepared with different MW GC polymers.*

To investigate how molecular weight affects transfection efficiency, four GC polymers creating a range of Mw values were chosen. GC37 and GC57 showed similar transfection efficiency with 66 % and 53 % of Lipofectamine's transfection potential (2.8 ± 0.04 mU/well), considered to be 100%. GC37/β-Gal polyplexes resulted in 1.84 ± 0.04 mU/well active β-Galactosidase enzyme while GC57/β-Gal DNA nanocomplexes yielded 1.49 ± 0.17 mU/well. GC100/β-Gal DNA nanocomplexes resulted in 0.37 ± 0.17 mU/well active β-Gal enzyme (13 % of Lipofectamine's transfection efficiency). GC21/β-Gal polyplexes and naked β-Gal showed no transfection efficiency in U87 cell with 0.05 ± 0.004 mU/well and -0.52 ± 0.03 mU/well, **Figure 4-15**. Our data identified a 30 – 60 kDa Mw "sweet spot" for transfection efficiency in U87 cells. This result emphasizes the importance of molecular weight for transfection efficiency [257]. In parallel with our findings of defining a "sweet spot " for molecular weight, *Ishii et al.* reported that a 40 kDa and a 84 kDa chitosan polymers showed the highest levels of transfection in SOJ cells [179]**.**

4.3.4.2 Size and polydispersity of GC nanocomplexes

Since a polyplex results from a polymer-mediated packaging of a cargo nucleic acid, we have also considered size and polydispersity as more representative parameters characterising the resulting polyplex rather than the carrier in search of a potential explanation for the observed differences in performance. The comparison of size showed that GC57/β-Gal DNA and GC37/β-Gal DNA polyplexes package the plasmid into nanoparticles of similar hydrodynamic diameter: 163 nm and 149 nm respectively (red and black bars, **Figure 4-16, A**). The high molecular weight GC100 forms larger nanoparticles of about 200 nm, while GC21 forms the smallest in size nanoparticles of 106 nm. Nanoparticles are internalised by different endocytic pathways depending on their size. Nanoparticles with a diameter smaller than 1 μm are thought to enter the cell by micropinocytosis, a dimeter between 10 – 300 nm is associated with clathrin-mediated endocytosis [258], while internalisation of particles with a diameter of ~ 80 nm is thought to be mediated through the caveolin endocytic pathway [259]. This is important as the type of endocytic pathway will determine also the fate of the cargo. Clathrin-mediated endocytosis is an endolytic pathway, which involves degradation of the cargo in the lysosome, while caveolae-mediated endocytosis evades the lysosome. While lipoplex gene delivery is widely associated with clathrin-mediated endocytosis [260,261], polyplex gene delivery is reported to happen simultaneously through different endocytic pathways, rather than just one. [261] [96]. Since the present study did not investigate the mechanisms involved in the internalisation of GC polyplexes and due to the complex nature of polymer-mediated gene transfer we cannot attribute differences in performance due to the different sizes of the GC nanocomplexes. Furthermore, statistical analysis did not show any significant difference between the size or the polydispersity of GC37/β-Gal and GC100/β-Gal, GC57/β-Gal, GC21/β-Gal nanocomplexes (**Figure 4-16, A** and **B**).

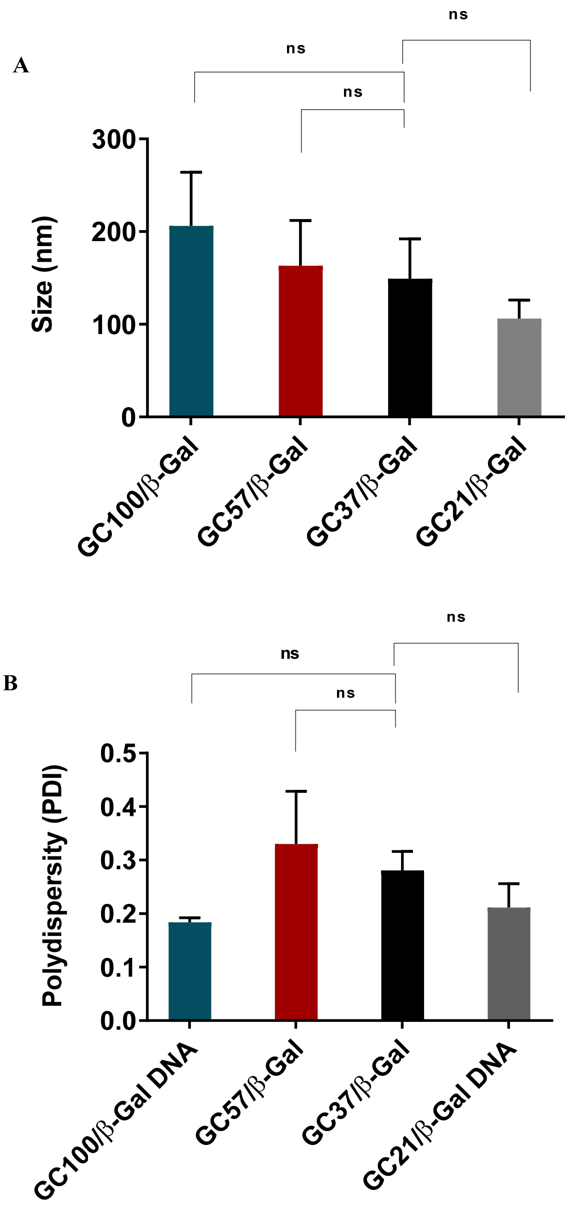

Figure 4-16: *Size distribution of GC polyplexes (GC100/β-Gal DNA: 200 ± 58nm, GC57/β-Gal DNA: 163 ± 49, GC37/β-Gal DNA: 149 nm ± 43 nm and GC21/β-Gal DNA: 106 nm ± 20 nm),* ***A****. Polydispersity of the polyplexes (GC100/β-Gal DNA: 0.184 ± 0.008, GC57/β-Gal DNA:0.330 ± 0.098, GC37/β-Gal DNA: 0.280 ± 0.035 and GC21/β-Gal DNA: 0.211 ± 0.044),* ***B****.*

4.3.4.3 Zeta potential of GC nanocomplexes

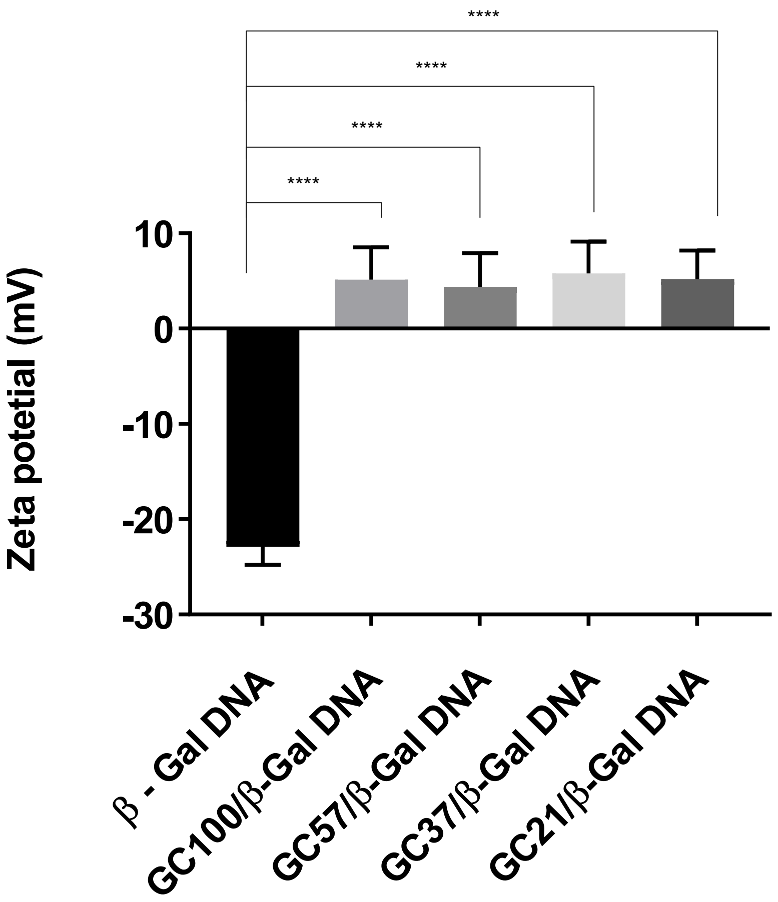

Figure 4-17: *Zeta potential of GC polyplexes prepared with different Mw GC polymers at 1 to 60 of β-Gal DNA to GC mass ratio (pH=6.8).*

The zeta potential measurements showed a slight positive charge of ~ +5mV for all the GC polyplexes regardless of the Mw (**Figure 4-17**). Additionally, different mass ratios of all the GC polyplexes (1 to 10, 1 to 20, 1 to 30, 1 to 50 and 1 to 60) showed positive charge in the range of +5 mV to +10 mV, however no trend was observed for the increase of mass ratio of polymer to DNA or the different Mw of the polymer and charge (data not shown).

4.3.4.4 Gel retardation assays

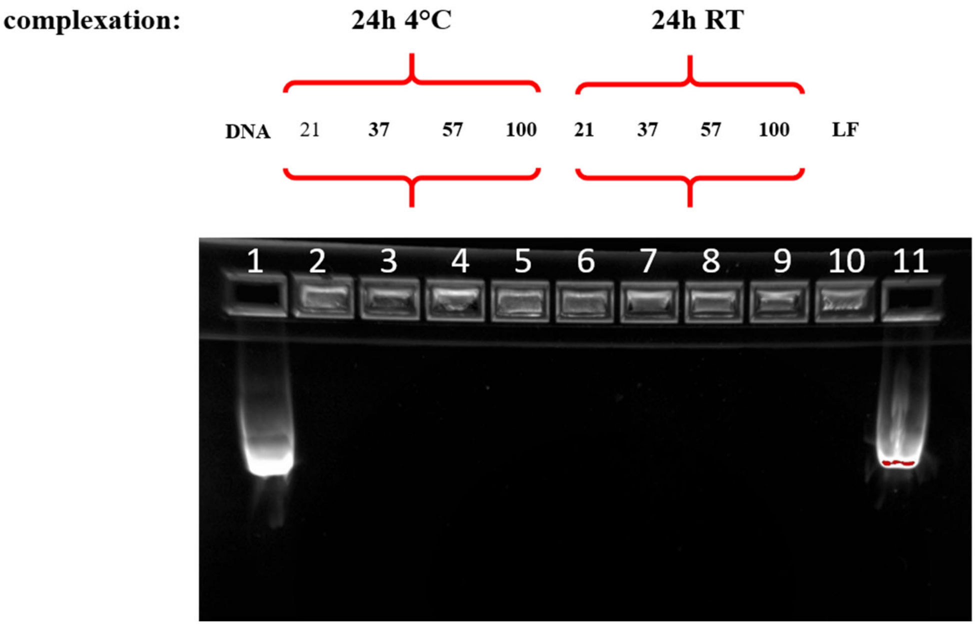

Figure 4-18: *Gel retardation assays of GC nanocomplexes with β-Gal DNA at a 60 to 1 polymer to β-Gal DNA mass ratio (lane 2 to lane 9). Lipofectamine/β-Gal DNA at a 2 to 1 mass ratio (lane 10). Lanes 1 and 11 contain naked β-Gal DNA. Free plasmid DNA was not detected for any of the nanocomplexes regardless of the molecular weight (lanes, 2 to 10).*

The gel retardation assay of GC polyplexes stored at different temperatures during the 24 h period of complexation time showed no difference between polyplexes stored at RT and 4° C to package the β-Gal plasmid. Full retardation of the DNA was confirmed with the absence of bands corresponding to naked β-Gal DNA in lane 1 and 11 for any of the GC polyplexes regardless of their Mw (**Figure 4-18**).

4.3.5 Characterisation of BS PEG (5) bis spermidine nanocomplexes

BS PEG (5) bis spermidine/β-Gal DNA were prepared at 1 to 1, 1 to 20, 1 to 30 1 to 40, 1 to 50 and 1 to 60 β-Gal DNA to oligomer mass ratios. The nanocomplexes were prepared as described in **section 4.2.2.2** and left for 2 h at room temperature. Nanocomplex formation and zeta potential at the different mass ratios was monitored by DLS.

4.3.4.1. Size and zeta potential of BS PEG (5) bis spermidine nanocomplexes

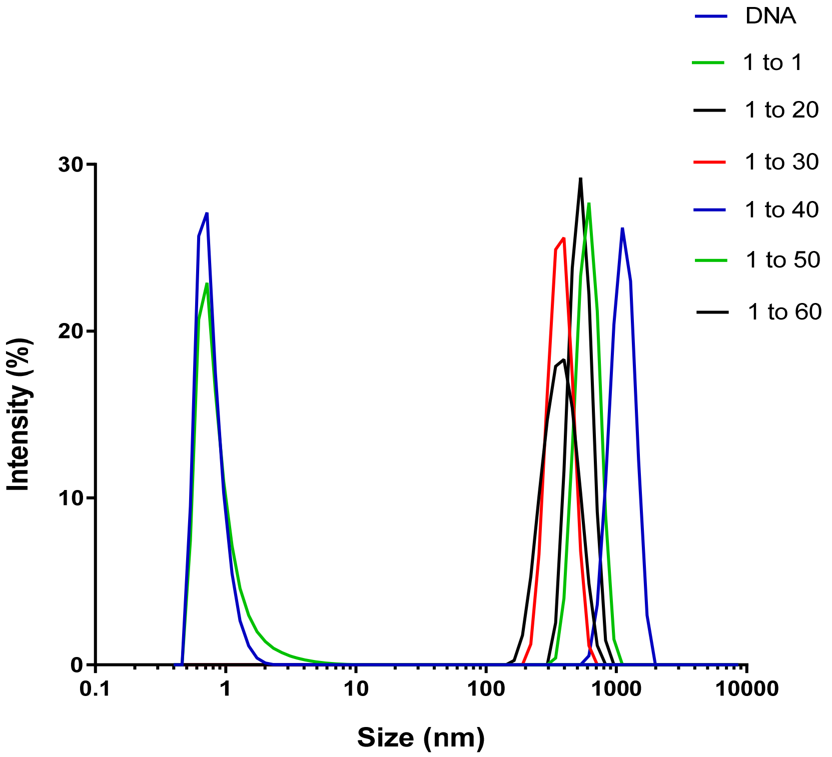

Figure 4-19: *Representative intensity size graphs of BS PEG (5) bis spermidine nanocomplexes at different mass ratios of bis PEG to β-Gal DNA after 2 h of complexation time at RT in water . Each experiment was conducted independently two times in triplicates (n = 2)*

Table 4-4: *Size and polydispersity values for BS PEG (5) bis spermidine/β-Gal at different BS PEG (5) bis spermidine to β-Gal DNA mass ratios.*

BS PEG (5) bis spermidine to DNA (mass ratios)	Size (nm)	Polydispersity PDI
1 to 20	358 ± 30	0.561 ± 0.123
1 to 30	873 ± 15	0.567 ± 0.091
1 to 40	1481 ±1 65	0.463 ± 0.006
1 to 50	843 ± 62	0.502 ± 0.127
1 to 60	869 ± 23	0.504 ± 0.023

The intensity size graphs showed the presence of one peak for all the ratios except mass ratio 1 to 1 where a peak of about 3.5 nm and a peak about 996 nm were detected (green line, **Figure 4-19**). The small peak at 3.5 nm was also detected in a sample of naked β-Gal DNA alone (blue line, **Figure 4-19**). Interestingly, for the rest of the mass ratios the size and PDI of the nanocomplexes (except for 1 to 20: 358 nm ± 30 nm and 1 to 40: 1481 nm ± 165 nm, **Table 4-4**) resulted in similar values for both size and PDI. The data suggests mass ratio of ≤ 20 results in the formation of large nanocomplexes with high PDI values.

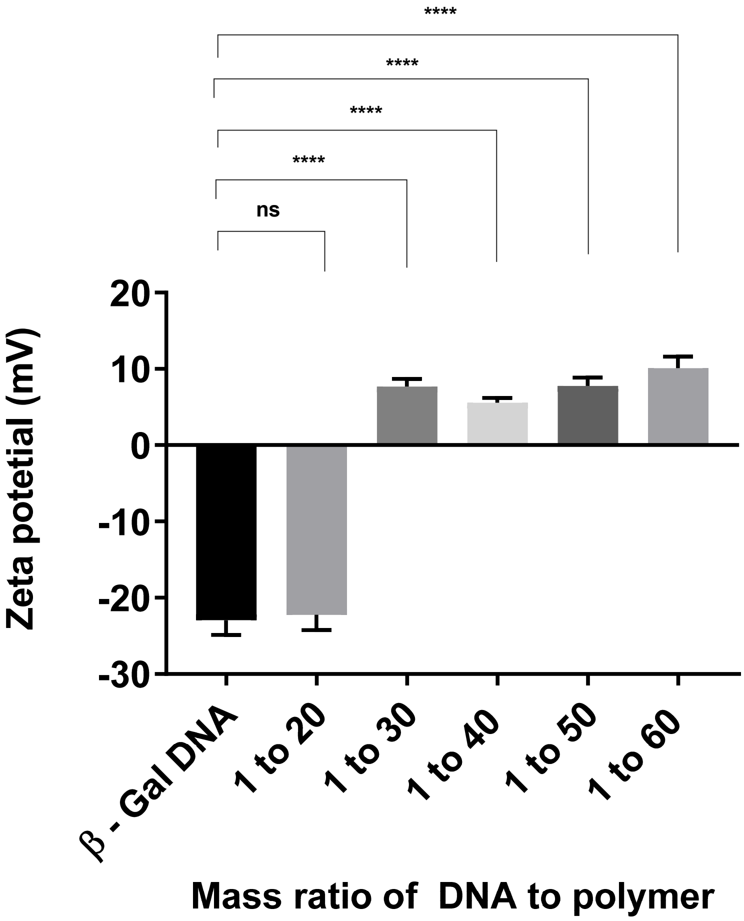

Figure 4-20: *Zeta potential of BS PEG (5) bis spermidine nanocomplexes after 2 h of complexation time at RT in water . The graph shows average results of three measurements on three different days (n=3 ± SD)*

The zeta potential measurements are in accordance with the size data. The 1 to 20 mass ratio showed a negative zeta potential of (~ -20mV), which is the charge of naked β-Gal DNA (**Figure 4-5**). The increasing mass ratios showed a slight increase of charge with a maximum of ~ +10 mV for mass ratio 1 to 60.

4.3.4.2. Gel retardation assays

The gel retardation assay showed that neither of the mass ratios of bis PEG 5 to β - Gal DNA tested (1 to 20, 1 to 40, 1 to 50 and 1 to 60), **Figure 4-21** was able to retain the plasmid, since a band was present in all lanes corresponding to lane 1, where naked β-Gal DNA was used as a control**.** The small functionalised oligomer with 5 ethylene glycol monomers was unable to package the plasmid even at the highest 1 to 60 mass ratio. Studies with a non-coding siRNA showed that at the same ratios there was no band corresponding to free siRNA indicating that nanocomplex formation was possible with a smaller in size nucleic acid such as siRNA, but not DNA (20/25 bp vs 7430 bp respectively (**Figure 9-7**, see Appendix).

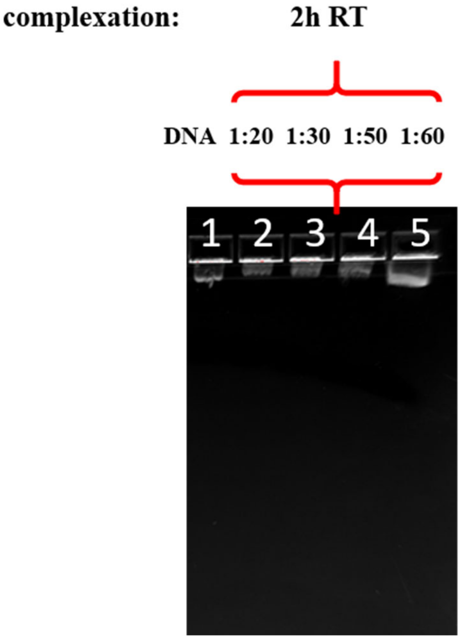

Figure 4.21: *Gel retardation assay of BS PEG (5) bis spermidine/β-Gal DNA . The different mass ratios of BS PEG (5) bis spermidine to β-Gal DNA (1 to 20, 1 to 30, 1 to 50 and 1 to 60, lanes 2, 3, 4 and 5 respectively) show no retardation of the plasmid indicated by the presence of a band corresponding to the band present in lane 1 (naked β-Gal DNA)*

In parallel with the light scattering data and the zeta potential measurements, the gel retardation assay showed that even the highest ratios of BS PEG (5) bis spermidine to β-Gal DNA is not able to package the plasmid. Although 1 % agarose gel seem to be recommended for plasmids ranging from (500 – 10,000 bp) and β-Gal plasmid is 6820 bp, the electrophoretic mobility of the plasmid seems to be affected in that particular experiment as visible from **Figure 4-21** where the band in lane 1 corresponding to naked plasmid hasn't moved far in the gel. This can be explained with some problems with the chamber voltage during the run, however regardless of this, release of the plasmid is evident for all DNA to BS PEG (5) bis spermidine mass ratios (lane 2 to 5, **Figure 4-21**). TEM imaging confirmed that there are no nanocomplexes formed since no particles were visible, but a highly disorganised area of increased electron density representative of naked β-Gal DNA or aggregation (**Figure 9-12**, see Appendix). Transfection experiments in U87 cells showed no efficiency at any of the tested ratios, hence we made the decision not to continue the work with the short amine functionalised PEG.

4.4 **Discussion**

This chapter describes the characterisation of nanocomplexes prepared either from a glycol chitosan-based polymer or the amine functionalised short BS PEG (5) bis spermidine with a reporter gene coding for β-Galactosidase enzyme. Here, we focus on the performance of the obtained nanocomplexes to deliver the reporter plasmid in the glioma cell line U87 and the optimisation of the parameters of transfection using the glycol chitosan-based polyplexes. We discuss important factors affecting the efficiency of our delivery nanosystems in U87 cells in an attempt to shed light on the reasons for the differences in performance caused by changes in complexation time, temperature during complexation time, treatment time and complexation medium.

A pure sample of β-Gal DNA was prepared after extraction from the transformed DH5 α strain of *Escherichia coli* and purity was confirmed by the ratio between absorbance at 260 nm and 280 nm, which was measured to be 1.86. DNA has an absorbance maximum at 260 nm (A_{280}), while proteins have absorbance maxima at 280 nm and 200 nm (A_{260} and A_{200}). A ratio (A_{260}/A_{288}) of approximately 1.8 for DNA is considered a pure sample, free of protein contamination [262]. The β-Gal DNA was used in complexation experiments with different mass ratios of the low, medium and high substitution level EAGC variants. Prior to the complexation experiments with U87 cells, a growth curve of the U87 cells showed that the cells enter exponential phase after 72 h, hence this time point was chosen for the start of the transfection experiments (**Figure 4-1**).

Transfection experiments require optimisation for a specific cell line and optimal parameters for one cell line may be ineffective in another, which is also true in reverse. As a starting point for the complexation studies EAGC polymers at 1 to 1, 1 to 10, 1 to 40 and 1 to 60 mass ratio (w:w) of polymer to β-Gal DNA were used and 2 h complexation time at room temperature and in water as a complexation medium.

Dynamic light scattering was used to study the interactions of the polymers with the plasmid. Our data showed that after 2 h of complexation at room temperature, the low and medium substituted EAGC variants resulted in a bimodal size distribution for mass ratios 1 to 10, 1 to 40 and 1 to 60 (**Figure 4-2, Table 4-1** and **Figure 4-3, Table 4-2**), suggesting a less compact conformation of the polyplexes with some fusion effects/aggregation with the increase of the amount of polymer used. Since the measurements for the two different days given in different rows in **Table 4-1**, **Table 4-2** and **Table 4-3** are similar and the same trend is observed for convenience the data from the first day is used in the comparisons made below. EA13GC37/β-Gal nanocomplexes showed two populations of particles, smaller and larger in size with similar percentage abundance for 1:40 and 1:60 mass ratios: 83 nm ± 14 nm (41%), 320 nm ± 61 nm (57 %) and 138 nm ± 15 nm (45 %), 787 nm ± 45 nm (45 %) respectively (**Table 4-2**). A slight predominance of the larger polyplexes was observed for EA6GC37/β-Gal DNA for the same ratios with a size of 86 nm ± 15 nm (25%), 260 nm ± 31 nm (75 %) and 64 nm ± 15 nm (24 %), 320 nm ± 45 nm (76 %) (**Table 4-1**). The higher percentage abundance for the larger particles at mass ratios 1 to 40 and 1 to 60 for EA6GC37/β-Gal DNA polyplexes could be due to the lower ethyl-amino substitution levels of EA6GC37 when compared to EA13GC37, which can contribute to more fusion effects and increased chances of aggregation. At this point it was important to understand if the observed effects are due to incomplete complexation, or differences in the interaction dynamics between the polymer and the DNA with an effect on the conformation of the polyplexes. Interestingly, gel retardation assays showed that EA6GC37/β-Gal and EA13GC37/β-Gal nanocomplexes at the higher (≤ 1 to 10 mass ratios) can fully package β-Gal DNA as there was no band for the nanocomplexes corresponding to the free DNA in lane 1 (**Figure 4-6**). A similar trend was observed for both nanocomplexes, where the increase in the amount of polymer for both systems led to an increase in polydispersity. Altogether these observations can provide some evidence that regardless of the less compact conformation, both nanocomplexes are able to retain the plasmid. By contrast the highest level of ethyl-amino substitution polymer (EA23GC37) showed an unimodal size distribution (**Figure 4-4**) for the resulting polyplexes where the hydrodynamic diameter was measured to be approximately 300 nm (1 to 10, 1 to 40 and 1 to 60 mass ratios, **Table 4-3**). The polydispersity value for EA23GC37/β-Gal DNA for the 1 to 60 mass ratios was the smallest (PDI:0.158 and 0,180, **Table 4-3**) when compared to EA13C37/β-Gal (PDI: 0.515 and 0.611, **Table 4-2**) and EA6GC37/β-Gal DNA (PDI:0.415 and 0.380, **Table 4-1**) all at the same mass ratio. The monodisperse population of particles of EA23GC37/β-Gal for the 1 to 60 indicates the formation of more compact polyplexes, since this is the polymer with the highest ethyl-amino substitution level. The different polymer to DNA mass ratios showed similar charge for the obtained polyplexes (ζ: +35 mV to ζ: +40 mV, **Figure 4-5**) regardless of the level of ethyl-amino substitution. TEM microscopy confirmed the presence of spherical particles with a darker core and size between 70 nm and 200 nm (EA13GC37/β-Gal at 1 to 10 mass ratio, **Figure 4-7 Left**). Conversely naked β-Gal DNA in the absence of cationic charges provided by the polymer appeared as areas of increased electron density, of random shape (**Figure 4-7 Right**).

BS PEG (5) bis spermidine at any of the tested mass ratios (1 to 20, 1 to 30, 1 to 40, 1 to 50 and 1 to 60 did not result in nanocomplex formation with β-Gal DNA as visible from the gel retardation assays, showing release of DNA for all the mass ratios tested after 2 h of complexation time at RT in water (**Figure 4-21).** The size data showed the presence of large aggregates of > 800 nm and PDI values higher than 0.5 (**Figure 4-19** and **Table 4-4)**. Although higher mass ratios resulted in a slightly positive zeta potential, which could suggest some level of DNA packaging, there were no particles detected by TEM (data not shown). Finally, no transfection efficiency was measured for the BS PEG (5) bis spermidine/β-Gal "complexes" at any of the mass ratios of BS PEG (5) bis spermidine to β-Gal DNA.

It has been reported previously that particle size, polydispersity and aggregation depend strongly on the preparation parameters such as mixing speed, order of mixing and complexation time [263,264]. To test how complexation time affects the performance of the polyplexes to transfect U87 cells we conducted a high-throughput screening of the tested ratios and the different EAGC variants and used a variety of incubation time points during complexation at room temperature in water (0.5 h, 1 h, 2 h, 3 h and 24 h, **Figure 4-8**). The polyplexes obtained with EA13GC37 showed ~ 20 % of Lipofectamine's transfection efficiency after 2 h and 24 h of complexation time at room temperature in water.

Polyplex heterogeneity during complexation have been reported to affect transient gene expression for PEI-DNA polyplexes in transfection experiments with 293 F cell [247]. 293-F cells are fast-growing clonal isolates derived from transformed human embryonal kidney (HEK cells) adapted to grow in suspension in the absence of serum. The authors report on increasing polyplex size and stability over 2 h complexation time and a trend for a decrease in endocytosis. On the other hand, they showed that a certain level of stability of the polyplex is needed for nuclear transport, since the highest levels of transfection was achieved when PEI and DNA were detected in the nucleus in their dispersed forms. They also showed that polyplexes obtained after only 5 mins of complexation time with the lowest stability are ineffective, which they hypothesise is likely due to the intracellular dissociation of DNA and PEI prior to nuclear entry.

Our screen identified EA13GC37/β-Gal nanocomplexes with ~ 20 % of Lipofectamine's transfection efficiency after 2 h and 24 h complexation time at room temperature in water at a 60 to 1 mass ratio as successful transfection platforms after a 4 h treatment time. For convenience since lipoplexes showed transfection efficiency after 2 h of complexation as well, we chose to continue using 2 h complexation time for the consecutive transfection experiments. Surprisingly, live confocal imaging with a 4 h treatment period, revealed that β-Gal DNA carried by EA13GC37 is still outside the cell surrounding the cell membrane (**Figure 4-10, Left panel**), while β-Gal carried by Lipofectamine is already in the nucleus (**Figure 4-10, Right panel**). Taking into consideration these results we carried out transfection experiments with prolonged treatment times from 4 h, to 6 h and 17 h. After 17 h we observed an increase of the levels of active β-Gal enzyme and about 55 % of Lipofectamine's transfection efficiency (1.38 ± 0.63 β-Gal activity mU/well, **Figure 4-9**). The shorter incubation times produced similar levels of active enzyme and were both approximately 5 times less efficient than Lipofectamine to deliver the β-Gal plasmid (0.46 ± 0.13 mU/well and 0.37 ± 0.13 mU/well active β-Gal enzyme after 4 h and 6 h treatment time respectively, (**Figure 4-9**). In accordance with our findings *Jackobsen et al.* showed that expression levels with FuGENE 6 a commercially available transfection agent continuously increased with the increase in treatment time from 0.5 h up to 48 h in CHO-K1 cells derived from the ovarian epithelium of Chinese hamsters. Additionally, *Ogris et al.*, report on a 20 fold increase in transfection levels after 48 h transfection time in the murine neuroblastoma cell line Neuro2A with PEI/DNA particles of smaller size (30 nm – 60 nm), while larger particles (of about 600 nm) [265] remain unaffected by the prolonged treatment time.

As visible from **Figure 4-11**, there is some variation for the transfection efficiency of the EA13GC37/β-Gal polyplexes during the 17 h treatment time (S.D = 22 %), which we wanted to investigate. By contrast, lipoplex mediated transfection efficiency resulted in more stable levels of active β-Galactosidase enzyme. In attempts to find the reason for the fluctuations in transfection efficiency we considered incubating the polyplexes prepared in water at RT and 4° C, however this did not result in any improvement (**Figure 4-11**). Interestingly, increasing the complexation time to 24 h and replacing the complexation medium with 20 mM PBS, pH=6.8 showed a temperature effect for the efficiency of EA13GC37/β-Gal polyplexes prepared at 4° C and at RT. Moreover, the transfection levels were considerably more stable for both temperatures. Polyplexes prepared at 4° C appeared more effective resulting in 1.14 ± 0.15 mU active β-Gal enzyme or about 43 % of Lipofectamine's transfection efficiency, while the polyplexes incubated at RT resulted in 0.48 ± 0.09 mU/well active β-Gal enzyme or 18 % of Lipofectamine's transfection efficiency. In parallel with these findings, increasing further the temperature during complexation to 37° C resulted in even lower transfection levels (**Figure 4-12**). Less variation of size and PDI values for EA13GC37/β-Gal polyplexes was observed regardless of the temperature during complexation over 24 h in PBS when compared to complexation in water (**Figure 4-13** and **Figure 4-14).** At a constant pH of the buffer, the protonation environment during complex formation is consistent for the amine groups, resulting in more controlled interaction between the polymer and the DNA and less variable transfection efficiency of the polyplexes. On the other hand lower pH values and low ionic strength of the complexation medium are reported to increase transfection efficiency for PEI/DNA polyplexes [266] . A study by *Sharma et al.* showed that PEI/DNA polyplexes prepared in 165 mM PBS, pH=7.4 and stored at RT failed to transfect the monkey kidney tissue cell line COS 7, while polyplexes stored at 4° C retained 2/3 of their initial transfection potential. These findings were explained by the slower rate of aggregation at 4° C estimated by means of turbidity measurements [267].

Polyplex formation is often discussed in the light of electrostatic interactions between the positive charges of the carrier and the negative charges of the nucleic acid, however there are also other important interactions, which are often overlooked. Hydrogen bonds in the structure of the polymer as well as between the polymer and the DNA play a role in the stability of the formed polyplex. Our data showed that with an increase in temperature (up to 40° C) hydrogen bonds in the glycol chitosan structure are broken down proven by the characteristic downfield shift in the ^{1}H-NMR due to dishelming effects (**Figure 9-6,** see Appendix). Hydrogen bonds ensure an additional stability of the polyplex [268] and changes in the protonation state due to uncontrolled pH or temperature during complexation can result in different polyplex conformation hence different transfection efficiency. This can explain the observed temperature dependence and emphasize further on the importance of polyplex conformation for entry, release and uptake by the nucleus. A gel retardation assay with different Mw GC polyplexes incubated at 4° C and RT for 24 h in PBS showed no free DNA at 1 to 60 mass ratio, however subtle difference in conformation, would not necessarily translate into DNA release in such assays.

After defining the optimal conditions for the performance of EA13GC37/β-Gal nanocomplexes in U87 cells it was necessary to compare the transfection efficiency of the unmodified GC37 polymer to its EAGC variant. It was important to verify our strategy to facilitate release in the cytoplasm by introducing ionizable groups in the structure of the polymer to improve endosomal escape. Our data showed that GC37 as a carrier exerted improved ability to deliver the target gene wit 66 % of Lipofectamine's transfection efficiency (1.84 ± 0.04 mU/well active β-Gal enzyme) when compared to its modified derivative EA13GC37 with 44 % of Lipofectamine's transfection efficiency (1.06 ± 0.14 mU/well, $^{**}p < 0.01$). Additionally, we performed a side by side comparison of different Mw GC polymers and identified a Mw "sweet spot" for transfection efficiency in U87 cells (30 – 60 kDa). The activity of β-Gal enzyme as a result of GC57 and GC37 mediated gene transfer were comparable with a 12 % difference in favour of GC37. High Mw GC100 resulted in 13 % of the transfection efficiency of Lipofectamine, while low Mw GC21 showed as a completely ineffective gene carrier, since no active β-Gal enzyme was detected. We considered size and PDI as parameters characterising the polyplexes rather than just focusing on the Mw of the polymer. GC57/β-Gal and GC37/β-Gal polyplexes packaged the plasmid in particles of similar size (**Figure 4-16 A**) with similar PDI values (**Figure 4-16 B**). A trend of decreasing polyplex size with decreasing Mw seems to be present, although statistical analysis showed no differences in both size (**Figure 4-16 A**) and between the different Mw GC polymers (**Figure 4-16 B**). Literature data is puzzling when it comes to pinpoint polyplex size as a cell entry requirement. The complex nature of polymer-mediated gene transfer and the variations in the test transfection protocols result in ambiguous results. *Rejman et al.* suggested that particles smaller than 200 nm utilise the clathrin-dependent mechanism, whereas larger particles (200 nm – 500 nm) use caveolae-mediated endocytosis [269]. Others concluded that polyplexes with > 200 nm size use micropinocytosis, medium sized particles enter the cell by clathrin coated pits and small polyplexes of ≤ 100 nm enter through caveolae-mediated endocytic pathway [270]. Additionally, different endocytic pathways have been reported for the same PEI/DNA polyplexes in different cell lines [271,272]. It is important to identify the endocytic pathway, which is used by polyplexes since some endocytic pathways are described to result in higher transfection efficiency than others [261,273]. Charge, on the other hand is believed to play a role not only for complexation/release but also as a pre-requisite for cell uptake [274,275]. It is still difficult to attribute the complete dependence of any of the stages of polymer-mediated delivery to charge only, or for that matter any other isolated parameter. Our data did not show any significant difference in the charge of both EAGC and GC nanocomplexes for the different mass ratios expressed by zeta potential measurements (**Figure 4-5** and **Figure 4-17**). More importantly GC37/β-Gal polyplexes showed a considerably lower charge when compared to EA13GC37/β-Gal polyplexes at the 1 to 60 ratio. Nevertheless, GC37 appeared to be the superior gene carrier with 66% of Lipofectamine's transfection efficiency when compared to its derivative EA13GC37, which achieved 43 % of Lipofectamine's transfection efficiency in U87 cells.

4.5 **Conclusions**

By using the standard transfection protocol, a high-throughput screen of the polymers at 1 to 1, 1 to 10, 1 to 40 and 1 to 60 β-Gal to polymer mass ratio after 2 h and 24 h complexation time in water identified the middle substituted EAGC variant (EA13GC37) with 23 % and 15 % of Lipofectamine's transfection potential respectively. Surprisingly none of the other mass ratios and complexation times for the rest of the EAGC variants resulted in transfection. Thus, EA13GC37/β-Gal was used for the optimisation of the transfection protocol in U87 cells at a 1 to 60 β-Gal to polymer ratio. Increasing the treatment time from 4 h to 6 h did not seem to improve the transfection efficiency of the polyplex, however the longest treatment time of 17 h resulted in 55 % of Lipofectamine's transfection efficiency (***$p < 0.001$). However, transfection in this case was highly variable. By contrast complexation over 24 h in 20 mM PBS resulted in more stable transfection levels for EA13GC37/β-Gal than complexation over 2 h and in water. Moreover, complexation at 4°C in 20 mM PBS, pH=6.8 resulted in significantly higher transfection levels than complexation at RT in 20 mM PBS, pH=6.8 (****$p < 0.0001$) or complexation at 37° C (****$p < 0.0001$) for EA13GC37/β-Gal. The optimised transfection protocol was applied to unmodified GC polymers with a variety of molecular weights (GC100, GC57, GC37 and GC21). A molecular weight "sweet spot" was identified between 37 kDa and 57 kDa with 66 % and 53 % of Lipofectamine's transfection potential respectively. GC100 showed only 13 % of Lipofectamine's transfection efficiency and GC21 was not able to deliver the reporter gene to U87 cells (GC37/β-Gal DNA vs GC57/β-Gal DNA, *$p < 0.05$; GC37/β-Gal vs GC100/β-Gal, ****$p < 0.0001$; GC37/β-Gal vs GC21/β-Gal, ****$p < 0.0001$). Interestingly, the polydispersity and size of all the GC polyplexes were not significantly different.

5 Preparation and characterisation of hyaluronidase coated nanocomplexes

5.1 **Introduction**

The solid tumour microenvironment has been shown to be a significant barrier for the successful delivery of anti-cancer agents to tumour cells [25]. The movement of therapeutics within the tumour microenvironment includes the process of convection for vascular agents and then diffusion in the interstitial space in the stroma to reach the target cells. The process of convection or crossing the vessel wall depends widely on pressure gradients, while the diffusion through the stroma is highly dependent on the density of the stromal matrix [276].

The tumour microenvironment is characterised by elevated tumour interstitial pressure (TIP), which can be attributed to the so called fluid pressure and the solid stress [277]. The fluid pressure in the tumour tissues arises due to the fast-expanding mass of cells with poor vascularization. The process is heightened by the aberrant permeability of the tumour vessels and the leakage of fluids in the ECM alongside with the absence of normal lymphatic drainage. The solid stress is caused by expression of abnormal levels of ECM components by the increased number of fibroblasts in tumour tissues. These include hyaluronic acid, collagen fibres, proteolytic enzymes and proteoglycans [278]. Both solid and fluid pressure contribute to upregulation in the production of cytokines such as VEGF and TNF, which stimulate angiogenesis of tortuous and hyperpermeable tumour vasculatures aggravating the process [279]. Therefore, the presence of fluid pressure impedes the convection process of anti-cancer agents, while the solid pressure poses an additional physical barrier for their diffusion deeper into the tumour and they both lead to heterogeneous intratumoral distribution and limited efficacy.

Different TIP modulating strategies have been reported as ways of improving the response to cancer therapy and subsequently treatment outcomes. Strategies targeting the fluid pressure include the use of vasculature disrupting agents (VDAs) and vasculature targeting drugs (VTAs). While VDAs focus on disrupting the existing tumour vasculature, VTAs target the formation of new tumour vessels. The group of Taxane drugs (paclitaxel, docetaxel) have both disruptive and targeting properties inhibiting VEGF production and binding to microtubules, which stimulates apoptosis and results in decreased cell density and decompressed blood vessels [280].

Solid pressure alleviating approaches include the use of glycosyl hydrolase enzymes for the degradation of ECM components. Both hyaluronidase and collagenase have been used in attempts to reduce the stiffness and rigidness of the tumour ECM by digesting hyaluronan to N-acetyl glucosamine [281] or by cleaving collagen and destroying its association with vessels [282]. Human pegylated recombinant hyaluronidase (PEGPH20) is in Phase III clinical trials as an adjuvant therapy for the treatment of pancreatic adenocarcinoma [283]. PEGPH20 is also currently in phase I clinical trials as a chemo-adjuvant for other types of solid tumours[284].

With the development of nanomedicines as an alternative for cancer therapy, using an ECM targeting approach in a nanoparticulate formulation with an anti-cancer agent appears even more attractive than employing it as an adjuvant therapy. The peritumoral injection of immobilised hyaluronidase on silica nanoparticles showed improved efficiency in melanoma tumours in comparison to the free enzyme [285]. The improved efficacy of immobilised hyaluronidase on nanoparticles loaded with a chemotherapeutic drug was demonstrated also in a very recent study by *Zhou et al.* [286]. The study is also the first one to show systemic application of hyaluronidase functionalised PLGA-PEG NPs with doxorubicin in mice with breast cancer. The authors demonstrated that the NPs maintained their enzymatic activity and showed both improved penetrations/diffusion in the ECM and increased accumulation of doxorubicin in the tumours. However, enzyme immobilisation on nanoformulations can cause irreversible changes to the structure of the enzyme and its function [287]. This led to the development of alternative ideas for the preparation of nanoparticles with an ECM targeting capacity. A very recent study by *Hong et al.* reported on the development of doxorubicin loaded exosome nanoparticles with native GPI anchored PH20 hyaluronidase (Exo-PH20^{Dox}), which successfully enhanced drug distribution in a PC3 pancreatic xenograft tumour model and inhibited growth efficiently after an intratumoral injection [288]. Additionally, strategies using electrostatic interactions as a basis for nanoparticle assembly have been also explored. *Dai et al.* report on the preparation of a multi-component system based on electrostatic interactions, which incorporates polymeric nanoparticles encapsulating epirubicin (EPI) with hyaluronidase (NPs-EPI-HA-ase) and an RGD sequence for cell internalisation. The hyaluronidase coated nanoparticles delivered EPI to the least accessible area in tumour tissues, where tumour stem cells reside after systemic administration in a hepatocellular tumour carcinoma model [289].

This chapter will focus on the preparation and characterisation of hyaluronidase coated polyplexes based on electrostatic interactions. Our data shows that we successfully applied a strategy to coat the polyplexes and quantify the amount of enzyme bound. Additionally, we have been able to prove that the ternary complex with hyaluronidase retains approximately 50% of hyaluronidase activity to digest hyaluronic acid *in vitro* when compared to the free enzyme. This is to the best of our knowledge the first time a ternary complex is prepared by electrostatic interactions, which incorporates a gene therapy and an ECM targeting approach for cancer treatment.

5.2 **Materials and Methods**

5.2.1 Materials

Materials	Purity	Supplier
Hyaluronidase Type I S- 400 – 1000 units mg $^{-1}$	N/A	Sigma Aldrich (Gillingham, UK)
Sodium chloride	≥ 99.5 %	Sigma Aldrich (Gillingham, UK)
Trifluoroacetic acid (TFA)	> 99%	Promega (Southampton, UK)
Acetonitrile HPLC garde	≥ 99.5 %	Thermo Fisher Scientific (Loughborough, UK)
Hyaluronic acid (Mw 70 kDa – 90 kDa)	N/A	Sigma Aldrich (Dorset, UK)
Bovine Serum Albumin (BSA)	≥ 96%	Sigma Aldrich (Gillingham, UK)
Sodium Acetate -anhydrous	≥ 99 %	Sigma Aldrich (Gillingham, UK)

5.2.2 Methods

5.2.2.1 Preparation of hyaluronidase coated nanocomplexes

Polyplexes were prepared at 6 µg ml^{-1} in 20 mM PBS, pH=6.8 in a total volume of 250 µl and stored for 24h at 4° C as described in **section 4.2.2.2**. Hyaluronidase enzyme (Type I S 400-1000 units/mg solid) was dissolved in 20 mM NaCl (pH=12) to 4 mg ml $^{-1}$. Working solutions of the enzyme were prepared (2 mg ml^{-1}, 1 mg ml $^{-1}$, 0.6 mg ml $^{-1}$ 0.4 mg ml $^{-1}$ and 0.2 mg ml $^{-1}$). 250 µl of each working solution was added to 250 µl of polyplex drop-wise in a 7 ml glass container under magnetic stirring for 30 mins. After that the ternary complexes were stored for another 24 h at 4° C.

5.2.3 Characterisation of hyaluronidase coated nanocomplexes

5.2.3.1 Dynamic Light Scattering

Size and zeta potential measurements were both performed in a reusable zeta cell (Malvern Panalytical, Malvern UK). The ternary complexes (500 µl) were topped up with 200 µl of Milli-Q water (Synergy Simpak 1, Millipore UK) prior to the measurements. Size measurements were performed first, followed by a zeta potential measurement.

5.2.3.2 Reversed-Phase High Performance Liquid Chromatography (RP - HPLC)

HPLC is the most powerful analytical technique due to its capacity to separate and quantify individual compounds from complex mixtures by a single analytical procedure [290]. The separation principle in RP-HPLC is based on the hydrophobicity of the solute and more specifically on the interactions of the solute present in the mobile phase with the hydrophobic immobilised ligand (stationary phase) [291]. The separation in RP-HPLC depends on the reversible adsorption/desorption of molecules, with a range of hydrophobicities to the hydrophobic stationary phase. Typically, separation is achieved by incorporating conditions in an analytical method, which includes several fundamental steps. The first step is to use aqueous starting conditions to allow the sample to interact with the stationary phase and adsorption to occur. Next a gradient of the mobile phase (different percentage of organic to aqueous solvent) is used to allow the start of desorption of molecules from the stationary phase. The most polar molecules elute first, followed by less polar, while at the highest percentage of organic (apolar) solvent in the gradient the most hydrophobic molecules elute [292]. A variety of detectors can be coupled to a HPLC system, depending on the application and the properties of the analyte of interest (UV detector, fluorescence, evaporative light scattering).

RP-HPLC was performed using Agilent Technologies 1200 series chromatographic system, which consisted of a vacuum degasser, a quaternary pump, an auto-sampler, a column compartment with a thermostat and a UV detector controlled by ChemStation software (Agilent Technologies, Santa Cruz, USA). The analysis was performed on a reverse-phase PRLP-S column (100Å 4.6 x 50 mm, 3 µm, Agilent Technologies, Santa Cruz USA) fitted with a guard column. The flow rate was gradually set to 0.7 mL min $^{-1}$ in increments of 0.1 until the column reached 80° C for the start of the method at a stable pressure of 100-105 bars. Injection volume was set to 10 µl and analysis was performed using a solvent gradient listed in **Table 5-1** in 0.1 % Trifluoroacetic acid (TFA)/Acetonitrile (ACN) at a wavelength of 280 nm**.** Samples were prepared in 0.1% TFA and analysed using a standard curve ($y = 708.13x – 5.6753$, $r^2 = 0.991$) prepared with a concentration range of 0.025 – 1 mg ml $^{-1}$.

Table 5-1: *HPLC gradient method for hyaluronidase determination*

Min	%(A) 0.1%TFA/water	% (B) ACN
0.50	90	10
0.51	10	90
4.00	10	90
4.01	90	10

Free hyaluronidase and ternary complexes were filtered through a 0.22 µm syringe filter (Milex GP-syringe filter, Merck Millipore UK).

5.2.3.3 Hyaluronic acid digestion potential of the hyaluronidase coated nanocomplexes using a turbidity assay

A turbidity assay is used for measuring the activity of hyaluronidase. The assay relies on the formation of an electrostatic complex between negatively charged hyaluronic acid of high molecular weight binding to acidic albumin, which results in a turbid solution [293]. Upon enzymatic digestion of high molecular weight hyaluronic acid to lower molecular weight fragments or di- and monosaccharides there is no complex formation, hence the solution is transparent. Therefore, turbidity can be used as a function of hyaluronic acid concentration and can then be related to enzymatic activity.

10 mg of hyaluronic acid (70 kDa – 90 kDa) were dissolved in phosphate buffer (0.3 M sodium phosphate, pH=5.35). The solution was then heated to 90° C with stirring until all the hyaluronic acid was dissolved, followed by cooling down to 37° C in a water bath. For the hyaluronic acid calibration curve ($y = 2.0644x-0.0289$, $R^2 = 0.992$) a solution of 1 mg ml $^{-1}$ hyaluronidase was prepared in 20 mM phosphate buffer supplemented with 77 mM NaCl and 0.01 % (w/v) Bovine Serum Albumin (BSA), pH= 7. Acidic albumin solution was prepared by dissolving 2.5 g of BSA in 250 ml of 0.5 M sodium acetate buffer pH=4.2. The hyaluronidase stock solution was diluted to a range of concentrations (0.0125 – 0.5 mg ml $^{-1}$) in 20 mM sodium phosphate buffer pH=7 to a total volume of 1 ml in a 14 ml glass vial. 0.5 ml of 0.4 mg ml $^{-1}$ hyaluronic acid solution was added to 0.5 ml of each of the hyaluronidase concentrations. The vials were incubated for 10 minutes at 37° C, after which the enzyme was inactivated by denaturation in boiling water bath for 5 mins. The samples were then cooled to room temperature in an ice-cold water bath and 9 ml of acidic albumin was added. The absorbance was then measured at 540 nm after 0.2 ml of the samples were transferred to a 96 well plate. The procedure was repeated for the ternary complexes (GCPH and EPH), where 0.5 ml of each ternary complex was added to 0.5 ml of 0.4 mg ml $^{-1}$ hyaluronic acid solution. The amount of the undigested hyaluronic acid was calculated from the calibration curve for each of the enzyme concentrations. Then the formula below was used to calculate the amount of digested hyaluronic acid in percentage.

$$\text{Hyaluronic acid digested (mg)} = (0.2 - \text{HA undigested}) \times 100$$

5.2.3.4 Statistical analysis

All data sets were analysed using either One-way or Two-way ANOVA, multiple comparisons with the Bonferroni test on GrapPad Prism 7.

5.3 **Results**

5.3.1 Size and Zeta potential of hyaluronidase at different pH

The predicted molecular size of globular proteins can be calculated by an in-built script in the Zetasizer Software analysis package. Additionally an online calculator based on number of amino acid residues was also used [294] for the estimation of the molecular size of hyaluronidase. The predicted size of hyaluronidase by both scripts was ~ 6 nm. The average size of hyaluronidase analysed by DLS was measured to be 5 - 11 nm (**Figure 5-1 A, B** and **C**). The intensity distribution graph of hyaluronidase in 20 mM PBS indicated the presence of particles of 700 nm (**Figure 5-1 A**, blue intensity plot) due to aggregation. Aggregates scatter light a lot more than smaller molecules but are not predominant in the sample as evident from the volume and number size distribution plots (**Figure 5-1 B and C,** blue intensity plots). Zeta potential measurements showed a pronounced negative charge for the enzyme dissolved in 20 mM NaCl, pH=12 (- 26 mV) in comparison to the enzyme dissolved in 20 mM PBS pH 6.8 (- 4.5 mV). Therefore, we chose 20 mM NaCl, pH=12 for the complexation studies with EA13GC37/β-Gal.

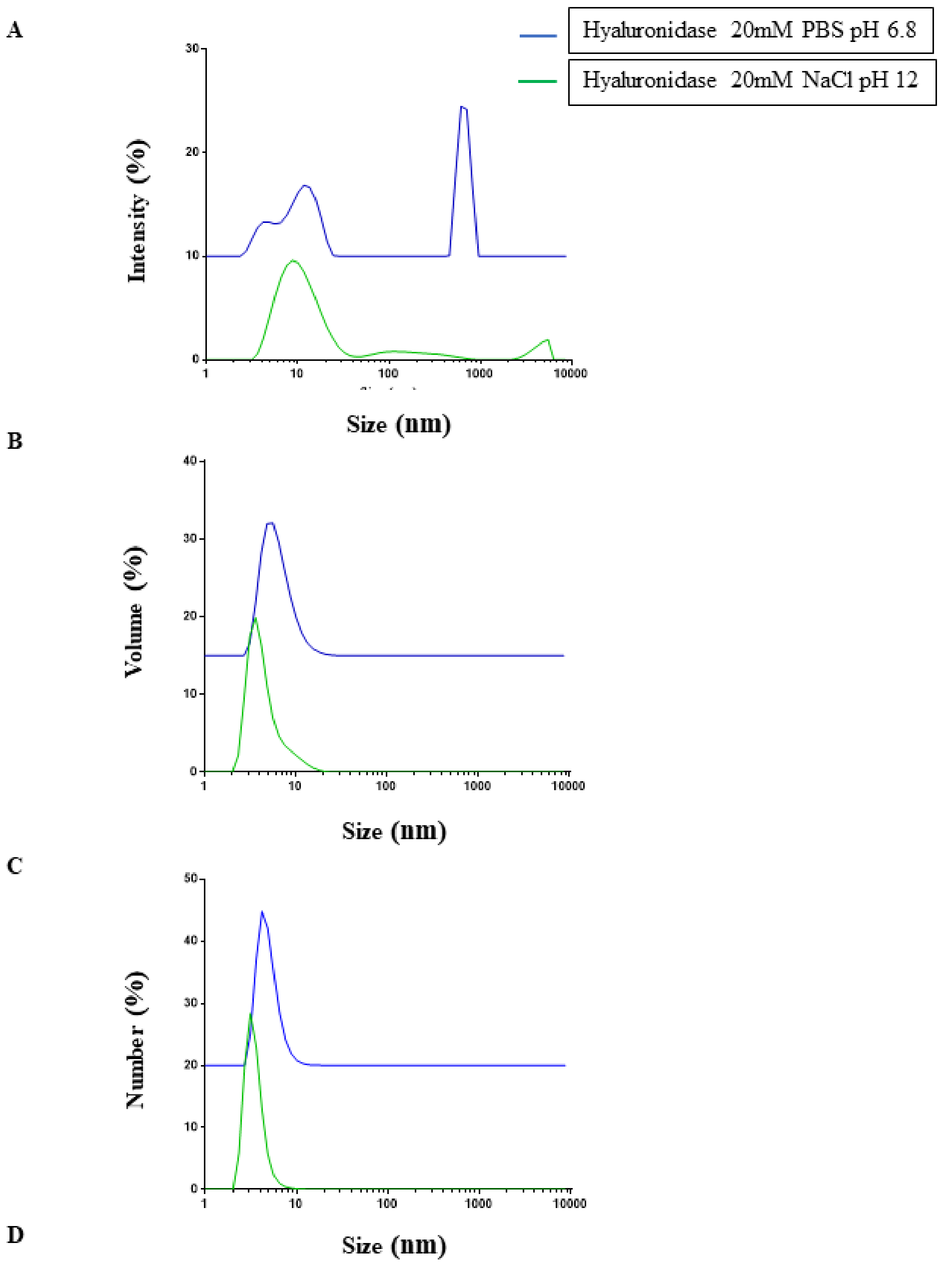

D

Hyaluronidase	Size (nm)	PDI	Zeta potential (mV)
20mM PBS, pH= 6.8	4.6 (14%) 11 (42%), 700 (44%)	0.280 ± 0.076	-4.5 ± 1.2
20mM NaCl, pH=12	11 (82%), 206 (11%)	0.541 ± 0.096	-26 ± 3.1

Figure 5-1: *Size distribution plots of hyaluronidase by intensity (**A**), volume (**B**) and number (**C**) in 20 mM PBS, pH=6.8 (blue plots) and 20 mM NaCl pH=12 (green plots). Size, PDI and zeta potential of hyaluronidase in 20mM PBS, pH=6.8 and 10mM NaCl, pH=12. The data is representative of three independent experiments (Mean ± S.D, n=3)*

5.3.2 Assembling the ternary complex

5.3.2.1 EA13GC37/β-Gal/Hyaluronidase or EPH

A range of hyaluronidase concentrations (0.1 mg ml $^{-1}$, 0.2 mg ml $^{-1}$, 0.3 mg ml $^{-1}$, 0.5 mg ml $^{-1}$, 1 mg ml $^{-1}$ and 2 mg ml $^{-1}$) were used to identify a concentration window at which enzyme coating of the polyplex is achieved. DLS was used to monitor both particle size and changes in zeta potential measurements during the complexation studies. A general trend for increase in size is visible with the increase in enzyme concentration for both size distribution plots by intensity and volume (**Figure 5.2**, **A** and **B**). Concentrations 0.2, 0.3 and 0.5 mg ml $^{-1}$ of hyaluronidase resulted in a unimodal size distribution of EPH complexes. Additionally, no free enzyme was detected for any of the concentrations confirmed by the absence of a peak between (5 - 11nm) (**Figure 5-2 A** and **B**). By contrast EPH complexes prepared with 1 mg ml $^{-1}$ and 2 mg ml $^{-1}$ hyaluronidase showed a multimodal size distribution and the presence of free enzyme.

A further confirmation for the presence of enzyme coated polyplexes at these three concentrations was the characteristic decrease in zeta potential observed with the increase in enzyme concentration (**Figure 5-3 A).** In fact, the charge of EA13GC37/β-Gal (EP) dropped from +35mV to about +3mV at 0.5 mg ml $^{-1}$ hyaluronidase concentration (****$p < 0.0001$). The last two concentrations gave negative charges for the obtained ternary complexes. However, the latter is likely due to the presence of free enzyme as visible from the intensity and even more from the volume size distribution plots for EPH 1 mg ml $^{-1}$ and 2 mg ml $^{-1}$ (**Figure 5-2**, **A** and **B**). Additionally, the PDI of the ternary complexes increased with the lowest 0.1 mg ml $^{-1}$ concentration of hyaluronidase (****$p < 0.0001$), while concentrations of the enzyme up to 0.5 mg ml $^{-1}$ resulted in similar (ns), stable and much lower values before they increased again with the two high enzyme concentrations tested (1 mg ml $^{-1}$ and 2 mg ml $^{-1}$, **Figure 5-3 B**) ****$p < 0.0001$ and ***$p < 0.001$ respectively. EPH 0.2, EPH 0.3 and EPH 0.5 showed 200 - 300 nm particles in size (**Figure 5-3 C).**

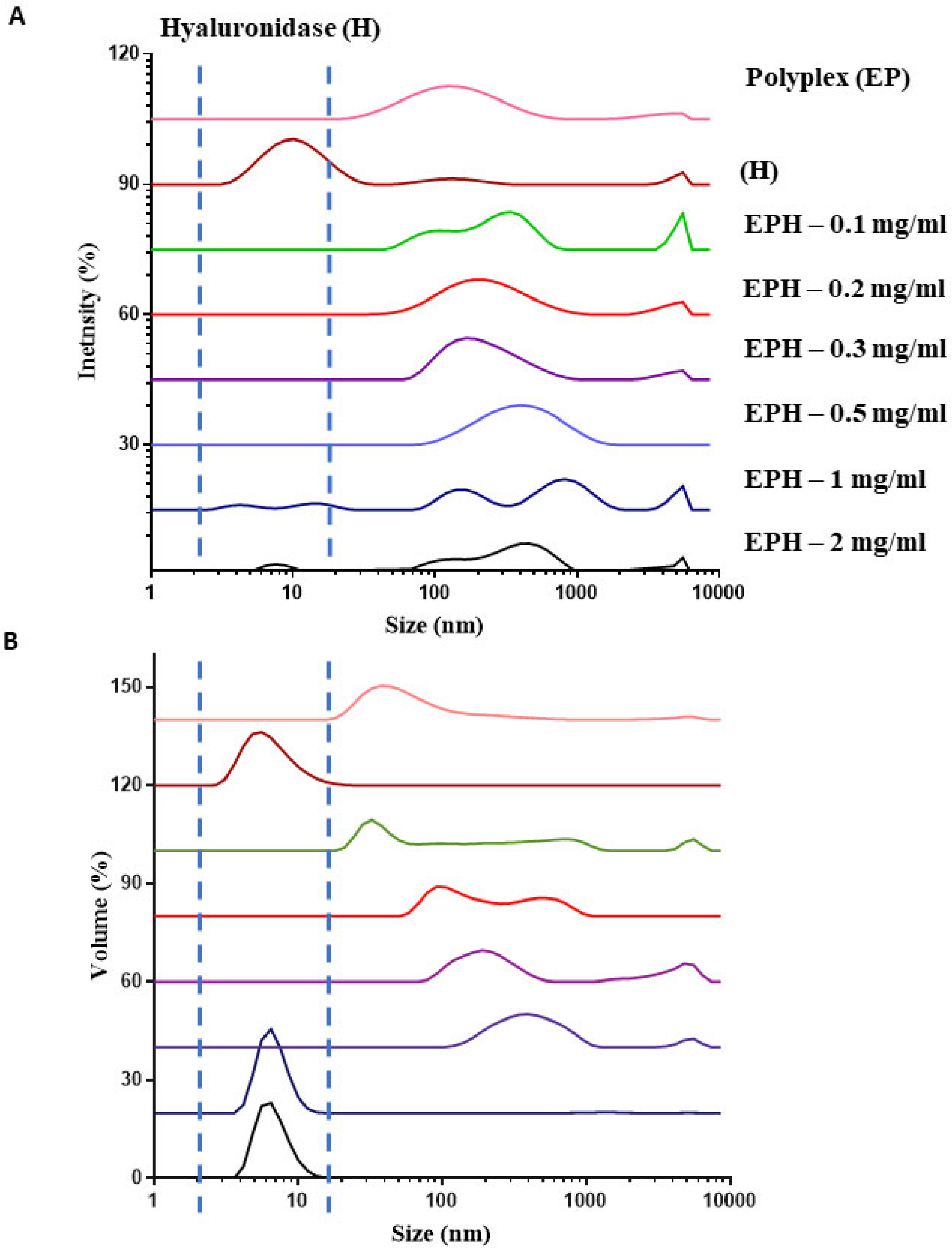

Figure 5-2: *Representative size distribution plots by intensity (**A**) and by volume (**B**) of EPH ternary complex of ternary complexes with different concentration of hyaluronidase.*

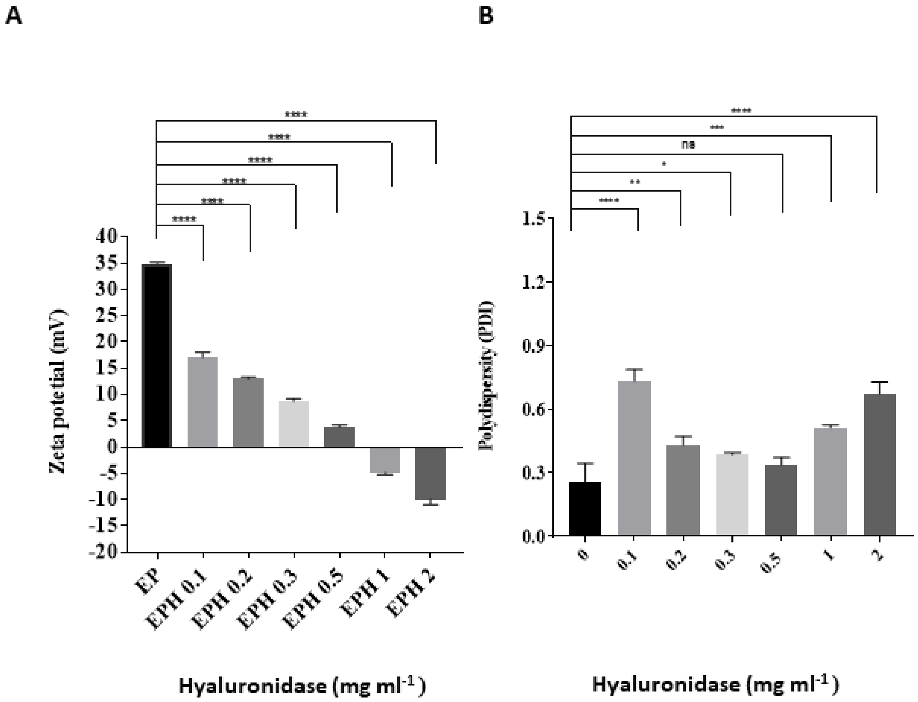

C

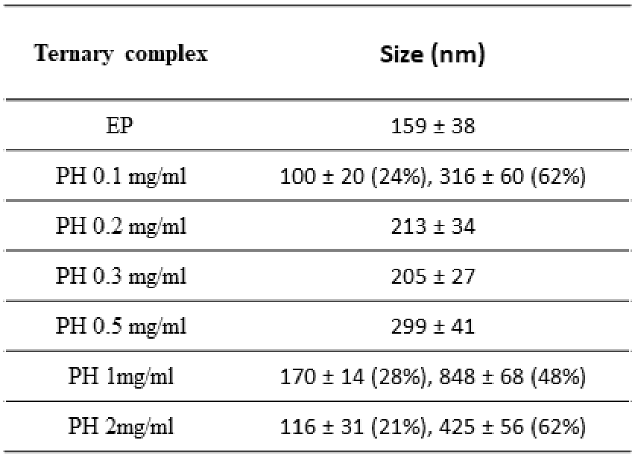

Ternary complex	Size (nm)
EP	159 ± 38
PH 0.1 mg/ml	100 ± 20 (24%), 316 ± 60 (62%)
PH 0.2 mg/ml	213 ± 34
PH 0.3 mg/ml	205 ± 27
PH 0.5 mg/ml	299 ± 41
PH 1mg/ml	170 ± 14 (28%), 848 ± 68 (48%)
PH 2mg/ml	116 ± 31 (21%), 425 ± 56 (62%)

Figure 5-3: *Zeta potential (**A**), PDI (**B**) and size by intensity (**C**) of EPH ternary complexes with different concentrations of hyaluronidase The experiment represents three independent measurements (Mean ± S.D), n = 3*

5.3.2.2 GC37/β-Gal DNA/Hyaluronidase or GCPH

Similarly, to EPH, GCPH complexes with 0.3 and 0.5 mg ml $^{-1}$ hyaluronidase did not show free enzyme in the size distribution plots (**Figure 5-4 A** and **B**). A drop in zeta potential was also observed for GCPH 0.3 and GCPH 0.5, *p < 0.05 and ***p < 0.001 respectively (**Figure 5-5 A**). However, in comparison to EPH 0.5 complexes which appeared almost neutral (~ +3 mV), GCPH 0.5 were negatively charged (~ -12mV). A negative charge was only present for the higher concentrations of enzyme (EPH 1 and EPH 2), where not all the hyaluronidase appeared complexed at the 24 h time point when measurements were performed. Conversely the GCPH 0.5 size distribution plots for intensity and volume, showed no free enzyme. The same trend of increased size was observed for both EPH and GCPH ternary complexes with increasing amounts of hyaluronidase. Interestingly, GCPH 0.5 ternary complexes were larger in size when compared to EPH 0.5 ternary complexes (459 nm and 299 nm respectively, **Figure 5-5 B** and **Figure 5-3 C).** The PDI of GCPH ternary complexes remained unchanged and was comparable to the polyplex before the enzyme was added (**Figure 5-5 B**).

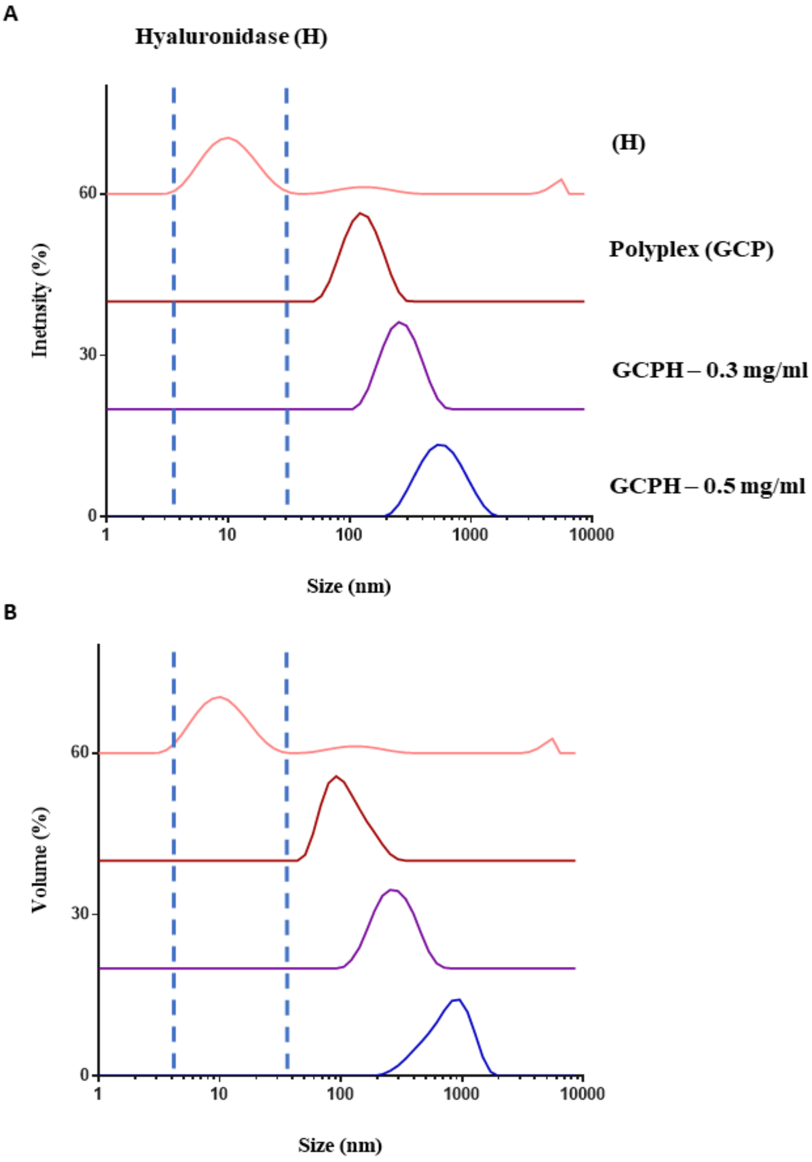

Figure 5-4: *Representative size distribution plots of GCPH ternary complex by intensity (**A**) and by volume (**B**) of ternary complexes with different concentration of hyaluronidase*

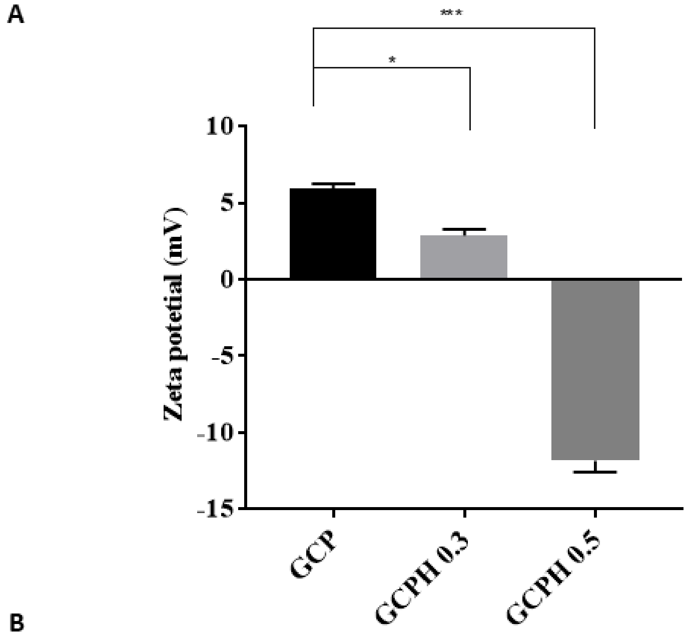

B

Ternary complex	Size (nm)	PDI
GCP	119 ± 25	0.185 ± 0.023
GCPH 0.3	235 ± 37	0.227 ± 0.061
GCPH 0.5	459 ± 56	0.257 ± 0.075

***Figure 5-5:** Zeta potential (**A**), size and PDI by intensity (**B**) of GCPH ternary complexes with different concentration of hyaluronidase . The experiment represents three independent measurements (Mean ± S.D), n = 3*

1.1.1. Quantification of free enzyme by HPLC

The DLS experiments for both GCPH and EPH ternary complexes showed that using 0.5 mg ml $^{-1}$ of hyaluronidase for both polyplexes resulted in an enzyme coated particle of increased size and a different charge due to the surface coating with hyaluronidase. A step further in the characterisation of the ternary complexes was to use a quantitative method to estimate the amount of complexed enzyme. A calibration curve using the HPLC method described in **section 5.2.3.2** (R^2 = 0.9907) was used (**Figure 5-6 A**). Since EPH 0.5 and EPH 1 ternary complexes had sizes larger than 200 nm, a 0.22 µm filter was used to separate free enzyme from the assembled ternary complex. Hyaluronidase recovery after filtration through a 0.22 filter was calculated to be 87 % ± 3 %. EPH 0.5 showed no corresponding free enzyme peak in the chromatogram after filtration (**Figure 5-6 B**), while EPH 1 showed a peak with a RT of 1.921, which is the retention time of hyaluronidase (**Figure 5-6 B and Figure**

5-6 A). It was estimated using area under the curve that the amount of free hyaluronidase is (34 % ± 5 %).

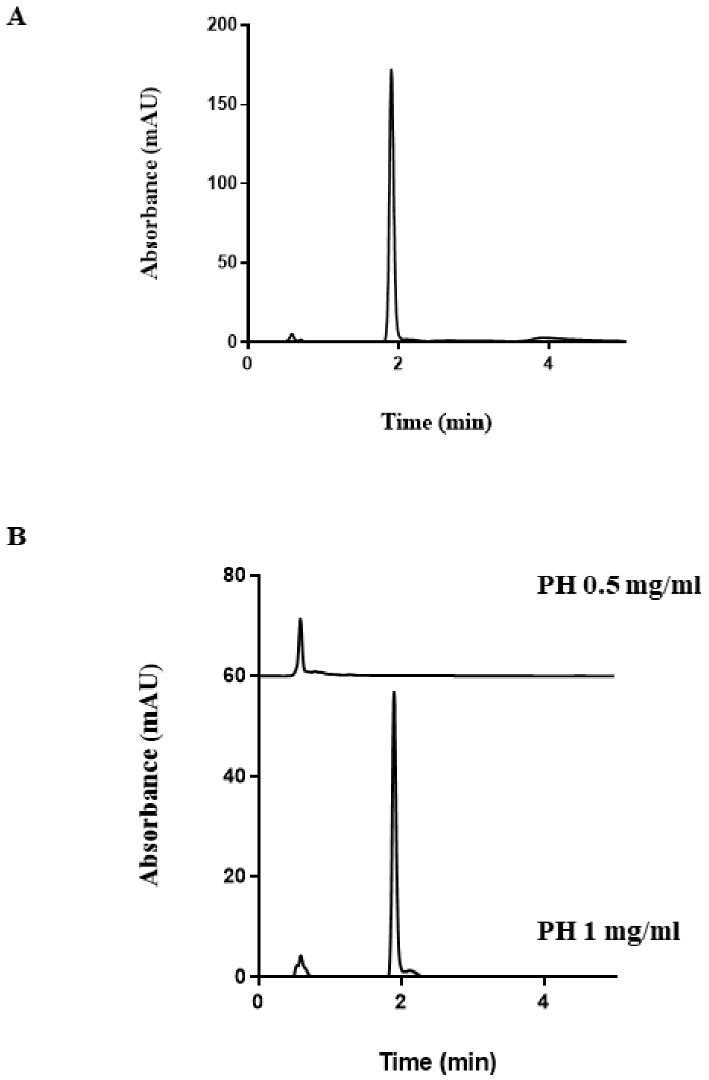

Figure 5-6: *Hyaluronidase 1mg ml $^{-1}$ (**A**) PH 0.5 mg ml $^{-1}$ and PH 1 mg ml $^{-1}$ after filtration through 0.22 µm (**B**)*

5.3.3 Enzymatic activity of EPH and GCPH

The *in vitro* hyaluronic acid digestion assay showed that all ternary complexes retained approximately 50 % of their potential to break down hyaluronic acid when compared to the free enzyme (**Figure 5-7**).

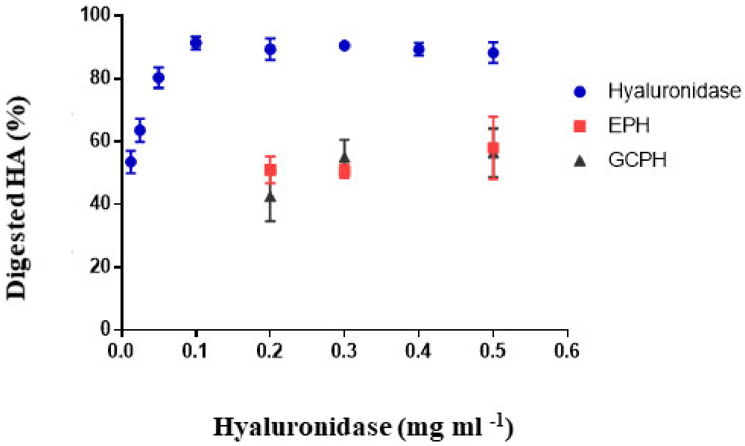

Figure 5-7: *Hyaluronic acid digestion potential of ternary complexes and free enzyme*

5.4 Discussion

The isoelectric point (pI) of crude hyaluronidase isolated from bovine testes is reported to be 5.4 [295]. Since our objective was to assemble a ternary electrostatic complex with a positively charged polyplex, we considered dissolving the enzyme in 20 mM PBS, pH=6.8 (the complexation medium used to prepare the polyplex) and 20 mM NaCl solution, pH=12. Theoretically pH values above the pI of an enzyme will result in a net negative charge for the protein, which is desired for the interaction between the positively charged polyplex and the negatively charged enzyme. 20 mM NaCl pH 12 resulted in a more pronounced negative charge for the enzyme, because of the extreme pH when compared to 20 mM PBS. pH=6.8 (-26 mv and -4.5 mV respectively, **Figure 5-1 D**). Additionally, the size distribution of hyaluronidase in 20 mM NaCl showed the presence of particles of about 11 nm with 82 % abundance as clear from the intensity size distribution plot and 5 – 6 nm with 100 % abundance from the volume and number size distribution plots (**Figure 5-1 A**, **B** and **C**). The dissolution of hyaluronidase in 20 mM PBS showed the presence of larger particles as visible from the intensity size plot (**Figure 5-1 A**), which could be an indication for aggregates being formed due to the close to neutral charge of the enzyme (**Figure 5-1 A**). Although this was not the predominant fraction of particles since the volume and number size distribution plots showed only particles between 4 – 11 nm both with a 100 % abundance. Based on the enhanced negative zeta potential of hyaluronidase and the fact that dissolution in 20 mM NaCl, pH=12 resulted in less aggregation this was the preferred solvent chosen for the consecutive complexation studies with EA13GC37/β-Gal (EP) and GC37/β-Gal (GCP).

For the complexation studies a range of concentrations of hyaluronidase were tested (0.1, 0.2, 0.3, 0.5, 1 and 2 mg ml $^{-1}$) and size and zeta potential measurements were performed for the obtained ternary complexes. The DLS studies identified a concentration window of hyaluronidase (0.1 – 0.5 mg ml $^{-1}$) where no free enzyme was detected by both intensity and volume size distribution plots (**Figure 5-2 A** and **B**), while the two higher concentrations (1 and 2 mg ml $^{-1}$) showed a peak corresponding to free hyaluronidase. Although no enzyme peak was detected for EPH 0.1 partial coating of the polyplexes is likely the reason for the multimodal size distribution observed. By contrast the multimodal size distribution observed for EPH 1 mg ml $^{-1}$ and EPH 2 mg ml $^{-1}$ is due to the presence of hyaluronidase in excess and is likely due to the fact that the ternary complexes haven't reached equilibrium after the 24 h incubation time point when measurements were performed. EPH 0.2, EPH 0.3 and EPH 0.5 showed stable PDI values of about 0.4 as visible from **Figure 5-3 C**. Furthermore, zeta potential values gradually decreased with an increase in enzyme concentration (**Figure 5-3 A**). The change from a highly positively charged polyplex EP (+35 mV) to almost neutral charge for EPH 0.5 (+3 mV) provides some proof for surface coating of the polyplexes ****$p < 0.0001$. Similarly, GC37 polyplexes coated with 0.3 and 0.5 mg ml $^{-1}$ hyaluronidase (GCPH 0.3 and GCPH 0.5) showed no free enzyme, unimodal size distribution plots by intensity and volume (**Figure 5-4 A** and **B**) and a decrease in zeta potential from approximately +5 mV (GCP) to about -12 mV (GCPH 0.5), ***$p < 0.001$, **Figure 5-5 A**. Both EPH and GCPH ternary complexes increased in size with the increase of enzyme concentration (**Figure 5-3 C** and **Figure 5-5 B**). In parallel with our findings *Dai et al.* observed a zeta potential drop and an increase in size for their multi-component nanoparticles comprised of a polymeric shell, an anti-cancer drug, gelatine-RGD and hyaluronidase all assembled in one electrostatic complex [289]. The authors report on the multi-component system showing improved diffusion of the nanoparticles in tumour spheroids when compared to the control nanoparticles without the enzyme. By contrast GCPH 0.3, GCPH 0.5, EPH 0.3 and EPH 0.5 were unable to deliver β-Gal DNA to U87 cells *in vitro (*data not shown*)*. It is worth mentioning that our 2D *in vitro* cell culture experiments were not suitable to test the ternary complexes for their potential and a 3d spheroid model would be more appropriate to compare the diffusion of the coated nanoparticles in a mimic of the tumour microenvironment.

An HPLC method was developed in an attempt to quantify the amount of free/bound enzyme to the ternary complexes. The retention time (RT) of hyaluronidase was measured to be 1.921 (**Figure 5-6 A**). Since the size of EPH 0.5 and EPH 1 ternary complexes was estimated to be ≥ 300 nm (**Figure 5-3 C** and **Figure 5-5 B**) this allowed us to use a 0.22 μm filter to separate coated particles and free enzyme (~ 6nm). Unfortunately, the filtrate of free hyaluronidase showed 87 % ± 3 % recovery after HPLC analysis with remaining 13 % of enzyme was left in the filter's dead volume. The filtrates of EPH 0.5 and EPH 1 were analysed and EPH 1 but not EPH 0.5 showed a peak with RT 1.921 in the chromatogram (**Figure 5-6 B**). By using area under the curve, it was quantified that 34 % ± 5 % or 0.34 mg ml $^{-1}$ of free hyaluronidase was present in EPH 1. Due to the filter dead volume we were unable to claim with confidence that all the remaining enzyme is complexed. However, the absence of a peak in the chromatogram of EPH 0.5 ternary complexes along with the size and zeta potential data provide strong evidence suggesting that at a concentration of 0.5 mg ml $^{-1}$ hyaluronidase, EP and GCP polyplexes are fully surface coated with the enzyme.

Immobilisation strategies of enzymes on nanoparticle have been proven to affect the function of the enzyme due to structural changes during the immobilisation process [287,296]. Although an assembly based on electrostatic interactions does not involve chemical modifications to the structure of the enzyme, a pH alteration could hinder important amino acid residues, which can negatively influence the enzyme function [297]. Therefore, to check the potential of the ternary complexes to digest hyaluronic acid *in vitro* when compared to the free enzyme a hyaluronic acid digestion assay was used. All ternary complexes retained approximately 50 % of their enzymatic activity when compared to the free enzyme regardless of the concentration used (**Figure 5-7**). Similarly, the multi-component electrostatic complex with hyaluronidase described by *Dai et al.* showed half of the hyaluronic acid digestion potential when compared to the free enzyme [289]. Hence using electrostatic interactions for complex assembly affects the enzyme function but does not result in a complete loss of activity. Interestingly in a very recent study by *Hong et al.* exosomes displaying PH20 with a native GPI anchoring domain important for enzyme activity [298] appeared 2.5 times more active than the free recombinant truncated rHuPH20 human hyaluronidase missing the GPI anchor [288].

5.5 **Conclusions**

Our data shows that we successfully surface coated EP and GCP polyplexes with hyaluronidase in an attempt to combine a gene therapy approach with a strategy targeting the increased solid pressure in tumours. By using a concentration range of hyaluronidase to EP and GCP polyplexes we were able to identify 0.5 mg ml $^{-1}$ of the enzyme as an optimal amount enough to provide fully coated nanoparticles as proven by the increased size and decreased zeta potential for the ternary complexes. The change from a highly positively charged polyplex EP (+35 mV) to almost neutral charge for EPH 0.5 (+3 mV) provides surface coating of the polyplexes ****$p < 0.0001$. Similarly, GC37 polyplexes coated with 0.3 and 0.5 mg ml $^{-1}$ hyaluronidase (GCPH 0.3 and GCPH 0.5) showed a decrease in zeta potential from approximately +5 mV (GCP) to about -12 mV (GCPH 0.5), ***$p < 0.001$.Furthermore, a quantitative HPLC method was used to determine with precision the amount of bound/free enzyme of the ternary complexes, a strategy that hasn’t been used previously. Finally, GCPH and EPH complexes retained 50 % of their enzymatic activity in an *in vitro* assay to break down hyaluronic acid, although they showed no transfection efficiency in the glioma cell line U87.

6 *In vivo* efficiency of GC37/β-Gal nanocomplexes

6.1 Introduction

Non-viral gene delivery *in vivo* is a challenging task and the routes of administration must be carefully selected based on the therapeutic strategy. Systemic application is desired since it has the capacity to reach disseminated targets throughout the body, but it is unquestionably more demanding than local administration. The transport of cationic nanocomplexes in the bloodstream leads to interactions with negatively charged plasma proteins and erythrocytes. This causes aggregation and potential risks of embolization in the lungs [299] or opsonization and clearance from the body [300]. The opsonised particles are cleared within minutes by the high amount of phagocytic cells residing in the liver and the spleen [301]. On the other hand, local administration offers the advantage of circumventing the contact of the nanocomplexes with the blood components, but the requirement for particle diffusion through the tissues remains.

Strategies to reduce the systemic associated toxicity of polyplexes *in vivo* have been employed, most commonly PEG shielding was proven to decrease the association with blood components and the consecutive aggregation resulting in improved circulation kinetics and target tissue accumulation [302]. However PEGylated polyplexes are still reported to have shorter blood circulation half-lives and rapid clearance when compared to PEGylated liposomes [303]. Currently the *in vivo* jet-PEI® system is the most widely used *in vivo* polymeric platform with polyethyleneimine (PEI) for the delivery of nucleic acids with seven clinical trials for a variety of cancers and conditions, five of which are using a local administration strategy [304].

In addition to that non-invasive routes for polyplex administration have gained interest and some even predict that this might be the future for the application of gene therapies [1]. Intranasal delivery is a non-invasive administration route targeting the CNS and bypassing the BBB, a major obstacle for the delivery of therapeutics following systemic application. There are three major routes by which intranasally administered molecules reach the CNS: directly through the olfactory neural pathway, the trigeminal pathway using the trigeminal nerves or indirectly through blood vasculature or lymphatic system, the systemic pathway [305]. The latter being an exception to the bypassing of the BBB rule. The olfactory neural pathway involves the rapid extracellular transport of molecules between cells in the nasal epithelium to reach the olfactory bulbs, the brain parenchyma and the CSF. By contrast the intracellular trafficking facilitated either by passive diffusion or receptor-mediated endocytosis in olfactory neurons results in a very slow axonal transport to the olfactory bulb and other brain regions [305]. Rapid delivery with high concentration levels in the CNS almost immediately or up to one hour after administration have been reported for many molecules [306–308], hence an extracellular pathway is most likely operating.

The first report on using an intranasal route for the delivery of a reporter plasmid to the brain was by *Harmon et al.* The authors demonstrated that the 30mer peptide with a PEGylated lysine residue was able to deliver DNA coding for green fluorescent protein (GFP) to multiple brain regions and predominantly to the frontal cortex [309]. Additionally PEI and chitosan coated magnetic micelles were shown to deliver a reporter plasmid coding for red fluorescent protein (RFP) to the cortex and hippocampus of treated rats after a traumatic brain injury [310].

This chapter will focus on investigating a subcutaneous and an intranasal route of administration for GC-based nanocomplexes and lipoplexes. First, IC50 values for the polymer and lipid nanocarriers were determined based on cytotoxicity experiments in U87 cells. Then, low and high dose nanoformulations with a different size for the resulting particles were tested in mice for their ability to deliver the reporter β-Gal plasmid to the mouse brain. Additionally, ternary complexes with hyaluronidase were investigated for their ability to improve the diffusion of the particles in the connective tissue or in the nasal cavity *en route* to the brain.

6.2 **Materials and Methods**

6.2.1 Materials

Materials	Purity	Supplier
CellTiter 96® AQ$_{ueous}$ One Solution Cell Proliferation Assay		Promega (Southampton, UK)
Corning Cell culture plates, 96 well		VWR (VWR BDH Prolabo (Fontenay-sous-Bois, France)
pSV-40 β-Galactosidase control vector	A 260/280 ≥ 1.80	Promega (Southampton, UK)
Beta - Glo® system		Promega (Southampton, UK)
Triton™ X -100		Sigma Aldrich (Gillingham, UK)
Magnesium chloride hexahydrate ($MgCl_2$ x $6H_20$)	≥ 96%	Sigma Aldrich (Gillingham, UK)
Isoflurane	≥ 99.7 – 100%	Sigma Aldrich (Gillingham, UK)
Luciferin		Perkin Elmer (MA, United States)
T-PER™ tissue protein extraction reagent		Thermo Fisher (Loughborough, UK)
EDTA free Halt Protease Inhibitor Cocktail		Thermo Fisher (Loughborough, UK)

6.2.2 Methods

6.2.2.1 MTS assay

The MTS [3-(4,5-dimethylthiazol-2-yl)-5-(3-carboxymethoxyphenyl)-2-(sulfophenyl)-2H-tetrazolium, inner salt; MTS] [311] and an electron coupling reagent (phenazine ethosulfate; PES) are used in a colorimetric reaction for determining the number of viable cells in cytotoxicity assays. Live cells in culture medium reduce the MTS to a coloured soluble formazan product and this is achieved by NADPH (nicotinamide adenine dinucleotide phosphate) to NADH conversion by dehydrogenase enzymes in metabolically active live cells [312]. The amount of soluble formazan generated is directly proportional to the number of live cells. The absorbance of the formazan produced by the cells can be measured with a spectrophotometer at a wavelength of 490 nm after 1 - 4h of incubation [311,313].

U87 cells were seeded in 96 well plates at a density of 10^3 cells per well in total volume of 100 µl and left for 72 h to reach exponential phase (**Figure 4-1**). 2-fold serial dilutions across the plate were performed for Lipofectamine at a starting concentration of 0.5 mg ml $^{-1}$, while the starting concentration for GC37 was 5 mg ml $^{-1}$. Due to the more narrow cytotoxicity window for GC37, instead of 2-fold serial dilutions, individual dilutions were prepared including the following concentrations (5 mg ml $^{-1}$, 4,6 mg ml $^{-1}$, 4.4 mg ml $^{-1}$, 4,0 mg ml $^{-1}$, 3,6 mg ml $^{-1}$, 3,0 mg ml $^{-1}$, 2,6 mg ml $^{-1}$, 2,2 mg ml $^{-1}$ and 1,8 mg ml $^{-1}$) The outer walls of the 96 well plates were filled with 100 µl of FBS containing medium and left without any treatment to prevent evaporation during the incubation and to provide the background absorbance later used for the analysis. The cells were left incubating with the treatment for 17 h in FBS free medium as for the transfection protocol and recovered in 100 µl per well FBS containing medium for 24 h before adding the MTS reagent. Five wells containing cells without any treatment were left as a negative control and 5 wells treated with 0.05 % Triton X 100 were used as a positive control. 100 µl of 0.05 % Triton X 100 were added to the positive control wells and the plate was incubated for 20 mins at 37° C. 20 µl of the MTS reagent was added to all the wells and absorbance at 490 nm was measured using a spectrophotometer after 2 h.

For analysis an average of the five repeats for the controls and the treatments were generated. The average value of the outer wells containing FBS medium was subtracted from the average values of both the positive and negative control along with the average for the wells containing the treatments. The percentage of viable cells was calculated as a ratio of average absorbance values of treated and non-treated cells.

IC 50 or inhibitory concentration 50 is the concentration at which 50 % of the cells are viable as a result of the treatment. IC50 values were calculated from equations generated by fitting data pots to a liner regression model in GraphPad Prism ($Y = -29.3*X + 151.1$, $R^2 = 0.9592$ for GC37 and $Y = -119.8*X + 94.74$ with $R^2 = 0.9606$ for Lipofectamine). Cytotoxicity data is presented as an average of three independent repeats performed on different dates ± standard deviation.

6.2.2.2 Preparation and low and high dose nanocomplexes for intranasal and subcutaneous administration

Nanocomplexes for subcutaneous dosing were prepared at a high (16.6 and 8.3 µg β-Gal) and a low (4.15 µg β-Gal) dose in a total volume of 100 µl, (166 µg ml $^{-1}$, 83 µg ml $^{-1}$ and 41.5 µg ml $^{-1}$ respectively). Equal volumes of β-Gal plasmid DNA (50 µl) and polymer or lipofectamine (50 µl) at a 60 to 1 and 2 to 1 mass ratios were used respectively. The polyplexes were prepared in 20 mM PBS pH=6.8 and were left incubating for 24 h at 4° C prior subcutaneous administration. Polyplexes for ternary complexes with hyaluronidase were prepared as descried in **section 5.2.2.1,** but in a total volume of 50. 50 µl of hyaluronidase at a concentration of 27,6 mg ml $^{-1}$ and a concentration of 13,8 mg ml $^{-1}$ were added to the high and 6,8 mg ml^{-1} to the low dose ternary complexes respectively (mass ratio of plasmid to hyaluronidase 1 to 84) followed by incubation at 4° C for another 24 h prior subcutaneous administration. Hyaluronidase was dissolved in 20mM NaCl, pH=12.

Nanocomplexes for intranasal dosing were prepared at a high (1.35 µg β-Gal) and a low (0.675 µg β-Gal DNA) dose in a total volume of 16 µl (84 µg ml $^{-1}$ and 42 µg ml $^{-1}$ respectively). Equal volumes of plasmid DNA (8 µl) and polymer or Lipofectamine (8 µl) at a 60 to 1 and 2 to 1 mass ratios were used respectively. The nanocomplexes were prepared in 20 mM PBS, pH=6.8 and were left incubating for 24 h at 4° C prior intranasal administration. Lipoplexes were prepared in OptiMeM and left incubating at RT for 2 h. Polyplexes for ternary complexes with hyaluronidase were prepared as descried in **section 5.2.2.1,** but in total volume of 8 µl. 8 µl of hyaluronidase at a concentration of 27,6 mg ml $^{-1}$ and 8 µl of hyaluronidase at a concentration of 13,8 mg ml $^{-1}$ were added to the high and 6,8 mg ml $^{-1}$ to the low dose ternary complexes respectively (mass ratio of plasmid to hyaluronidase 1 to 84), followed by incubation at 4°C for another 24 h prior intranasal administration. Hyaluronidase was dissolved in 20 NaCl, pH=12. For the intranasal study ternary polyplexes were prepared with luciferase DNA instead of β-Gal DNA.

6.2.2.3 Combined luciferase β-Gal assay

Luciferin-galactoside substrate (6-O-β-galactopyranosylluciferin) or LuGal is cleaved by β-Galactosidase (a product of the reporter plasmid) to form luciferin and galactose [314] . The enzyme is a tetrameric protein with a molecular weight of approximately 116 kDa. It hydrolyses the bonds between galactose and glucose in a lactose molecule. The LuGal assay utilizes the intrinsic hydrolytic activity of β-Galactosidase, which catalyses the hydrolytic cleavage of galactose from glucose in the combined 6-O-β-galactopyranosyl-luciferin substrate. This results in the liberation of luciferin, which is used by firefly luciferase in the presence of Mg^{2+} and adenosine triphosphate (ATP) and converted to oxyluciferin with the concomitant emission of light.

The commercial vial with the lyophilised LuGal substrate (E4720) was dissolved in 10ml of PBS, pH=7.4 supplemented with 100 g L^{-1} $MgCl_2$ x 6 H_20 (magnesium hexahydrate) instead of the provided lysis buffer in order to be used *in vivo*.

6.2.2.4 Intranasal dosing

BABL/c mice were anesthetised in an isoflurane chamber with 3 - 4% isoflurane connected to an oxygen pump for 3 - 4 minutes. Intranasal dosing was performed using a P20 pipette by placing a drop on the tip of the nose of each mouse. The mice were left in a separate cage to recover fully after the anaesthesia. The nanocomplexes were administered and imaging was performed 24 h and 48 h post administration 15 mins and 1 h after intranasal dosing with 16 µl of the LuGal substrate (15 mg ml^{-1}). The animals dosed with the ternary nanocomplexes received luciferin substrate rather than LuGal since luciferase DNA instead of β-Gal DNA was used for their preparation of the ternary nanocomplexes. The luciferin substrate was prepared in the same way as the LuGal substrate.

6.2.2.5 Subcutaneous dosing

Subcutaneous dosing was performed using a 25 g needle fitted to a 1 ml syringe. The nanocomplexes were administered in the scruff of BALB/c mice by piercing the loose skin with the needle. Imaging was performed 24 h and 48 h post administration 15 mins after subcutaneous dosing with 100 µl of the LuGal substrate (15 mg ml^{-1})

6.2.2.6 *In vivo* Imaging system (IVIS)

The IVIS (IVIS®-Spectrum systems Xeno-gen-Caliper Life Sciences, Hopkinton, MA) machine consists of a cabinet and a CCD camera. The cabinet is connected to an isoflurane source and a controller board which can regulate isoflurane flow from the source to the cabinet and/or the chamber where anaesthesia is induced. The controller board includes a connection to an oxygen pump, which provides a constant flow of oxygen. All anaesthetic procedures were performed with 3 – 4 % isoflurane in the chamber and a maintaining dose of 2 % isoflurane during the imaging process from the oxygen cones in the IVIS cabinet.

The cabinet is supplied with a heated stage for the anaesthetised animals during imaging. A CCD camera (2048 x 2048 pixels) is fitted in the cabinet and a stage with space for five mice, which can be imaged simultaneously. The system is connected to a computer with a Living Image® 3.0 software. An image sequence of four exposure times was generated (30 s, 60 s, 120 s and 240 s). Comparisons between images was performed for the same exposure time.

Analysis of the collected images was performed on the Living Image® software where the min and max signal for the images was adjusted to the same scale, so the signal is normalised for the different animals. This allows for a comparison to be made between different images. A region of interest (ROI) was drawn on the place of the signal and the average counts were measured.

For the main study a mouse injected with LuGal substrate was used as a control to set up the baseline for the analysis of the images with the different treatment groups (**Figure 9-8**, see Appendix)

6.2.2.7 Brain dissection and tissue homogenisation

Mice were sacrificed by a CO_2 overdose followed by decapitation. Isolated brains were dissected on ice and olfactory bulb, cerebellum and cortex were collected in pre-weighed cryotubes. The tubes were then placed in a container with liquid nitrogen and transferred to the freezer. For downstream analysis the tubes were defrosted and weighed again to determine the weight of the respective organ. For ~1 mg of tissue 20 µl of T-PER reagent was added, according to the manufacturer's recommendation. T-PER reagent was supplemented with an EDTA free Halt Protease Inhibitor Cocktail 100 X (1 ml in 100 ml of T-PER reagent); The samples were then sonicated at a very low amplitude (3.5) on ice for one cycle of 60 s for the olfactory bulbs and three cycles of 60 s for cerebellum and cortex. After preparing the tissue homogenates the tubes were centrifuged at 10,000 g for 5 mins and the supernatants were collected. 100 µl of the supernatants were pipetted onto a black 96-well plate and 100 µl of the LuGal substrate were added to each well. Luminescence was measured on a SpecraMax series M plate reader. The signal from a control animal was subtracted from all the samples. To normalise the data, the relative luminescent units (RLU) per well were divided by the weight of the samples and converted to RLU/mg of tissue.

6.2.2.8 Statistical analysis

All data sets were analysed using either One-way or Two-way ANOVA, multiple comparisons with the Bonferroni test on GrapPad Prism 7. Comparison between IC50 of GC37 and Lipofectamine was performed using an unpaired student t-test GrapPad Prism 7.

6.3 Results

6.3.1 IC 50 of GC37 and Lipofectamine

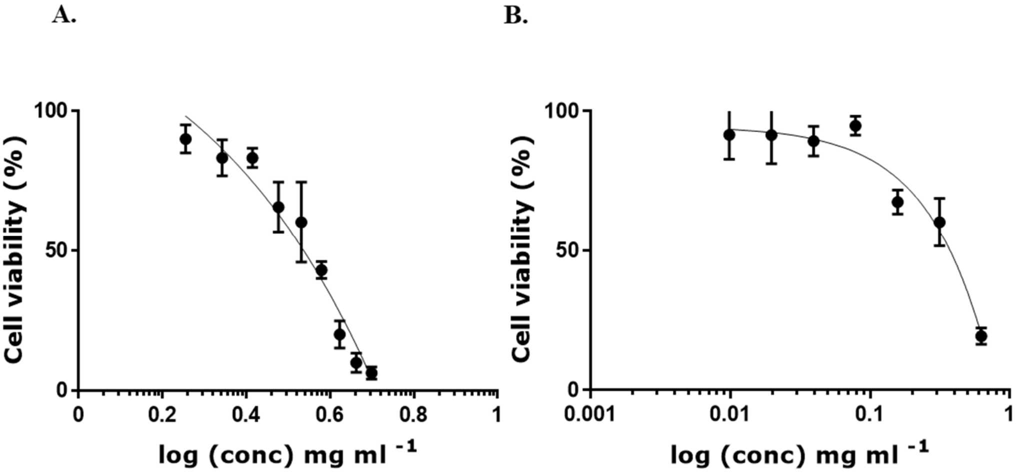

Figure 6-1: *Cytotoxicity of GC37 (**A**) and Lipofectamine (**B**) in U87 cells at different concentrations after 24 h. The results are representative of three independent experiments (n=3) Mean ± S.D.*

Table 6-1: *IC50 values for GC37 and Lipofectamine . GC37 is significantly less toxic than Lipofectamine (*p < 0.05).*

Treatment	IC 50 (mg ml $^{-1}$)
GC37*	3,41 ± 0,14
Lipofectamine	0,36 ± 0,02

Cytotoxicity experiments in U87 cells were performed prior to the *in vivo* administration of the nanocomplexes to determine the safe starting dose (**Figure 6.1 A** and **B**). GC37 as a polymer carrier was almost 10 times less toxic than the lipofectamine used as a control in all transfection experiments. Project licence guidelines advise on using not more than 1000 X the IC50 value of the carrier in weight per ml for a starting dose in weight per kg body weight [315]. In our case for GC37 polymer with an IC 50 of 3,41 mg ml $^{-1}$ the safe starting dose would be 68 mg, while the starting dose for Lipofectamine would be 7.2 mg per mouse with an average body weight of 20g. However, this requirement is limited by the solubility of the carrier. GC37 with an IC50 of 3.41 was administered at 0.5 mg for the high dose nanocomplexes and 0.25 mg for the low dose nanocomplexes respectively for the subcutaneous study and 0.081 mg and 0.040 mg for the intranasal one. Lipofectamine was administered at 16.6 µg and 8.3 µg for the high and low dose lipoplexes for the subcutaneous study respectively. The intranasal administration of Lipofectamine was performed at 0.0027 mg and 0.0013 mg. The dose was chosen based on the characterisation data for the nanocomplexes, since it was established that an increase in the amount of DNA used results in polyplex size increase.

6.3.2 Characterisation of low and high dose nanocomplexes

6.3.2.1 Size and zeta potential

The high and low dose polyplexes together with the ternary polyplexes incorporating hyaluronidase were characterised for their size and zeta potential prior to the *in vivo* experiments. It is well described in literature that scaling up the DNA dose of polyplexes for *in vivo* applications is limited by the increase in particle size [265,316–318]

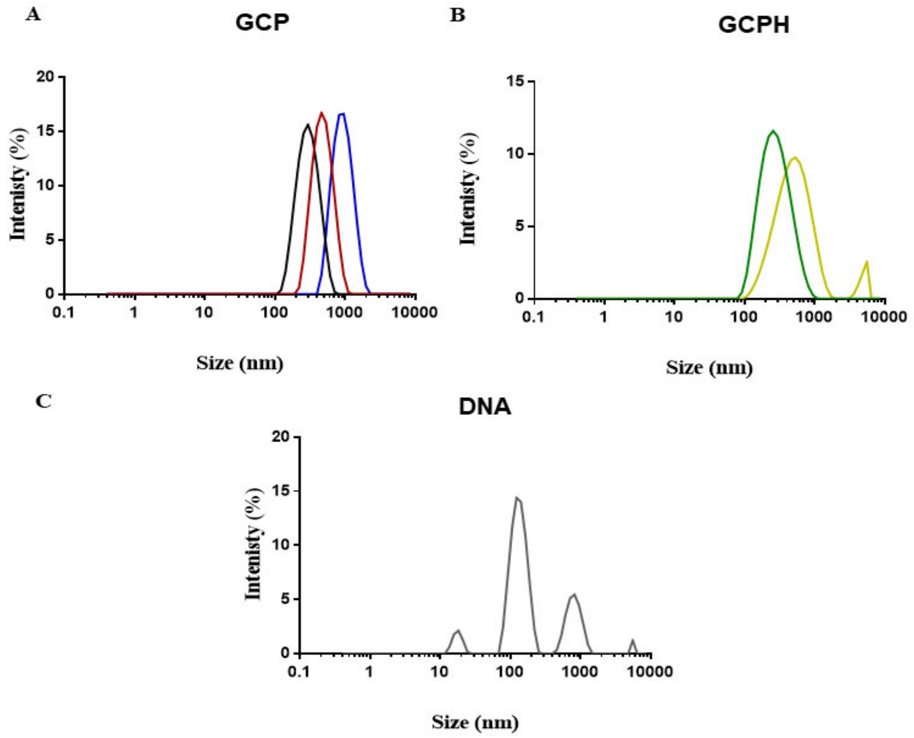

Figure 6-2: *Representative Intensity size plots of GCP, GCPH and naked β-Gal DNA . GC37/β-Gal nanocomplexes (GCP) with different amount of plasmid β-Gal DNA, 6 μg ml^{-1} – GCP1, 83 μg ml^{-1} – GCP2, 166 μg ml^{-1} – GCP3) (**A**) and ternary complexes with hyaluronidase containing 83 μg ml^{-1} and 41.5 μg ml^{-1} β-Gal DNA (GCPH2 and GCPH3) with 6.8 mg ml^{-1} and 3,4 mg ml^{-1} hyaluronidase respectively (**B**), naked β-Gal DNA (**C**).*

Table 6-2: *Size, PDI and zeta potential of GCP, GCPH and DNA . The data is representative of three independent measurements (Mean ± S.D), n = 3*

Polyplex	**Size (nm)**	**PDI**	**Zeta potential (mV)**
GCP1	863 ± 28	0.229 ± 0.033	+ 7 ± 3
GCP2	482 ± 36	0.113 ± 0.023	+ 9 ± 4
GCP3	308 ± 27	0.161 ± 0.021	+ 6 ± 3
GCPH 2	534 ± 71	0.464 ± 0.041	- 8 ± 4
GCPH 3	526 ± 14	0.578 ± 0.053	- 10 ± 2
DNA	140 ± 31 (65%) 950 ± 61 (23%) 20 ± 9 (7%)	0.589 ± 0.077	-26 ± 5

Our data is in parallel with these findings where **Figure 6-2 A** shows an increase of particle size with the increase in the concentration of plasmid DNA. The intensity size distribution graphs show monomodal size distribution with low PDI regardless of the amount of DNA used. No aggregation was present for any of the nanocomplexes. Similarly, the ternary polyplexes with the enzyme, GCPH2 and GCPH3 gave a single peak in the size distribution plots by intensity. The charge of the coated polyplexes GCPH2 (- 8mV) and GCPH3 (-10mV, **Table 6.1)** were also comparable with the charge of GCPH or the ternary complex prepared with 6 µg ml $^{-1}$ of β-Gal DNA for the *in vitro* studies (-12mV, **Figure 5.5 A**). DNA on its own showed a multimodal size distribution by intensity with three peaks with a high PDI and pronounced negative charge (- 26mV, **Figure 6-2 C** and **Table 6-2).**

The characterisation data for the scaled-up formulation showed that the hyaluronidase coating step of the polyplexes is reproducible regardless of the amount of DNA used.

6.3.3 *In vivo* administration of low and high dose nanocomplexes

To assess the suitability of the GC37 carrier to deliver the reporter plasmid locally and to compare its efficacy with naked DNA and Lipofectamine a subcutaneous route of administration was chosen. Additionally, to investigate effects occurring away from the injection site of the polyplexes and the ternary complexes an intranasal route of administration was also explored. **Table 6-3** shows the used dose kg-^{1} for both the intranasal and the subcutaneous study. The dose for the pilot and the main study were kept the same.

***Table 6-3**: Details of formulations used in vivo for SC and IN pilot and main study*

Administration route	**Dose β-Gal DNA (mg kg-^{1})**		**Number of animals**	
	High dose	Low dose	pilot	Main
Subcutaneous (SC)	0.415	0.207	1	4
Intranasal (IN)	0.0675	0.034	1	4

6.3.3.1 Subcutaneous pilot study

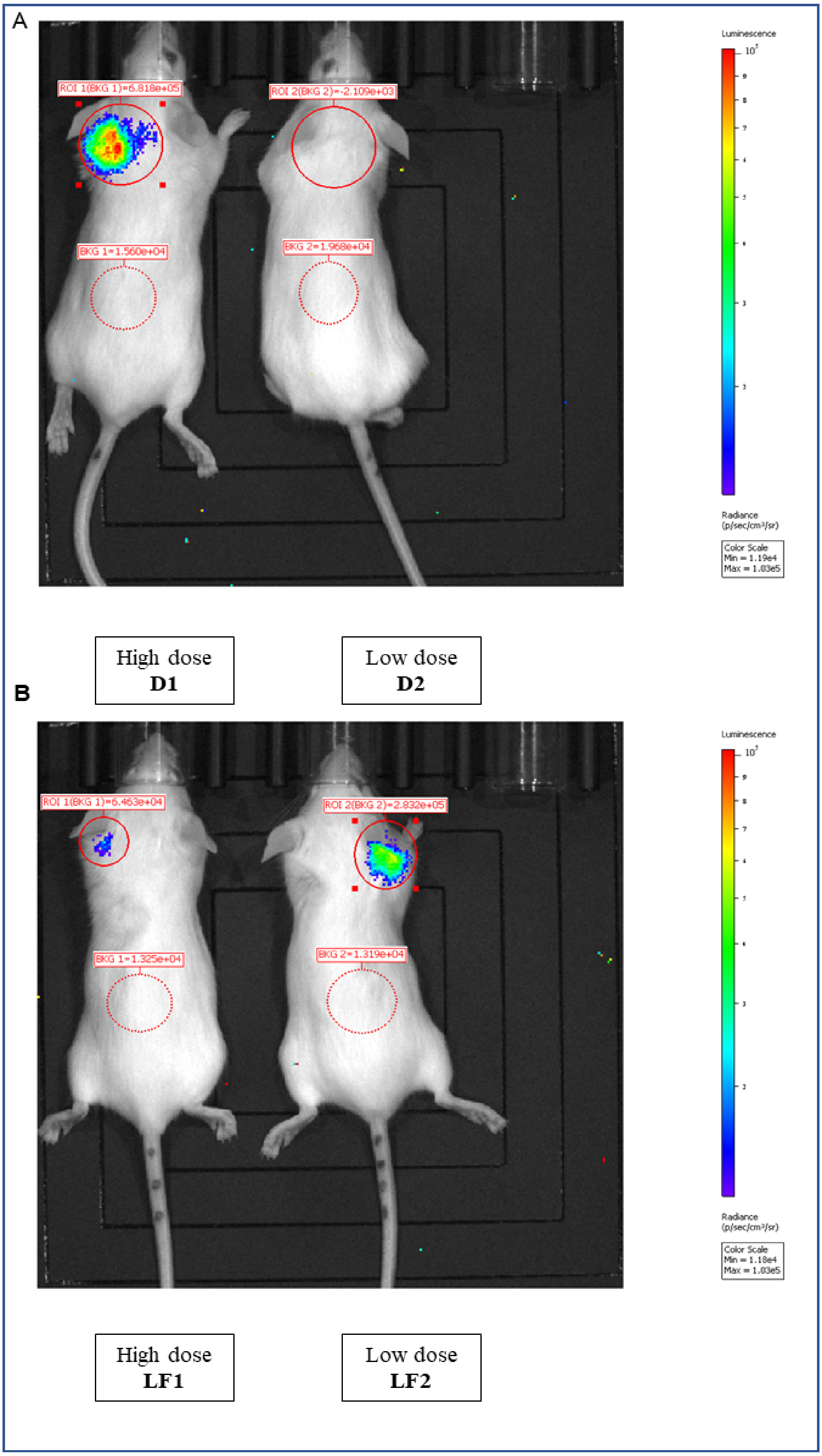

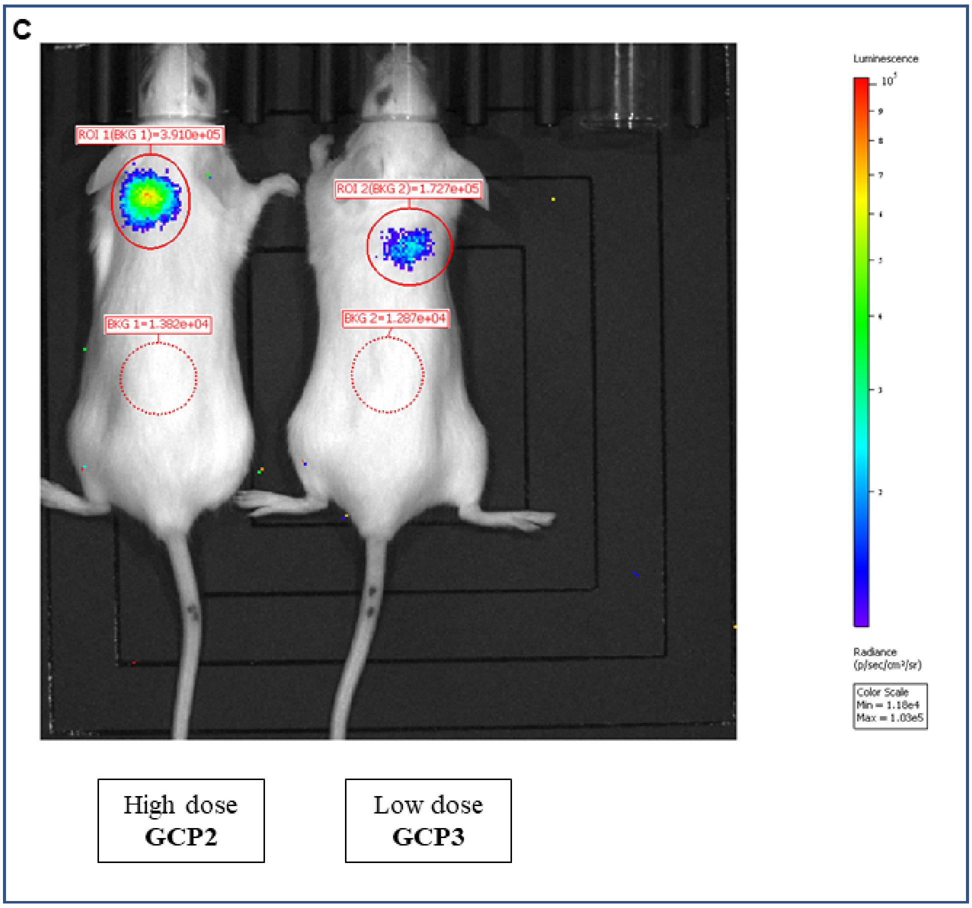

Figure 6-3: *IVIS images from pilot in vivo subcutaneous study with high and lose dose nanocomplexes. Naked β-Gal DNA high dose - D1 (0.415 mg kg^{-1}) and low dose D2 (0.207 mg kg^{-1}) (**A**), Lipofectamine lipoplex with high dose β-Gal DNA - LF1 (0.415 mg kg^{-1}) and Lipofectamine lipoplex with low dose β-Gal DNA - LF2 (0.207 mg kg^{-1})(**B**) and GC37 polyplex with high dose β-Gal DNA - GCP2 (0.415 mg kg^{-1}) and GC37 polyplex with low dose β-Gal DNA - GCP3 (0.207 mg kg^{-1}) (**C**). Imaging was taken 48 h post subcutaneous administration of the treatments and 15 mins after subcutaneous administration of the LuGal substrate for a 240 s exposure time.*

The pilot study included one animal per treatment low and high dose: naked β-Gal DNA - D1 and D2, polyplexes GCP2 and GCP3, lipoplexes LF1 and LF2 and ternary complexes GCPH2 and GCPH3. The study identified cross reactivity with the combined LuGal substrate and hyaluronidase, which was later confirmed in an *in vitro* assay (data not shown).

At an earlier time point or 24 h after subcutaneous administration of the treatment and 15 minutes post subcutaneous injection of the LuGal substrate no signal was detected in any of animals. This led to a second round of substrate administration 48 h post treatment with the nanocomplexes (**Figure 6-3 A**, **B** and **C**). Low dose nanocomplexes appeared more effective than high dose nanocomplexes with GCP3 and LF2 having almost the same radiance (1.727×10^5 and 2.832×10^5 p/sec/cm^2/sr respectively, **Figure 6-3 B** and **C**). Additionally, D2 appeared completely ineffective to deliver the β-Gal gene upon subcutaneous administration, although surprisingly high dose naked plasmid showed the highest signal among all the treatments in the pilot. Interestingly, high dose GCP2 polyplexes showed almost no signal, unlike high dose lipoplexes LF1, which doubled the amount of emitted light with twice as much DNA when compared to the low dose lipoplexes. Particle size have been proven to affect the uptake and cellular trafficking of both lipo - and polyplexes [319,320], The current study does not focus on investigating the physical characteristics of lipofectamine and their effect on transfection potential and so it is unclear if the increased amount of DNA in the lipoplex resulted in a larger particle size. Interestingly, unlike the existing proven relationship for polyplex size, which increases with an increase in DNA concentration, lipoplex size increase seem to be reported only when more lipid is used for the preparation of the lipoplexes [321,322] rather than higher DNA concentrations. We can then speculate that the retained efficacy of the high dose lipoplexes when compared to the high dose polyplexes is due to particle size remaining unchanged. Further experiments are needed in order to confirm that.

6.3.3.2 Subcutaneous main study

Since the identified cross-reactivity with the LuGal substrate and hyaluronidase, luciferase DNA (luc DNA) was used for the preparation of the ternary complexes instead of β-Gal DNA. There was no signal detected for the animals treated with the nanocomplexes prepared with luc DNA (GCP3 luc and GCPH3 luc) (**Figure 6-4 A**). One potential explanation could be that the main study used a commercial β-Gal plasmid for GCP3, D2, LF2 and an "in house" prepared luc DNA. It is clear that the maximum signal for the pilot study (LF2) is much lower in magnitude compared to (LF2) in the main study (**Figure 6-3 B** and **Figure 6-4 A**).

The analysis of the results showed there's no difference between D2 (naked DNA) and GCP3 as well as D2 and LF2 (**Figure 6-4 B**). These findings are not unusual since naked DNA is used for subcutaneous delivery to stimulate immune response and wound healing [323–326]. Local administration of DNA directly to the organ or the tumour has been proven successful, however low therapeutic efficacy has been reported compared to formulated DNA due to the relatively fast degradation kinetics of the naked plasmids [327].

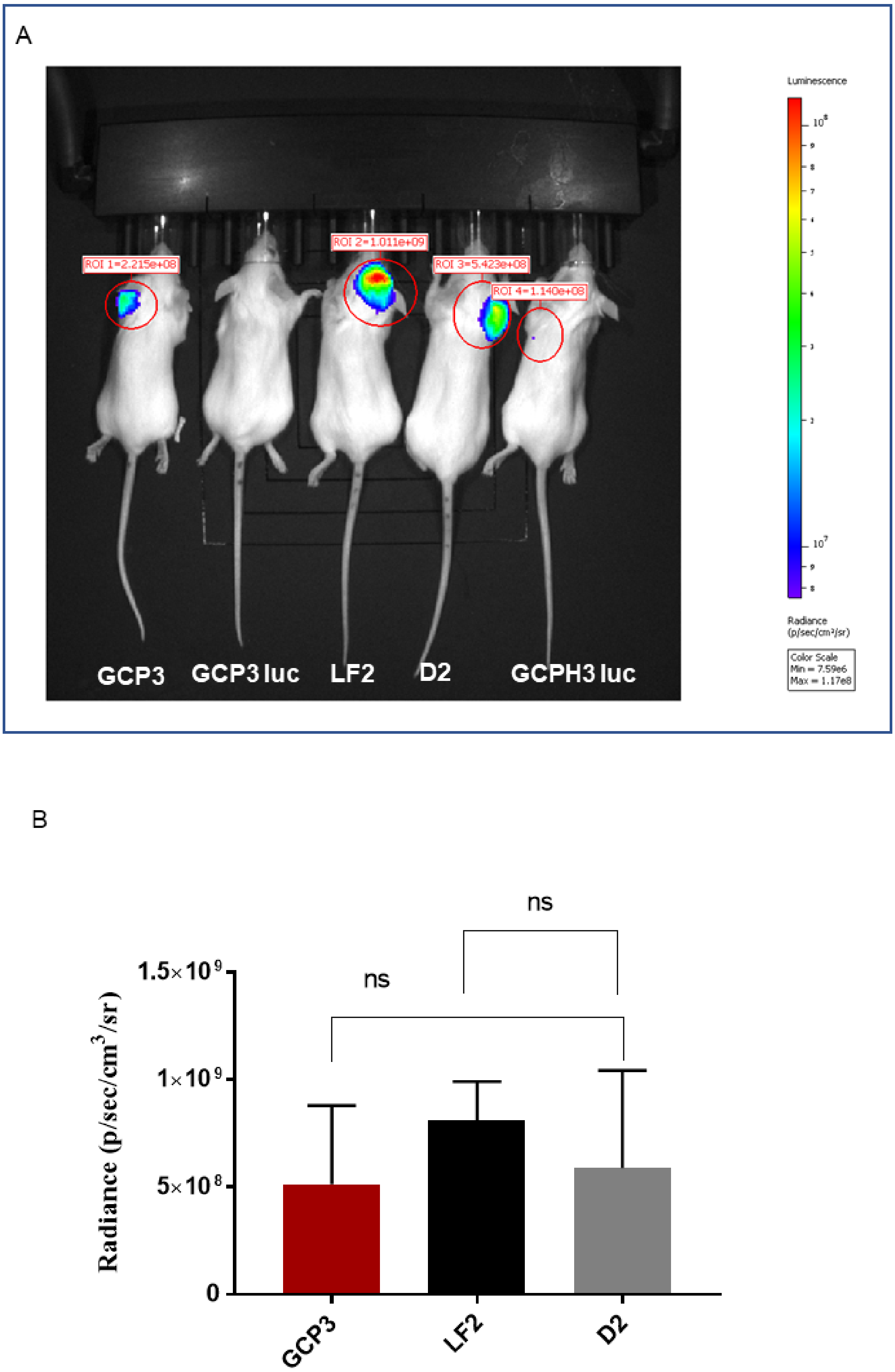

Figure 6-4: *Representative IVIS image of animals treated with low dose nanocomplexes after subcutaneous administration (dose of plasmid 0.207 mg kg $^{-1}$): GCP3 (GC37 polyplex with β-Gal DNA), GCP3 luc (GC37 polyplex with luc-DNA), LF2 (Lipofectamine lipoplex with β-Gal DNA), D2 (naked β-Gal) and GCPH3 luc (GC37 polyplex with luc-DNA coated with hyaluronidase). Images were analysed 48 h post administration of the treatments, 15 mins after LuGal and luciferin*

*administration at 60 s exposure time (**A**) No significant difference for GCP3 and LF2 when compared to naked DNA (D2) (**B**). The results represent Mean ± SD for four animals per treatment (n=4)..No signal was detected for nanocomplexes prepared with luciferase DNA (GCP3 luc and GCPH3 luc, A).*

6.3.3.3 Intranasal pilot study

To investigate if the GC-based polyplexes can deliver the reporter plasmids to the brain and to test if non-formulated DNA shows transfection potential away from the administration site intranasal delivery of the nanocomplexes was also explored. By contrast to the 48 h time point for the subcutaneous pilot study, the intranasal pilot identified 24 h as optimum for analysis. Images were taken 15 minutes and 1 h after intranasal delivery of the LuGal substrate. The 15 minutes time point resulted in an enhanced signal in the nasal cavity (data not shown). The later time point allowed more time for the substrate to reach to brain structures, hence it was the chosen time point for the interpretation of the results after nasal administration of the nanocomplexes. (**Figure 6-5**).

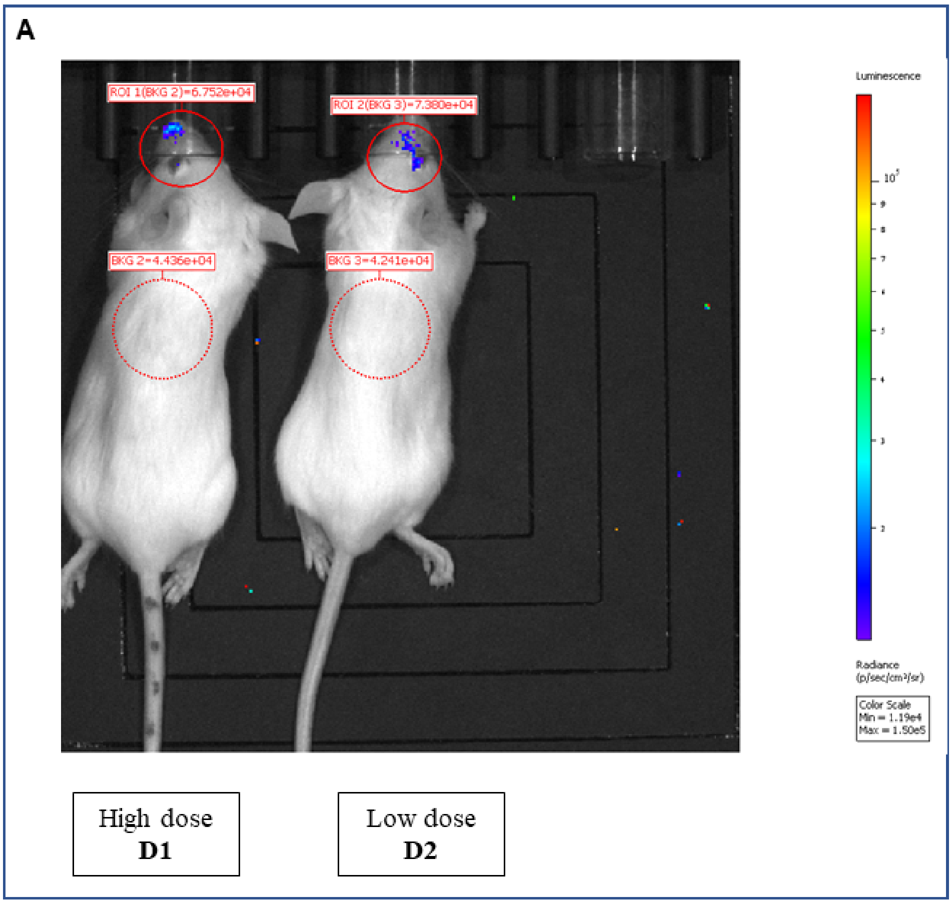

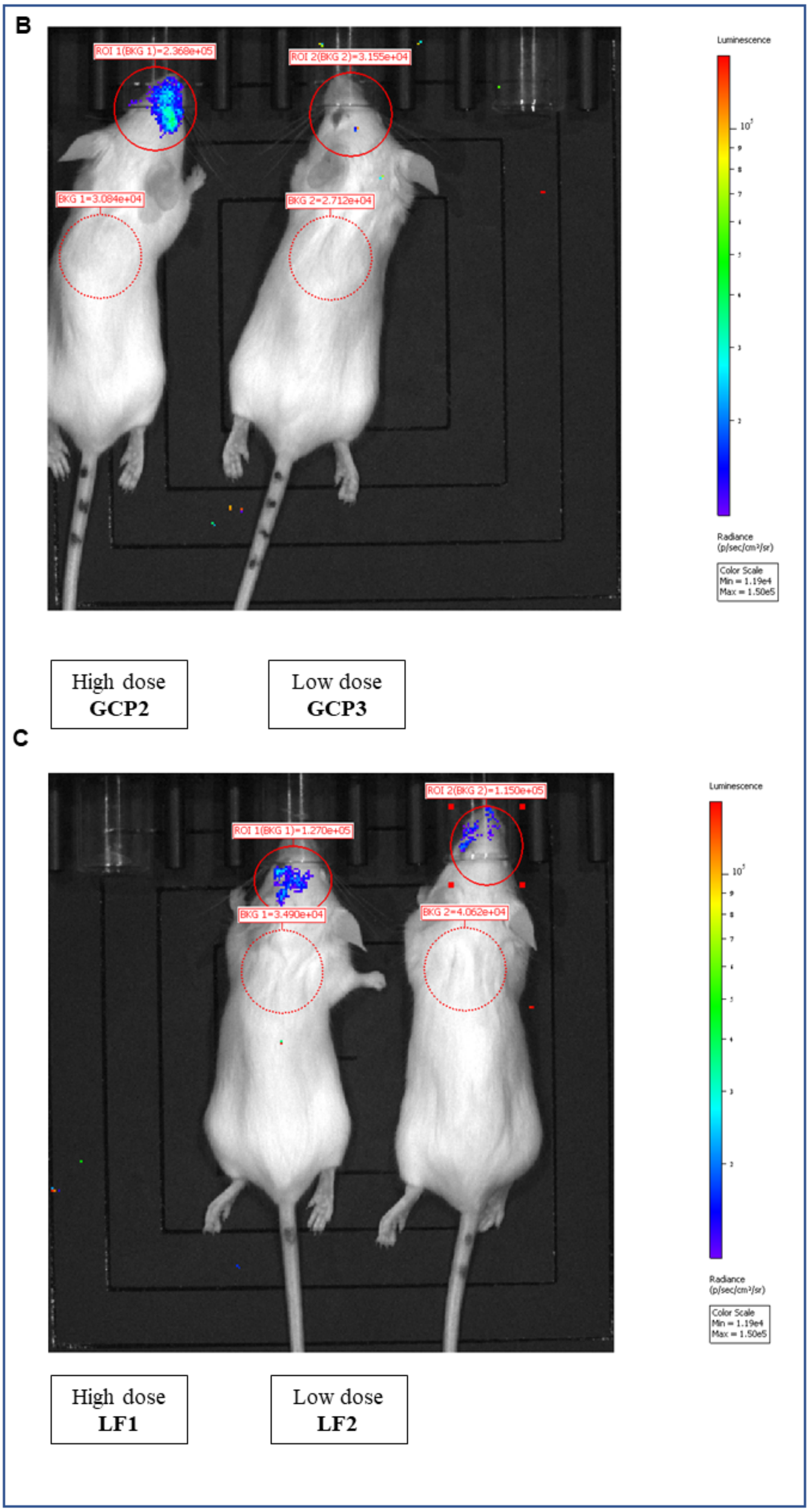
B
ROI 1(BKG 1)=2.368e+05
ROI 2(BKG 2)=3.155e+04
BKG 1=3.084e+04
BKG 2=2.712e+04
Luminescence
10^5
Radiance (p/sec/cm²/sr)
Color Scale
Min = 1.19e4
Max = 1.50e5
High dose
GCP2
Low dose
GCP3
C
ROI 1(BKG 1)=1.270e+05
ROI 2(BKG 2)=1.150e+05
BKG 1=3.490e+04
BKG 2=4.062e+04
Luminescence
10^5
Radiance (p/sec/cm²/sr)
Color Scale
Min = 1.19e4
Max = 1.50e5
High dose
LF1
Low dose
LF2

Figure 6-5: IVIS images from pilot *in vivo* intranasal study with high and low dose nanocomplexes . Naked β-Gal DNA high dose - D1 (0.0675 mg kg^{-1}) and low dose D2 (0.034 mg kg^{-1}) (**A**) ,GC37 polyplex with high dose β-Gal DNA - GCP2 (0.0675 mg kg^{-1}) and GC37 polyplex with low dose β-Gal DNA - GCP3 (0.034 mg kg^{-1}), (**B**) and Lipofectamine lipoplex with high dose β-Gal DNA - LF1 (0.0675 mg kg^{-1}) and Lipofectamine lipoplex with low dose β-Gal DNA - LF2 (0.034 mg kg^{-1}), (**C**). Imaging was taken 24 h post subcutaneous administration of the treatments and 15 mins after subcutaneous administration of the LuGal substrate for a 240 s exposure time.

By contrast to the subcutaneous study the high dose polyplex in the intranasal pilot GCP3 appeared more effective at delivery β-Gal DNA than the low dose GCP2 since no signal was detected for the mice treated with GCP2 and the measured radiance was identical to the background signal (**Figure 6.5 B**). Both low and high dose naked DNA (D1 and D2) showed weak signal in the nasal cavity (**Figure 6.5 A**). Interestingly, expression of the β-Gal enzyme for LF1 treatment and not for LF2 appeared with a different location than the nasal cavity, but with comparable intensity to the polyplexes (**Figure 6-5 C**).

Since IVIS does not allow us to correlate protein expression with specific olfactory bulb/ brain regions, downstream analysis was performed after brain dissection. Protein expression and activity of β-Gal was quantified in tissue homogenates prepared from olfactory bulbs, cortex and cerebellum of mice treated with the high dose nanocomplexes (**Figure 9-9**, see Appendix). Protein expression from GCP2 nanoparticles occurred in the olfactory bulbs (7381.91 RLU/mg of tissue), **Figure 9-9 A,** see Appendix. Interestingly, protein expression from LF1 lipoplexes were almost undetectable in the olfactory bulbs after 24h (0.23 RLU/mg of protein, but protein expression was found in the cortex of the treated animal (228 RLU/mg of tissue, **Figure 9-9 B,** see Appendix). This data is in accordance with the images taken with IVIS (**Figure 6-5**) A very weak luminescent signal was identified after the administration of naked β-Gal DNA in the olfactory bulbs and the cortex (0.16 and 0.18 RLU/mg of tissue respectively, which correlates with the IVIS data (**Figure 6-5 A**).

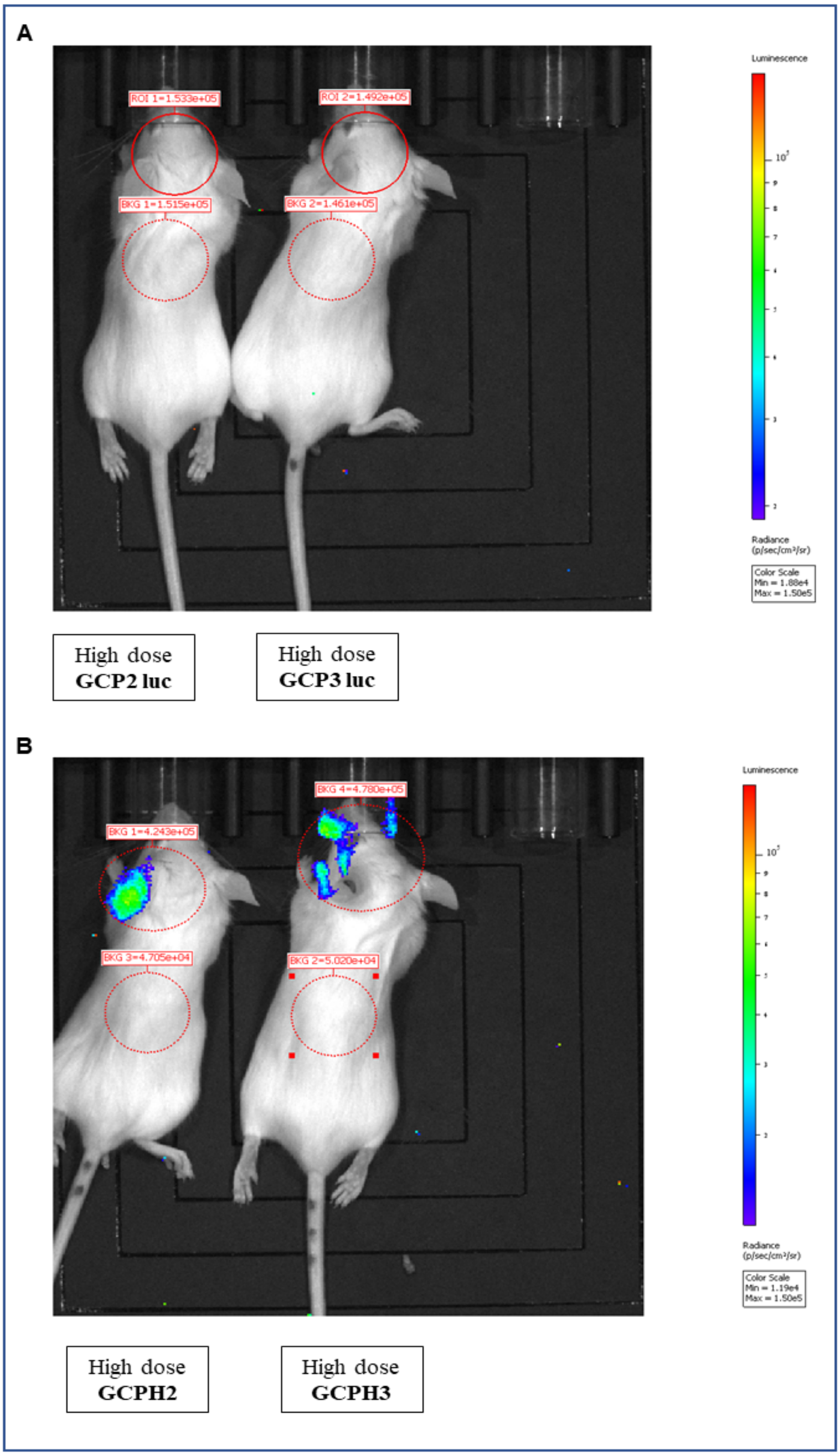

Figure 6-6*: IVIS images from pilot in vivo intranasal study of high (GCPH2) and low dose (GCPH3) ternary complexes with hyaluronidase. Luc-DNA (0.0675 mg kg $^{-1}$ and 0.034 mg kg $^{-1}$), GC37 polyplex, high dose and low dose - GCP2 luc and GCP3 luc (****A****), GC37 polyplexes, high and low dose coated with hyaluronidase - GCPH2 luc and GCPH3 luc (****B****). Images were taken 24 h post intranasal administration of the treatments and 1 h after intranasal administration of luciferin.*

In vivo transfection was detected for the ternary complexes GCPH2 luc and GCPH3 luc but not for the polyplexes GCP2 luc and GCP3 luc (**Figure 6-6 A** and **B)**. Signal localization from mice treated with the low dose GCPH3 luc ternary complex appeared at various locations (**Figure 6-6 B**). Unfortunately, downstream analysis did not show active β-Gal enzyme for any of the brain regions.

6.3.3.4 Intranasal main study

The main intranasal study with four animals per group showed background levels of luminescence except for four animals which had higher levels of β-Gal enzyme after either D1 or GCP2 treatment in the olfactory bulbs and the cortex (**Figure 6-7 A** and **B**). Additionally, one of the treated animals also showed some active β-Gal enzyme in the cerebellum (**Figure 6-7**, **C**). Unfortunately, the main study did not yield any conclusive results. A repeat of the experiment with higher dose may be considered, since the dose might be the reason for the observed inconstancies, although a higher DNA dose might result in an increase in particles size as discussed previously. During the design of the *in vivo* experiments our goal was to keep the concentration of the polyplexes the same for the *in vivo* administration (83 μg ml $^{-1}$ and 41.5 μg ml $^{-1}$). This is because the generated characterisation data at these concentrations showed a trend for a size increase with the increase of the concentration of the plasmid (**Figure 6-2 A**).

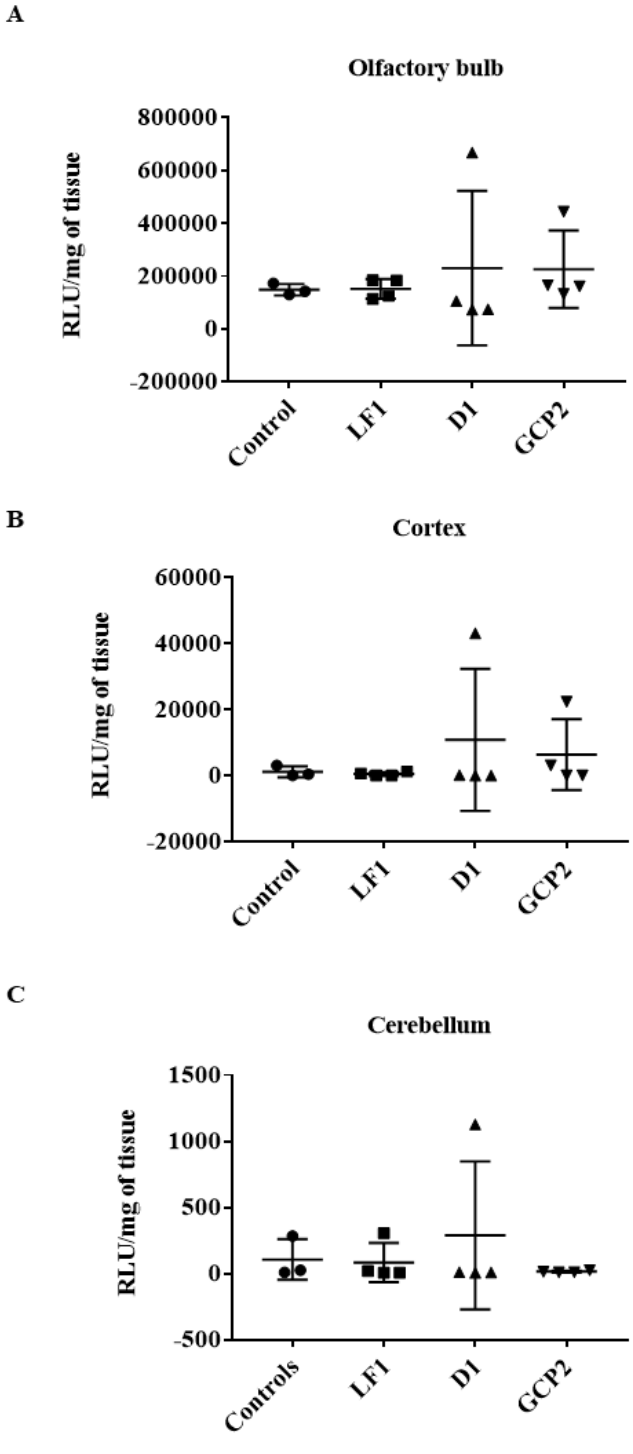

Figure 6-7: *β-Gal activity assay of tissue homogenates from olfactory bulbs, cortex and cerebellum after intranasal administration of high dose nanocomplexes in mice (0.067 mg kg $^{-1}$ β-Gal). LF1, Lipofectamine lipoplex, GCP 2 (GC37 polyplex) and D1 (naked β-Gal DNA). The control group of animals was dosed with the LuGal substrate.*

6.4 **Discussion**

As a naturally derived polymer chitosan is often considered biocompatible by default. Indeed, it is biodegradable *in vivo* by endogenous enzymes in the body such as chitosanase and lysozyme to N-acetylglucosamine. The latter being a building block of biomacromolecules such as glycoproteins, proteoglycans, glycosaminoglycans (GAGs) and other components of the connective tissues[328]. However, biocompatibility has to be considered in rμμμelation to the structural parameters of the polymer, dosage form, the route of administration and the intended use [329].

A positive relationship exists between elevated levels of cytotoxicity and increased charge density along with decreased degree of deacetylation for chitosan carriers [330]. Chitosan carriers in solution and chitosan-based nanoparticles are known to have different behaviour due to their different conformation, so speculations for the difference in cytotoxicity also exist, however literature data proves the opposite. Unformulated chitosan in solution and chitosan nanoparticles are reported to possess similar cytotoxicity [330,331]. Furthermore chitosan coating of alginate microspheres has been reported to be non-toxic to Caco-2 cells in contrast to chitosan solutions, which showed a dose-dependent cytotoxicity [332]. The present study investigated the effect of GC37 and Lipofectamine as carriers rather than formulations on the toxicity in U87 cells.

To conduct the *in vivo* experiments, we needed to determine a safe starting dose, which is based on the cytotoxicity profile of the carriers and their IC50 values. IC50 values for GC37 and Lipofectamine were determined in U87 cells. GC37 showed significantly less toxic than Lipofectamine (IC 50 3.41mg ml $^{-1}$ and 0.36mg ml $^{-1}$ respectively, **Figure 6-1 A** and **B and Table 6-1**) Although it is proven that cytotoxicity is cell type dependent [333] experiments in one cell line can give a rough estimation of the cytotoxicity profile of the carriers. The starting dose was fixed, based on guidelines outlined in the Home office project licence, the solubility of the carriers and the particle size of the resulting polyplexes.

Size measurements showed an increase of particle size with an increase in the amount of DNA used, an observation which has also been reported by others [265,316–318]. Polyplexes with three different amounts of β-Gal DNA were prepared (GCP1, GCP2 and GCP3 with 166 µg ml $^{-1}$, 83 µg ml $^{-1}$ and 41,5 µg ml $^{-1}$ with a resulting size of the nanocomplexes of 863 ± 28, 482 ± 36 and 308 ± 27 respectively in comparison to GCP with 119 ± 25 and 6 µg ml $^{-1}$, the latter being used in all *in vitro* testing, (**Figure**

6-2 A and Table 6-2). GCP2 and GCP3 showed a monodisperse population of particles as determined by DLS with PDI values of < 0.2 (**Table 6-2 D**). By contrast unformulated β-Gal DNA was presented with high PDI (> 0.5) and three distinct peaks as visible from the intensity size plot (**Figure 6-2 C** and **Table 6-2**). The low GCPH2 and high GCPH3 dose ternary complexes showed almost identical in size (532 ± 71 and 526 ± 14) with high PDI ≥ 0.5 (**Figure 6-2 B and Table 6-2**). A slight positive charge was measured for all nanocomplexes ranging from +4 mV to +9 mV except for GCPH2 and GCPH3 which were negatively charged (**Table 6-2**)

Particle size is an important parameter to be considered for the delivery of nanocomplexes where the target location and the route of administration define the size requirements. Delivery to the lymph nodes to target the high number of residing dendritic cells (DC) have been reported to be more effective with particles < 100nm after a subcutaneous injection [334]. Similarly the subcutaneous injection of PEGylated liposomes resulted in an increased amount of particles of < 100 nm in the lymph nodes than after an intravenous or intraperitoneal injections [335]. Particles of up to 200 nm have been reported to reach the nasal mucosa, while larger ones (more than 500 nm) are likely to be phagocytosed by the respiratory macrophages [336]. Additionally if tumour targeting is considered, generally a 200 nm particle size cut-off has been identified as optimum to allow extravasation from the leaky tumour vasculature and to benefit from the enhanced permeation and retention effect (EPR) for delivery to the solid tumour upon systemic application [154].

Due to the large size of GCP1 nanocomplexes we chose to test the *in vivo* transfection potential of GCP2 and GCP3 nanocomplexes using a subcutaneous and an intranasal route of administration. The pilot subcutaneous study identified low dose GCP3 nanocomplexes as the best delivery platform with luminescent signal levels similar to LF2 lipoplexes (**Figure 6-3 B and C)**. Additionally, cytotoxicity testing identified GC37 as significantly less toxic than Lipofectamine in U87 cells (**Figure 6-1** and **Table 6.1**). Surprisingly, low dose naked β-Gal DNA showed background levels of luminescence in the pilot study but appeared with comparable signal intensity to GCP3 in the main subcutaneous study (n=4), **Figure 6-4 A and B**. Statistical analysis identified no significant differences between the mice treated with unformulated plasmid and both GCP3 and LF2 (**Figure 6-4 B**). Triggering an immune response by naked DNA using the classical routes of vaccine administration: subcutaneous, intradermal and intramuscular is proven to be effective and well known as the DNA vaccination approach [323–326]. In fact the Journal of Gene Medicine reports on 17.7%

of the 2000 clinical trials approved up to 2014 to be with naked DNA as the test material [83]. However it is worth mentioning that passive transport through the nuclear pores would be only possible with nucleic acids of less than 300 bp [337], so the need for condensation by non-viral vectors or the presence of a nuclear import sequence are crucial for the delivery of larger DNA molecules.

By contrast the intranasal pilot identified the larger nanoparticles or the high dose polyplexes GCP2 as superior to the low dose ones GCP3 (**Figure 6-5 B**). A dose independent response was visible for naked β-Gal DNA, where both D1 and D2 showed a weak signal in the area of the nasal cavity 24 h post treatment and 1 h after administration of the substrate (**Figure 6-5 A**). LF1 and not LF2 showed the presence of active enzyme further away from the administration site (**Figure 6-5 C**). The downstream analysis of tissue homogenates from olfactory bulb, cortex and cerebellum of animals treated with the high dose nanocomplexes showed a trend similar to the IVIS data. GCP2 delivered the reporter plasmid to the olfactory bulb/brain of the mice (7382 RLU/mg of tissue) (**Figure 9-9 A**, see Appendix), while LF1 lipoplexes resulted in protein expression in the cortex (228 RLU/mg of tissue), **Figure 9-9 B**, see Appendix. Samples from animals dosed with naked DNA showed a weak luminescent signal in the olfactory bulbs and the cortex (0.16 and 0.18 RLU/mg of tissue respectively) **Figure 9-9 A** and **B,** see Appendix**.** The main intranasal study with four animals per treatment did not result in any conclusive findings. Olfactory bulb and cortex homogenates of four animals treated with D1 or GCP2 nanocomplexes prepared on different days showed higher than baseline levels of active β-Gal enzyme (**Figure 6-7 A** and **B**). Only one animal showed low levels of luminescence in the cerebellum after treatment with naked β-Gal DNA. An experiment with a dose increase of the plasmid, may provide us with more consistent results since dose precision is difficult for nasal administration due to mucocilliary clearance and the administered dose appeared insufficient to show reproducible results [338]. Additionally, a parallel experiment to the enzyme activity assay using X-Gal as a substrate of β-Gal in brain sections may give us a precise indication of the brain regions where protein expression occurs.

Ramos et al. report on the intranasal delivery of Mn^{2+} incorporating chitosan nanoparticles (MNPs) carrying a dsDNA coding for red fluorescent protein (RFP). MNPs of 122 nm size were shown to deliver the reporter plasmid to olfactory bulbs, striatum, hippocampus and cortex with the highest protein expression measured to be in the striatum [339].

GCPH3 luc and GCP3 luc did not show any *in vivo* transfection in the main subcutaneous study. There could be several reasons for that, which need to be addressed with more experiments. In the main subcutaneous study, animals dosed with the commercial β-Gal plasmid were simultaneously imaged with animals dosed with the "in house" prepared luc DNA plasmid. The analysis of the pictures included background luminescence elimination (caused by unspecific conversion of the substrate) by adjusting the minimum radiance of the images of the treated animals. It is possible this resulted in "masking" the weaker luminescent signal from the "in house" prepared plasmid when compared to the commercial one. A weaker luminescent signal was visible from the images of the pilot subcutaneous study with the "in house" prepared β-Gal (max radiance 1.5 x 10^{5} p/sec/cm^3/sr) when compared to the main one with the commercial β-Gal DNA (max radiance 1.17 x 10^8 p/sec/cm3/sr, **Figure 6-3** and **Figure 6-4 A)**. When animals treated with nanocomplexes prepared with luc DNA were imaged separately in the intranasal pilot study, the low dose ternary complexes GCPH3 luc showed some promise as protein expression appeared to be detected in different areas of the brain. However downstream analysis of the brain regions did not show the presence of active β-Gal enzyme in olfactory bulbs, cortex and cerebellum.

6.5 **Conclusions**

In conclusion we have successfully developed a potent gene delivery nanosystem with a GC37 polymer, which is significantly less toxic than Lipofectamine (IC 50 of GC37-3.41mg ml^{-1}, IC50 of Lipofectamine – 0.36 mg ml^{-1}, *$p < 0.05$) and has comparable *in vivo* transfection efficiency. The full potential of the GC-based gene delivery platform is yet to be discovered. Nevertheless, the work described here proves that GC37 is an attractive candidate for polymer-mediated gene therapy. Our findings raised more research questions and showed the need for fine tuning the parameters governing transfection efficiency, which would reveal the full potential of GC37 as a gene delivery vector.

7 Limitations and future work

This work describes the synthesis and characterization of two classes of biocompatible potential gene delivery platforms with GC or PEG backbones functionalized with amine containing moieties. Additionally, it sheds light on important parameters for both *in vitro* and *in vivo* transfection efficiency. It also describes a novel approach to tackle the increased solid stress pressure of tumor by designing a three-component system incorporating a nucleic acid, a polymer and an enzyme. However, due to the complexity of polymer-mediated gene transfer and the ambitious objectives of the project there are a number of research questions which remain to be addressed. Certain limitations of the current work did not allow us to reveal the full potential of our glycol chitosan-based gene carriers, but undoubtedly pointed out the promise they hold.

Polymer–mediated gene transfer with pDNA includes three main events: entry of the polyplex, endosomal escape and nuclear import. While the present work focused on the correlation of a polymer/polyplex characteristic with transfection efficiency, a set of different experiments are needed in order to decipher how these characteristics affect the individual stages. This is crucial for the tailored design of polymer vectors. To gain an insight into the intracellular trafficking of the polyplexes fluorescence colocalization microscopy studies [340] could be used along with subcellular localization studies. Moreover, subcellular fractionation in combination with quantitative PCR can be used to estimate the number of copies of plasmid delivered to the nucleus [341]. Additionally, high resolution TEM can provide information on the unfolding and dissociation of the carrier from the payload [342,343]. To better understand the dynamics of polyplex formation between different Mw GCs as a potential explanation for the observed differences in their transfection efficiency a set of isothermal titration calorimetry (ITC) experiments could be considered.

As mentioned previously our work describes also a strategy for the successful assembly of an electrostatic complex between EA13GC37/β-Gal, GC37/β-Gal and hyaluronidase to form EPH and GCPH ternary complexes. It also provides information on the actual quantity of bound hydrolytic enzyme to GCP and EP polyplexes. A major limitation presented in this work is the fact that the ternary complexes were only tested for their transfection potential in 2 D cell cultures, while spheroids with extracellular matrix components would be far more suitable testbeds.

Due to the low toxicity and comparable to lipofectamine transfection efficiency GC37 polyplexes were also used in *in vivo* studies exploring two different administration routes: a subcutaneous and an intranasal one. The main subcutaneous study with four animals per group did not show significant differences between Lipofectamine/β-Gal DNA (LF2), GC37/β-Gal (GCP3) and naked β-Gal (D2) all at the same dose (0.207 mg kg^{-1} β-Gal DNA) with respect to reporter gene delivery as measured by IVIS, 48 h post treatment. Local administration of naked DNA is proven effective and used in DNA vaccination techniques. To test the potential of the nanocomplexes to deliver the reporter gene to the brain and to compare their efficiency to that of naked plasmid and Lipofectamine, an intranasal route of administration was also used. The main intranasal study with four animals per group (0.067 mg kg^{-1}) with Lipofectamine/ β-Gal (LF1), GC37/β-Gal (GCP2) and naked β-Gal DNA (D1) showed baseline levels of bioluminescence after downstream analysis of olfactory bulbs, cortex and cerebellum 24 h post treatment. Surprisingly lipoplexes did not result in any active β-Gal enzyme, while D1 and GCP2 both showed higher than baseline levels of active β-Gal enzyme in the olfactory bulbs and cortex in four different animals. The experiment raised questions regarding the suitability of the enzyme assay for this application. An immunohistochemistry experiment with brain sections and X-Gal substrate, which results in dark blue staining in the areas of β-Gal expression could prove more robust as a technique for identifying brain regions to which the plasmid was delivered. Additionally an antibody against β-Gal could be used as a double staining analysis approach, which is a powerful tool for detection of transgene expression [344].

Luciferin is most commonly used with an intraperitoneal injection, however a study using different administration routes of luciferin such as intravenous, intraperitoneal showed the highest bioluminescent levels in the nasal cavity and the lungs after intranasal administration [345]. The study, however, does not give any information about luminescence in the brain after intranasal administration. Since luciferin is known to cross the BBB either by simple diffusion or with the help of transporters [346] it would have been interesting to do a parallel experiment with an intravenous injection and compare it to intranasal administration. Intranasal administration has a few limitations such as difficulties with dose precision due to mucocilliary clearance and different anatomy of individual nasal cavities [338]. This information would be useful when coupled to an experiment with a dose increase since variability during nasal administration could have completely undermined the effect of the nasally administered nanocomplexes. Another limitation of the present work is related to the lack of experiments investigating glycol chitosan's immunogenicity. The literature data is confusing when it comes to chitosan's immune stimulatory activity. Certainly, the physicochemical characteristics: such as degree of deacetylation, molecular weight, purity and viscosity are the ones that play a role, therefore full characterization of the polymers is necessary. However, while some authors suggest that low molecular weight chitosan (10kDa) is more immunogenic [347], other demonstrate the greater efficacy of higher molecular weight chitosan (300 kDa) as an immunostimulant [348]. Moreover, the lack of information on the content of endotoxin, heavy metals, nucleic acids could have an additional influence on the immune response triggered by chitosan.

Finally, if the reporter gene in vivo studies showed promise therapeutic experiments may be considered with both siRNA and pDNA. An immunotherapy approach may be used for the delivery of a plasmid coding for IL-12. IL-12 is a cytokine which acts as a molecular link between adaptive and innate immunity along with a stimulating capability on the synthesis of IFN – γ (Interferon γ), which is a cytokine controlling natural anticancer defence mechanisms [349]. On the other hand siRNA silencing experiments targeting survivin (an anti-apoptotic protein overexpressed in glioblastomas [350]) may be also employed. Survivin is present in around 83% of primary glioblastomas and around 46% in secondary glioblastomas [351]. Survivin siRNA treatment via intracranial injection in rat orthotopic tumour models has shown the inhibition of glioma growth in vivo [352]. Alternatively, the use of siRNA against the ubiquitin ligase ITCH may be also considered. ITCH controls p73 (a member of the p53 transcription factors) levels by ubiquitination and subsequent targeting to the proteasome for degradation. It has been already demonstrated that co-administration of dendrimers carrying ITCH siRNA with suboptimal doses of gemcitabine in pancreatic cancer xenograft models supressed fully tumour growth for 17 days [353.]

8 BIBLIOGRAPHY

1. Villate-Beitia, I. *et al.* First Insights into Non-invasive Administration Routes for Non-viral Gene Therapy. in *Gene Therapy - Principles and Challenges* (InTech, 2015). doi:10.5772/61060

2. Rosenberg, S. A. *et al.* Gene Transfer into Humans — Immunotherapy of Patients with Advanced Melanoma, Using Tumor-Infiltrating Lymphocytes Modified by Retroviral Gene Transduction. *N. Engl. J. Med.* **323**, 570–578 (1990).

3. Chen, Y., Dalwadi, G. & Benson, H. A. E. Drug delivery across the blood-brain barrier. *Curr. Drug Deliv.* **1**, 361–76 (2004).

4. Begley, D. J. Delivery of therapeutic agents to the central nervous system: the problems and the possibilities. *Pharmacol. Ther.* **104**, 29–45 (2004).

5. Abbott, N. J., Patabendige, A. A. K., Dolman, D. E. M., Yusof, S. R. & Begley, D. J. Structure and function of the blood–brain barrier. *Neurobiol. Dis.* **37**, 13–25 (2010).

6. van Tellingen, O. *et al.* Overcoming the blood–brain tumor barrier for effective glioblastoma treatment. *Drug Resist. Updat.* **19**, 1–12 (2015).

7. Ostrom, Q. T. *et al.* CBTRUS Statistical Report: Primary Brain and Other Central Nervous System Tumors Diagnosed in the United States in 2011–2015. *Neuro. Oncol.* **20**, iv1-iv86 (2018).

8. Hottinger, A. F., Stupp, R. & Homicsko, K. Standards of care and novel approaches in the management of glioblastoma multiforme. *Chin. J. Cancer* **33**, 32–9 (2014).

9. Madrid, Y., Langer, L. F., Brem, H. & Langer, R. New Directions in the Delivery of Drugs and Other Substances to the Central Nervous System. *Adv. Pharmacol.* **22**, 299–324 (1991).

10. Dwibhashyam, V. S. N. M. & Nagappa, A. N. Strategies for enhanced drug delivery to the central nervous system. *Indian J. Pharm. Sci.* **70**, 145–53 (2008).

11. Kamaly, N., Xiao, Z., Valencia, P. M., Radovic-Moreno, A. F. & Farokhzad, O. C. Targeted polymeric therapeutic nanoparticles: design, development and clinical translation. *Chem. Soc. Rev.* **41**, 2971 (2012).

12. Karanth, H. & Ramachandra Murthy, R. S. *Nanotechnology in Brain Targeting*.

13. Masserini, M. Nanoparticles for Brain Drug Delivery. *ISRN Biochem.* **2013**, 1–18 (2013).

14. Banks, W. A. Characteristics of compounds that cross the blood-brain barrier. *BMC Neurol.* **9 Suppl 1**, S3 (2009).

15. Pozzoli, M. *et al.* Dry powder nasal drug delivery: challenges, opportunities and a study of the commercial Teijin Puvlizer Rhinocort device and formulation. *Drug Dev. Ind. Pharm.* **42**, 1660–1668 (2016).

16. Pardeshi, C. V. & Belgamwar, V. S. Direct nose to brain drug delivery *via* integrated nerve pathways bypassing the blood–brain barrier: an excellent platform for brain targeting. *Expert Opin. Drug Deliv.* **10**, 957–972 (2013).

17. Selvaraj, K., Gowthamarajan, K. & Karri, V. V. S. R. Nose to brain transport pathways an overview: potential of nanostructured lipid carriers in nose to brain targeting. *Artificial Cells, Nanomedicine and Biotechnology* **46**, 2088–2095 (2018).

18. Liu, X.-F., Fawcett, J. R., Hanson, L. R. & Frey, W. H. The window of opportunity for treatment of focal cerebral ischemic damage with noninvasive intranasal insulin-like growth factor-I in rats. *J. Stroke Cerebrovasc. Dis.* **13**, 16–23 (2004).

19. Arora, P., Sharma, S. & Garg, S. Permeability issues in nasal drug delivery. *Drug Discov. Today* **7**, 967–75 (2002).

20. Thorne, R. G., Pronk, G. J., Padmanabhan, V. & Frey, W. H. Delivery of insulin-like growth factor-I to the rat brain and spinal cord along olfactory and trigeminal pathways following intranasal administration. *Neuroscience* **127**, 481–496 (2004).

21. Alexander, A. & Saraf, S. Nose-to-brain drug delivery approach: A key to easily accessing the brain for the treatment of Alzheimer's disease. *Neural Regen. Res.* **13**, 2102 (2018).

22. Crowe, T. P., Greenlee, M. H. W., Kanthasamy, A. G. & Hsu, W. H. Mechanism of intranasal drug delivery directly to the brain. *Life Sciences* **195**, 44–52 (2018).

23. Erdő, F., Bors, L. A., Farkas, D., Bajza, Á. & Gizurarson, S. Evaluation of intranasal delivery route of drug administration for brain targeting. *Brain Res. Bull.* **143**, 155–170 (2018).

24. Järveläinen, H., Sainio, A., Koulu, M., Wight, T. N. & Penttinen, R. Extracellular Matrix Molecules: Potential Targets in Pharmacotherapy. *Pharmacol. Rev.* **61**, (2009).

25. Frantz, C., Stewart, K. M. & Weaver, V. M. The extracellular matrix at a glance. *J. Cell Sci.* **123**, 4195–4200 (2010).

26. Rozario, T. & DeSimone, D. W. The extracellular matrix in development and morphogenesis: A dynamic view. *Dev. Biol.* **341**, 126–140 (2010).

27. Ramshaw, J. A. ., Shah, N. K. & Brodsky, B. Gly-X-Y Tripeptide Frequencies in Collagen: A Context for Host?Guest Triple-Helical Peptides. *J. Struct. Biol.* **122**, 86–91 (1998).

28. Brodsky, B. & Ramshaw, J. A. M. The collagen triple-helix structure. *Matrix Biol.* **15**, 545–554 (1997).

29. De Wever, O., Demetter, P., Mareel, M. & Bracke, M. Stromal myofibroblasts are drivers of invasive cancer growth. *Int. J. Cancer* **123**, 2229–2238 (2008).

30. Mithieux, S. M. & Weiss, A. S. Elastin. in 437–461 (2005). doi:10.1016/S0065-3233(05)70013-9

31. Lucero, H. A. & Kagan, H. M. Lysyl oxidase: an oxidative enzyme and effector of cell function. *Cell. Mol. Life Sci.* **63**, 2304–2316 (2006).

32. Alberts, B., Jonhson, A. & Lewis, J. Noncollagen Components of the Extracellular Matrix. in *Molecular Biology of the cell* 816–821 (Garlard Science, 2002).

33. Ruoslahti, E. RGD AND OTHER RECOGNITION SEQUENCES FOR INTEGRINS. *Annu. Rev. Cell Dev. Biol.* **12**, 697–715 (1996).

34. Schaefer, L. & Schaefer, R. M. Proteoglycans: From structural compounds to signaling molecules. *Cell and Tissue Research* **339**, 237–246 (2010).

35. Smith, M. L. *et al.* Force-Induced Unfolding of Fibronectin in the Extracellular Matrix of Living Cells. *PLoS Biol.* **5**, e268 (2007).

36. Scott, J. E. Structure and function in extracellular matrices depend on interactions between anionic glycosaminoglycans. *Pathol. Biol. (Paris).* **49**, 284–9 (2001).

37. Kusche-Gullberg, M. Sulfotransferases in glycosaminoglycan biosynthesis. *Curr. Opin. Struct. Biol.* **13**, 605–611 (2003).

38. Goldoni, S. & Iozzo, R. V. Tumor microenvironment: Modulation by decorin and related molecules harboring leucine-rich tandem motifs. *Int. J. Cancer* **123**, 2473–2479 (2008).

39. Iozzo, R. V., Zoeller, J. J. & Nystr?m, A. Basement membrane proteoglycans: Modulators Par Excellence of cancer growth and angiogenesis. *Mol. Cells* **27**, 503–513 (2009).

40. Weigel, P. H., Hascall, V. C. & Tammi, M. Hyaluronan synthases. *J. Biol. Chem.* **272**, 13997–4000 (1997).

41. Csoka, A. B., Frost, G. I. & Stern, R. The six hyaluronidase-like genes in the human and mouse genomes. *Matrix Biol.* **20**, 499–508 (2001).

42. Mao, Y., Keller, E. T., Garfield, D. H., Shen, K. & Wang, J. Stromal cells in tumor microenvironment and breast cancer. *Cancer Metastasis Rev.* **32**, 303–15 (2013).

43. Barlow, K. D., Sanders, A. M., Soker, S., Ergun, S. & Metheny-Barlow, L. J. Pericytes on the tumor vasculature: jekyll or hyde? *Cancer Microenviron.* **6**, 1–17 (2013).

44. Hughes, C. C. W. Endothelial-stromal interactions in angiogenesis. *Curr. Opin. Hematol.* **15**, 204–9 (2008).

45. Man, Y.-G. *et al.* Tumor-infiltrating immune cells promoting tumor invasion and metastasis: existing theories. *J. Cancer* **4**, 84–95 (2013).

46. Butcher, D. T., Alliston, T. & Weaver, V. M. A tense situation: forcing tumour progression. *Nat. Rev. Cancer* **9**, 108–22 (2009).

47. Kessenbrock, K., Plaks, V. & Werb, Z. Matrix metalloproteinases: regulators of the tumor microenvironment. *Cell* **141**, 52–67 (2010).

48. Whatcott, C. J. *et al.* NIH Public Access. **1**, 291–296 (2012).

49. Radotra, B. & McCormick, D. Glioma invasion in vitro is mediated by CD44-hyaluronan

interactions. *J. Pathol.* **181**, 434–8 (1997).

50. Pluen, A. *et al.* Role of tumor-host interactions in interstitial diffusion of macromolecules: cranial vs. subcutaneous tumors. *Proc. Natl. Acad. Sci. U. S. A.* **98**, 4628–33 (2001).

51. Wenning, L. A. & Murphy, R. M. Coupled cellular trafficking and diffusional limitations in delivery of immunotoxins to multicell tumor spheroids. *Biotechnol. Bioeng.* **62**, 562–75 (1999).

52. Li, Z.-Y., Ni, S., Yang, X., Kiviat, N. & Lieber, A. Xenograft models for liver metastasis: Relationship between tumor morphology and adenovirus vector transduction. *Mol. Ther.* **9**, 650–7 (2004).

53. Giese, A. & Westphal, M. Glioma invasion in the central nervous system. *Neurosurgery* **39**, 235-50; discussion 250–2 (1996).

54. Louis, D. N. *et al.* The 2007 WHO classification of tumours of the central nervous system. *Acta Neuropathol.* **114**, 97–109 (2007).

55. Alifieris, C. & Trafalis, D. T. Glioblastoma multiforme: Pathogenesis and treatment. *Pharmacol. Ther.* **152**, 63–82 (2015).

56. Holland, E. C. Glioblastoma multiforme: The terminator. *Proc. Natl. Acad. Sci.* **97**, 6242–6244 (2000).

57. Cohen, M. H., Shen, Y. L., Keegan, P. & Pazdur, R. FDA Drug Approval Summary: Bevacizumab (Avastin(R)) as Treatment of Recurrent Glioblastoma Multiforme. *Oncologist* **14**, 1131–1138 (2009).

58. Jhanwar-Uniyal, M., Labagnara, M., Friedman, M., Kwasnicki, A. & Murali, R. Glioblastoma: molecular pathways, stem cells and therapeutic targets. *Cancers (Basel).* **7**, 538–55 (2015).

59. Vogelstein, B. & Kinzler, K. W. The multistep nature of cancer. *Trends Genet.* **9**, 138–41 (1993).

60. Verhaak, R. G. W. *et al.* Genetic Pathways to Primary and Secondary Glioblastoma. *Cancer Cell* **17**, 98–110 (2010).

61. Kleihues, P. & Ohgaki, H. Primary and secondary glioblastomas: From concept to clinical diagnosis. *Neuro. Oncol.* **1**, 44–51 (1999).

62. Su Huang, H. *et al. The Enhanced Tumorigenic Activity of a Mutant Epidermal Growth Factor Receptor Common in Human Cancers Is Mediated by Threshold Levels of Constitutive Tyrosine Phosphorylation and Unattenuated Signaling* Downloaded from. THE JOURNAL OF BIOLOGICAL CHEMISTRY* **272**, (1997).

63. Hay, N. & Sonenberg, N. Upstream and downstream of mTOR. *Genes Dev.* **18**, 1926–1945 (2004).

64. Reitman, Z. J. & Yan, H. Isocitrate dehydrogenase 1 and 2 mutations in cancer: alterations at a crossroads of cellular metabolism. *J. Natl. Cancer Inst.* **102**, 932–41

(2010).

65. Penard-Lacronique, V. & Bernard, O. A. IDH1, Histone Methylation, and So Forth. *Cancer Cell* **30**, 192–194 (2016).

66. Bellail, A. C., Hunter, S. B., Brat, D. J., Tan, C. & Van Meir, E. G. Microregional extracellular matrix heterogeneity in brain modulates glioma cell invasion. *Int. J. Biochem. Cell Biol.* **36**, 1046–69 (2004).

67. Delpech, B. *et al.* Hyaluronan and hyaluronectin in the extracellular matrix of human brain tumour stroma. *Eur. J. Cancer* **29**, 1012–1017 (1993).

68. Mali, P. *et al.* RNA-guided human genome engineering via Cas9. *Science* **339**, 823–6 (2013).

69. Jinek, M. *et al.* A Programmable Dual-RNA-Guided DNA Endonuclease in Adaptive Bacterial Immunity. *Science (80-.).* **337**, 816–821 (2012).

70. Remaut, K. *et al.* Nucleic acid delivery: Where material sciences and bio-sciences meet. *Mater. Sci. Eng. R Reports* **58**, 117–161 (2007).

71. Manjila, S. B. *et al.* Novel gene delivery systems. *Int. J. Pharm. Investig.* **3**, 1–7 (2013).

72. Zabner, J., Fasbender, A. J., Moninger, T., Poellinger, K. A. & Welsh, M. J. Cellular and molecular barriers to gene transfer by a cationic lipid. *J. Biol. Chem.* **270**, 18997–9007 (1995).

73. Agrawal, N. *et al.* RNA interference: biology, mechanism, and applications. *Microbiol. Mol. Biol. Rev.* **67**, 657–85 (2003).

74. Hannon, G. J., Hammond, S. M., Bernstein, E. & Beach, D. An RNA-directed nuclease mediates post-transcriptional gene silencingin Drosophila cells. *Nature* **404**, 293–296 (2000).

75. Carthew, R. W. *et al.* Origins and Mechanisms of miRNAs and siRNAs. *Cell* **136**, 642–655 (2009).

76. Tomari, Y. & Zamore, P. D. Perspective: machines for RNAi. *Genes Dev.* **19**, 517–29 (2005).

77. Robbins, P. D. & Ghivizzani, S. C. Viral vectors for gene therapy. *Pharmacol. Ther.* **80**, 35–47 (1998).

78. Nayerossadat, N., Maedeh, T. & Ali, P. A. Viral and nonviral delivery systems for gene delivery. *Adv. Biomed. Res.* **1**, 27 (2012).

79. Sheridan, C. Gene therapy finds its niche. *Nat. Biotechnol.* **29**, 121–8 (2011).

80. Vicente, T., Peixoto, C., Carrondo, M. J. T. & Alves, P. M. Virus Production for Clinical Gene Therapy. in 447–470 (Humana Press, 2009). doi:10.1007/978-1-59745-561-9_24

81. Goswami, R. *et al.* Gene therapy leaves a vicious cycle. *Front. Oncol.* **9**, 297 (2019).

82. Burnett, J. R., Hooper, A. J. & Hegele, R. A. *Familial Lipoprotein Lipase Deficiency*. *GeneReviews(®)* (University of Washington, Seattle, 1993).

83. Gene Therapy Clinical Trials Worldwide. Available at: http://www.abedia.com/wiley/index.html. (Accessed: 4th August 2019)

84. Mellott, A. J., Forrest, M. L. & Detamore, M. S. Physical Non-Viral Gene Delivery Methods for Tissue Engineering. *Ann. Biomed. Eng.* **41**, 446–468 (2013).

85. Chou, T. W., Biswas, S. & Lu, S. Gene Delivery Using Physical Methods: An Overview. in *Gene Delivery to Mammalian Cells* 147–166 (Humana Press, 2004). doi:10.1385/1-59259-649-5:147

86. Hirai, H. *et al.* Use of EBV-based Vector/HVJ-liposome complex vector for targeted gene therapy of EBV-associated neoplasms. *Biochem. Biophys. Res. Commun.* **241**, 112–8 (1997).

87. Wasungu, L. & Hoekstra, D. Cationic lipids, lipoplexes and intracellular delivery of genes. *J. Control. Release* **116**, 255–264 (2006).

88. Zhang, X.-X., McIntosh, T. J. & Grinstaff, M. W. Functional lipids and lipoplexes for improved gene delivery. *Biochimie* **94**, 42–58 (2012).

89. Zhang, S. *et al.* Cationic compounds used in lipoplexes and polyplexes for gene delivery. *J. Control. Release* **100**, 165–180 (2004).

90. Esposito, C., Generosi, J., Mossa, G., Masotti, A. & Castellano, A. C. The analysis of serum effects on structure, size and toxicity of DDAB?DOPE and DC-Chol?DOPE lipoplexes contributes to explain their different transfection efficiency. *Colloids Surfaces B Biointerfaces* **53**, 187–192 (2006).

91. Kenny, G. D. *et al.* Novel multifunctional nanoparticle mediates siRNA tumour delivery, visualisation and therapeutic tumour reduction in vivo. *J. Control. Release* **149**, 111–116 (2011).

92. Liang, W. & W. Lam, J. K. Endosomal Escape Pathways for Non-Viral Nucleic Acid Delivery Systems. in *Molecular Regulation of Endocytosis* (InTech, 2012). doi:10.5772/46006

93. Marsh, M. & McMahon, H. T. The structural era of endocytosis. *Science* **285**, 215–20 (1999).

94. Parton, R. G. & Simons, K. The multiple faces of caveolae. *Nat. Rev. Mol. Cell Biol.* **8**, 185–194 (2007).

95. Falcone, S. *et al.* Macropinocytosis: regulated coordination of endocytic and exocytic membrane traffic events. *J. Cell Sci.* **119**, (2006).

96. Rejman, J., Conese, M. & Hoekstra, D. Gene Transfer by Means of Lipo- and Polyplexes: Role of Clathrin and Caveolae-Mediated Endocytosis. *J. Liposome Res.* **16**, 237–247 (2006).

97. Wong, A. W., Scales, S. J. & Reilly, D. E. DNA internalized via caveolae requires

microtubule-dependent, Rab7-independent transport to the late endocytic pathway for delivery to the nucleus. *J. Biol. Chem.* **282**, 22953–63 (2007).

98. Lu, J. J., Langer, R. & Chen, J. A Novel Mechanism Is Involved in Cationic Lipid-Mediated Functional siRNA Delivery. *Mol. Pharm.* **6**, 763–771 (2009).

99. Hafez, I. M., Maurer, N. & Cullis, P. R. On the mechanism whereby cationic lipids promote intracellular delivery of polynucleic acids. *Gene Ther.* **8**, 1188–1196 (2001).

100. and, Y. X. & Francis C. Szoka, J. *,. Mechanism of DNA Release from Cationic Liposome/DNA Complexes Used in Cell Transfection†,‡. (1996). doi:10.1021/BI9602019

101. Lewis, R. N. A. H. & McElhaney, R. N. Surface Charge Markedly Attenuates the Nonlamellar Phase-Forming Propensities of Lipid Bilayer Membranes: Calorimetric and 31P-Nuclear Magnetic Resonance Studies of Mixtures of Cationic, Anionic, and Zwitterionic Lipids. *Biophys. J.* **79**, 1455–1464 (2000).

102. Adams, D., Koike, H., Slama, M. & Coelho, T. Hereditary transthyretin amyloidosis: a model of medical progress for a fatal disease. *Nat. Rev. Neurol.* **15**, 387–404 (2019).

103. Tang, M. X. & Szoka, F. C. The influence of polymer structure on the interactions of cationic polymers with DNA and morphology of the resulting complexes. *Gene Ther.* **4**, 823–832 (1997).

104. Morille, M., Passirani, C., Vonarbourg, A., Clavreul, A. & Benoit, J.-P. Progress in developing cationic vectors for non-viral systemic gene therapy against cancer. *Biomaterials* **29**, 3477–3496 (2008).

105. Baba, T. *et al.* Ultrastructural study of echinocytes induced by poly (ethylene glycol)-cholesterol. *Histochem. Cell Biol.* **122**, 587–592 (2004).

106. Lockman, P. R., Koziara, J. M., Mumper, R. J. & Allen, D. D. Nanoparticle Surface Charges Alter Blood–Brain Barrier Integrity and Permeability. *J. Drug Target.* **12**, 635–641 (2004).

107. Kozielski, K. L., Tzeng, S. Y., Hurtado De Mendoza, B. A. & Green, J. J. Bioreducible Cationic Polymer-Based Nanoparticles for Efficient and Environmentally Triggered Cytoplasmic siRNA Delivery to Primary Human Brain Cancer Cells. *ACS Nano* **8**, 3232–3241 (2014).

108. Zhong, Z. *et al.* Low Molecular Weight Linear Polyethylenimine- *b* -poly(ethylene glycol)- *b* -polyethylenimine Triblock Copolymers: Synthesis, Characterization, and in Vitro Gene Transfer Properties. *Biomacromolecules* **6**, 3440–3448 (2005).

109. Fischer, D., Bieber, T., Li, Y., Elsässer, H. P. & Kissel, T. A novel non-viral vector for DNA delivery based on low molecular weight, branched polyethylenimine: effect of molecular weight on transfection efficiency and cytotoxicity. *Pharm. Res.* **16**, 1273–9 (1999).

110. Mastrobattista, E. & Hennink, W. E. Polymers for gene delivery: Charged for success. *Nat. Mater.* **11**, 10–12 (2011).

111. Kapoor, M. & Burgess, D. J. Efficient and safe delivery of siRNA using anionic lipids: Formulation optimization studies. *Int. J. Pharm.* **432**, 80–90 (2012).

112. MAO, S. *et al.* Synthesis, characterization and cytotoxicity of poly(ethylene glycol)-graft-trimethyl chitosan block copolymers. *Biomaterials* **26**, 6343–6356 (2005).

113. Zhang, C. Y. *et al.* Native chemical ligation for conversion of sequence-defined oligomers into targeted pDNA and siRNA carriers. *J. Control. Release* **180**, 42–50 (2014).

114. Akinc, A., Thomas, M., Klibanov, A. M. & Langer, R. Exploring polyethylenimine-mediated DNA transfection and the proton sponge hypothesis. *J. Gene Med.* **7**, 657–663 (2005).

115. Buyens, K. *et al.* Monitoring the disassembly of siRNA polyplexes in serum is crucial for predicting their biological efficacy. *J. Control. Release* **141**, 38–41 (2010).

116. Cho, S. K. & Kwon, Y. J. Polyamine/DNA polyplexes with acid-degradable polymeric shell as structurally and functionally virus-mimicking nonviral vectors. *J. Control. Release* **150**, 287–297 (2011).

117. Benjaminsen, R. V, Mattebjerg, M. A., Henriksen, J. R., Moghimi, S. M. & Andresen, T. L. The Possible "Proton Sponge " Effect of Polyethylenimine (PEI) Does Not Include Change in Lysosomal pH. *Mol. Ther.* **21**, 149–157 (2013).

118. Lächelt, U. *et al.* Fine-tuning of proton sponges by precise diaminoethanes and histidines in pDNA polyplexes. *Nanomedicine Nanotechnology, Biol. Med.* **10**, 35–44 (2014).

119. Niidome, T. *et al.* Binding of Cationic α-Helical Peptides to Plasmid DNA and Their Gene Transfer Abilities into Cells. *J. Biol. Chem.* **272**, 15307–15312 (1997).

120. Wyman, T. B. *et al.* Design, Synthesis, and Characterization of a Cationic Peptide That Binds to Nucleic Acids and Permeabilizes Bilayers [†]. *Biochemistry* **36**, 3008–3017 (1997).

121. van Gaal, E. V. B. *et al.* DNA Nuclear Targeting Sequences for Non-Viral Gene Delivery. *Pharm. Res.* **28**, 1707–1722 (2011).

122. Bai, H., Lester, G. M. S., Petishnok, L. C. & Dean, D. A. Cytoplasmic transport and nuclear import of plasmid DNA. *Biosci. Rep.* **37**, (2017).

123. Lechardeur, D. *et al.* Metabolic instability of plasmid DNA in the cytosol: a potential barrier to gene transfer. *Gene Ther.* **6**, 482–497 (1999).

124. Wittrup, A. *et al.* Visualizing lipid-formulated siRNA release from endosomes and target gene knockdown. *Nat. Biotechnol.* **33**, 870–876 (2015).

125. Hirsch, M. & Helm, M. Live cell imaging of duplex siRNA intracellular trafficking. *Nucleic Acids Res.* **43**, 4650–4660 (2015).

126. Bausinger, R. *et al.* The Transport of Nanosized Gene Carriers Unraveled by Live-Cell Imaging. *Angew. Chemie Int. Ed.* **45**, 1568–1572 (2006).

127. Akita, H. *et al.* Particle Tracking of Intracellular Trafficking of Octaarginine-modified Liposomes: A Comparative Study With Adenovirus. *Mol. Ther.* **18**, 955–964 (2010).

128. Miller, A. M. & Dean, D. A. Tissue-specific and transcription factor-mediated nuclear entry of DNA. *Adv. Drug Deliv. Rev.* **61**, 603–613 (2009).

129. Grandinetti, G., Smith, A. E. & Reineke, T. M. Membrane and Nuclear Permeabilization by Polymeric pDNA Vehicles: Efficient Method for Gene Delivery or Mechanism of Cytotoxicity? *Mol. Pharm.* **9**, 523–538 (2012).

130. Lam, A. P. & Dean, D. A. Progress and prospects: nuclear import of nonviral vectors. *Gene Ther.* **17**, 439–447 (2010).

131. Hu, Q. *et al.* Intracellular pathways and nuclear localization signal peptide-mediated gene transfection by cationic polymeric nanovectors. *Biomaterials* **33**, 1135–1145 (2012).

132. Ni, R. *et al.* Synthetic Approaches for Nucleic Acid Delivery: Choosing the Right Carriers. *Life* **9**, 59 (2019).

133. Li, H.-J., Wang, H.-X., Sun, C.-Y., Du, J.-Z. & Wang, J. Shell-detachable nanoparticles based on a light-responsive amphiphile for enhanced siRNA delivery. *RSC Adv.* **4**, 1961–1964 (2014).

134. Yang, X.-Z. *et al.* Sheddable Ternary Nanoparticles for Tumor Acidity-Targeted siRNA Delivery. *ACS Nano* **6**, 771–781 (2012).

135. Tan, J.-K. Y., Choi, J. L., Wei, H., Schellinger, J. G. & Pun, S. H. Reducible, dibromomaleimide-linked polymers for gene delivery. *Biomater. Sci.* **3**, 112–120 (2015).

136. Kwon, Y. J. Before and after Endosomal Escape: Roles of Stimuli-Converting siRNA/Polymer Interactions in Determining Gene Silencing Efficiency. *Acc. Chem. Res.* **45**, 1077–1088 (2012).

137. Okura, H., Smith, C. A. & Rutka, J. T. Gene therapy for malignant glioma. *Mol. Cell. Ther.* **2**, 21 (2014).

138. Rainov, N. G. A Phase III Clinical Evaluation of Herpes Simplex Virus Type 1 Thymidine Kinase and Ganciclovir Gene Therapy as an Adjuvant to Surgical Resection and Radiation in Adults with Previously Untreated Glioblastoma Multiforme. *Hum. Gene Ther.* **11**, 2389–2401 (2000).

139. Takahashi, M. *et al.* Radiosensitization of gliomas by intracellular generation of 5-fluorouracil potentiates prodrug activator gene therapy with a retroviral replicating vector. *Cancer Gene Ther.* **21**, 405–410 (2014).

140. Fischer, U. *et al.* Mechanisms of thymidine kinase/ganciclovir and cytosine deaminase/ 5-fluorocytosine suicide gene therapy-induced cell death in glioma cells. *Oncogene* **24**, 1231–1243 (2005).

141. Aghi, M. *et al.* AT-02 * INTRATUMORAL DELIVERY OF THE RETROVIRAL REPLICATING VECTOR (RRV) TOCA 511 IN SUBJECTS WITH RECURRENT HIGH GRADE GLIOMA:

INTERIM REPORT OF PHASE 1 STUDY (NCT 01156584). *Neuro. Oncol.* **16**, v8–v8 (2014).

142. Wainwright, D. A., Dey, M., Chang, A. & Lesniak, M. S. Targeting Tregs in Malignant Brain Cancer: Overcoming IDO. *Front. Immunol.* **4**, 116 (2013).

143. Xu, S. *et al.* Synergy between the ectoenzymes CD39 and CD73 contributes to adenosinergic immunosuppression in human malignant gliomas. *Neuro. Oncol.* **15**, 1160–1172 (2013).

144. Chiocca, E. A. *et al.* Phase IB Study of Gene-Mediated Cytotoxic Immunotherapy Adjuvant to Up-Front Surgery and Intensive Timing Radiation for Malignant Glioma. *J. Clin. Oncol.* **29**, 3611–3619 (2011).

145. Wheeler, L. A. *et al.* Phase II multicenter study of gene-mediated cytotoxic immunotherapy as adjuvant to surgical resection for newly diagnosed malignant glioma. *Neuro. Oncol.* **18**, 1137–1145 (2016).

146. Kieran, M. W. *et al.* Phase I study of gene-mediated cytotoxic immunotherapy with AdV-tk as adjuvant to surgery and radiation for pediatric malignant glioma and recurrent ependymoma. *Neuro. Oncol.* **21**, 537–546 (2019).

147. Ishii, N. *et al.* Frequent co-alterations of TP53, p16/CDKN2A, p14ARF, PTEN tumor suppressor genes in human glioma cell lines. *Brain Pathol.* **9**, 469–79 (1999).

148. Badie, B., Drazan, K. E., Kramar, M. H., Shaked, A. & Black, K. L. Adenovirus-mediated p53 gene delivery inhibits 9L glioma growth in rats. *Neurol. Res.* **17**, 209–16 (1995).

149. Inoue, R. *et al.* Infectious delivery of the 132 kb CDKN2A/CDKN2B genomic DNA region results in correctly spliced gene expression and growth suppression in glioma cells. *Gene Ther.* **11**, 1195–1204 (2004).

150. Lang, F. F. *et al.* Phase I Trial of Adenovirus-Mediated p53 Gene Therapy for Recurrent Glioma: Biological and Clinical Results. *J. Clin. Oncol.* **21**, 2508–2518 (2003).

151. Uchegbu, I. F. Pharmaceutical nanotechnology: polymeric vesicles for drug and gene delivery. *Expert Opin. Drug Deliv.* **3**, 629–40 (2006).

152. Gabizon, A. A. Pegylated liposomal doxorubicin: metamorphosis of an old drug into a new form of chemotherapy. *Cancer Invest.* **19**, 424–36 (2001).

153. Brigger, I., Dubernet, C. & Couvreur, P. Nanoparticles in cancer therapy and diagnosis. *Adv. Drug Deliv. Rev.* **54**, 631–51 (2002).

154. Peer, D. *et al.* Nanocarriers as an emerging platform for cancer therapy. *Nat. Nanotechnol.* **2**, 751–60 (2007).

155. Kwiatkowska, A., Nandhu, M. S., Behera, P., Chiocca, E. A. & Viapiano, M. S. Strategies in gene therapy for glioblastoma. *Cancers (Basel).* **5**, 1271–305 (2013).

156. Reszka, R. C., Jacobs, A. & Voges, J. Liposome-Mediated Suicide Gene Therapy in Humans. in 200–208 (2005). doi:10.1016/S0076-6879(05)91012-4

157. Yoshida, J. *et al.* Human Gene Therapy for Malignant Gliomas (Glioblastoma

Multiforme and Anaplastic Astrocytoma) by *In Vivo* Transduction with Human Interferon *β* Gene Using Cationic Liposomes. *Hum. Gene Ther.* **15**, 77–86 (2004).

158. Phase II Study of Combined Temozolomide and SGT-53 for Treatment of Recurrent Glioblastoma - Full Text View - ClinicalTrials.gov. Available at: https://clinicaltrials.gov/ct2/show/NCT02340156. (Accessed: 12th August 2019)

159. Jensen, S. A. *et al.* Spherical Nucleic Acid Nanoparticle Conjugates as an RNAi-Based Therapy for Glioblastoma. *Sci. Transl. Med.* **5**, 209ra152-209ra152 (2013).

160. Yin, T. *et al.* Ultrasound-sensitive siRNA-loaded nanobubbles formed by hetero-assembly of polymeric micelles and liposomes and their therapeutic effect in gliomas. *Biomaterials* **34**, 4532–4543 (2013).

161. Li, J. *et al.* The use of myristic acid as a ligand of polyethylenimine/DNA nanoparticles for targeted gene therapy of glioblastoma. *Nanotechnology* **22**, 435101 (2011).

162. Han, L. *et al.* Tat-BMPs-PAMAM Conjugates Enhance Therapeutic Effect of Small Interference RNA on U251 Glioma Cells *In Vitro* and *In Vivo*. *Hum. Gene Ther.* **21**, 417–426 (2010).

163. Liu, S. *et al.* Gene and doxorubicin co-delivery system for targeting therapy of glioma. *Biomaterials* **33**, 4907–4916 (2012).

164. Liu, Y. *et al.* A Bacteria Deriving Peptide Modified Dendrigraft Poly- l -lysines (DGL) Self-Assembling Nanoplatform for Targeted Gene Delivery. *Mol. Pharm.* **11**, 3330–3341 (2014).

165. Kodama, Y. *et al.* Application of biodegradable dendrigraft poly- l -lysine to a small interfering RNA delivery system. *J. Drug Target.* **25**, 49–57 (2017).

166. Kodama, Y. *et al.* Biodegradable nanoparticles composed of dendrigraft poly-l-lysine for gene delivery. *Eur. J. Pharm. Biopharm.* **87**, 472–479 (2014).

167. Tang, M., Dong, H., Li, Y. & Ren, T. Harnessing the PEG-cleavable strategy to balance cytotoxicity, intracellular release and the therapeutic effect of dendrigraft poly- l -lysine for cancer gene therapy. *J. Mater. Chem. B* **4**, 1284–1295 (2016).

168. Mastorakos, P. *et al.* Biodegradable DNA Nanoparticles that Provide Widespread Gene Delivery in the Brain. *Small* **12**, 678–685 (2016).

169. Chauhan, V. P., Stylianopoulos, T., Boucher, Y. & Jain, R. K. Delivery of molecular and nanoscale medicine to tumors: transport barriers and strategies. *Annu. Rev. Chem. Biomol. Eng.* **2**, 281–98 (2011).

170. Van Woensel, M. *et al.* Development of siRNA-loaded chitosan nanoparticles targeting Galectin-1 for the treatment of glioblastoma multiforme via intranasal administration. *J. Control. Release* **227**, 71–81 (2016).

171. Muzzarelli, R. A. A. Natural chelating polymers; alginic acid, chitin, and chitosan. - NLM Catalog - NCBI. *Int. Ser. Monogr. Anal. Chem. ; v. 55* **55**, (1937).

172. Ahmed, S. & Ikram, S. Chitosan Based Scaffolds and Their Applications in Wound

Healing. *Achiev. Life Sci.* **10**, 27–37 (2016).

173. Ko, J. A., Park, H. J., Park, Y. S., Hwang, S. J. & Park, J. B. Chitosan microparticle preparation for controlled drug release by response surface methodology. *J. Microencapsul.* **20**, 791–797 (2003).

174. Yuan, Q., Shah, J., Hein, S. & Misra, R. D. K. *Controlled and extended drug release behavior of chitosan-based nanoparticle carrier*. *Acta Biomaterialia* **6**, (2010).

175. MacLaughlin, F. C. *et al.* Chitosan and depolymerized chitosan oligomers as condensing carriers for in vivo plasmid delivery. *J. Control. Release* **56**, 259–272 (1998).

176. Klausner, E. A., Zhang, Z., Chapman, R. L., Multack, R. F. & Volin, M. V. Ultrapure chitosan oligomers as carriers for corneal gene transfer. *Biomaterials* **31**, 1814–1820 (2010).

177. Lee, M. *et al.* Water-Soluble and Low Molecular Weight Chitosan-Based Plasmid DNA Delivery. *Pharm. Res.* **18**, 427–431 (2001).

178. Chooi, K. W. *et al.* Physical Characterisation and Long-Term Stability Studies on Quaternary Ammonium Palmitoyl Glycol Chitosan (GCPQ)?A New Drug Delivery Polymer. *J. Pharm. Sci.* **103**, 2296–2306 (2014).

179. Ishii, T., Okahata, Y. & Sato, T. Mechanism of cell transfection with plasmid/chitosan complexes. *Biochim. Biophys. Acta - Biomembr.* **1514**, 51–64 (2001).

180. Techaarpornkul, S. *et al.* Chitosan-mediated siRNA delivery in vitro: effect of polymer molecular weight, concentration and salt forms. *AAPS PharmSciTech* **11**, 64–72 (2010).

181. Liu, X. *et al.* The influence of polymeric properties on chitosan/siRNA nanoparticle formulation and gene silencing. *Biomaterials* **28**, 1280–1288 (2007).

182. Kiang, T., Wen, J., Lim, H. W. & Leong, K. W. The effect of the degree of chitosan deacetylation on the efficiency of gene transfection. *Biomaterials* **25**, 5293–5301 (2004).

183. Köping-Höggård, M. *et al.* Chitosan as a nonviral gene delivery system. Structure–property relationships and characteristics compared with polyethylenimine in vitro and after lung administration in vivo. *Gene Ther.* **8**, 1108–1121 (2001).

184. Yilmaz, E. Chitosan: A Versatile Biomaterial. in 59–68 (Springer, Boston, MA, 2004). doi:10.1007/978-0-306-48584-8_5

185. Zhang, W. *et al.* Inhibition of respiratory syncytial virus infection with intranasal siRNA nanoparticles targeting the viral NS1 gene. *Nat. Med.* **11**, 56–62 (2005).

186. Sugimoto, M., Morimoto, M., Sashiwa, H., Saimoto, H. & Shigemasa, Y. Preparation and characterization of water-soluble chitin and chitosan derivatives. *Carbohydr. Polym.* **36**, 49–59 (1998).

187. Dung, P. le, Milas, M., Rinaudo, M. & Desbrières, J. Water soluble derivatives obtained

by controlled chemical modifications of chitosan. *Carbohydr. Polym.* **24**, 209–214 (1994).

188. Muzzarelli, R. A. A., Lough, C. & Emanuelli, M. The molecular weight of chitosans studied by laser light-scattering. *Carbohydr. Res.* **164**, 433–442 (1987).

189. Carreño-Gómez, B. & Duncan, R. Evaluation of the biological properties of soluble chitosan and chitosan microspheres. *Int. J. Pharm.* **148**, 231–240 (1997).

190. Seunglee Kwon *et al.* Physicochemical Characteristics of Self-Assembled Nanoparticles Based on Glycol Chitosan Bearing 5β-Cholanic Acid. (2003). doi:10.1021/LA0350608

191. Wei Wang, †, Anne Marie McConaghy, †, Laurence Tetley, ‡ and & Ijeoma F. Uchegbu*, †. Controls on Polymer Molecular Weight May Be Used To Control the Size of Palmitoyl Glycol Chitosan Polymeric Vesicles. (2001). doi:10.1021/LA001078W

192. Kean, T., Roth, S. & Thanou, M. Trimethylated chitosans as non-viral gene delivery vectors: Cytotoxicity and transfection efficiency. *J. Control. Release* **103**, 643–653 (2005).

193. Kim, T. H., Ihm, J. E., Choi, Y. J., Nah, J. W. & Cho, C. S. Efficient gene delivery by urocanic acid-modified chitosan. *J. Control. Release* **93**, 389–402 (2003).

194. Knight, D. K., Shapka, S. N. & Amsden, B. G. Structure, depolymerization, and cytocompatibility evaluation of glycol chitosan. *J. Biomed. Mater. Res. - Part A* **83**, 787–798 (2007).

195. Alamoudi, A. Engineered Nanoparticles - Safe and Efficient Vectors For Nucleic Acid Delivery. *Conf. Pap.* (2016).

196. Simao Carlos, M. I. *et al.* Limiting the level of tertiary amines on polyamines leads to biocompatible nucleic acid vectors. *Int. J. Pharm.* **526**, 106–124 (2017).

197. Williams, D. H. & Fleming, I. Spectroscopic Methods in Organic Chemistry. in *Spectroscopic Methods in Organic Chemistry* 145–154 (1995).

198. Claridge, T. D. W. *High-resolution NMR techniques in organic chemistry*. (Elsevier, 2009).

199. Williams, T. Gel permeation chromatography: A review. *J. Mater. Sci.* **5**, 811–820 (1970).

200. de Levie, R. The Henderson-Hasselbalch Equation: Its History and Limitations. *J. Chem. Educ.* **80**, 146 (2003).

201. Gores, D. H. F. Tips & Tricks GPC/SEC: System Peaks or Ghost Peaks in GPC/SEC.

202. I.Simao. Carlos, M. Nucleic Acid Delivery - Biocopmatible, yet effcient platforms. *Int. J. Pharm. Investig.* (2014).

203. Layman, J. M., Ramirez, S. M., Green, M. D. & Long, T. E. Influence of polycation molecular weight on poly(2-dimethylaminoethyl methacrylate)-mediated DNA

delivery in vitro. *Biomacromolecules* **10**, 1244–52 (2009).

204. Ren, Y., Jiang, X., Pan, D. & Mao, H.-Q. Charge density and molecular weight of polyphosphoramidate gene carrier are key parameters influencing its DNA compaction ability and transfection efficiency. *Biomacromolecules* **11**, 3432–9 (2010).

205. Ji, W., Panus, D., Palumbo, R. N., Tang, R. & Wang, C. Poly(2-aminoethyl methacrylate) with well-defined chain length for DNA vaccine delivery to dendritic cells. *Biomacromolecules* **12**, 4373–85 (2011).

206. Carlos, M. I. S., Sch?tzlein, A. & Uchegbu, I. Polymer Based Gene Silencing: In Vitro Delivery of SiRNA. in *Methods in molecular biology (Clifton, N.J.)* **1445**, 149–157 (2016).

207. Piest, M. & Engbersen, J. F. J. Effects of charge density and hydrophobicity of poly(amido amine)s for non-viral gene delivery. *J. Control. Release* **148**, 83–90 (2010).

208. Wang, D. *et al.* Novel branched poly(ethylenimine)-cholesterol water-soluble lipopolymers for gene delivery. *Biomacromolecules* **3**, 1197–207

209. Wang, W., Mcconaghy, A. M., Tetley, L. & Uchegbu, I. F. Controls on Polymer Molecular Weight May Be Used To Control the Size of Palmitoyl Glycol Chitosan Polymeric Vesicles. doi:10.1021/la001078w

210. Soundararajan, R. ENHANCING THE BIOAVAILABILITY OF BCS CLASS IV DRUGS USING POLYMERIC NANOPARTICLE. (2016).

211. Ethan A. Englund, Hosahudya N. Gopi, and & Appella*, D. H. An Efficient Synthesis of a Probe for Protein Function: 2,3-Diaminopropionic Acid with Orthogonal Protecting Groups. (2003). doi:10.1021/OL0361599

212. Lundt, B. F., Johansen, N. L., V?lund, A. & Markussen, J. REMOVAL OF t-BUTYL AND t-BUTOXYCARBONYL PROTECTING GROUPS WITH TRIFLUOROACETIC ACID. *Int. J. Pept. Protein Res.* **12**, 258–268 (2009).

213. Waters. Beginner's guide to Size-Exclusion Chromatography. Available at: http://www.waters.com/waters/en_GB/Calibration-of-the-GPC-System/nav.htm?cid=10167839&locale=en_GB.

214. Chen, W. Y., Hsu, C. H., Huang, J. R., Tsai, M. L. & Chen, R. H. Effect of the ionic strength of the media on the aggregation behaviors of high molecule weight chitosan. *J. Polym. Res.* **18**, 1385–1395 (2011).

215. Stulik, K., Pacakova?, V. & Ticha, M. Some potentialities and drawbacks of contemporary size-exclusion chromatography. *J. Biochem. Biophys. Methods* **56**, 1–13 (2003).

216. Thomas*, T. & Thomas, T. J. Polyamines in cell growth and cell death: molecular mechanisms and therapeutic applications. *Cell. Mol. Life Sci.* **58**, 244–258 (2001).

217. Tabor, C. W. & Tabor, H. Polyamines. *Annu. Rev. Biochem.* **53**, 749–790 (1984).

218. Heby, O. Role of polyamines in the control of cell proliferation and differentiation.

Differentiation. **19**, 1–20 (1981).

219. Pegg, A. E. Mammalian polyamine metabolism and function. *IUBMB Life* **61**, 880–94 (2009).

220. Gerner, E. W. & Meyskens, F. L. Polyamines and cancer: old molecules, new understanding. *Nat. Rev. Cancer* **4**, 781–792 (2004).

221. Kurihara, H., Matsuzaki, S., Yamazaki, H., Tsukahara, T. & Tamura, M. Relationship between Tissue Polyamine Levels and Malignancy in Primary Brain Tumors. *Neurosurgery* **32**, 372–375 (1993).

222. Nair, S. K. *et al.* Synergistic apoptosis of MCF-7 breast cancer cells by 2-methoxyestradiol and bis(ethyl)norspermine. *Cancer Lett.* **250**, 311–322 (2007).

223. Frydman, B. *et al.* A novel polyamine analog (SL-11093) inhibits growth of human prostate tumor xenografts in nude mice. *Cancer Chemother. Pharmacol.* **51**, 488–492

224. Huang, Y., Pledgie, A., Casero, R. A. & Davidson, N. E. Molecular mechanisms of polyamine analogs in cancer cells. *Anticancer. Drugs* **16**, 229–41 (2005).

225. Casero, R. A. & Marton, L. J. Targeting polyamine metabolism and function in cancer and other hyperproliferative diseases. *Nat. Rev. Drug Discov.* **6**, 373–390 (2007).

226. Frydman, L. *et al.* Interactions between natural polyamines and tRNA: an 15N NMR analysis. *Proc. Natl. Acad. Sci. U. S. A.* **89**, 9186–90 (1992).

227. Ouameur, A. A. & Tajmir-Riahi, H.-A. Structural Analysis of DNA Interactions with Biogenic Polyamines and Cobalt(III)hexamine Studied by Fourier Transform Infrared and Capillary Electrophoresis. *J. Biol. Chem.* **279**, 42041–42054 (2004).

228. Jiang, H.-L. *et al.* Chitosan-graft-spermine as a gene carrier in vitro and in vivo. *Eur. J. Pharm. Biopharm.* **77**, 36–42 (2011).

229. Huang, X., Li, X., Chen, L. & Li, L. Spermine Modified Starch-based Carrier for Gene Delivery: Structure-Transfection Activity Relationships. *Carbohydr. Polym.* (2017). doi:10.1016/j.carbpol.2017.05.099

230. Kim, Y. K., Cho, C. S., Cho, M. H. & Jiang, H. L. Spermine-alt-poly(ethylene glycol) polyspermine as a safe and efficient aerosol gene carrier for lung cancer therapy. *J. Biomed. Mater. Res. - Part A* **102**, 2230–2237 (2014).

231. Viola, J. R. *et al.* Fatty acid–spermine conjugates as DNA carriers for nonviral in vivo gene delivery. *Gene Ther.* **16**, 1429–1440 (2009).

232. Xie, R. L. *et al.* A novel potential biocompatible hyperbranched polyspermine for efficient lung cancer gene therapy. *Int. J. Pharm.* **478**, 19–30 (2015).

233. Hermanson, G. T. The Reactions of Bioconjugation. *Bioconjugate Tech.* 229–258 (2013). doi:10.1016/B978-0-12-382239-0.00003-0

234. Yamauchi, K., Kuroki, S. & Ando, I. The amide proton NMR chemical shift and hydrogen-bonded structure of glycine-containing peptides and polypeptides in the

solid state as studied by multi-pulse-associated high-speed MAS 1H NMR. *J. Mol. Struct.* **602**–**603**, 9–16 (2002).

235. Fulmer, G. R. *et al.* NMR Chemical Shifts of Trace Impurities: Common Laboratory Solvents, Organics, and Gases in Deuterated Solvents Relevant to the Organometallic Chemist. (2010). doi:10.1021/om100106e

236. Frassineti, C. *et al.* Nuclear Magnetic Resonance as a Tool for Determining Protonation Constants of Natural Polyprotic Bases in Solution. *Anal. Biochem.* **231**, 374–382 (1995).

237. Sarneski, J. E., Surprenant, H. L., Molen, F. K. & Reilley, C. N. Chemical shifts and protonation shifts in carbon-13 nuclear magnetic resonance studies of aqueous amines. *Anal. Chem.* **47**, 2116–2124 (1975).

238. Nguyen, J. & Szoka, F. C. Nucleic Acid Delivery: The Missing Pieces of the Puzzle? *Acc. Chem. Res.* **45**, 1153–1162 (2012).

239. Pack, D. W., Hoffman, A. S., Pun, S. & Stayton, P. S. Design and development of polymers for gene delivery. *Nat. Rev. Drug Discov.* **4**, 581–593 (2005).

240. Mislick, K. A. & Baldeschwieler, J. D. Evidence for the role of proteoglycans in cation-mediated gene transfer. *Proc. Natl. Acad. Sci.* **93**, 12349–12354 (1996).

241. Khalil, I. A. Uptake Pathways and Subsequent Intracellular Trafficking in Nonviral Gene Delivery. *Pharmacol. Rev.* **58**, 32–45 (2006).

242. Guo, W. & Lee, R. J. Efficient gene delivery using anionic liposome-complexed polyplexes (LPDII). *Biosci. Rep.* **20**, 419–32 (2000).

243. Cao, Z. Q., Liu, W. G., Liang, D. C., Guo, G. & Zhang, J. Y. Design of Poly(vinyldiaminotriazine)-Based Nonviral Vectors via Specific Hydrogen Bonding with Nucleic Acid Base Pairs. *Adv. Funct. Mater.* **17**, 246–252 (2007).

244. Zheng, Y., Wang, X., Qiu, F. & Yin, L. Amphiphilic polymer to improve polyplex stability for enhanced transfection efficiency. *Polym. Bull.* **76**, 2471–2479 (2019).

245. Cheng, Y. *et al.* Development of switchable polymers to address the dilemma of stability and cargo release in polycationic nucleic acid carriers. *Biomaterials* **127**, 89–96 (2017).

246. Wei, H. *et al.* Dual responsive, stabilized nanoparticles for efficient in vivo plasmid delivery. *Angew. Chem. Int. Ed. Engl.* **52**, 5377–81 (2013).

247. Han, X. *et al.* The heterogeneous nature of polyethylenimine-DNA complex formation affects transient gene expression. *Cytotechnology* **60**, 63–75 (2009).

248. Koontz, L. Agarose Gel Electrophoresis. *Methods Enzymol.* **529**, 35–45 (2013).

249. Carpenter, D. K. Dynamic Light Scattering with Applications to Chemistry, Biology, and Physics (Berne, Bruce J.; Pecora, Robert). *J. Chem. Educ.* **54**, A430 (1977).

250. FORD, J. L. Particle Size Analysis in Pharmaceutics and Other Industries. Theory and

Practice. *J. Pharm. Pharmacol.* **45**, 1015–1015 (1993).

251. Rimer, Ludwig, Kohl, H. Introduction to Transmission Electron Microscopy. in *Transmission Electron Microscopy* 1–15 (Springer New York). doi:10.1007/978-0-387-40093-8_1

252. Inoué, S. Foundations of Confocal Scanned Imaging in Light Microscopy. in *Handbook Of Biological Confocal Microscopy* 1–19 (Springer US, 2006). doi:10.1007/978-0-387-45524-2_1

253. Hsu, C. Y. & Uludag, H. Effects of size and topology of DNA molecules on intracellular delivery with non-viral gene carriers. *BMC Biotechnol.* **8**, 23 (2008).

254. Sim?o Carlos, M. I. Nucleic Acid Delivery – Biocompatible Yet Efficient Platforms. (2004).

255. Jones, N. A. *et al.* Polymer chemical structure is a key determinant of physicochemical and colloidal properties of polymer-DNA complexes for gene delivery. *Biochim. Biophys. Acta* **1517**, 1–18 (2000).

256. Grigsby, C. L. & Leong, K. W. Balancing protection and release of DNA: tools to address a bottleneck of non-viral gene delivery. *J. R. Soc. Interface* **7**, (2010).

257. Uchegbu, I. F. *et al.* Gene Transfer with Three Amphiphilic Glycol Chitosans—the Degree of Polymerisation is the Main Controller of Transfection Efficiency. *J. Drug Target.* **12**, 527–539 (2004).

258. Ehrlich, M. *et al.* Endocytosis by Random Initiation and Stabilization of Clathrin-Coated Pits. *Cell* **118**, 591–605 (2004).

259. Conner, S. D. & Schmid, S. L. Regulated portals of entry into the cell. *Nat.* **422**, 37–44 (2003).

260. Zuhorn, I. S., Kalicharan, R. & Hoekstra, D. Lipoplex-mediated Transfection of Mammalian Cells Occurs through the Cholesterol-dependent Clathrin-mediated Pathway of Endocytosis. *J. Biol. Chem.* **277**, 18021–18028 (2002).

261. Rejman, J., Bragonzi, A. & Conese, M. Role of clathrin- and caveolae-mediated endocytosis in gene transfer mediated by lipo- and polyplexes. *Mol. Ther.* **12**, 468–474 (2005).

262. Desjardins, P. & Conklin, D. NanoDrop microvolume quantitation of nucleic acids. *J. Vis. Exp.* (2010). doi:10.3791/2565

263. Kasper, J. C., Schaffert, D., Ogris, M., Wagner, E. & Friess, W. The establishment of an up-scaled micro-mixer method allows the standardized and reproducible preparation of well-defined plasmid/LPEI polyplexes. *Eur. J. Pharm. Biopharm.* **77**, 182–185 (2011).

264. Kennedy, M. T., Pozharski, E. V, Rakhmanova, V. A. & Macdonald, R. C. *Factors Governing the Assembly of Cationic Phospholipid-DNA Complexes*. (2000). doi:10.1016/S0006-3495(00)76714-2

265. Ogris, M. *et al.* The size of DNA/transferrin-PEI complexes is an important factor for gene expression in cultured cells. *Gene Ther.* **5**, 1425–1433 (1998).

266. Boussif, O. *et al.* A versatile vector for gene and oligonucleotide transfer into cells in culture and in vivo: polyethylenimine. *Proc. Natl. Acad. Sci. U. S. A.* **92**, 7297–301 (1995).

267. Sharma, V. K., Thomas, M. & Klibanov, A. M. Mechanistic studies on aggregation of polyethylenimine-DNA complexes and its prevention. *Biotechnol. Bioeng.* **90**, 614–620 (2005).

268. Vasiliu, T. *et al.* Optimization of Polyplex Formation between DNA Oligonucleotide and Poly(ʟ-Lysine): Experimental Study and Modeling Approach. *Int. J. Mol. Sci.* **18**, (2017).

269. Rejman, J., Oberle, V., Zuhorn, I. S. & Hoekstra, D. Size-dependent internalization of particles via the pathways of clathrin- and caveolae-mediated endocytosis. *Biochem. J.* **377**, 159–69 (2004).

270. Grosse, S. *et al.* Potocytosis and cellular exit of complexes as cellular pathways for gene delivery by polycations. *J. Gene Med.* **7**, 1275–1286 (2005).

271. von Gersdorff, K. *et al.* The Internalization Route Resulting in Successful Gene Expression Depends on both Cell Line and Polyethylenimine Polyplex Type. *Mol. Ther.* **14**, 745–753 (2006).

272. Manunta, M. *et al.* Gene delivery by dendrimers operates via different pathways in different cells, but is enhanced by the presence of caveolin. *J. Immunol. Methods* **314**, 134–146 (2006).

273. Vercauteren, D. *et al.* Flotillin-dependent endocytosis and a phagocytosis-like mechanism for cellular internalization of disulfide-based poly(amido amine)/DNA polyplexes. *Biomaterials* **32**, 3072–3084 (2011).

274. Harush-Frenkel, O., Rozentur, E., Benita, S. & Altschuler, Y. Surface Charge of Nanoparticles Determines Their Endocytic and Transcytotic Pathway in Polarized MDCK Cells. *Biomacromolecules* **9**, 435–443 (2008).

275. Peng, S.-F. *et al.* Effects of the nanostructure of dendrimer/DNA complexes on their endocytosis and gene expression. *Biomaterials* **31**, 5660–5670 (2010).

276. Ariffin, A. B., Forde, P. F., Jahangeer, S., Soden, D. M. & Hinchion, J. Releasing Pressure in Tumors: What Do We Know So Far and Where Do We Go from Here? A Review. *Cancer Res.* **74**, 2655–2662 (2014).

277. Stylianopoulos, T. *et al.* Coevolution of Solid Stress and Interstitial Fluid Pressure in Tumors During Progression: Implications for Vascular Collapse. *Cancer Res.* **73**, 3833–3841 (2013).

278. Isaka, N., Padera, T. P., Hagendoorn, J., Fukumura, D. & Jain, R. K. Peritumor Lymphatics Induced by Vascular Endothelial Growth Factor-C Exhibit Abnormal Function. *Cancer Res.* **64**, 4400–4404 (2004).

279. Jain, R. K. & Stylianopoulos, T. Delivering nanomedicine to solid tumors. (2010). doi:10.1038/nrclinonc.2010.139

280. Ferretti, S. *et al.* Patupilone Induced Vascular Disruption in Orthotopic Rodent Tumor Models Detected by Magnetic Resonance Imaging and Interstitial Fluid Pressure. *Clin. Cancer Res.* **11**, 7773–7784 (2005).

281. Provenzano, P. P. *et al.* Enzymatic Targeting of the Stroma Ablates Physical Barriers to Treatment of Pancreatic Ductal Adenocarcinoma. *Cancer Cell* **21**, 418–429 (2012).

282. Eikenes, L., Bruland, Ø. S., Brekken, C. & Davies, C. de L. Collagenase Increases the Transcapillary Pressure Gradient and Improves the Uptake and Distribution of Monoclonal Antibodies in Human Osteosarcoma Xenografts. *Cancer Res.* **64**, 4768–4773 (2004).

283. Oh, D.-Y. *et al.* 260TiPPhase 3, randomized, double-blind, placebo-controlled study of PEGylated recombinant human hyaluronidase PH20 (PEGPH20)+nab-paclitaxel/gemcitabine in patients with previously untreated, hyaluronan-high, stage IV pancreatic ductal adenocarcinoma (PDA). *Ann. Oncol.* **28**, (2017).

284. A Study of PEGylated Recombinant Human Hyaluronidase in Combination With Nab-Paclitaxel Plus Gemcitabine Compared With Placebo Plus Nab-Paclitaxel and Gemcitabine in Participants With Hyaluronan-High Stage IV Previously Untreated Pancreatic Ductal Adenoca. Available at: https://clinicaltrials.gov/ct2/show/NCT02715804. (Accessed: 6th June 2016)

285. Scodeller, P. *et al.* Hyaluronan degrading silica nanoparticles for skin cancer therapy. *Nanoscale* **5**, 9690–9698 (2013).

286. Zhou, H. *et al.* Hyaluronidase Embedded in Nanocarrier PEG Shell for Enhanced Tumor Penetration and Highly Efficient Antitumor Efficacy. *Nano Lett.* acs.nanolett.6b00820 (2016). doi:10.1021/acs.nanolett.6b00820

287. Fernandez-Lafuente, R. molecules Editorial Special Issue: Enzyme Immobilization 2016. doi:10.3390/molecules22040601

288. Hong, Y. *et al.* Exosome as a Vehicle for Delivery of Membrane Protein Therapeutics, PH20, for Enhanced Tumor Penetration and Antitumor Efficacy. *Adv. Funct. Mater.* **28**, 1703074 (2018).

289. Dai, J. *et al.* Preparation and evaluation of tumour microenvironment response multistage nanoparticles for epirubicin delivery and deep tumour penetration. *Artif. Cells, Nanomedicine, Biotechnol.* **46**, 860–873 (2018).

290. Prathap, B. S., Dey, A., Rao, G. S., Johnson, P. L. & Arthanariswaran, P. A Review-Importance of RP-HPLC in Analytical Method Development. (2013).

291. Dorsey, J. G. & Cooper, W. T. Retention mechanisms of bonded-phase liquid chromatography. *Anal. Chem.* **66**, 857A–867A (1994).

292. *Reversed Phase Chromatography Principles and Methods*.

293. Dorfman, A. & Ott, M. L. *A TURBIDIMETRIC METHOD FOR THE ASSAY OF*

HYALURONIDASE Downloaded from.

294. CalcTool: Protein size calculator. Available at: http://www.calctool.org/CALC/prof/bio/protein_size. (Accessed: 16th January 2019)

295. Monroe Freeman, R. E., Anderson, P., Wezster, M. E. & Dorfman, A. *ETHANOLIC FRACTIONATION OF BOVINE TESTICULAR HYALURONIDASE Downloaded from*.

296. Hanefeld, U., Cao, L. & Magner, E. Enzyme immobilisation: fundamentals and application. *Chem. Soc. Rev.* **42**, 6211 (2013).

297. Karmakar, S. Enzyme Activity - an overview | ScienceDirect Topics. in *Handbook of Nanomaterials for Industrial Applications* (2018).

298. Arming, S., Strobl, B., Wechselberger, C. & Kreil, G. In Vitro Mutagenesis of PH-20 Hyaluronidase from Human Sperm. *Eur. J. Biochem.* **247**, 810–814 (1997).

299. Verbaan, F. J. *et al.* The fate of poly(2-dimethyl amino ethyl)methacrylate-based polyplexes after intravenous administration. *Int. J. Pharm.* **214**, 99–101 (2001).

300. OWENSIII, D. & PEPPAS, N. Opsonization, biodistribution, and pharmacokinetics of polymeric nanoparticles. *Int. J. Pharm.* **307**, 93–102 (2006).

301. Moghimi, S. M., Hunter, A. C. & Murray, J. C. Long-circulating and target-specific nanoparticles: theory to practice. *Pharmacol. Rev.* **53**, 283–318 (2001).

302. Verbaan, F. J. *et al.* Steric stabilization of poly(2-(dimethylamino)ethyl methacrylate)-based polyplexes mediates prolonged circulation and tumor targeting in mice. *J. Gene Med.* **6**, 64–75 (2004).

303. DEWOLF, H. *et al.* Effect of cationic carriers on the pharmacokinetics and tumor localization of nucleic acids after intravenous administration. *Int. J. Pharm.* **331**, 167–175 (2007).

304. Nyamay'antu, A., Dumont, M., Kedinger, V. & Erbacher, P. Non-Viral Vector Mediated Gene Delivery: the Outsider to Watch Out For in Gene Therapy. doi:10.18609/cgti.2019.007

305. Dhuria, S. V., Hanson, L. R. & Frey, W. H. Intranasal delivery to the central nervous system: Mechanisms and experimental considerations. *J. Pharm. Sci.* **99**, 1654–1673 (2010).

306. Hashizume, R. *et al.* New therapeutic approach for brain tumors: Intranasal delivery of telomerase inhibitor GRN163. *Neuro. Oncol.* **10**, 112–120 (2008).

307. Nonaka, N., Farr, S. A., Kageyama, H., Shioda, S. & Banks, W. A. Delivery of Galanin-Like Peptide to the Brain: Targeting with Intranasal Delivery and Cyclodextrins. *J. Pharmacol. Exp. Ther.* **325**, 513–519 (2008).

308. Charlton, S. T. *et al.* Evaluation of Direct Transport Pathways of Glycine Receptor Antagonists and an Angiotensin Antagonist from the Nasal Cavity to the Central Nervous System in the Rat Model. *Pharm. Res.* **25**, 1531–1543 (2008).

309. Harmon, B. T. *et al.* Intranasal administration of plasmid DNA nanoparticles yields successful transfection and expression of a reporter protein in rat brain. *Gene Ther.* **21**, 514–521 (2014).

310. Das, M., Wang, C., Bedi, R., Mohapatra, S. S. & Mohapatra, S. Magnetic micelles for DNA delivery to rat brains after mild traumatic brain injury. *Nanomedicine Nanotechnology, Biol. Med.* **10**, 1539–1548 (2014).

311. Cory, A. H., Owen, T. C., Barltrop, J. A. & Cory, J. G. Use of an aqueous soluble tetrazolium/formazan assay for cell growth assays in culture. *Cancer Commun.* **3**, 207–12 (1991).

312. Berridge, M. V. & Tan, A. S. Characterization of the Cellular Reduction of 3-(4,5-dimethylthiazol-2-yl)-2,5-diphenyltetrazolium bromide (MTT): Subcellular Localization, Substrate Dependence, and Involvement of Mitochondrial Electron Transport in MTT Reduction. *Arch. Biochem. Biophys.* **303**, 474–482 (1993).

313. Ford, C. H. J., Richardson, V. J. & Tsaltas, G. Comparison of tetrazolium colorimetric and [3H]-uridine assays for in vitro chemosensitivity testing. *Cancer Chemother. Pharmacol.* **24**, 295–301 (1989).

314. Geiger, R., Schneider, E., Wallenfels, K. & Miska, W. A new ultrasensitive bioluminogenic enzyme substrate for beta-galactosidase. *Biol. Chem. Hoppe. Seyler.* **373**, 1187–91 (1992).

315. Uchegbu, I. F. *Home Office*. (2017).

316. Piao, J.-G., Yan, J.-J., Wang, M.-Z., Wu, D.-C. & You, Y.-Z. A new method to cross-link a polyplex for enhancing in vivo stability and transfection efficiency. *Biomater. Sci.* **2**, 390–398 (2014).

317. Mann, A., Richa, R. & Ganguli, M. DNA condensation by poly-l-lysine at the single molecule level: Role of DNA concentration and polymer length. *J. Control. Release* **125**, 252–262 (2008).

318. Cherng, J. Y., Talsma, H., Verrijk, R., Crommelin, D. J. & Hennink, W. E. The effect of formulation parameters on the size of poly-((2-dimethylamino)ethyl methacrylate)-plasmid complexes. *Eur. J. Pharm. Biopharm.* **47**, 215–24 (1999).

319. Chono, S., Tanino, T., Seki, T. & Morimoto, K. Uptake characteristics of liposomes by rat alveolar macrophages: influence of particle size and surface mannose modification. *J. Pharm. Pharmacol.* **59**, 75–80 (2007).

320. Yin Win, K. & Feng, S.-S. Effects of particle size and surface coating on cellular uptake of polymeric nanoparticles for oral delivery of anticancer drugs. *Biomaterials* **26**, 2713–2722 (2005).

321. Eastman, S. . *et al.* Biophysical characterization of cationic lipid:DNA complexes. *Biochim. Biophys. Acta - Biomembr.* **1325**, 41–62 (1997).

322. Cardarelli, F. *et al.* The intracellular trafficking mechanism of Lipofectamine-based transfection reagents and its implication for gene delivery. *Sci. Rep.* **6**, 25879 (2016).

323. Meuli, M. *et al.* Efficient Gene Expression in Skin Wound Sites Following Local Plasmid Injection. *J. Invest. Dermatol.* **116**, 131–135 (2001).

324. Chesnoy, S. & Huang, L. Enhanced cutaneous gene delivery following intradermal injection of naked DNA in a high ionic strength solution. *Mol. Ther.* **5**, 57–62 (2002).

325. Guan, X. *et al.* Injection site-dependent induction of immune response by DNA vaccine: comparison of skin and spleen as a target for vaccination. *J. Gene Med.* n/a-n/a (2010). doi:10.1002/jgm.1432

326. Gaffal, E. *et al.* Comparative evaluation of CD8+CTL responses following gene gun immunization targeting the skin with intracutaneous injection of antigen-transduced dendritic cells. *Eur. J. Cell Biol.* **86**, 817–826 (2007).

327. Osborn, M. J. *et al.* Minicircle DNA-based Gene Therapy Coupled With Immune Modulation Permits Long-term Expression of α-L-Iduronidase in Mice With Mucopolysaccharidosis Type I. *Mol. Ther.* **19**, 450–460 (2011).

328. Chen, J.-K., Shen, C.-R. & Liu, C.-L. N-acetylglucosamine: production and applications. *Mar. Drugs* **8**, 2493–516 (2010).

329. Ksander, G. A. & Alto, P. Definitions in Biomaterials, Progress in Biomedical Engineering, Vol. 4. *Ann. Plast. Surg.* **21**, 291 (1988).

330. Huang, M., Khor, E. & Lim, L.-Y. *Uptake and Cytotoxicity of Chitosan Molecules and Nanoparticles: Effects of Molecular Weight and Degree of Deacetylation*. (2004).

331. Nafee, N., Schneider, M., Schaefer, U. F. & Lehr, C.-M. Relevance of the colloidal stability of chitosan/PLGA nanoparticles on their cytotoxicity profile. *Int. J. Pharm.* **381**, 130–139 (2009).

332. Silva, C. M., Veiga, F., Ribeiro, A. J., Zerrouk, N. & Arnaud, P. Effect of Chitosan-Coated Alginate Microspheres on the Permeability of Caco-2 Cell Monolayers. *Drug Dev. Ind. Pharm.* **32**, 1079–1088 (2006).

333. Sohaebuddin, S. K., Thevenot, P. T., Baker, D., Eaton, J. W. & Tang, L. Nanomaterial cytotoxicity is composition, size, and cell type dependent. *Part. Fibre Toxicol.* **7**, 22 (2010).

334. Dane, K. Y. *et al.* Nano-sized drug-loaded micelles deliver payload to lymph node immune cells and prolong allograft survival. *J. Control. Release* **156**, 154–160 (2011).

335. Allen, T. M., Hansen, C. B. & Guo, L. S. Subcutaneous administration of liposomes: a comparison with the intravenous and intraperitoneal routes of injection. *Biochim. Biophys. Acta* **1150**, 9–16 (1993).

336. Corthésy, B. & Bioley, G. Lipid-Based Particles: Versatile Delivery Systems for Mucosal Vaccination against Infection. *Front. Immunol.* **9**, 431 (2018).

337. Lukacs, G. L. *et al.* Size-dependent DNA Mobility in Cytoplasm and Nucleus. *J. Biol. Chem.* **275**, 1625–1629 (2000).

338. Gänger, S. & Schindowski, K. Tailoring Formulations for Intranasal Nose-to-Brain

Delivery: A Review on Architecture, Physico-Chemical Characteristics and Mucociliary Clearance of the Nasal Olfactory Mucosa. *Pharmaceutics* **10**, 116 (2018).

339. Sanchez-Ramos, J. *et al.* Chitosan-Mangafodipir nanoparticles designed for intranasal delivery of siRNA and DNA to brain. *J. Drug Deliv. Sci. Technol.* **43**, 453–460 (2018).

340. BOLTE, S. & CORDELIÈRES, F. P. A guided tour into subcellular colocalization analysis in light microscopy. *J. Microsc.* **224**, 213–232 (2006).

341. Cohen, R. N., van der Aa, M. A. E. M., Macaraeg, N., Lee, A. P. & Szoka Jr., F. C. Quantification of plasmid DNA copies in the nucleus after lipoplex and polyplex transfection. *J. Control. Release* **135**, 166–174 (2009).

342. Almofti, M. R. *et al.* Cationic liposome-mediated gene delivery: biophysical study and mechanism of internalization. *Arch. Biochem. Biophys.* **410**, 246–53 (2003).

343. Wan, L., You, Y., Zou, Y., Oupický, D. & Mao, G. DNA Release Dynamics from Bioreducible Poly(amido amine) Polyplexes. *J. Phys. Chem. B* **113**, 13735–13741 (2009).

344. Seymour, P. A. & Sander, M. Immunohistochemical Detection of β-Galactosidase or Green Fluorescent Protein on Tissue Sections. in *Reporter Genes* 13–23 (Humana Press). doi:10.1007/978-1-59745-549-7_2

345. Buckley, S. M. K. *et al.* Luciferin Detection After Intranasal Vector Delivery Is Improved by Intranasal Rather Than Intraperitoneal Luciferin Administration. *Hum. Gene Ther.* **19**, 1050–1056 (2008).

346. Mofford, D. M. & Miller, S. C. Luciferins Behave Like Drugs. *ACS Chem. Neurosci.* **6**, 1273–1275 (2015).

347. Ghendon, Y. *et al.* Evaluation of properties of chitosan as an adjuvant for inactivated influenza vaccines administered parenterally. *J. Med. Virol.* **81**, 494–506 (2009).

348. Dzung, N. A. *et al. Chitosan Nanoparticle as a Novel Delivery System for A/H1n1 Influenza Vaccine: Safe Property and Immunogenicity in Mice*. (2011).

349. Jakóbisiak, M., Lasek, W. & Gołąb, J. Natural mechanisms protecting against cancer. *Immunol. Lett.* **90**, 103–122 (2003).

350. Xie, D. *et al.* Expression of cytoplasmic and nuclear Survivin in primary and secondary human glioblastoma. *Br. J. Cancer* **94**, 108–14 (2006).

351. Ohgaki, H. & Kleihues, P. Genetic Pathways to Primary and Secondary Glioblastoma. *Am. J. Pathol.* **170**, 1445–53 (2007).

352. Liu, Y., Miao, C., Wang, Z., He, X. & Shen, W. Survivin small interfering RNA suppresses glioblastoma growth by inducing cellular apoptosis. *Neural Regen. Res.* **7**, 924–31 (2012).

353. de la Fuente, M. *et al.* A nano-enabled cancer-specific ITCH RNAi chemotherapy booster for pancreatic cancer. *Nanomedicine Nanotechnology, Biol. Med.* **11**, 369–377 (2015).

9 APPENDIX

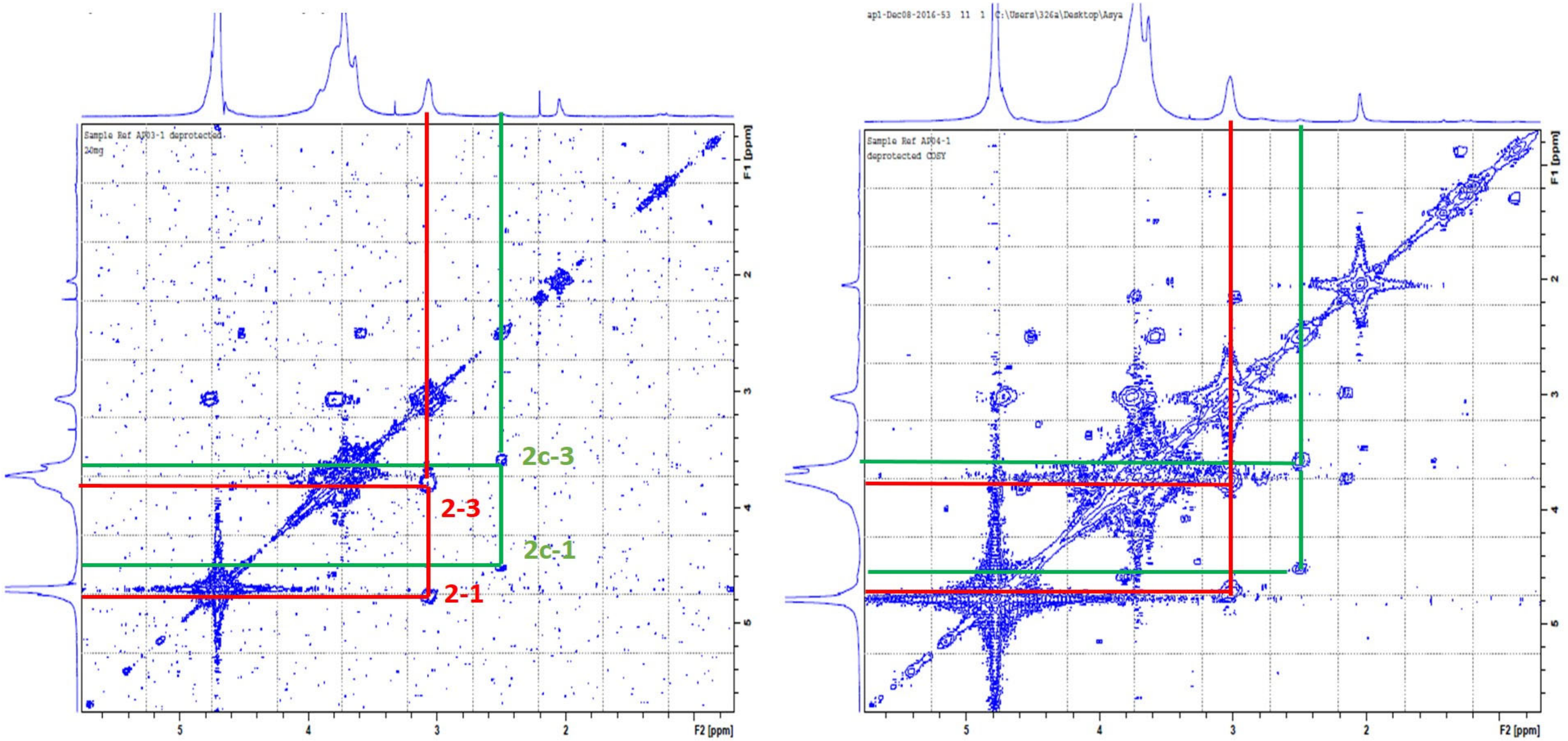

Figure 9-1: *Low substitution EAGC variants, (^1H-^1H COSY NMR of EA6GC37 and EA9GC21) (D_2O) , the 2D spectrum shows the protons* ***(2c),*** *which have the same correlations as protons* ***(2)****.*

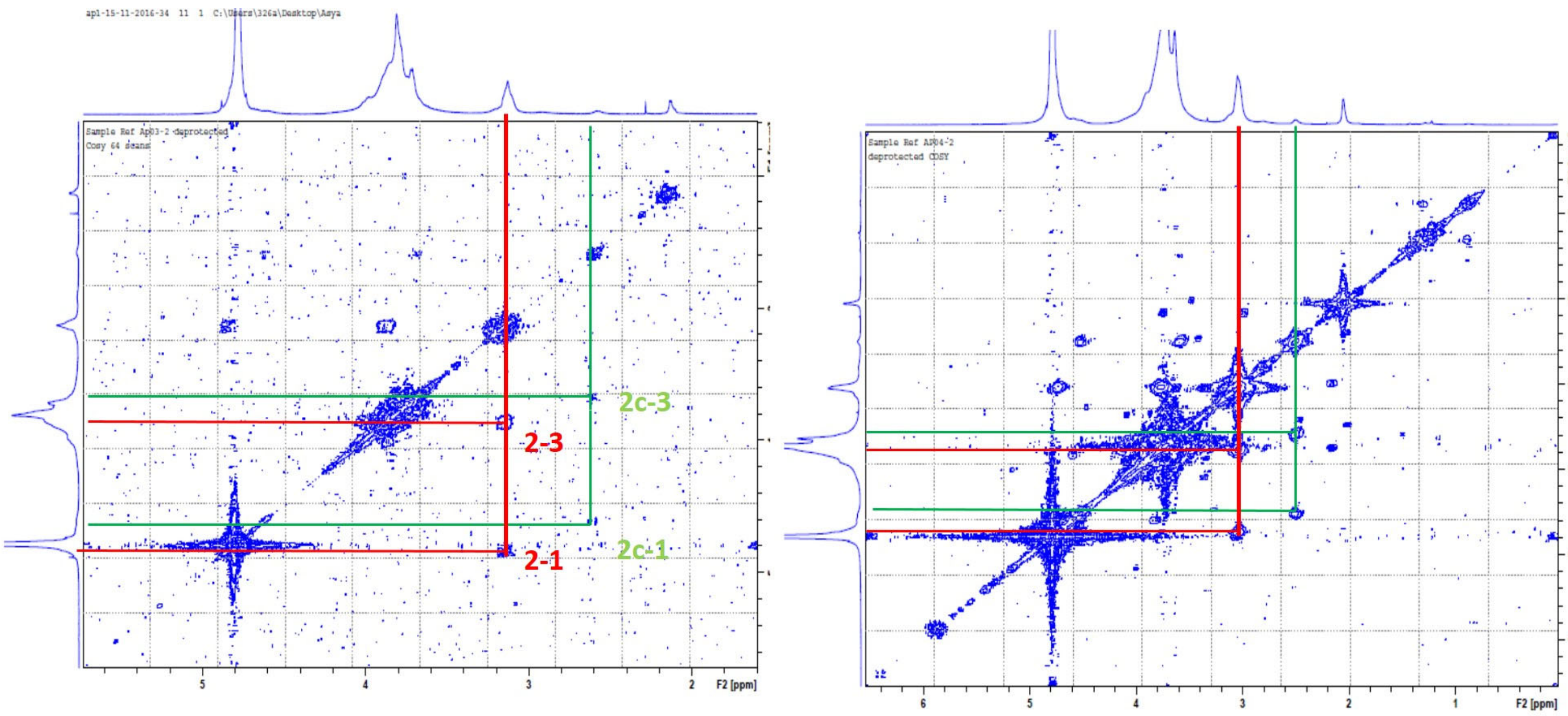

Figure 9-2: *Medium substitution EAGC variants,* *(^{1}H-^{1}H COSY NMR of EA13GC37 and EA16GC21) (D_2O) , the 2D spectrum shows the protons* ***(2c),*** *which have the same correlations as protons* ***(2)***

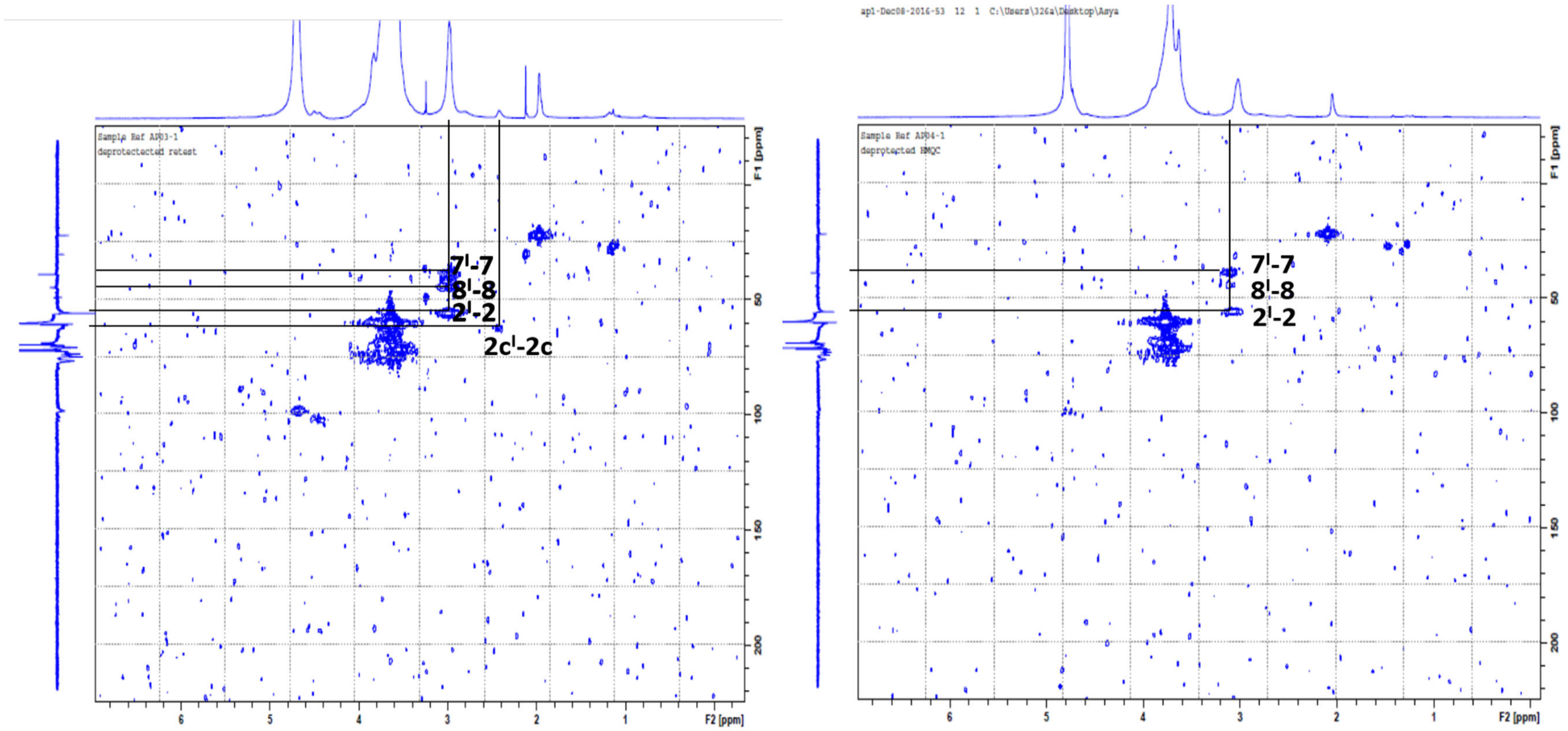

Figure 9-3:^{1}H-NMR – ^{13}C DEPT NMR) of EA6GC37 and EA9GC21 The ^{13}C spectrum is shown on the y axis, the carbons attached to the protons shown on the x axis are marked with the same number, but with a I as superscript. On the y axis **7^I** δ_{38}=[-**C**H$_2$-CH$_2$-NH$_2$, ethyl amino group], **8^I** δ_{44}=[-CH$_2$-**C**H$_2$-NH$_2$,, ethyl amino group],**2^I** $\delta_{55.3}$=[-CH-(OH)-**C**H-(NH$_2$)], ,**2c^I** δ_{61}= [-**C**H-N-(CH$_2$-CH$_2$NH$_2$)$_2$, double ethyl amino substitution of **2^I**,.

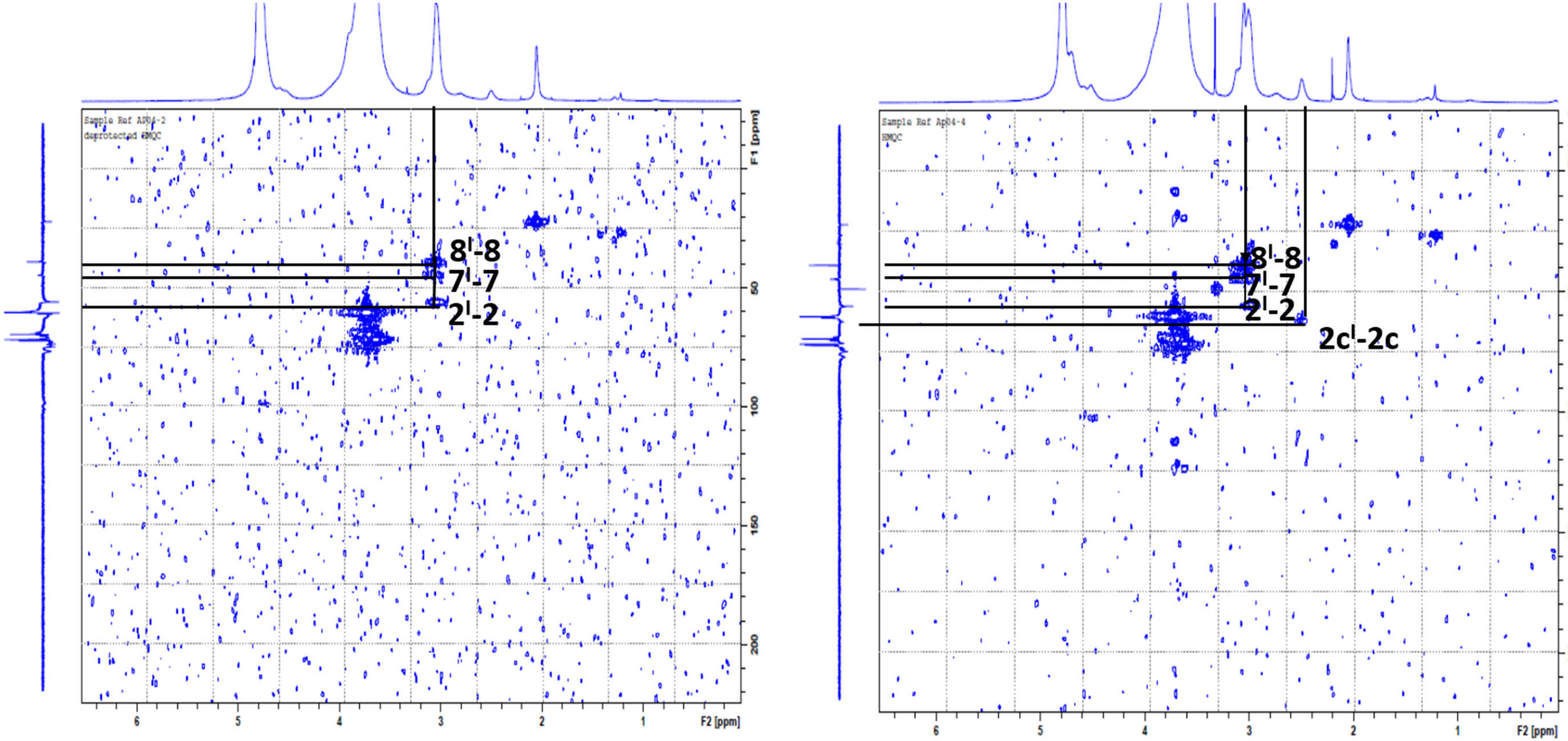

Figure 9-4: *^{1}H-NMR – ^{13}C DEPT NMR) of EA13GC37 and EA16GC21 The ^{13}C spectrum is shown on the y axis, the carbons attached to the protons shown on the x axis are marked with the same number, but with a I as superscript. On the y axis* ***7^I*** *δ_{38}=[-**C**H$_2$-CH$_2$-NH$_2$, ethyl amino group],* ***8^I*** *δ_{44}=[-CH$_2$-**C**H$_2$-NH$_2$,, ethyl amino group],**2^I** $\delta_{55.3}$=[-CH-(OH)-**C**H-(NH$_2$)], ,**2c^I** δ_{61}= [-**C**H-N-(CH$_2$-CH$_2$NH$_2$)$_2$, double ethyl amino substitution of **2^I**,.*

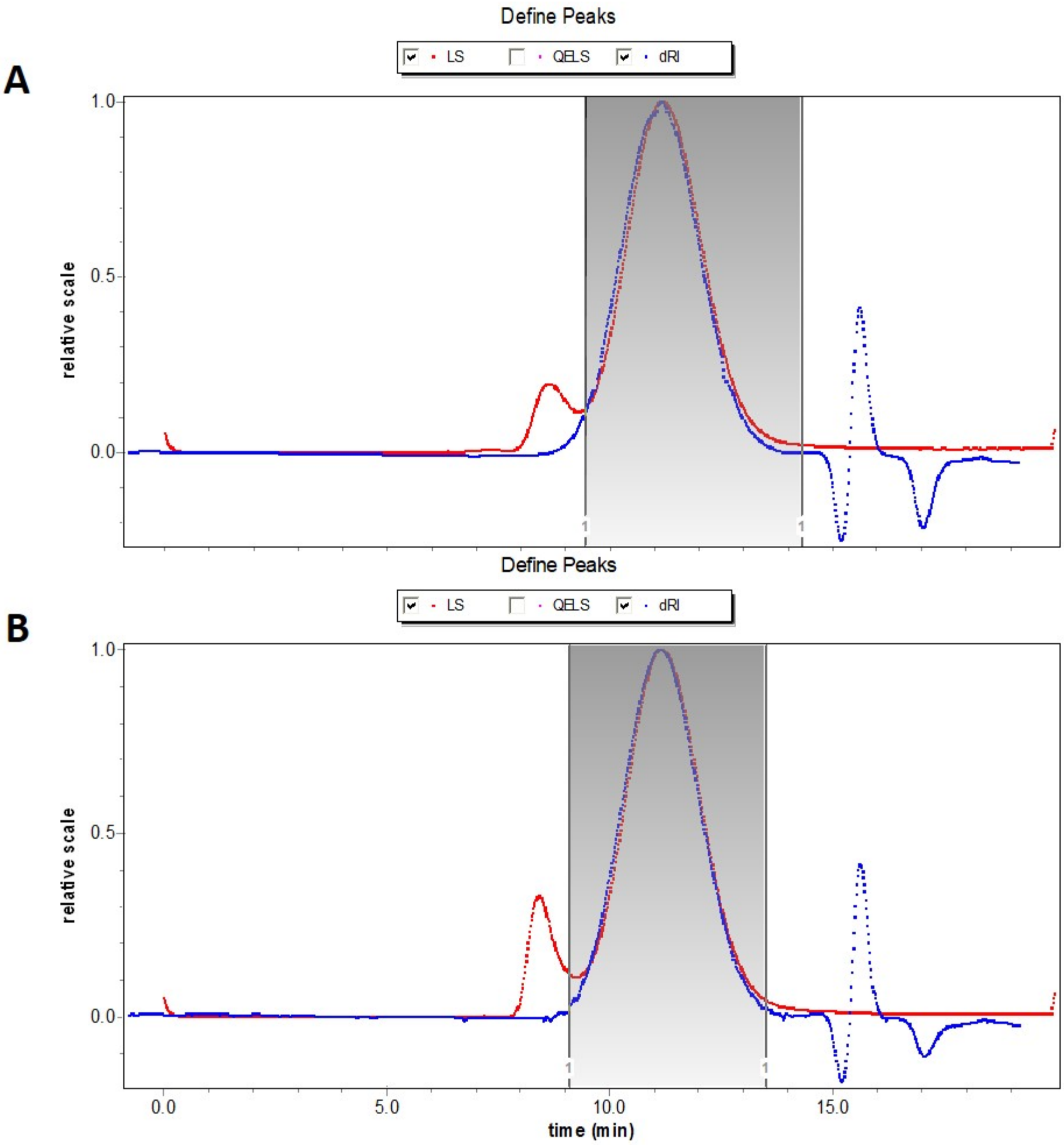

Figure 9-5:_LS and dRI spectra of EA24GC21 . The shoulder peak is visible after immediate addition of the running buffer to the sample and analysis **(A)** the intensity of the shoulder peak in the light scattering is increasing (**B**) after the sample is left incubating in the running buffer overnight._

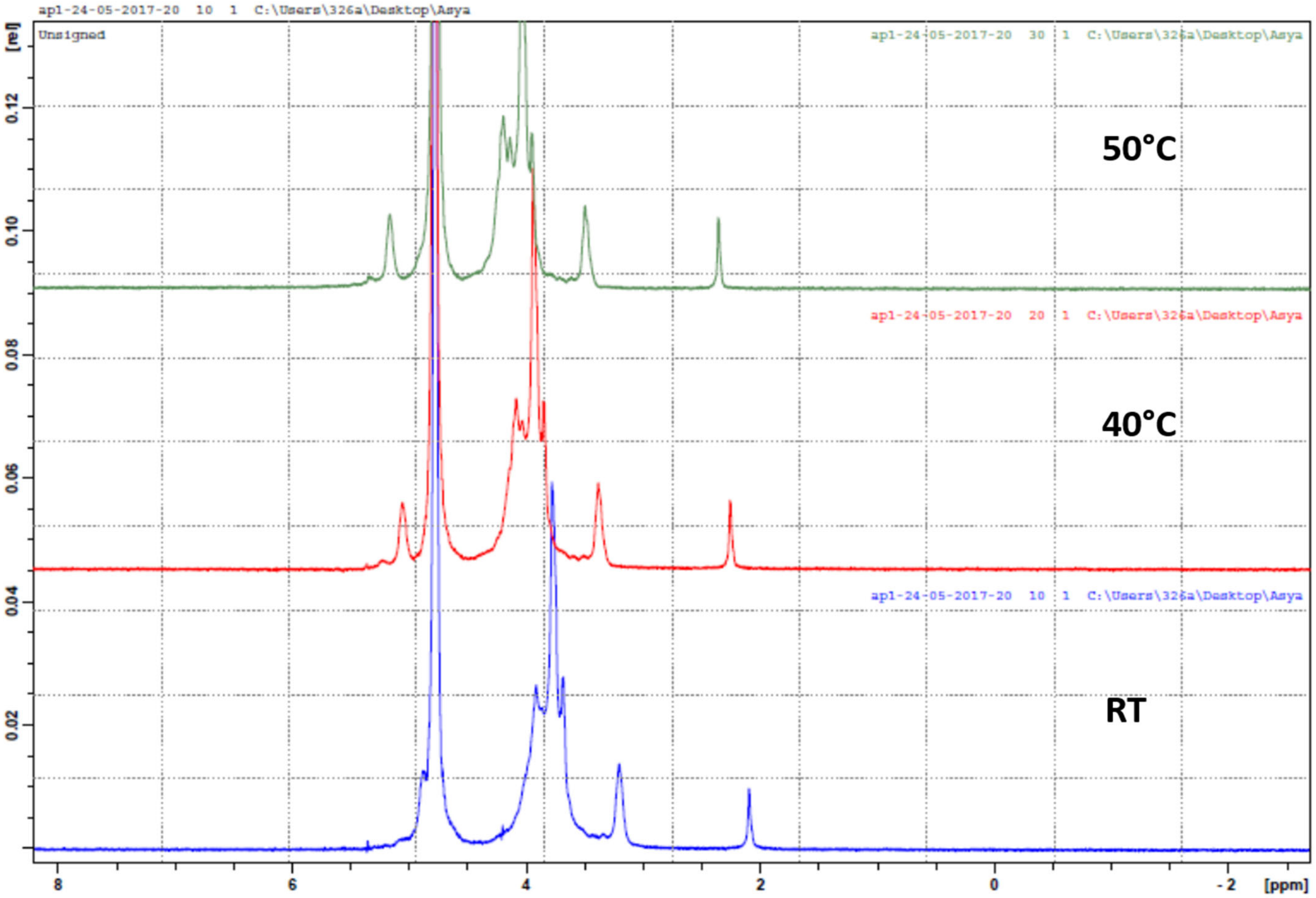

Figure 9-6: Temperature dependent downfield shift of the ^{1}H-^{1}H NMR spectrum of GC37 at pH < 2

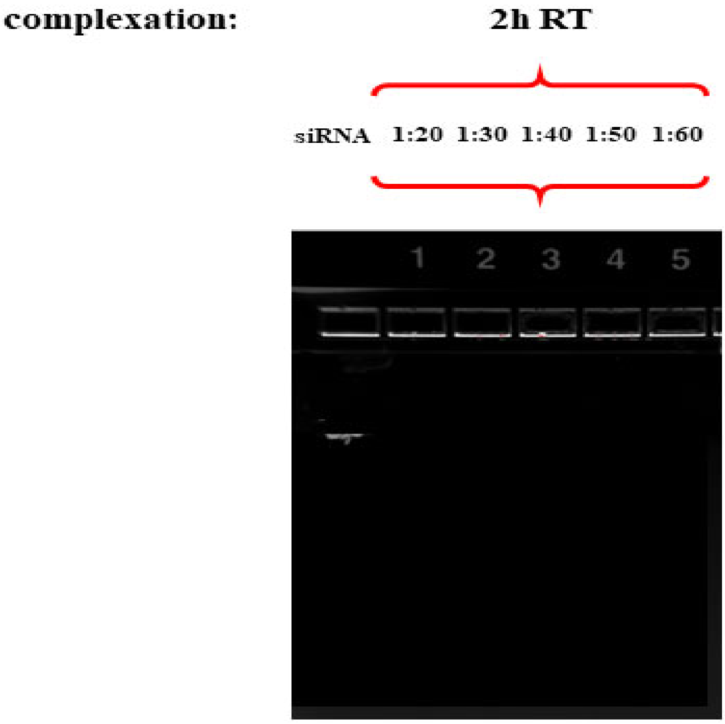

Figure 9-7 *Gel retardation assay with different mass ratios BS PEG (5) bis spermidine and siRNA*

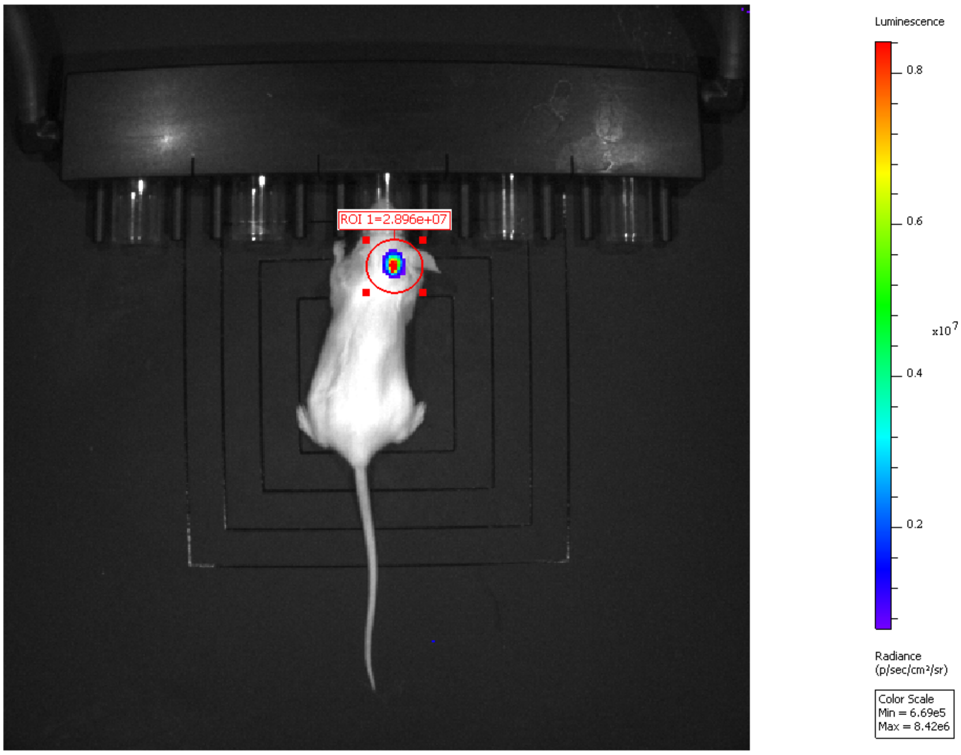

Figure 9-8: *Background luminesce after dosing LuGal substarte subcutaneously*

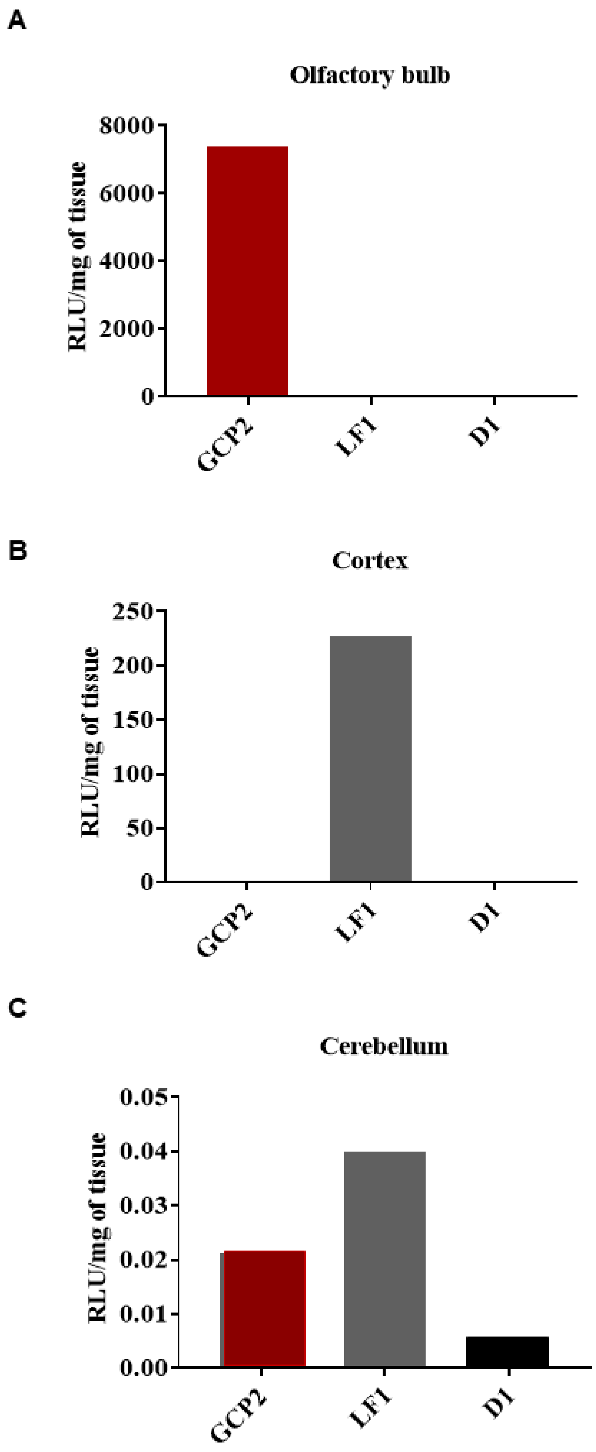

Figure 9-9: *β-Gal activity in tissue brain homogenates from olfactory bulb (**A**), cortex (**B**) and cerebellum (**C**) . GCP 2 results in high levels of active β-Gal enzyme in the olfactory bulb/brain (7382 RLU/mg of tissue) and low levels in the cerebellum (0.02 RLU/mg of tissue) and the cortex (0.05 RLU/mg of tissue). LF1 delivers β-Gal DNA predominantly to the cortex (228 RLU/mg of tissue) and olfactory bulb (0.23 RLU/mg of tissue) and very low levels in the cerebellum (0.04 RLU/mg of tissue). D1 showed almost not detectable levels of active enzyme in any of the organs.*

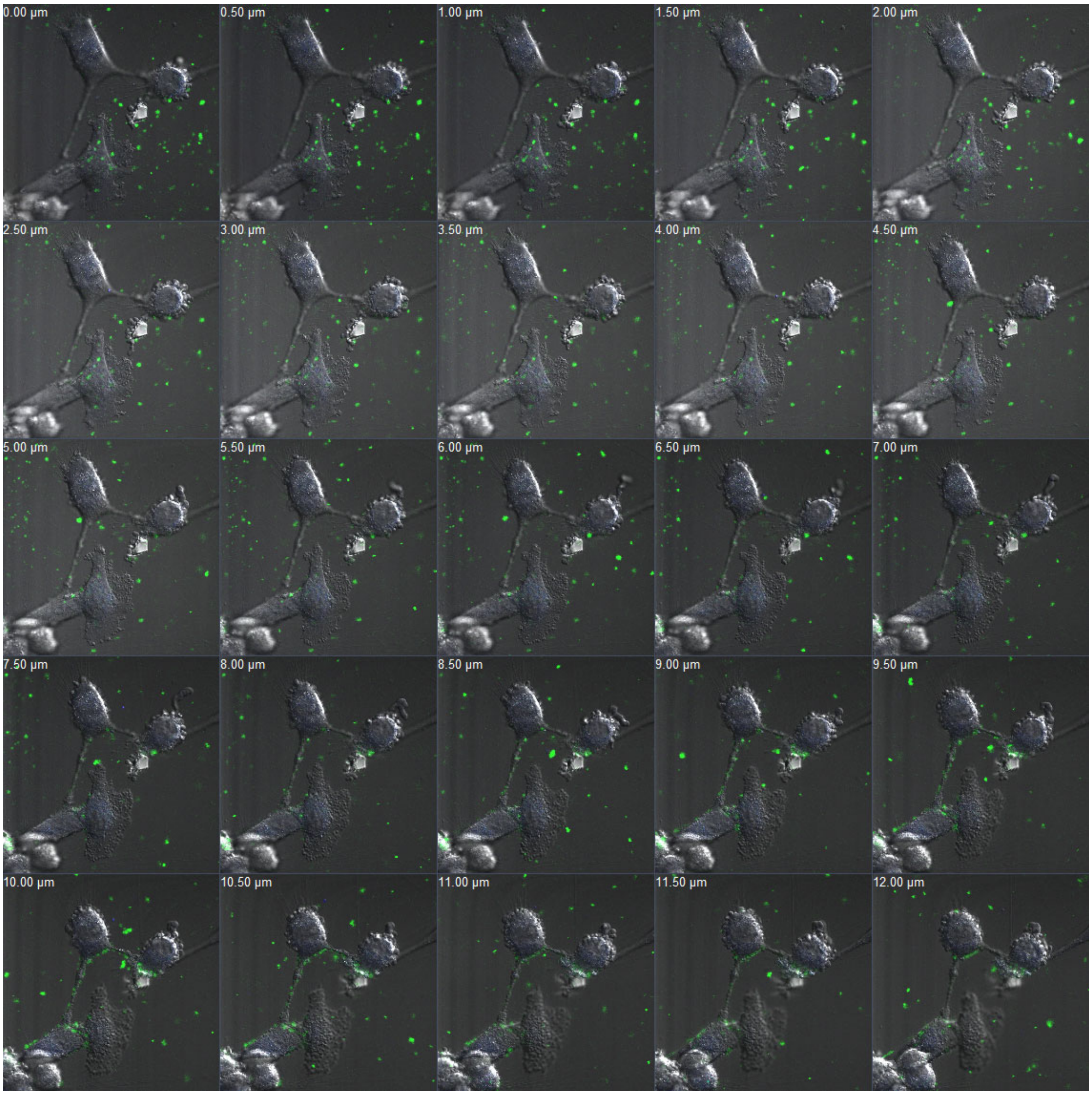

Figure 9-10: Z-stack of polyplex showing the polyplex (in green) is still outside the cell after 4 h treatment time.

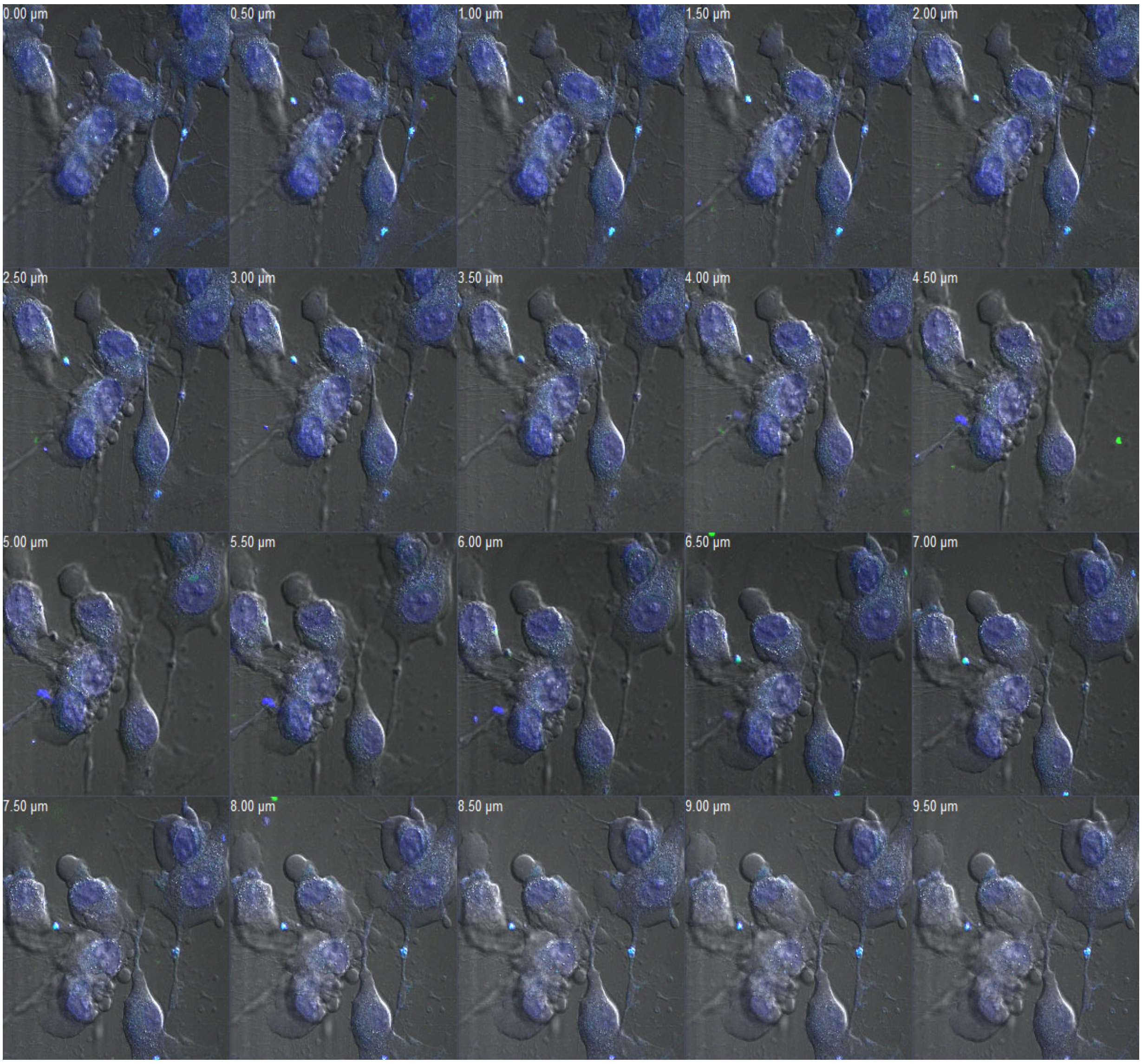

Figure 9-11: *Z stack of Lipofectamine/β-Gal DNA confirming lipofectamine delivered β-Gal to the nucleus of U87 cells 4 h after treatment. The nucleus is stained in blue, while the β-Gal DNA (green). Colocalization (cyan) is visible in the nucleus in all optical sections.*

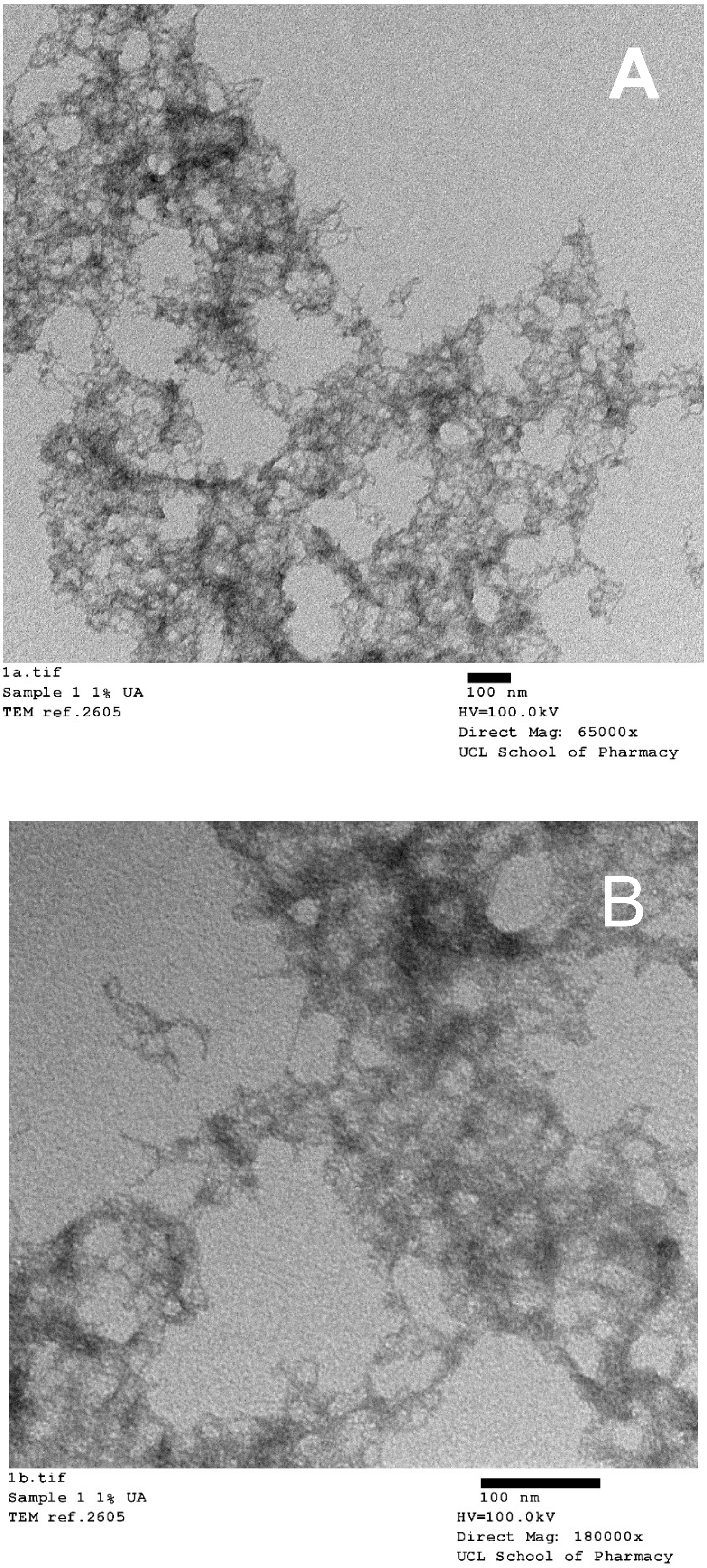

***Figure 9-12**: Representative TEM images of BS PEG (5) bis spermidine and β-Gal DNA at 30 to 1 (**A**) and 60 to 1 (**B**) mass ratios.*

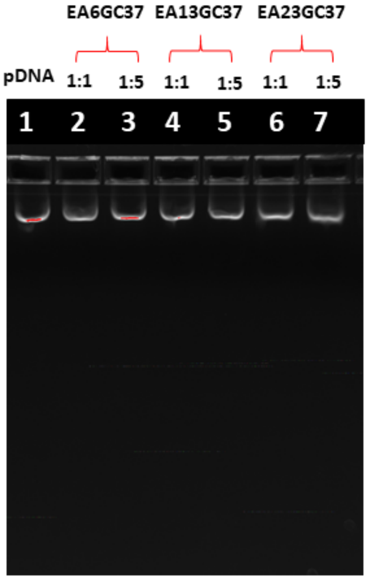

Figure 9-13: *Gel retardation assay of all EAGC variants at a 1 to 1 and 1 to 5 polymer to DNA ratio. Release of DNA is present for all polyplexes represented by a band corresponding to the one in lane 1, which is plasmid DNA alone.*